Engineering of Supramolecular Non-Gated and Gated Channels for Transmembrane Transport of Cation-Anion and Proton

विद्या वाचस्पति की
उपाधि की अपेक्षाओं की आंशिक पूर्ति में प्रस्तुत शोध प्रबंध

A Thesis
Submitted in Partial Fulfillment of the Requirements of the Degree of

Doctor of Philosophy

द्वारा / **By**

संदीप चट्टोपाध्याय / Sandip Chattopadhayay

पंजीकरण सं. / **Registration No: 20172020**

शोध प्रबंध पर्यवेक्षक: प्रो. पिनाकी तालुकदार

Thesis Supervisor: Prof. Pinaki Talukdar

भारतीय विज्ञान शिक्षा एवं अनुसंधान संस्थान पुणे
INDIAN INSTITUTE OF SCIENCE EDUCATION AND RESEARCH PUNE
2024

Dedicated to…

Maa Baba

INDIAN INSTITUTE OF SCIENCE EDUCATION AND RESEARCH (IISER), PUNE
(An Autonomous Institution, Ministry of Human Resource Development, Govt. of India)
Department of Chemistry, Main building,
Dr. Homi Bhaba Road, Pashan, Pune India 411008.

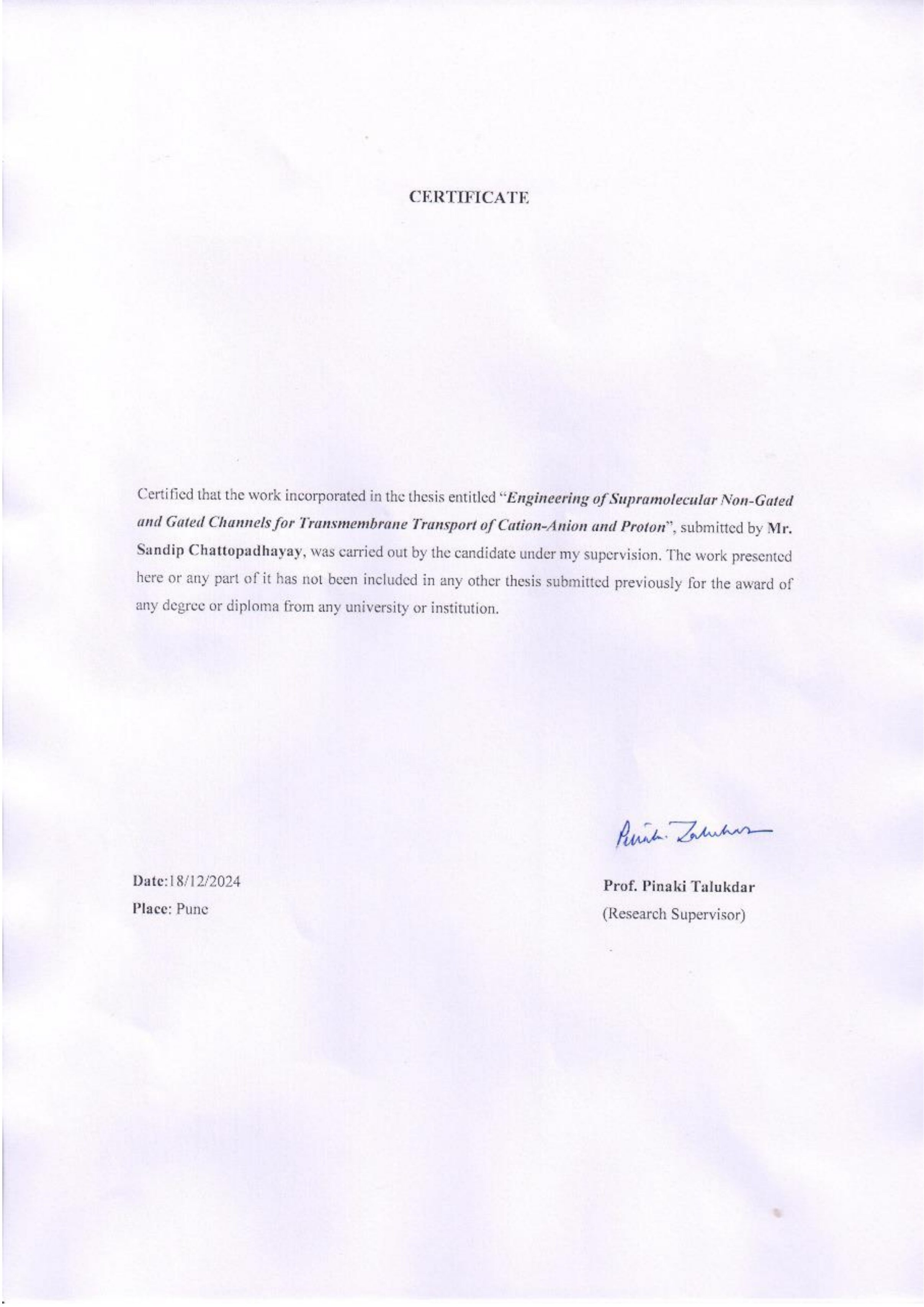

CERTIFICATE

Certified that the work incorporated in the thesis entitled "*Engineering of Supramolecular Non-Gated and Gated Channels for Transmembrane Transport of Cation-Anion and Proton*", submitted by **Mr. Sandip Chattopadhayay**, was carried out by the candidate under my supervision. The work presented here or any part of it has not been included in any other thesis submitted previously for the award of any degree or diploma from any university or institution.

Date:18/12/2024
Place: Pune

Prof. Pinaki Talukdar
(Research Supervisor)

Email: ptalukdar@iiserpune.ac.in
Ph: +91-20-25908098

Indian Institute of Science Education and Research (IISER), Pune

Declaration

Name of Student: **Sandip Chattopadhayay**

Reg. No.: **20172020**

Thesis Supervisor(s): **Prof. Pinaki Talukdar**

Department: **Chemistry**

Date of joining program: **1st August, 2017**

Date of Pre-Synopsis Seminar: **26th June, 2024**

Title of Thesis: **Engineering of Supramolecular Non-Gated and Gated Channels for Transmembrane Transport of Cation-Anion and Proton.**

I declare that this written submission represents my idea in my own words and where others' ideas have been included; I have adequately cited and referenced the original sources. I declare that I have acknowledged collaborative work and discussions wherever such work has been included. I also declare that I have adhered to all principles of academic honesty and integrity and have not misrepresented or fabricated or falsified any idea/data/fact/source in my submission. I understand that violation of the above will be cause for disciplinary action by the Institute and can also evoke penal action from the sources which have thus not been properly cited or from whom proper permission has not been taken when needed.

The work reported in this thesis is the original work done by me under the guidance of Prof. Pinaki Talukdar.

Sandip Chattopadhayay

Date: 24/12/2024

Sandip Chattopadhayay
Reg. No.: 20172020

Acknowledgement

Throughout the course of my Ph.D. experience, I have had the distinct honour of engaging with numerous remarkable individuals whose encouragement and support were instrumental in fulfilling this academic endeavour. In the subsequent section, I wish to express my heartfelt appreciation to these esteemed contributors.

I extend my profound gratitude to my thesis supervisor, Prof. Pinaki Talukdar, for graciously accepting me as his student and for introducing me to the captivating discipline of different research fields of supramolecular chemistry. I deeply appreciate the opportunity he provided for me to conduct my research within his laboratory, which was essential for the completion of my thesis work. His extensive expertise in the research domain, along with his constructive critiques, insightful suggestions, unwavering encouragement, and continual support, have been indispensable in the successful completion of my thesis. Finally, I convey my heartfelt appreciation to him for helping me to understand science by looking at it from a different perspective and helping to grow the seeds of knowledge in me, which will undoubtedly help me in every way of my life.

I extend my gratitude to the former Director, Prof. K. N. Ganesh, Prof. Jayant B. Udgaonkar, and the current director, Prof. Sunil S. Bhagwat, for providing exceptional infrastructure and state-of-the-art research facilities at the Indian Institute of Science Education and Research Pune.

I would like to acknowledge the former chairman of the Chemistry department, Prof. M. Jayakannan, Prof. Hosahudya N. Gopi, the current chairman, Prof. Nirmalya Ballav, and all faculty members and support staff of the chemistry department for their invaluable assistance.

I express my heartfelt thanks to Prof. Ayan Datta from the Indian Association for the Cultivation of Science and Dr. Jagannath Mondal from TIFR Hyderabad for their enlightening discussions and support, which were instrumental in the advancement of the molecular dynamics (MD) simulation model of ion channels and enriched our understanding of their ion permeation across the bilayer membrane. Furthermore, I wish to acknowledge Dr. Nixon M. Abraham from IISER Pune and Dr. Shilpy Sharma from Savitribai Phule Pune University (SPPU) for their valuable discussions and assistance in exploring the biological studies of our transporter molecules. I am also appreciative of their students, Mr. Anupam Ghosh, Dr. Titas Kumar Mukhopadhyay, Dr. Susmita Sarkar, Mrs. Karishma Shaw, and Ms. Triveni Sodnawar, for their contributions.

I would like to thank Prof. Thomas J. Pucadyil from IISER Pune and his student, Dr. Soumya Bhattacharyya, for their assistance during the imaging of giant unilamellar vesicles (GUVs).

Acknowledgement

I would like to thank Dr. DebanjanTewari, Institute of Physiology II University Hospital FSU, Jena, for his valuable discussion.

I wish to convey my profound gratitude to my past and present laboratory colleagues, including Dr. Sopan Valiba Shinde, Dr. Harshali Khatod, Dr. Javid Ahmad Malla, Dr. Debashis Mondal, Dr. Manzoor Ahmad, Dr. Rashmi Sharma, Dr. Avisikta Upadhyay, Dr. Abhishek Mondal, Dr. Swati B. Salunke, Dr. Naveen Joseph Roy, Akram, Debarati, Debraj, Payel, Soumyajit, Neelam, Shaharukh, Tanvi, Umesh, Ranjit, Arshad, Anjana, Anurag, Parappa, Paras, Kshitij, Ankit, Shradha, Shouvik, Ronedy, Arkajit, Kavan, Shreya, Ahan, Mayur, and Anirban. They fostered a collegial and jovial atmosphere within the laboratory, and without their collaborative efforts, the completion of this research endeavour would have been unattainable.

I extend my heartfelt appreciation to Sandeep Kanade, Ravinder Malothu, Nitin Dalvi, Dr. Sandeep Mishra, Mayuresh Kulkarni, Mahesh Jadav, Ganesh Dimbar, Tushar Kurulkar, and Sayalee Damle for their valuable assistance.

I wish to acknowledge the Prime Minister's Research Fellowship (PMRF) and the Indian Institute of Science Education and Research (IISER) Pune for their support throughout my research endeavour.

I am grateful to all of my IPhD-2017 cohort for their immeasurable support during my doctoral journey.

I consider myself fortunate to have remarkable friends, including Dr. Sumanta Let, Dr. Kingshuk Roy, Dr. Debashree Roy, Shahidkhan Pathan, Gourab K. Dam, Rishu Kumar Pandey, Chhabi Pal, and Dr. Suprovo Ghosh, whose unwavering support and affection enabled me to navigate this unforgettable journey.

I wish to express my gratitude to my family within IISER Pune, comprising Susobhan, Arindam, and Sanyukta for their steadfast support during the fluctuating journey of my Ph.D. life. I cannot express their help in a few words.

Finally, I am deeply grateful for the unconditional love, encouragement, and support of my family members [Maa, Baba, Dada, my sister-in-law Dola, and my beloved nephew Adrish (rik)] and Ankita, without whom I couldn't have attained this milestone.

Sandip Chattopadhayay

Table of Contents

Chapter 1: Introduction to Membrane Transport

Chapter 2: Supramolecular Barrel-Rosette Ion Channel Based on 3,5-Diaminobenzoic Acid for Cation-Anion Symport

Chapter 3: Heteroditopic "Pinakindole" [2]Catenanes as Molecular Wobbler Ion Channel for Transmembrane Transport of Ion-Pairs

Chapter 4: Ligand-Gated *Meta*-Dipropynylbenzene-Based Trimeric Barrel-Rosette Ion Channel for Cation-Anion Cotransport

Chapter 5: *Meta*-Dipropynylbenzene-Based Reversibly Ligand-Gated Dimeric Barrel-Rosette Channel with OFF–ON Proton Transport Activity

Abbreviations and Symbols

A

α	Alpha
Å	Angstrom
ATP	Adenosine Tri-Phosphate
ACN	Acetonitrile
Abs	Absorbance
ANTS	8-Aminonaphthalene-1,3,6-trisulfonic acid, disodium salt
a.u.	Arbitrary unit

B

BLM	Black lipid membrane/ Bilayer lipid membrane
Boc	Tert-butoxycarbonyl

C

c	Concentration
cm	Centimeter
CF	Carboxyfluorescein
$CuCl_2$	Copper chloride
Calc.	Calculated
CTD	Cytosolic domain
$CHCl_3$	Chloroform
$CDCl_3$	Deuterated chloroform
CH_3CN	Acetonitrile
CsCl	Cesium chloride
CCDC	Cambridge Crystallographic Data Centre
CGenFF	CHARMM General Force Field
Chol	Cholesterol
COSY	Correlation spectroscopy
CPK	Corey–Pauling–Koltun

D

δ	Delta (Chemical shift)
°C	Degree Celsius

D	Diffusion coefficient
d	Doublet
dd	Doublet of doublet
ddd	Doublet of doublet of doublet
dt	Doublet of triplet
DOPC	1,2-Dioleoyl-sn-glycero-3-phosphocholine
DPhPC	2-diphytanoyl-sn-glycero-3-phosphocholine
DMSO-d_6	Deuterated dimethylsulfoxide
DMSO	Dimethylsulfoxide
DCM	Dichloromethane
DFT	Density Functional Theory
DIPEA	*N*,*N*-Diisopropylethylamine
DOSY	Diffusion Ordered Spectroscopy
DMAP	4-Dimethylaminopyridine
DMF	Dimethylformamide
DPX	*p*-Xylene-bis-pyridinium bromide

E

EYPC	L-α-phosphatidylcholine from egg-yolk
EC_{50}	Effective concentration at half maximal activity
EtOAc	Ethylacetate
NEt_3	Triethylamine
ESI	Electrospray ionization
EDC·HCl	1-(3-Dimethylaminopropyl)-3-ethylcarbodiimide hydrochloride

F

F_t	Fluorescence intensity at time t
FCCP	Carbonyl cyanide-p-trifluoromethoxyphenylhydrazone

G

G_{hyd}	Free energy of hydration
GUV	Giant unilamellar vesicle
GABA	Gamma-aminobutyric acid

gA	Gramicidin

H

Hz	Hertz
h	Hour
HPTS	8-Hydroxypyrene-1,3,6-trisulfonate trisodium salt
HOBt	Hydroxybenzotriazole
HEPES	4-(2-hydroxyethyl)-1-piperazineethanesulfonic acid
HCl	Hydrochloric acid
HRMS	High Resolution Mass Spectrometry
H_2PO_4	Dihydrogen phosphate

I

I_F	Normalized Fluorescence Intensity
IR	Infrared spectroscopy
ISE	Ion selective electrode

J

J	Coupling constant

K

KCC	Potassium-chloride cotransporter
KGluconate	Potassium Gluconate
K_a	Association constant
Kcal	Kilocalorie
KCl	Potassium chloride
K_2EDTA	Dipotassium ethylenediaminetetraacetic acid
KOH	Potassium hydroxide
$KClO_4$	Potassium perchlorate

L

λ	Lambda
LUV	Large unilamellar vesicle

logP	Logarithmic form of a ratio of Partition Coefficient
LiCl	Lithium chloride

M

m	Multiplet
M	Molar
μM	Micromolar
μL	Microliter
MHz	Mega hertz
min	Minute(s)
max	Maxium
mg	Miligram(s)
mol	Mole
mmol	Milimole(s)
mM	Milimolar
mL	Mililiter
M.W.	Molecular weight
MeOH	Methanol
MD	Molecular dynamics

N

ν	Nu (for Infrared spectroscopy)
n	Hill coefficient
nm	Nanometer
nM	Nanomolar
NMR	Nuclear magnetic resonance
NIS	Na^+/I^- symporter
NCC	Sodium-chloride cotransporter
NaF	Sodium fluoride
NaCl	Sodium chloride
NaBr	Sodium bromide
Na_2SO_4	Sodium sulfate
$NaNO_3$	Sodium nitrate

$NaClO_4$	Sodium perchlorate
NaSCN	Sodium thiocyanate
NaOAc	Sodium acetate
NaOH	Sodium hydroxide
$NaPF_6$	Sodium hexafluorophosphate
NOESY	Nuclear Overhauser Effect Spectroscopy

O

obs	Observed
ORTEP	Oak Ridge Thermal Ellipsoid plot

P

pH	Potential of hydrogen
ppm	Parts per million
p-TSOH	*p*-Toluenesulfonic acid,
p	Pentet
PE	Pet ether
pKa	Negative logarithm of acid dissociation constant

Q

q	Quartet

R

R	Ideal gas constant
ρ	Resistivity
rt	Room tempeture
RbCl	Rubidium chloride

S

SGLT1	Sodium-glucose cotransporter 1
s	Singlet
s	Second(s)
SCXRD	Single crystal X-ray diffraction

T

t	Triplet
td	Triplet of doublets
t	Time
T_x	Triton X-100
TMD	Transmembrane domain
TLC	Thin Layer Chromatography
TBAF	Tetrabutylammonium fluoride
TBACl	Tetrabutylammonium chloride
TOF	Time of flight
THF	Tetrahydrofuran
TBA	Tetrabutyl ammonium
TES	2-[Tris(hydroxymethyl)-methylamino]-ethanesulfonic acid

V

Val	Valinomycin
VDW	van der Waals
V_{rev}	Reversible voltage

Y

Y	Fractional fluorescence intensity

Synopsis

The thesis entitled “***Engineering of Supramolecular Non-Gated and Gated Channels for Transmembrane Transport of Cation-Anion and Proton***” comprises five chapters.

This thesis aims to develop small molecule-based channel systems for the selective transport of cation-anion and proton across the membrane. The cation-anion cotransport is essential for adequate maintenance of the ionic concentration across the cellular membrane for appropriate physiological functions, including osmotic balance regulation, stabilization of resting potential, cell volume regulation, etc. Therefore, dysfunctions of these channels include different diseases collectively known as channelopathy. Alongside, the recent development of synthetic transporters has been shown in different therapeutic applications, including antibacterial, antimalarial, antimicrobial, and anticancer agents. Hence, decorating synthetic analogues will open up an avenue for utilizing these synthetic channels for different biomedical applications ranging from channelopathy to cancer. Here in this thesis, we engineered different supramolecular architectures to introduce different non-gated and gated cation-anion symporting channel systems. The ion transport behaviour of channels was conducted across various vesicular membranes and planer bilayer membranes.

Additionally, proton transfer stands out as perhaps the most vital and widespread chemical reaction that forms the backbone of biochemical activities, influencing the behaviour of ion channels, enzyme actions, charge distribution across membranes, pH modulation, etc. While certain proton pathways, like those present in bacteriorhodopsin and cytochrome c oxidase, have been thoroughly explored, the specific design principles for proton channels—including the necessary number of residues, their spatial arrangement, the number of pathways within a given molecule, and the pertinent pKa values of the involved residues are still insufficiently understood. Therefore, we have developed a proton channel system for selective translocation of the proton across the phospholipid membrane, which showed reversible ligand-gated OFF-ON proton transport behaviour.

Chapter 1: Introduction to Membrane Transport

Ion trafficking is meticulously regulated by specific membrane-embedded transmembrane proteins (carriers, channels, pores) to ensure precise modulation of ionic concentrations, which is essential for the maintenance of normal physiological functions. Cation-anion cotransporters represent a particular class of transmembrane proteins that facilitates the selective translocation of both cations and anions across the cellular membrane, thereby promoting the spontaneous establishment of transmembrane gradients. Nevertheless, mutations occurring in these intrinsic transmembrane proteins are implicated in various pathologies collectively referred to as channelopathies. The analysis of transmembrane protein structures and ion transport mechanisms encourages the scientific community to develop synthetic scaffolds to understand their properties and potential biomedical uses ranging from channelopathies to antibacterial agents to cancer. Therefore, we aimed to design different non-gated and gated supramolecular architectures with the intention of constructing synthetic cation-anion and proton channels.

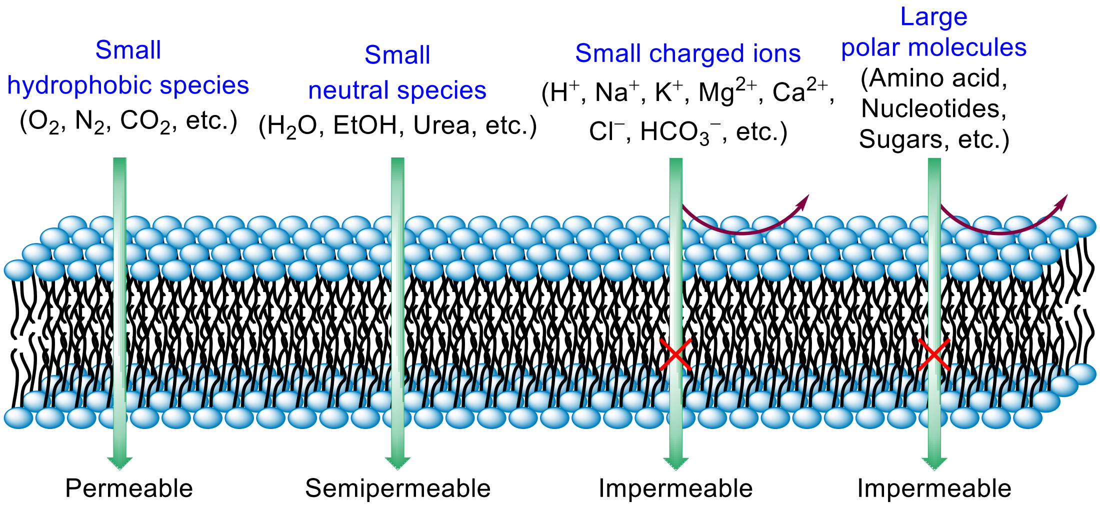

Figure 1 Schematic representation of transmembrane permeability of different species across the bilayer membrane.

Chapter 2: Supramolecular Barrel-Rosette Ion Channel Based on 3,5-Diaminobenzoic Acid for Cation-Anion Symport.

In this section, we have introduced a series of bis((*R*)-(−)-mandelic acid)-linked 3,5-aminobenzoic acid-based self-assembled barrel rosette ion channels. In-depth ion transport studies demonstrated compounds can transport both cations and anions via the symport process, having preferential selectivity towards the K^+ and ClO_4^- ions. The mode of ion transport was evaluated across the bilayer lipid membrane (BLM). The detailed experiments validated that the compound is forming an ion channel in the membrane for efficient cation-anion translocation. Further selectivity studies were carried out in the BLM, which confirmed that the channel has 2.1 times more permeable towards the ClO_4^- ion over the Cl^- ion and 1.5 times more permeable towards the K^+ ion over the Na^+ ion. An assessment of cation vs anion selectivity validated that the channel is 18.9 times more permeable towards the K^+ ion over the Cl^- ion. Finally, the detailed molecular dynamics (MD) simulation of the dimeric rosette validated that even for a very small extent of movement of Cl^- ion through the dimeric rosette the free energy barrier is significantly large, and therefore it is unlikely to pass through the cavity of the dimeric rosette channel. Further, MD simulation with the trimeric rosette of the channel confirmed the formation of the ion channel in the membrane and revealed of getting higher selectivity towards the $KClO_4$ over the KCl salt.

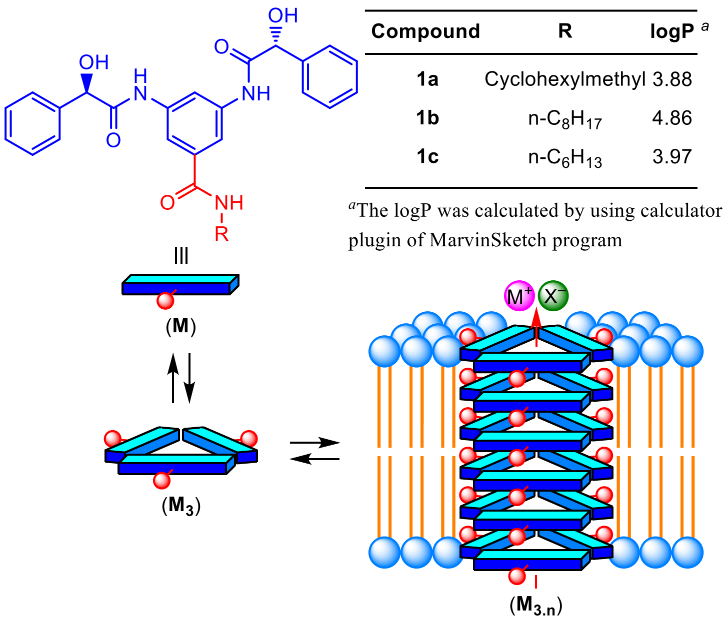

Compound	R	logP [a]
1a	Cyclohexylmethyl	3.88
1b	n-C_8H_{17}	4.86
1c	n-C_6H_{13}	3.97

[a]The logP was calculated by using calculator plugin of MarvinSketch program

Figure 2 Proposed model of barrel-rosette ion channel formation by these molecules **1a**–**1c** along with the structural description and logP values of designed channel molecules.

Chapter 2: Heteroditopic "Pinakindole" [2]Catenane as Molecular Wobbler Ion Channel for Transmembrane Transport of Ion-Pairs.

In this chapter, we developed a new supramolecular architecture to introduce an alternate synthetic ion channel system for transporting both cation and anion by forming a wobbler ion channel in the membrane. A detailed NOESY and DOSY NMR studies with **Pinakindole catenane 1** divulged the efficient molecular flipping of the compound upon sequential addition of the TBACl and $NAPF_6$ salts to effectively bind with both Na^+ and Cl^- ions in the respective ion binding pocket. Ion transport comparison validated that **Pinakindole catenane 1** has higher transport activity than its macrocyclic analogue **Pinakindole macrocycle 2**. In-depth, ion transport studies demonstrated that **Pinakindole catenane 1** efficiently supporting both cation and anion selectively across the membrane with the highest transport selectivity towards the Na^+ and Cl^- ions. A further mode of the transport process was evaluated with the bilayer lipid membrane (BLM) experiment, which divulged the formation of an ion channel in the membrane. Finally, theoretical studies were carried out to get an insight into the responsible conformational orientation of the **Pinakindole catenane 1** and the reason for molecular flipping in the presence of the salt.

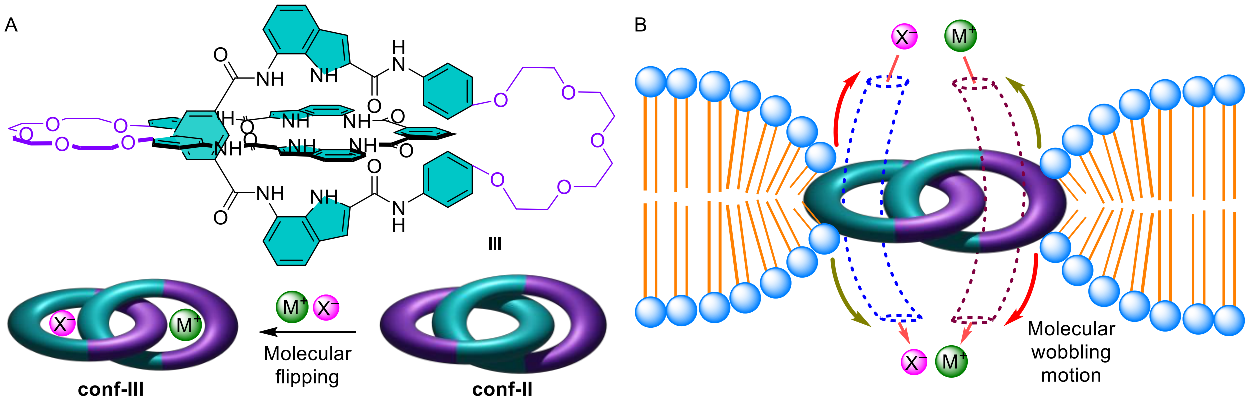

Figure 3 Channel structure and molecular flipping in the presence of metal-halide salt (A) and proposed model of wobbler ion channel formation by **Pinakindole catenane 1** within the bilayer membrane (B).

Chapter 4: Ligand-Gated *Meta*-Dipropynylbenzene-Based Trimeric Barrel-Rosette Ion Channel for Reversible OFF-ON Cation-Anion Cotransport.

In this section, we introduced the *meta*-dipropynylbenzene-based synthetic ion channel systems, which can synergistically transport cation and anion across the membrane. Self-assembly and morphological studies were carried out through the NMR and field emission scanning electron microscopy (FESEM), which indicated that the designed compound can self-aggregate and become more pronounced with an increase in the concentration of the compound. The ion transport property of the compound was investigated across the vesicular membrane using fluorometric experiments and NMR studies. Detailed ion transport studies confirmed that the compound has the tendency to transport both cation and anion across the membrane, having prominent selectivity towards the K^+ and Cl^- ions. An investigation into the mode of the transport process by utilizing the bilayer lipid membrane (BLM) validated that the compound is forming an ion channel in the membrane. Detailed selectivity studies in BLM validated that although the channel transports both K^+ and Cl^- ions, it has slightly preferential permeability towards the K^+ ion ($P_{Cl^-}/P_{K^+} = 0.35 \pm 0.9$). Furthermore, evaluation of the anion/anion and cation/cation selectivity validated the permeability ratio $P_{K^+}/P_{Na^+} = 3.5 \pm 0.8$ and $P_{Cl^-}/P_{Br^-} = 2.6 \pm 0.4$ confirmed that the channel has higher permeability towards the K^+ and Cl^- ions in comparisons with the Na^+ and Br^- ions, respectively. Interestingly, it was noticed that the compound is showing selectivity towards both the cation and anion under the physiological pH ranges (pH= 7.0-7.4). Ligand-gated chelation studies confirmed that the compound formed a 2:1 complex with Cu^{2+} ion, and the addition of K_2EDTA removed the chelated Cu^{2+} ion from the complex and regenerated the free channel molecule. A reversible chelation-deceleration upon sequential addition of $CuCl_2$ and K_2EDTA conformed compound showed efficient complexation and decomplexation even after five cycles. The ligand-gated reversible OFF-ON ion transport process was checked sequentially adding $CuCl_2$ and K_2EDTA using fluorescence and electrophysiological experiments, confirming that compound can be utilized as a reversible ligand-gated cation-anion channel. Finally, molecular dynamics simulation was investigated with the hexameric layer of the trimeric rosette to unveil the ion translocation pathways and investigate the reason for the higher permeability of the channel towards K^+ ion compared to the Cl^- ion, which showed well agreement with the experimental results. Hence, in this chapter, we successfully introduced an inaugural example of the ligand-gated reversible OFF-ON cation-anion symporter ion channel, which can pave a new avenue for generating synthetic reversible stimuli-gated cation-anion synthetic channel systems.

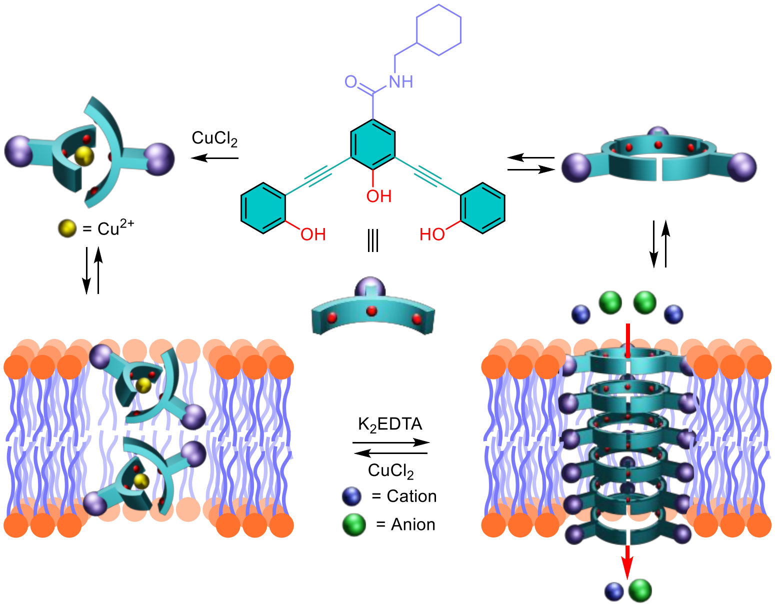

Figure 4 Structure of channel-forming compound and its ligand-gated reversible OFF-ON cotransport activity in the presence of $CuCl_2$ and K_2EDTA across the bilayer membrane.

Chapter 5: Reversibly Ligand-Gated OFF-ON Proton Transport Utilizing *Meta*-Dipropynylbenzene-Based Dimeric Barrel-Rosette Channel.

In the chapter, we introduced *meta*-dipropynylbenzene-based barrel-rosette channel which can transport the proton across the phospholipid bilayer membrane through the water wire present in the dimeric rosette structure by following the Grotthuss mechanism. The crystal structure of the compound showed the presence of the water wire in the cavity of the dimeric rosette of the compound, indicating the possible path for the proton translocation process. Fluorescence microscopy was utilized to check to understand the colocalization of the compound on the membrane. Proton transport activity of the compound was checked utilizing different HPTS, Lucigenin, and Safranin O based assays. A pH dependent proton transport studies confirmed that breakage of the water wire diminished the proton transport activity, confirming that the water wire is providing the path for translocating the proton through the dimeric rosette of the channel. Safranin O based assay verified the generation of the membrane potential due to the transport of the proton across the membrane. Cation and anion selectivity studies using the HPTS-based assay or Lucigenin-based assay confirmed that within the proton transport concentration ranges, the compound cannot transport the cation or anions. Proton transport comparison divulged that the compound exhibited approximately 1.3 and 2 times higher proton transport activity compared to FCCP and gramicidin (gA), respectively. Further, the ligand-gated OFF-ON proton transport activity was checked by sequential addition of the $CuCl_2$ and K_2EDTA across the vesicular membrane and the bilayer lipid membrane.

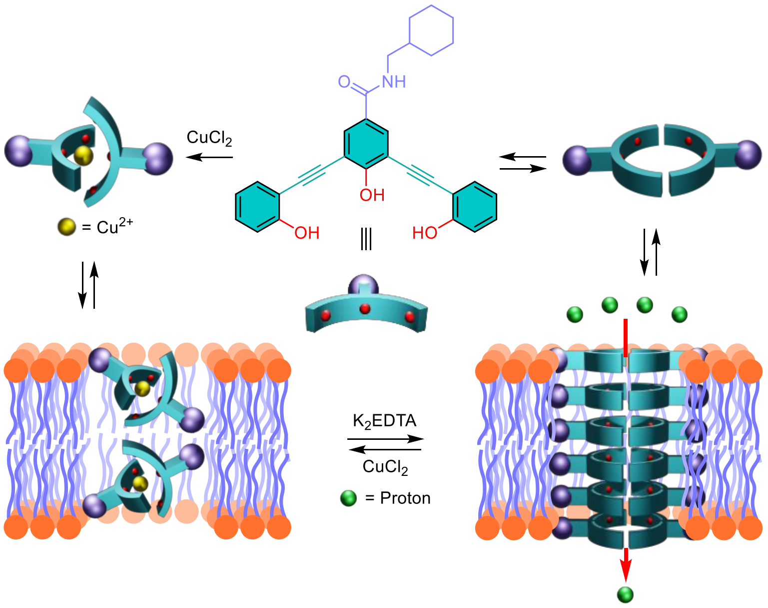

Figure 5 Structure of proton channel-forming compound and its ligand-gated reversible OFF-ON proton transport activity in the presence of $CuCl_2$ and K_2EDTA across the bilayer membrane.

Chapter 1

Introduction to Membrane Transport

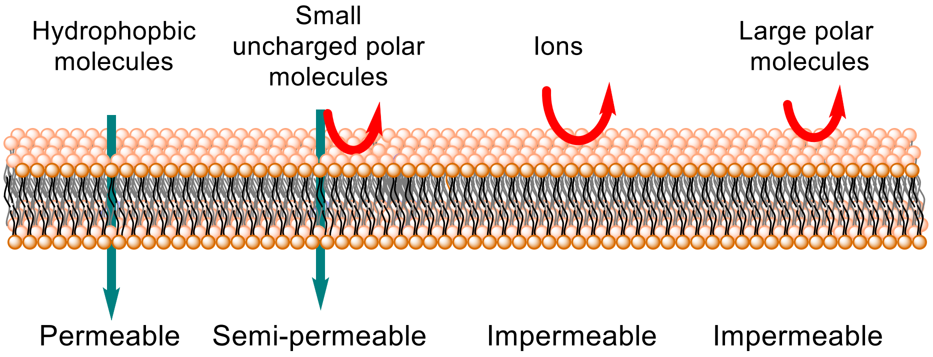

Cellular organelles operate different physiologically relevant functions by modulating the ion trafficking across the cellular membranes. The synergistic activities of these cells confer structural integrity to the organism's architecture and facilitate intricate processes essential for the sustenance of life. These intricate processes encompass the generation of energy through the assimilation of nutrients, the transmission of genetic information, and the signal transduction mechanisms necessary for the execution of diverse biological functions, among others. It harbors various specialized compartments referred to as cellular organelles, including mitochondria, endoplasmic reticulum, chloroplasts, Golgi apparatus, lysosomes, and others. Conversely, the nucleus is the repository of vital genetic information. The entirety of the cytoplasmic elements, comprising subcellular organelles and the nucleus, is encased by a pliable, hydrophobic membrane termed the plasma membrane, which serves as a protective barrier safeguarding the cellular compartments from the external milieu.[1]

1.1. Cellular membranes[2]

The membrane of a cell behaves as a protective layer of the organelles from the external environments and regulates the shape and size of the cells. Primarily, it consists of phospholipids, cholesterols, and glycolipids having a hydrophobic tail and hydrophilic head part. The cholesterol molecules enhance the permeability-barrier properties of the lipid bilayer. During the construction of the membrane, the hydrophilic head of the lipid faces the external and internal surroundings, whereas the internal core of the membrane contains the hydrophobic tail part (Figure 1.1). The hydrophobic thickness of the membrane varies from 30–40 Å, and this assembly is assisted by different noncovalent interactions. The presence of the hydrophilic outer and inner parts of the membrane helps to interact with the cell surroundings for communication and transport processes. This adequate orientation of the bilayer membrane provides a selective passage for the selective transportation of different essential ingredients for its healthy functions.[3]

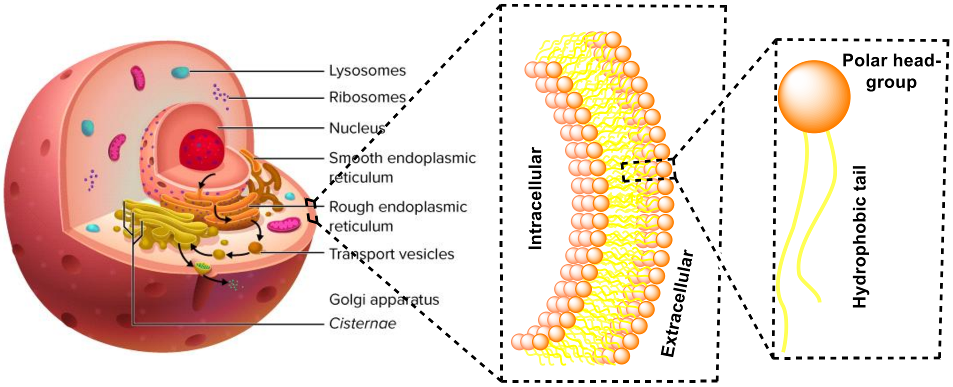

Figure 1.1 Schematic representation of the cell membranes containing basic phospholipids. Picture of the cells has been taken from https://www.ck12.org/flexi/biology/cell-structure/is-a-eukaryotic-cell-more-complex-than-a-prokaryotic-cell/.

1.2. Membrane permeability

The specific orientation of the bilayer membrane makes a thermodynamic energy barrier to cross any unwanted external solutes into the cells. Some small hydrophobic species (O_2, N_2, CO_2, etc.) can easily be diffused across the membrane, whereas some small molecules (H_2O, Urea, EtOH, etc.) remain semipermeable. However, small inorganic ions (H^+, Cl^-, HCO_3^-, Ca^{2+}, Mg^{2+}, Na^+, K^+, etc.) and large polar molecules (sugar, amino acid, nucleotides, etc.) remain membrane impermeable due to the high thermodynamic energy barrier of the hydrophobic core of the bilayer membrane (Figure 1.2). The movement of these ions or polar molecules is necessary to mediate different physiological functions that include pH regulation and maintaining cell volume, maintaining osmotic balance, and signal transduction, etc. Therefore, some membrane-embedded structurally and functionally complex transmembrane proteins provide a passage for the transport of the ions across the bilayer membrane, which are eventually known as transmembrane transporters.[3]

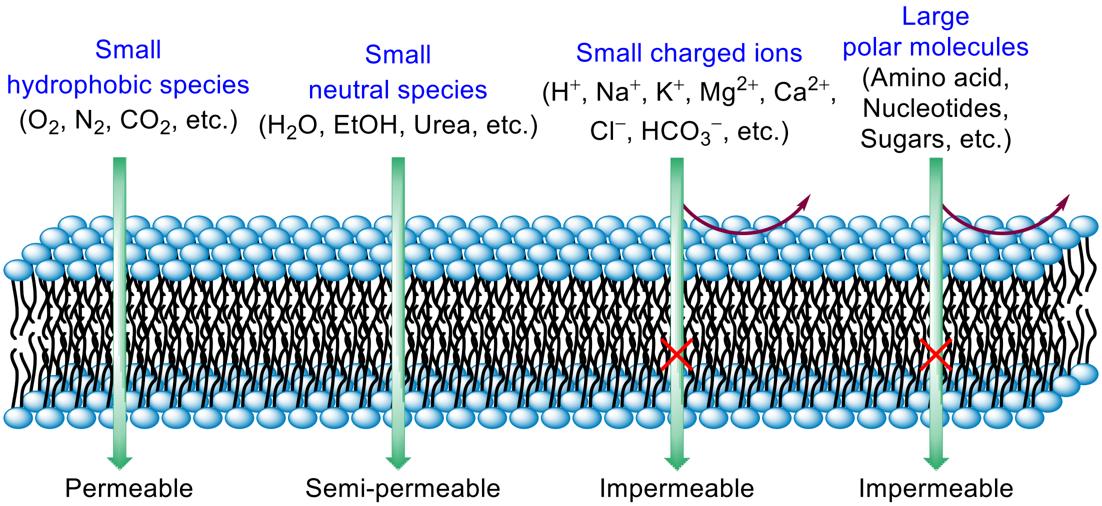

Figure 1.2 Schematic representation of transmembrane permeability of different species across the bilayer membrane.

1.3. Transmembrane ion transport

As described above, ion fluxing is usually mediated by families of protein and nonprotein-based entities called ion channels, pores, or ion carriers. In the case of an ion carrier, it does the to and fro movement across the membrane to flux the required ion across the membrane. Whereas ion channels and pores form a static hydrophilic pathway for ion translocation, incorporating an appropriate selectivity filter to mediate ion transport across the membrane, they also maintain a hydrophobic outer surface to stabilize the channel assembly within the membrane environment.[4] These ion transport processes can occur either via active transport or passive transport. In the case of passive transport, ions flow in the direction of the concentration gradient, whereas during active transport, the ion transport process occurs against the concentration gradient by using some external energy source.[5]

Furthermore, depending on the no of solutes involved in the transport process and the direction of the ion transport, ion transporters can be classified as uniport (a single solute is involved in the transport process) and cotransport (a minimum of two solutes are involved in the overall transport process). Cotransport is further subcategorized into symporters and antiporters. During symport, two oppositely charged species transport in the same direction, and during antiport, two same charged species transport in the same direction of the cellular membrane (Figure 1.3).[5]

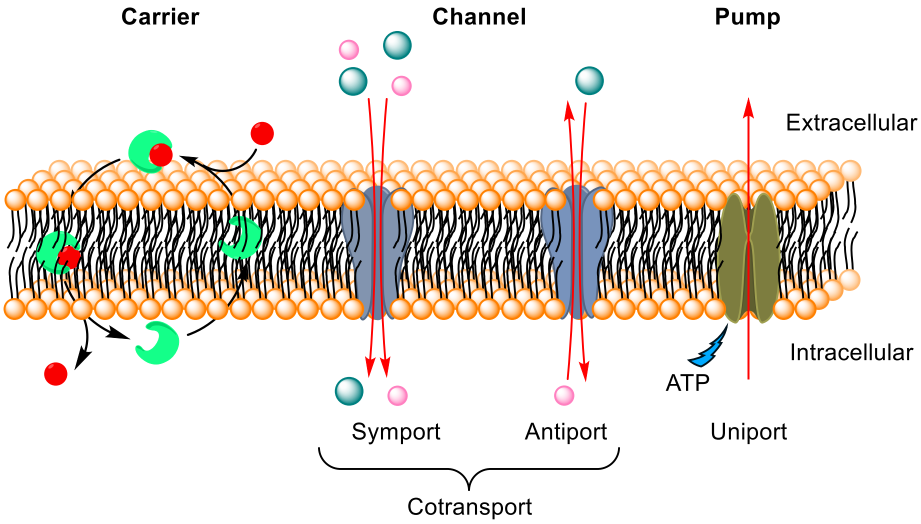

Figure 1.3 Schematic representation of different transport processes across the bilayer membrane.

1.4. Natural transmembrane cotransporters

Nature controlled the movement of physiologically relevant ions (e.g. Na^+, K^+, Cl^-, HCO_3^{2-}, HPO_4^{2-}, etc.) for adequate modulation of the ionic concentrations for functioning the physiological functions. Cation channels can transport cations selectively, and anions channels can transport anions selectively. Meanwhile, the cation-anion symporting channels can transport both cation and anion at the same time through the selectivity filter of the channel proteins. Sodium/iodide symporter (NIS) (Figure 1.4A) transports two sodium ions into the cell for every iodide ion transport.[6] NIS transmembrane proteins are essential for the synthesis of thyroid hormones, which control cell metabolism. Potassium-chloride cotransporters (KCC) (Figure 1.4B, C) transport both K^+ and Cl^- ions[7] across the plasma membrane and are involved in cell volume regulation, γ-aminobutyric acid (GABA), glycine-mediated inhibitory neurotransmission, etc. Sodium–chloride cotransporter (NCC) (Figure 1.4D) transports both Na^+ and Cl^- across the plasma membrane, which has a major role in salt reabsorption in the distal convoluted tubule of the nephron.[8] Sodium-dependent glucose cotransporter 1 (SGLT1) (Figure 1.4E),[9] a component of the main intestinal membrane transport system, plays an important role in intestinal glucose absorption. These symporters are large complex proteins that are dependent on posttranslational modifications, proper protein folding, cellular polarity, protein trafficking, and cellular organization for their function.

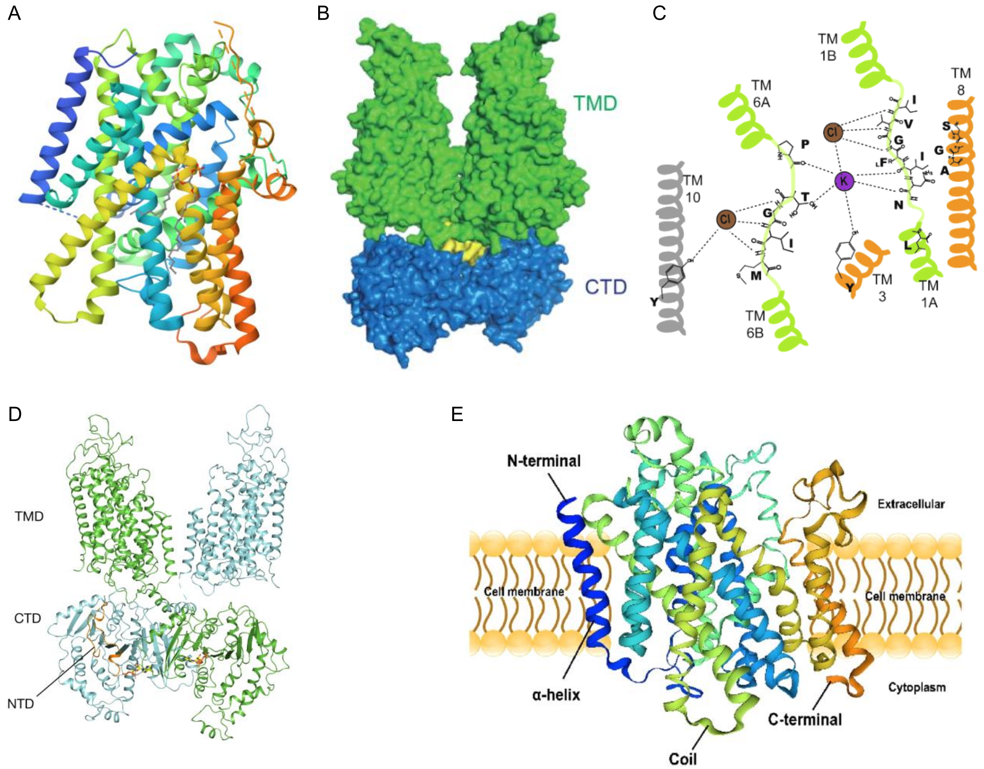

Figure 1.4 Crystal structure of the sodium/iodide symporter (NIS) in complex with perrhenate and sodium (structure has been taken from https://www.rcsb.org/structure/7UUZ) (A).[6] Surface maps of KCC2 showed direct interaction between the transmembrane domain (TMD, green) and cytosolic domain (CTD, blue), and scissor helix (yellow) (B).[7] Schematic representation of K^+ and Cl^- ion binding in KCC (bottom) (C).[7] The overall structure of the NCC dimer. Ribbon representation is viewed from the membrane. The two NCC protomers are coloured green and cyan, respectively and the N-terminal domain is colored orange. The bound nucleotides are shown as sticks (D).[8] Protein 3D structure prediction of Sglt1 in *Megalobrama amblycephala* (E).[9]

1.5. Requirement of synthetic transport systems

Although natural transport proteins control the ion movement across the membrane for proper physiological functions, mutation of these natural transmembrane proteins leads to different physiological disorders termed channelopathy[10,11] that include Gitelman syndrome, myotonias, long QT syndrome, Brugada syndrome, epilepsy, episodic ataxia, familial hemiplegic migraine, lambert-eaton myasthenic syndrome, Alzheimer's disease, Parkinson's disease, cystic fibrosis (CF), etc. Consequently, elucidating the structural intricacies and ion translocation mechanisms of these inherent transmembrane proteins motivates the scientific community to engineer synthetic scaffolds capable of replicating the functionalities of these natural transmembrane proteins. The decoration of a synthetic transporter helps gain insights into its structural and functional characteristics and explore diverse biomedical applications ranging from neuronal disorders to cancer.

1.6. Synthetic transmembrane cotransporters

Over the last few years, the scientific community decorated versatile cation-anion cotransporters to unveil the structure and function of the transmembrane cation-anion cotransporters. Smith and associates presented an inaugural example of synthetic KCl and NaCl symporters utilizing a salt-binding macrobicycle (Figure 1.5A).[12] Subsequently, Kyu-Sung Jeong and his team proposed a potassium binding motif that incorporates an azacrown, as well as a chloride binding motif utilizing urea (Figure 1.5B).[13] Gale and his research team devised a transporter utilizing meso-octamethylcalix[4]pyrrole specifically for the transport of CsCl and RbCl (Figure 1.5C). Matile and his associates established a ditopic transport framework that leverages anion-π interactions (Figure 1.5E).[14] Yun-Bao Jiang and his collaborators synthesized crown ether-thiourea conjugates with azobenzene linkers, effectively illustrating the ability to facilitate the transport of K$^+$, Cl$^-$, and Na$^+$ ions via a carrier mechanism (Figure 1.5D).[15] Madhavan and his research group also presented a metal halide symporter pore that exhibits a marked preference for anion transport over cations (Figure 1.5F).[16] Recently, our research team has engineered a fluorescent M$^+$/Cl$^-$ channel that demonstrates preferential transport of Cl$^-$ over K$^+$ (Figure 1.5G).[17] Despite these initiatives, instances of synthetic cation-anion symporter channels remain limited, underscoring the necessity for additional research in this domain.

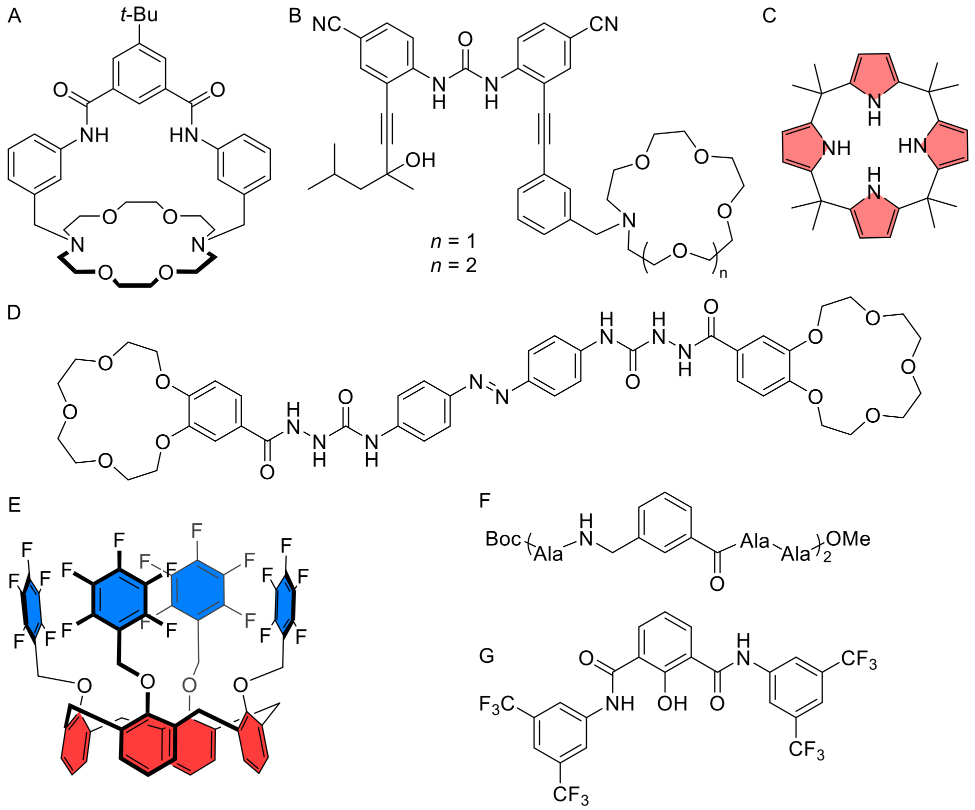

Figure 1.5 The structure of artificial cation-anion carriers (A-E) and channels (F, G).

1.7. Design principle synthetic transport systems

For designing an efficient synthetic transport system, some general guideline needs to be followed,

(a) The designed structure required a polar cavity to bind the ions and a hydrophobic outer surface to stabilize the hydrophobic environment of the lipid bilayer membrane.

(b) The designed structure required multivalent ion binding interactions between the ions and the polar cavity of the transporter.

(c) It must need to have the capability to overcome the hydration energy of the ions.

(d) It required an optimum membrane permeability (i.e., logP ~ 5) either to do the to and fro movement in the membrane (for carriers) or to get better permeation ability to form self-assembly in the membrane (for ion channels).

During the design of a synthetic ion channel, some additional design criteria are required as follows,

(e) During the design of a self-assembled ion channel, the assembly needs to be stabilized by utilizing different noncovalent interactions to create a more stable ion permeation pathway.

(f) The length of the designed ion channel needs to span the bilayer membrane for effective ion permeation.

(g) The engineered ion channels necessitated the incorporation of sufficient ion binding sites to facilitate the binding and translocation of the target ions. Furthermore, it was imperative to appropriately engineer the dimensional specifications of the ion channel cavity to ensure optimal ion selectivity.

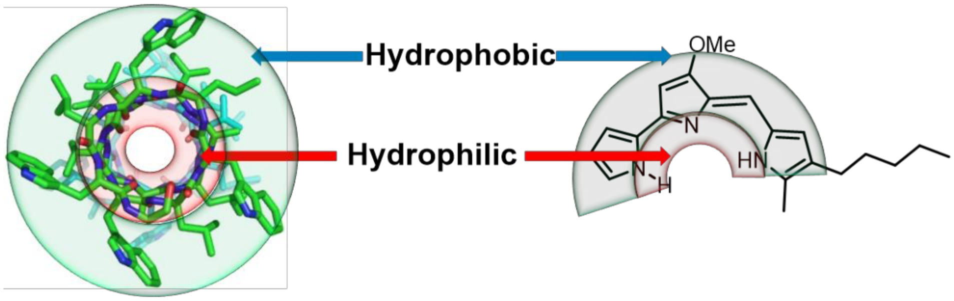

Figure 1.6 A general schematic representation of structural designing requirements for the construction of synthetic transporters.

1.8. Detection and quantification techniques of ion transport[18]

Ion transporters transport the different ions across the membrane, and therefore, for the diction and quantification of a synthetic transport system, it is essential to understand its efficiency in the ion transport process. The two most fundamental and well-accepted techniques that are used to address the transport efficiency of synthetic transport systems include liposome-based assays and planar bilayer membranes, often called black lipid membranes (BLM). Unilamellar phospholipid vesicles serve as straightforward, dependable, and reproducible systems. Therefore, it can be utilized to investigate the transport process as an alternate mimetic of the cell membrane. Liposomes present considerable adaptability, thereby enabling meticulous regulation of both intra- and extra-vesicular solutions. Concentration differentials can be established across vesicular membranes by substituting extravesicular ions, which can be achieved either via size exclusion chromatography or dialysis methodologies. The transport process facilitated by the synthetic transporter compound can be measured utilizing different techniques, including fluorescence, nuclear magnetic resonance (NMR), ion-selective electrodes, etc. On the contrary, the BLM technique is widely used to understand the formation of the ion channel in the membrane and to directly measure the conductance value and ion permeability of the synthetic ion channel system.

1.8.1. Fluorescence assays

In the fluorescence-based transport assays, the transport activity of the synthetic transport system was quantified by the change in fluorescence emission intensity of the encapsulated dyes. Various dyes responsive to pH, electrical potential, or ionic gradients were utilized to gain insights into the transport process. Commonly used dyes include 8-hydroxypyrene-1,3,6-trisulfonic acid trisodium salt (HPTS, a pH-sensitive dye),[19] Safranin O (a potential-sensitive dye),[20] and *N*,*N*-Dimethyl-9,9-biacridinium dinitrate (Lucigenin, a halide-sensitive dye),[21] which are widely employed to evaluate the transport efficiency of synthetic molecules.

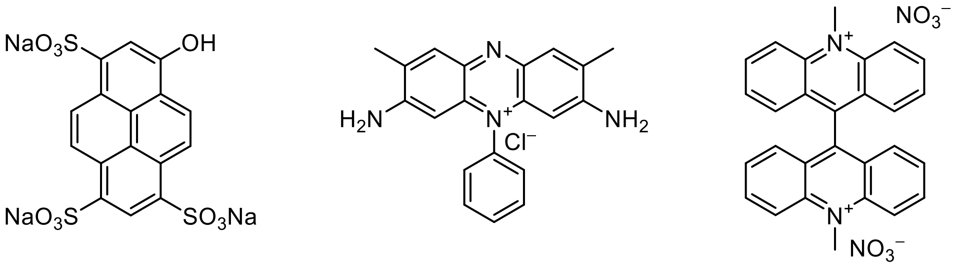

HPTS **Safranin O** **Lucigenin**

Figure 1.7 Frequently employed fluorescent probes in the analysis of ionic translocation utilizing vesicle-oriented assays.

Water-soluble, membrane-impermeable HPTS dye is a pH-dependent fluorescence indicator having a pKa of ≈ 7.3 in aqueous buffer solutions. Two distinct excitation wavelengths of HPTS dye at 403 nm and 460 nm correspond to its protonated and deprotonated states. Nevertheless, excitation at both wavelengths results in emission at a uniform wavelength (510 nm). In HPTS-based assays, a pH gradient is established, either in addition to the base or acid pulse across vesicles, and the transport process is elucidated by monitoring the emission intensity of HPTS dye after the addition of the transporter molecule (Figure 1.8A, B). The alteration in intravesicular pH following the administration of an anion transporter suggests that transport transpires via either antiport (OH^-/A^- or H^+/M^+ where A^- and M^+ are anions and cations) or symport (M^+/OH^-, M^+/A^- or H^+/A^-) mechanism. This assay facilitates the quantification of intravesicular pH by analyzing the ratio of protonated to deprotonated dye. Lucigenin is a halide-sensitive dye whose fluorescence activity gets quenched in the presence of halides while remaining unresponsive to oxoanions such as nitrate or sulfate. Therefore, Lucigenin assays provide a direct measurement of the anion transport process. The standard assay encompasses vesicles encapsulating NO_3^- along with the lucigenin dye, complemented by the establishment of a chloride gradient through the introduction of Cl^- into the extravesicular medium. The transport mechanism is characterized by observing the fluorescence quenching of the Lucigenin dye upon the addition of transporter molecules. The Cl^-/NO_3^- exchange is being monitored throughout the transport process (Figure 1.8C, D). Similarly, Safranin O demonstrates sensitivity to membrane potential, which is utilized to detect unidirectional ion transport. This cationic dye is associated with the membrane, and the generation of membrane potential through the addition of the transporter results in an increase in the fluorescence of safranin O.

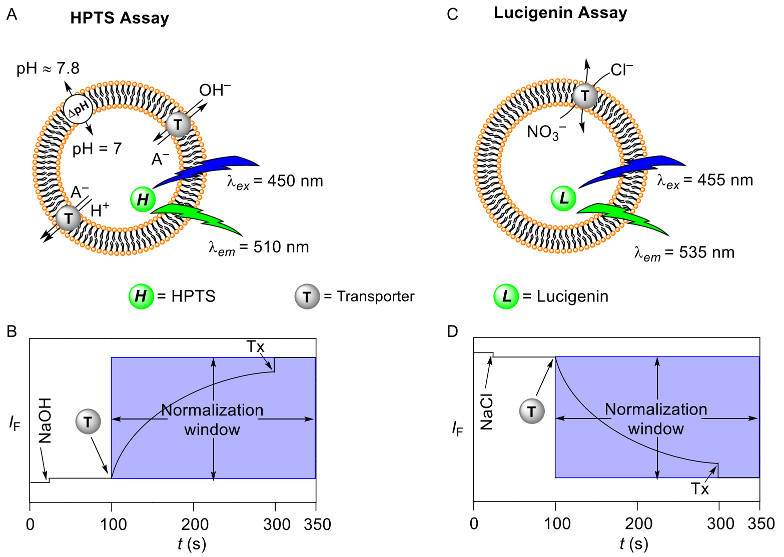

Figure 1.8 Schematic representation of HPTS (A) and Lucigenin (C) assays along with the corresponding fluorescent kinetic experiments during HPTS (B) and Lucigenin (D) assays.

Moreover the effect of the transporter molecule in the membrane was checked utilizing different fluorescent dyes that includes 5(6)-Carboxyfluorescein (CF, λ_{ex} = 492 nm, and λ_{em} = 517 nm)[17] or Calcein (λ_{ex} = 495 nm, and λ_{em} = 515 nm)[22] or 8-Aminonaphthalene-1,3,6-trisulfonic acid, disodium salt (ANTS, λ_{ex} = 353 nm, and λ_{em} = 520 nm) dye with the fluorescence quencher *p*-Xylene-bis(*N*-pyridinium bromide) (DPX).[23] CF and calcein are self-quenching dyes; at higher concentrations, their fluorescence activity quenches. Hence, the encapsulation of a higher concentration of CF dye or calcein dye in the lipid bilayer membrane quenched the fluorescence activity of CF dye or calcein dye. However, disruption of the membrane integrity or forming a large pore will leak out the encapsulated CF dye or calcein dye into the bulk solution, resulting in the enhancement of the CF or calcein fluorescence activity. Similarly, an ANTS-DPX assay encapsulating the ANTS dye with the DPX quencher in the vesicular membrane quenches the fluorescence activity of the ANTS due to the close proximity of the ANTS and DPX. However, the leakage of the dyes from the vesicular membrane into the bulk solution will increase the ANTS fluorescence activity due to the increase in the distance between ANTS and DPX. Therefore, the increment of the ANTS fluorescence after the addition of the transporter molecules is also attributed to the formation of either a large pore across the membrane or the presence of the transporter disintegrating the membrane.

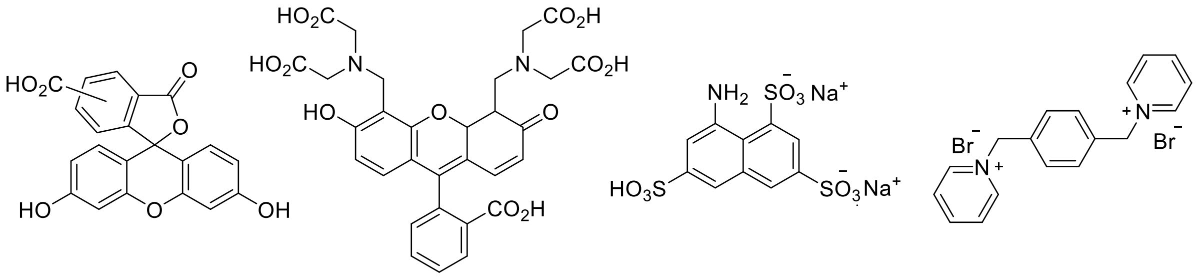

CF **Calcein** **ANTS** **DPX**

Figure 1.9 Frequently employed fluorescent dyes and quencher in the analysis of membrane leakage studies utilizing vesicle-oriented assays.

1.8.2. Ion selective electrode (ISE)-based assay

ISE-based assays are an alternate approach that has been used for direct quantification of the transported ions. For quantification of the ion transport process, the vesicles were entrapped with the NaCl salt, maintaining the pH = 7.0. The extravesicular NaCl was removed by utilizing the dialysis technique, and the vesicle suspensions were used for the ion transport quantification by immersing the vesicles into the $NaNO_3$ buffer medium. The Cl^- ion efflux was monitored over time after the addition of the transporter molecule using a chloride ion selective electrode (Figure 1.10). Hence, using an ion-selective electrode can provide direct evidence of the ion transport process.[24]

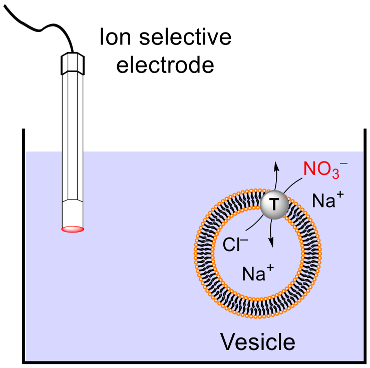

Figure 1.10 Schematic representation of the ion selective electrode based assay for transmembrane ion transport measurement.

1.8.3. NMR-based Assay[25,26]

The ion transport event of a synthetic transporter can also be monitored and quantified using NMR-based assays. To design a NMR-based transport study, the ion of interest has to be necessarily NMR active (for example, ^{23}Na, ^{39}K, ^{35}Cl, $H^{13}CO_3^-$, or $^{33}SO_4^{2-}$, etc.). During the experiment, large unilamellar vesicles were prepared by entrapping with MX salt ($M^+ = {}^{23}Na^+$, $^{39}K^+$, or any NMR active cation and $X^- = {}^{35}Cl^-$, $H^{13}CO_3^-$, $^{33}SO_4^{2-}$, or any NMR active anion). Different paramagnetic shift reagents (for example, Dy^{3+}, Co^{2+}, Mn^{2+}, etc.) are added to the extravesicular buffer. The addition of the paramagnetic shift reagent helps in resonating the exravesicular ion in different resonating frequencies as compared to the intravesicular ions, resulting in the appearance of the two distinct peaks in the NMR. The exchange of the internal and external ions is directly proportional to the line broadening observed in the NMR peaks. Therefore, the ion transport process by the transporter molecule can be visualized by the line broadening of the respective peaks due to the exchange of ions between the intra- and extravesicular ions. Change in the half-line width of the peaks helps estimate the ion transport rates across the membrane.

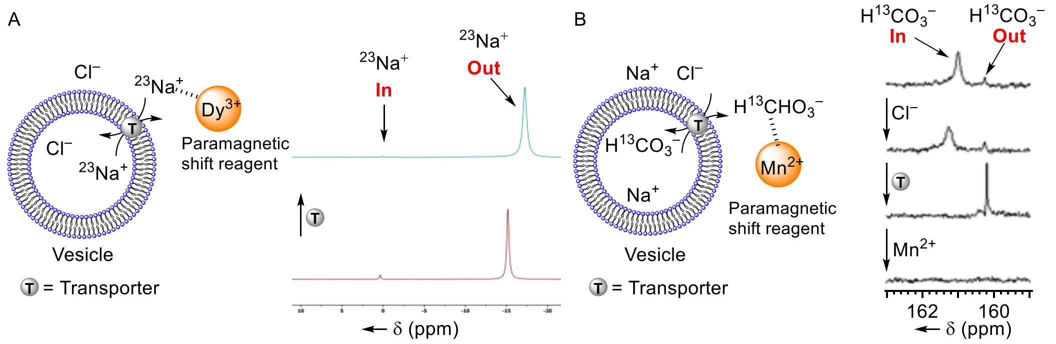

Figure 1.11 Schematic representation of $^{23}Na^+$ (A) and $H^{13}CO_3^-$ (B) ion transport study using NMR technique.

1.8.4. Conductance measurement across the planar lipid bilayer[27,28]

The bilayer lipid membrane (BLM) technique measured the conductivity of an ion channel system across the planar lipid bilayer membrane. The change in the conductance with time provides direct evidence of the formation of a synthetic ion channel in the membrane. During the experiment, two chambers (cis and trans) are separated by a polystyrene cup having 150 μm aperture diameter. Diphytanoylphosphatidylcholine lipid (DPhPC) is painted by using a glass rod to form a bilayer membrane across the aperture of the polystyrene cup. Both cis and trans chambers are filled with symmetrical 1 M KCl solutions (unbuffered or buffered). The transporter molecule addition in either the cis or trans chamber will create the opening-closing event at different holding potentials if the transporter molecule forms an ion channel, generating a conductive pathway for ion permeation. From this BLM technique, channel diameter, single-channel conductance, anion/cation, anion/anion, and cation/cation permeability of the synthetic channel molecule were experimentally calculated.

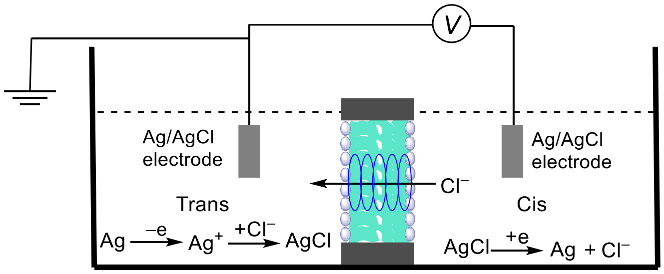

Figure 1.12 A general schematic representation of conductance measurement experiment of transporter molecule across the planar lipid bilayer membrane.

1.9. Proton transport across the bilayer membrane

Proton transfer is arguably the most critical and prevalent chemical reaction that underpins biochemical processes, including the functionality of ion channels, enzymatic reactions, balance charge across membranes, adjusting pH, and, in some cases, delivering protons for reactivity for energy storage or release, etc. The pH levels within various cellular compartments are stringently regulated, as this regulation is vital for the optimal operation of diverse organelles. The transfer of protons across cellular membranes, facilitated by mechanisms such as symporters, antiporters, and proton-pumping ATPases, constitutes an essential component of the cellular machinery that maintains distinct pH levels in cellular compartments, ranging from the lysosome (pH ≈ 4.7) to the cytosol (pH ≈ 7.2) and mitochondria (pH ≈ 8).[29,30] Consequently, the integration of proton pathways into synthetic systems is imperative for the optimization of proton transport; thus, deriving design principles from enzymes possessing well-established proton pathways would create a foundational framework for the development of synthetic conduits. Notwithstanding their comparatively diminutive size and elevated charge density in contrast to other ions, the translocation of protons continues to represent a significant challenge. Nevertheless, this process necessitates a strategic arrangement of proton transfer residues and/or water molecules to effectively promote such transport. Although certain proton pathways, such as those found in bacteriorhodopsin and cytochrome c oxidase, have been extensively investigated, the definitive design principles for proton channels, including the requisite number of residues, the spatial separation between residues, the number of pathways within a specific molecule, and the relative pKa values of the participating residues remain inadequately characterized.

1.9.1. Different mechanisms of the proton movement process

Movement of protons can occur by following different modes of transport mechanism that includes the Grotthuss mechanism, vehicular mechanism and surface mechanism (Figure 1.13).[31,32]

Grotthuss mechanism involves the movement of protons through the hydrogen-bonded water wires. In this process, covalent bonds between neighboring molecules are formed and broken, resulting in the net movement of protons from one end of the water wire to the other, thereby facilitating proton transport through the water wires. In the case of vehicular mechanism, the proton transport occurs as part of protonated molecules (e.g., H_3O^+, NH_4^+, etc.) together with the diffusion of uncharged vehicle molecules (e.g., H_2O, NH_3, etc.). On the contrary, in the case of the surface mechanism, proton hopping occurs with the help of the proton binding sites present on the surface of a protein or membrane, which helps to transfer the protons across the membrane with the help of the random walk of the water molecules.

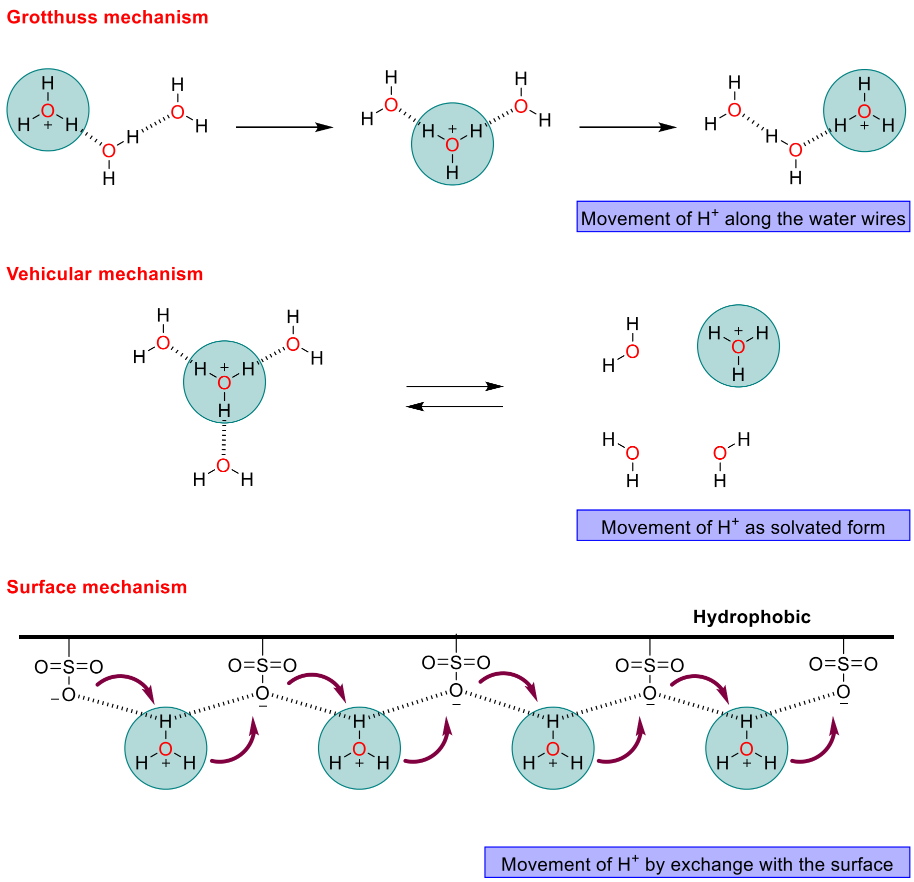

Figure 1.13 Schematic representation of proton transport with different mechanisms.

1.9.2. Naturally occurring proton channels

Nature constitutes different complicated architectures to build structurally and functionally complicated transmembrane proton channels for modulating different biological relevant functions. A voltage gated Hv1 protein channel (Figure 1.14A) facilitates the efflux of H^+ ions from the intracellular environment, thereby inducing alterations in the pH gradients across the membrane bilayer.[33] The electrochemical potential gradient that exists across the cellular membrane compels the voltage-gated proton channels to exhibit a responsive behavior, leading to the selective transport of protons through mechanisms of opening in reaction to membrane depolarization and closure during hyperpolarization. This inherent characteristic of Hv1 channels is instrumental in preserving a neutral intracellular pH and in modulating alkaline conditions within the cytoplasmic. Moreover, one of the smallest M2 protein channels (Figure 1.14B, C) obtained from the Influenza A virus has a single transmembrane helix, which forms four tightly packed transmembrane helices to generate the conducting pore. Presence of the His37 residue near the center of the transmembrane helix, acting as the pH-sensor of the channels. During proton translocation, it first binds to the histidine residues (His37), which act like a selectivity filter, and the water wires form across the conducting pathway.[34]

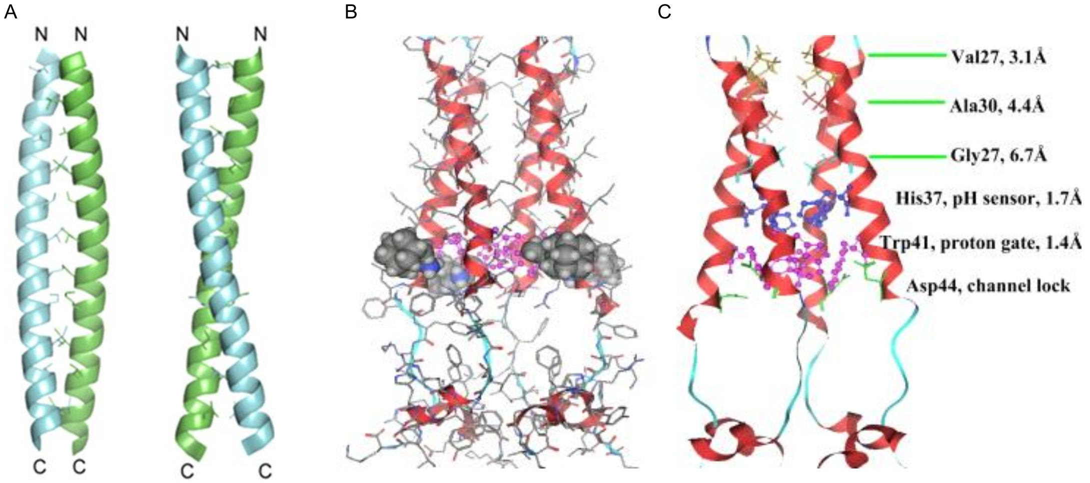

Figure 1.14 Crystal structure of the c-terminus of the Hv1 channel with parallel-oriented dimer forms a classic coil-coil architecture[33] (A). The tetrameric M2 channel in complex with rimantadine determined by NMR (B) along with the pore surface of M2 channel[34] (C).

1.9.3. Artificial proton channels

Motivated by the diverse mechanisms underlying proton transport processes, supramolecular chemists and biochemists have focused their efforts on the development of versatile synthetic analogues capable of facilitating proton translocation across bilayer membranes. This endeavor aims to establish a synthetic framework that emulates natural proton channels while simultaneously elucidating the intricate dynamics of proton translocation through simplified synthetic transport systems. In an effort to make a synthetic proton channel, Matile and coworkers introduced rigid rod-shaped polyols for the transmembrane transport of protons (Figure 1.15A, B).[35,36] Later, different scaffolds, including pillar[n]arene (Figure 1.15C),[37] foldamers (Figure 1.15D, E),[38,39] metal-organic frameworks (MOFs) (Figure 1.15F),[40] and nanotube [41] (Figure 1.15G) based channels were used to decorate the synthetic mimic of proton channels. Decoration of these synthetic proton channels will help us understand the proton translocation in complex membrane environments and be enlightened as an alternative for different biomedical applications.

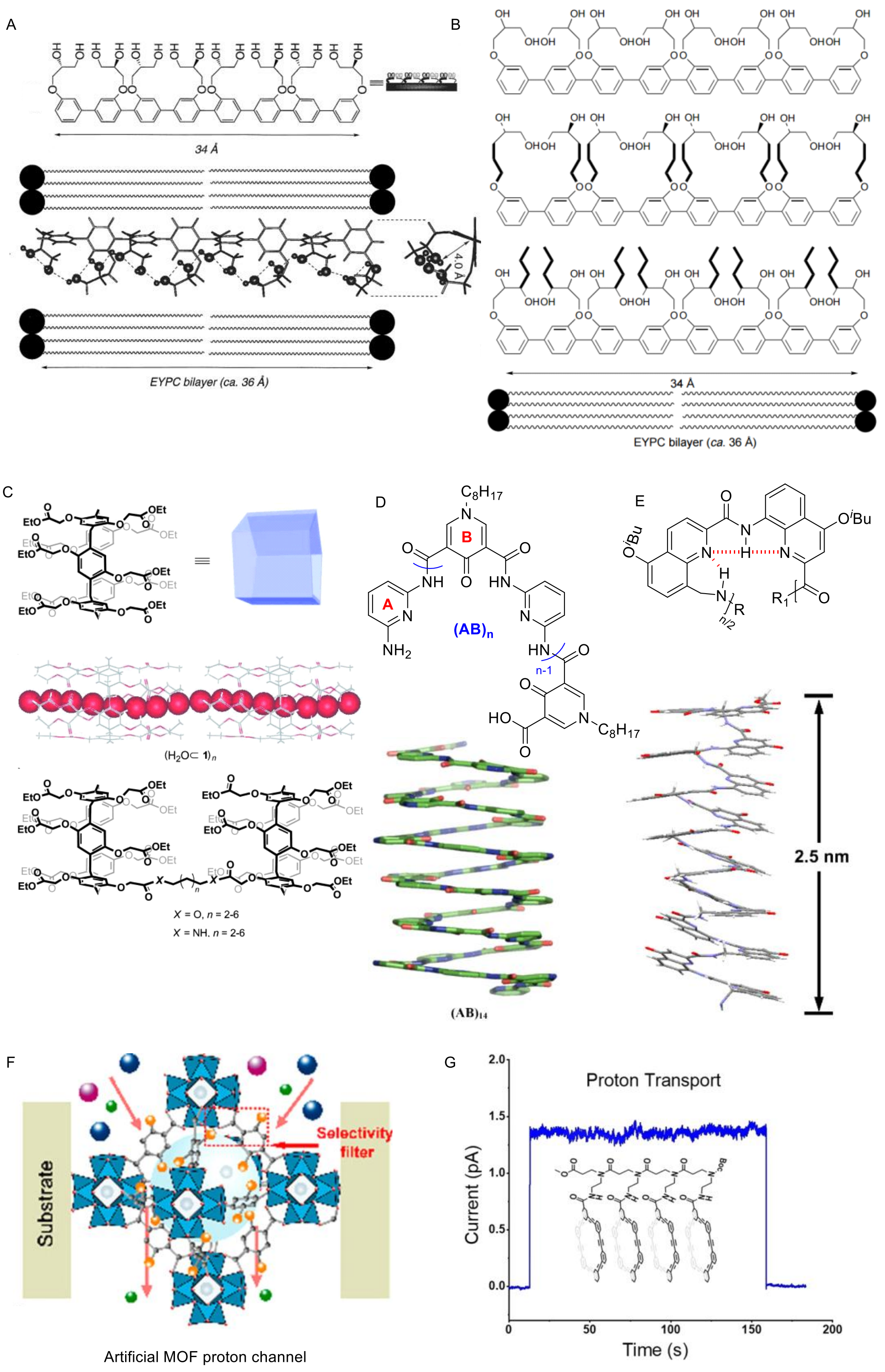

Figure 1.15 The structure of artificial proton channels: rigid rod-shaped polyols[35,36] (A, B), pillar[n]arene[37] (C), foldamer[38,39] (D, E), MOF[40] (F), and nanotube-based channel[41] (G).

1.10. References

(1) Busschaert, N.; Busschaert, N.; Wenzel, M.; Haynes, C. J. E.; Hiscock, J. R.; Kirby, I. L.; Karagiannidis, L. E.; Moore, S. J.; Wells, N. J.; Herniman, J.; Langley, G. J.; Horton, P. N.; Light, M. E.; Marques, I.; Costa, P. J.; Félix, V.; Frey, J. G.; Gale, P. A. *Chem. Sci.* **2013**, *4*, 3036–3045.

(2) Alberts, B.; Johnson, A.; Lewis, J.; Raff, M.; Roberts, K.; Walter, P. *Molecular Biology of the Cell, 4th edition*; Garland Science: New York, **2002**.

(3) Enkavi, G.; Javanainen, M.; Kulig, W.; Róg, T.; Vattulainen, I. *Chem. Rev.* **2019**, *119*, 5607–5774.

(4) Tobergte, D. R.; Curtis, S. *Biology and Mechanics of Blood Flows Part II: Mechanics and Medical Aspects*; Springer: New York, **2008**.

(5) Davis, J. T.; Okunola, O.; Quesada, R. *Chem. Soc. Rev.* **2010**, *39*, 3843–3862.

(6) Ravera, S.; Nicola, J. P.; Salazar-De Simone, G.; Sigworth, F. J.; Karakas, E.; Amzel, L. M.; Bianchet, M. A.; Carrasco, N. *Nature* **2022**, *612*, 795–801.

(7) Chew, T. A.; Zhang, J.; Feng, L. *J. Mol. Biol.* **2021**, *433*, 167056.

(8) Fan, M.; Zhang, J.; Lee, C. -L.; Zhang, J.; Feng, L. *Nature* **2023**, *614*, 788–793.

(9) Liang, H.; Ge, X.; Ren, M.; Zhang, L.; Xia, D.; Ke, J.; Pan, L. *Sci. Rep.* **2021**, *11*, 13962.

(10) Imbrici, P.; Liantonio, A.; Camerino, G. M.; De Bellis, M.; Camerino, C.; Mele, A.; Giustino, A.; Pierno, S.; De Luca, A.; Tricarico, D.; Desaphy, J. -F.; Conte, D. *Front. Pharmacol.* **2016**, *7*, 1–28.

(11) Bernard, G.; Shevell, M. I. *Pediatr. Neurol.* **2008**, *38*, 73–85.

(12) Koulov, A. V.; Mahoney, J. M.; Smith, B. D. *Org. Biomol. Chem.* **2003**, *1*, 27–29.

(13) Lee, J. H.; Lee, J. H.; Choi, Y. R.; Kang, P.; Choi, M. -G.; Jeong, K. -S. *J. Org. Chem.* **2014**, *79*, 6403–6409.

(14) Tong, C. C.; Quesada, R.; Sessler, J. L.; Gale, P. A. *Chem. Commun.* **2008**, 6321–6323.

(15) Zhao, Z.; Tang, B.; Yan, X.; Wu, X.; Li, Z.; Gale, P. A.; Jiang, Y. -B. *Front. Chem. Sci. Eng.* **2022**, *16*, 81–91.

(16) Basak, D.; Sridhar, S.; Bera, A. K.; Madhavan, N. *Org. Biomol. Chem.* **2016**, *14*, 4712–4717.

(17) Malla, J. A.; Umesh, R. M.; Vijay, A.; Mukherjee, A.; Lahiri, M.; Talukdar, P. *Chem. Sci.* **2020**, *11*, 2420–2428.

(18) Fyles, T. M. *Chem. Soc. Rev.* **2007**, *36*, 335–347.

(19) Gilchrist, A. M.; Wang, P.; Carreira-Barral, I.; Alonso-Carrillo, D.; Wu, X.; Quesada, R.; Gale, P. A. *Supramol. Chem.* **2021**, *33*, 325–344.

(20) Wezenberg, S. J.; Chen, L. -J.; Bos, J. E.; Feringa, B. L.; Howe, E. N. W.; Wu, X.; Siegler, M. A.; Gale, P. A. *J. Am. Chem. Soc.* **2022**, *144*, 331–338.

(21) Biwersi, J.; Tulk, B.; Verkman, A. S. *Anal. Biochem.* **1994**, *219*, 139–143.

(22) Sahoo, S.; Rehman, J. U.; Shah, M. R.; De, P.; Tecilla, P. *ACS Appl. Polym. Mater.* **2021**, *3*, 588–

593.

(23) Sordé, N.; Matile, S. *J. Supramol. Chem.* **2002**, *2*, 191–199.

(24) Wu, X.; Judd, L. W.; Howe, E. N. W.; Withecombe, A. M.; Soto-Cerrato, V.; Li, H.; Busschaert, N.; Valkenier, H.; Pérez-Tomás, R.; Sheppard, D. N.; Jiang, Y. -B.; Davis, A. P.; Gale, P. A. *Chem* **2016**, *1*, 127–146.

(25) Madhavan, N.; Robert, E. C.; Gin, M. S. *Angew. Chem., Int. Ed.* **2005**, *44*, 7584–7587.

(26) Davis, J. T.; Gale, P. A.; Okunola, O. A.; Prados, P.; Iglesias-Sánchez, J. C.; Torroba, T.; Quesada, R. *Nat. Chem.* **2009**, *1*, 138–144.

(27) Saha, T.; Gautam, A.; Mukherjee, A.; Lahiri, M.; Talukdar, P. *J. Am. Chem. Soc.* **2016**, *138*, 16443–16451.

(28) Huang, W. -L.; Wang, X. -D.; Ao, Y. -F.; Wang, Q. -Q.; Wang, D. -X. *J. Am. Chem. Soc.* **2020**, *142*, 13273–13277.

(29) Ives, H. E. and Rector Jr, F. C. *J. Clin. Invest.* **1984**, *73*, 285–290.

(30) Casey, J. R.; Grinstein, S.; Orlowski, J. *Nat. Rev. Mol. Cell Biol.* **2010**, *11*, 50–61.

(31) Ichikawa, T.; Yamada, T.; Aoki, N.; Maehara, Y.; Suda, K.; Kobayashi, T. *Chem. Sci.* **2024**, *15*, 7034–7040.

(32) Li, W. -H.; Deng, W. -H.; Wang, G. -E.; Xu, G. *EnergyChem* **2020**, *2*, 100029.

(33) Li, S. J.; Zhao, Q.; Zhou, Q.; Unno, H.; Zhai, Y.; Sun, F. *J. Biol. Chem.* **2010**, *285*, 12047–12054.

(34) Huang, R. -B.; Du, Q. -S.; Wang, C. -H.; Chou, K. -C. *Biochem. Biophys. Res. Commun.* **2008**, *377*, 1243–1247.

(35) Ni, C.; Matile, S. *Chem. Commun.* **1998**, 755–756.

(36) Weiss, L. A.; Sakai, N.; Ghebremariam, B.; Ni, C.; Matile, S. *J. Am. Chem. Soc.* **1997**, *119*, 12142–12149.

(37) Si, W.; Chen, L.; Hu, X. -B.; Tang, G.; Chen, Z.; Hou, J. -L.; Li, Z. -T. *Angew. Chem., Int. Ed.* **2011**, *50*, 12564–12568.

(38) Shen, J.; Ye, R.; Liu, Z.; Zeng, H. *Angew. Chem., Int. Ed.* **2022**, *61*, e202200259.

(39) Yan, T.; Liu, S.; Xu, J.; Sun, H.; Yu, S.; Liu, J. *Nano Lett.* **2021**, *21*, 10462–10468.

(40) Li, X.; Zhang, H.; Hou, J.; Ou, R.; Zhu, Y.; Zhao, C.; Qian, T.; Easton, C. D.; Selomulya, C.; Hill, M. R.; Wang, H. *J. Am. Chem. Soc.* **2020**, *142*, 9827–9833.

(41) Wu, C.-Y.; Su, S.; Zhang, X.; Liu, R.; Gong, B.; Lu, Z.-L. *Angew. Chem., Int. Ed.* **2023**, *62*, e202303242.

Chapter 2

Supramolecular Barrel-Rosette Ion Channel Based on 3,5-Diaminobenzoic Acid for Cation-Anion Symport

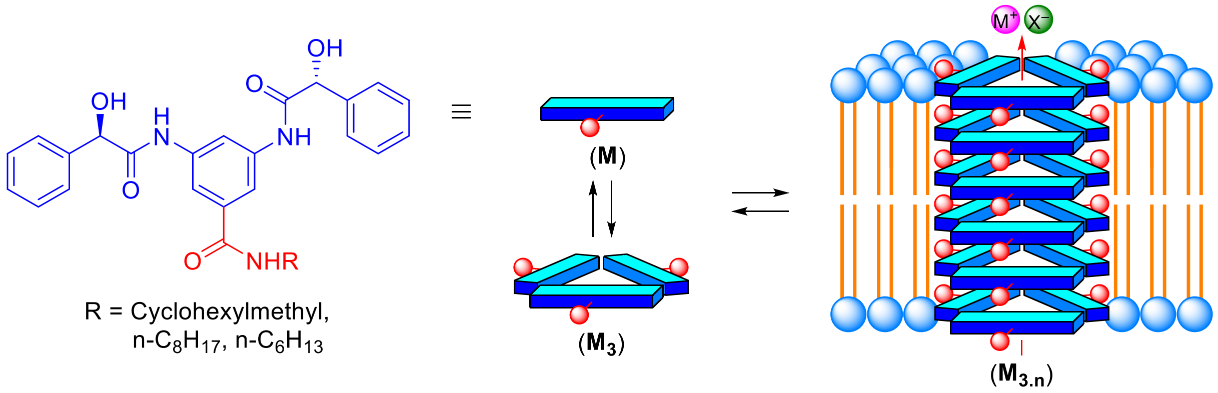

2.1. Introduction

As discussed in the ***Chapter 1*** nature endowed different structurally and functionally complicated transmembrane proteins (carriers, channels, pores) to continuing the appropriate functioning of different physiological functions. Abundant mutations in these transmembrane protein channels have been correlated with channel dysfunctions, eventually leading to therapeutically targeted channelopathies. To treat these channelopathies, one prospective methodology involves the investigation of the structural and functional intricacies of natural ion channels through the design of compact, intelligent supramolecular architectures equipped with specific functional groups. This methodology aspires to replicate the architecture and functionality of endogenous ion transport systems. As a result, the emphasis of scientific inquiry has transitioned from the development of unimolecular ion channels to the synthesis of small molecule-mediated cation channels. Furthermore, there is ongoing progress in the engineering of synthetic anion channels aimed at emulating the properties and functionalities of natural anion channels. Notwithstanding these advancements, synthetic cation-anion symporter channels have garnered minimal scrutiny due to the difficulties associated with the engineering of a channel selectivity filter capable of selectively and synergistically transporting both cations and anions. Despite attempts to fabricate synthetic channels exhibiting single-ion selectivity, formulating a universal strategy for dual-ion selectivity continues to pose a considerable challenge.

In this chapter, we introduce bis((*R*)-(−)-mandelic acid)-substituted 3,5-diaminobenzoic acid-based self-assembled barrel rosette ion channels engineered for the transport of both cations and anions. Through the utilization of varied substituents, we successfully modulated the lipophilicity of the molecule, thereby influencing its ion transport efficacy across the lipid bilayer. The 3,5-diaminobenzoic acid moiety is highly esteemed for its self-assembly characteristics, attributable to its capacity to establish robust intramolecular and intermolecular hydrogen bonds via its two H-bond donors (N-H) and one H-bond acceptor (C=O of the acid group).[1] Whereas (*R*)-(−)-mandelic acid is an interesting class of molecule that contains chirality. The presence of both hydrogen bond forming and lone pair donating groups in mandelic acid render it a favorable candidate for the construction of cation-anion symporter ion channels. The chirality of mandelic acid facilitates the formation of a well-organized and effective self-assembled architecture within the bilayer membrane. Moreover, the alcohol units of (*R*)-(−)-mandelic acid contribute to a hydrogen bonding network, facilitating ion transport across the bilayer through intramolecular and intermolecular hydrogen bonding within the self-assembled structure.

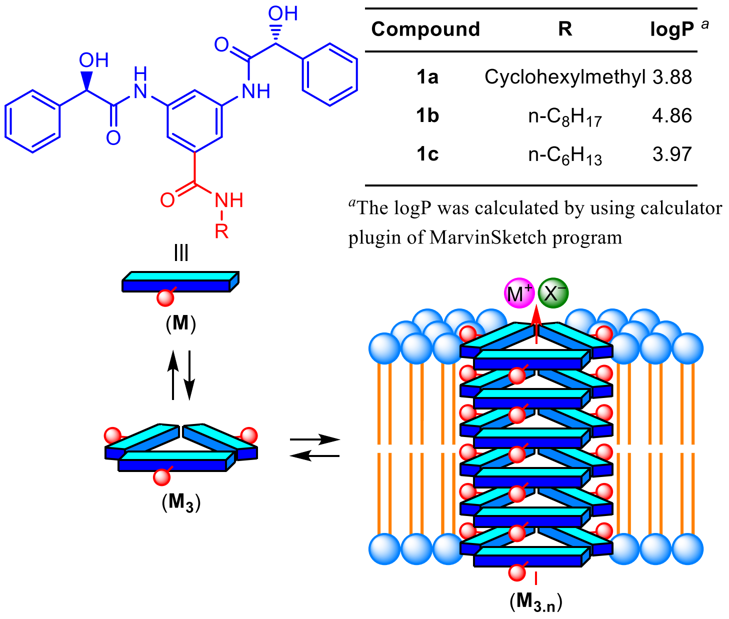

Compound	R	logP [a]
1a	Cyclohexylmethyl	3.88
1b	n-C_8H_{17}	4.86
1c	n-C_6H_{13}	3.97

[a]The logP was calculated by using calculator plugin of MarvinSketch program

Figure 2.1 Proposed model of barrel-rosette ion channel formation by these molecules **1a**–**1c** along with structural description and logP values of designed channel molecules.

2.2. Results and discussions

2.2.1. Synthesis

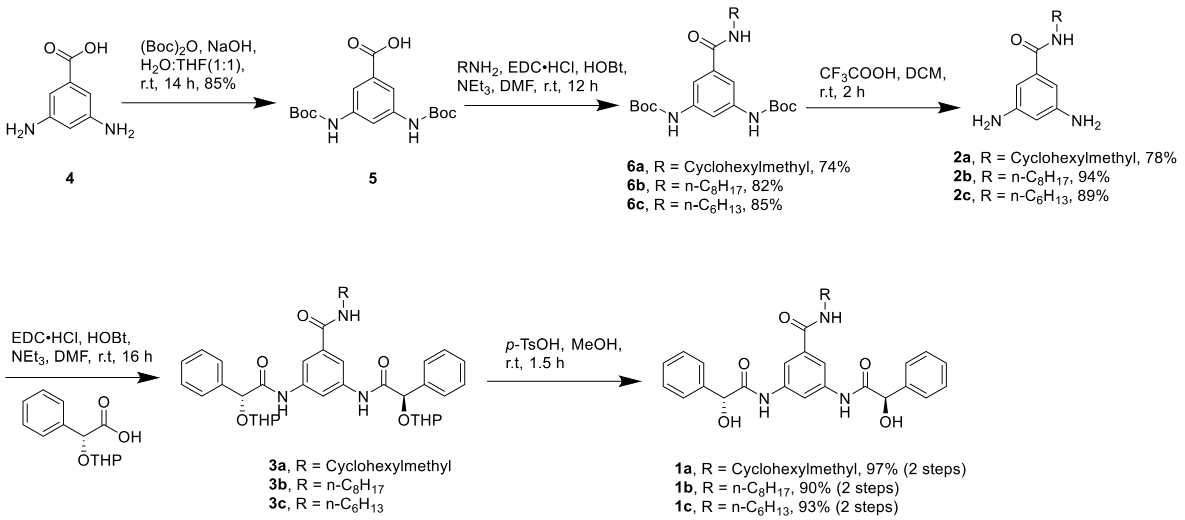

Scheme 2.1 Synthetic scheme for the compounds **1a**–**1c**.

Initially compound **5** was synthesized by using the reported literature protocol.[2] Compound **5** was coupled with different amines in the presence of 1-(3-dimethyl aminopropyl)-3-ethyl carbodiimide hydrochloride (EDC·HCl) and 1-hydroxy benzotriazole (HOBt) as a coupling agent in the presence of triethylamine (NEt_3) base at room temperature to obtained compound **6a**–**6c** with significant yield. Compound **6a**–**6c** was reacted further with trifluoroacetic acid (CF_3COOH) in DCM solvent to obtain compound **2a**–**2c**. Compounds **2a**–

2c were further coupled with (2*R*)-2-phenyl-2-((tetrahydro-2*H*-pyran-2-yl)oxy)acetic acid by using 1-(3-dimethylaminopropyl)-3-ethylcarbodiimide hydrochloride (EDC·HCl) and 1-hydroxybenzotriazole (HOBt) as coupling agents to get compounds **3a**–**3c**. Finally, acid-catalyzed deprotection of tetrahydropyranyl ethers provided the final compounds **1a**–**1c** with quantitative yield.

2.2.2. Ion transport studies

After the successful synthesis of compound **1a**–**1c**, their ion transport activity was evaluated across the egg yolk phosphatidylcholine large unilamellar vesicles (EYPC–LUVs), entrapping the pH-sensitive 8-hydroxypyrene-1,3,6-trisulfonic acid trisodium salt (HPTS, $pK_a = 7.2$) dyes. Initially, an ion transport activity comparison was carried out with a 20 μM concentration in the presence of extravesicular and intravesicular NaCl or $KClO_4$ salts. Regardless of the extravesicular and intravesicular salt environments, comparative data elucidate the activity sequence **1c** < **1a** < **1b** for both NaCl and $KClO_4$ salts, thereby suggesting that compound **1b** exhibits the most pronounced transport capability within the series (Figure 2.2). As anticipated, compound **1b** demonstrated superior transport efficacy among its analogues, attributable to its optimal logP value (logP = 4.86) and its effective incorporation into the phospholipid bilayer. It is noteworthy that the transport efficiency for each compound was markedly enhanced with $KClO_4$ salt in comparison to NaCl salt, thereby indicating that our channel-forming molecules possess a greater transport efficiency for $KClO_4$ salt relative to NaCl salt.

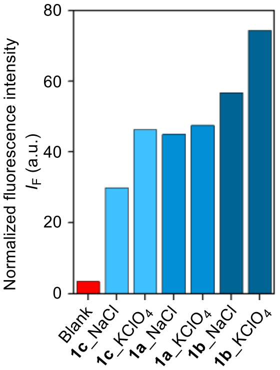

Figure 2.2 Ion transport activity comparison of **1a**–**1c** with both NaCl and $KClO_4$ salts at 20 μM concentration.

Subsequently, concentration-dependent transport activity was addressed across EYPC–LUVs⊃HPTS with NaCl salt and Hill analysis was carried out for compounds **1a**–**1c**. Hill analysis verified that **1b** has the lowest effective concentration at 50% activity (EC_{50}) value (11.97 ± 0.34 μM) (Figure 2.7) followed by compound **1a** (14.04 ± 0.42 μM) (Figure 2.6) and highest for compound **1c** (19.26 ± 0.59 μM) (Figure 2.8), which also supports the activity sequence of compounds **1a**–**1c**. Hill coefficient (n) ≈ 3 indicates that an active rosette was formed by the assembly of the trimeric unit of the molecules. Ion selectivity of was investigated with the highest active molecule **1b** by varying the intra- and extravesicular salts.[3,4] Cation selectivity demonstrated that it has selectivity towards cation with an activity sequence $K^+ > Cs^+ > Rb^+ > Li^+ > Na^+$ (Figure 2.3B). Anion selectivity also confirmed that compound **1b** has selectivity towards the anion with an activity sequence $ClO_4^- > NO_3^- > Br^- > Cl^- > SO_4^{2-}$ (Figure 2.3A). The ion selectivity sequence indicated that both the hydration energy and radius of ions (Figure 2.9) governed the ion selectivity of the compound **1b**.[5–7]

Further, to delve into the mechanistic pathway of the transport process, valinomycin assay was conducted across EYPC–LUVs by entrapping the 1 mM lucigening along with 200 mM $NaNO_3$ salt with pH = 7.0.[8] In the presence of an externally added NaCl ionic gradient, compound **1b** will initiate the chloride influx across EYPC–LUVs. If the transport process is mediated via the antiport mechanism, it is expected that in the presence of valinomycin (a K^+ ion transporter), compound **1b** will influx more amount of Cl^- ion, which will be reflected as the enhancement in the lucigenin fluorescence quenching. On the contrary, if the transport process happens via the symport mechanism, then compound **1b** will not couple with the externally added valinomycin, and hence, the fluorescence quenching of the lucigenin will remain unaltered. During the experiment, we noticed an insignificant change in the lucigenin fluorescence quenching (Figure 2.3C), confirming the symport mechanism by compound **1b**. Further NO_3^-/SO_4^{2-} assay[9] was conducted to reconfirm the transport mechanism, where vesicles were entrapped with the 1 mM lucigenin and 200 nM NaCl salt, keeping intravesicular pH 7.0. Since NaCl is present inside the vesicle, lucigenin remains in a fully fluorescence quenching state. During the experiment, the isoosmolar $NaNO_3$ and Na_2SO_4 salts were used as extravesicular buffer medium (200 mM $NaNO_3$ or 66.6 mM Na_2SO_4, 10 mM HEPES, pH = 7.0). Due to the higher charge density present over SO_4^{2-} ion it is difficult to translocate across the bilayer membrane. Hence fluorescence activity gaining of lucigenin dye will be expected to be affected if the transporter transports the ion via the antiport mechanism, whereas it is expected to remain unaltered if the transport process happens via the symport mechanism. Interestingly, we noticed an insignificant change in the lucigenin fluorescence activity (Figure 2.3D), which validates the antiport as a prime transport mechanism.

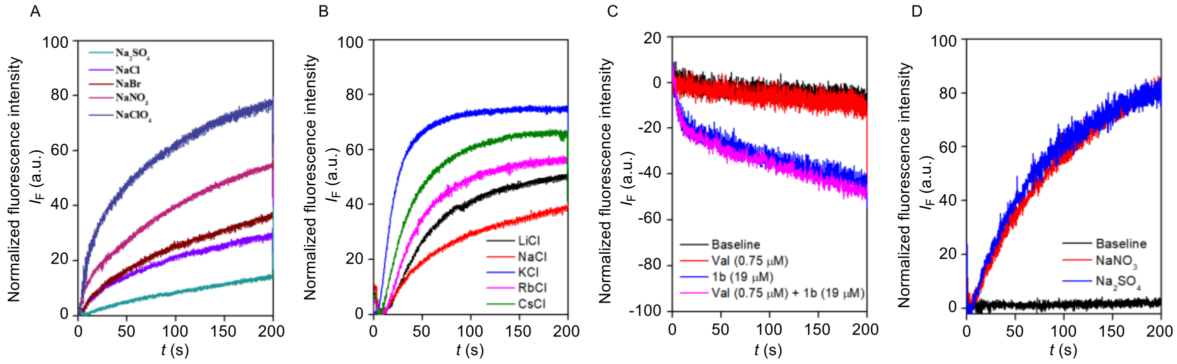

Figure 2.3 Anion (A) and cation (B) selectivity of **1b** across EYPC–LUVs⊃HPTS at 6 μM and 12 μM concentration, respectively. Mechanistic studies of the ion transport by valinomycin assay (C) and NO_3^-/SO_4^{2-} assay (D).

Further, the physiologically relevant Cl^- ion influxing ability of the high transport active compound **1b** was checked across EYPC–LUVs by entrapping the 1 mM lucigenin dye (a halide sensitive dye)[10] and 200 mM $NaNO_3$ salt with pH =7.0. During the assay, an anionic gradient was created by the addition of the 20 µL of 2 M NaCl salt extravesiculerly. If transporter **1b** influx the Cl^- ion, the lucigenin fluorescence quenching activity is expected to be enhanced.[11,12] A prominent change in the increase in the lucigenin fluorescence quenching (Figure 2.11) demonstrated that compound **1b** can efficiently influx the Cl^- ion across the bilayer membrane. Moreover, the cation selectivity was verified across EYPC–LUVs⊃lucigenin by varying the extravesicular MCl salts (M^+ = Li^+, Na^+, K^+, Rb^+, and Cs^+). A noticeable change in the lucigenin fluorescence quenching was observed upon variation of the extravesicular salt (Figure 2.12B), confirming the involvement of the cations in the transport process. The obtained selectivity sequence also corroborates with the cation selectivity obtained during the HPTS assay.

To verify the effect in the membrane for the presence of compound **1b**, ANTS-DPX assay was carried out.[13,14] ANTS is a fluorophore whose fluorescence activity decreases in the presence of the DPX quencher. During the assay, both ANTS and DPX were entrapped in the vesicles made of EYPC lipids. Since ANTS is in short contact with the quencher DPX, the fluorescence activity remains in a quenched state. If the presence of **1b** formed any large pore or disintegrated the membrane, then the leakage of ANTS will enhance its fluorescence activity. Interestingly, no increment of the ANTS fluorescence activity was observed during the assay (Figure 2.13B), even at different concentrations of compound **1b**, indicating that compound **1b** does not form any large pores or disintegrate the membrane.

Finally, the mode of the transport process (carrier or channel) was initially addressed by the cholesterol assay. Cholesterol loading makes the membrane rigid, and hence, excluding some exceptions,[15] it is expected for carrier mode of ion transport, that the ion transport activity will significantly decrease with an increase in the amount of cholesterol.[16] Whereas, for the channel mode of ion transport, the transport activity is expected to remain unaltered. Interestingly, insignificant changes in the transport activity both in the presence of 10% cholesterol and the absence of cholesterol (Figure 2.14) preliminary confirmed the channel mode of ion transport by compound **1b**. To confirm the channel more of ion transport electrophysiological experiment was carried out by using the unbuffered 1 M KCl solution in both cis and trans chamber. The real-time channel current of compound **1b** was monitored using diphytanoyl phosphatidylcholine (diPhyPC) bilayer lipid membrane (BLM). In this experiment, both the cis and trans chambers composed of 1 M KCl solution were separated by painting the n-decane solution of the diPhyPC lipid.[17,18] The addition of **1b** (30 µM) in the cis chamber rapidly triggered square-top shaped current flow with open-close transitions at different holding potentials (Figure 2.4A, B), confirming the formation of ion channels inside the bilayer membrane. The single channel conductance was found to be 57.3 ± 1.9 pS (Table 2.1) and the corresponding channel diameter was calculated 6.2 ± 1 Å by using the Hille equation. The change in current with voltage (*I*-*V* plot) was further monitored with a symmetrical unbuffered 1 M KCl solution. A linear increment of current was observed with an increase in voltage (Figure 2.4C), which confirms the ohmic behavior of the ion channel.

To recognize the selectivity of **1b** towards anion in comparison with cation, the permeability ratio P_{Cl^-}/P_{K^+} was calculated by using the Goldman-Hodgkin-Katz equation with unsymmetrical KCl solutions (i.e. KCl_{cis} = 1 M and KCl_{trans} = 0.5 M). It was perceived that K^+ transport rate is higher than the rate of Cl^- transport with a permeability ratio $P_{Cl^-}/P_{K^+} = 0.053 \pm 0.02$ (Figure 2.4C, 2.16, Table 2.2). Further anion/anion and cation/cation selectivities were evaluated in BLM to get a better visualization of ion selectivity.[19] Anion selectivity was performed by keeping 1 M NaCl and 1 M $NaClO_4$ in cis and trans chambers, respectively. A negative reversible potential ranging from −18.4 mV to −23.4 mV was observed with the average permeability ratio $P_{ClO_4^-}/P_{Cl^-} = 2.1$ (Figure 2.4D, Table 2.3). Conversely, cation/cation selectivity was performed with cis/trans = 1 M NaCl/ 1 M KCl setup. The *I*–*V* plot in the symmetrical cationic conditions gives reversible potential values ranging from −8.3 mV to –12.2 mV, which results in the average permeability ratio of $P_{K^+}/P_{Na^+} = 1.5$ (Figure 2.4D, Table 2.3). The ion selectivity data can be explained based on the size and binding efficiency of ions in the selectivity filter of the ion channel. Both ClO_4^- and K^+ ions are comparatively larger in size as compared to Cl^- and Na^+ ions. Hence, it can efficiently fit and bind in the selectivity filter and can be transported with a higher efficiency rate. Selectivity towards ClO_4^- and K^+ ions from BLM also corroborates with the ion selectivity data achieved from the fluorescence assay.

2.2.3. Theoretical calculations

X-ray crystal structure of compound **1a** showed a dimeric assembly of the molecule having a well-organized H-bonding network. Although this dimeric structure lacks a sufficient cavity for ion passage (Figure 2.17C). Molecular dynamic (MD) simulations were carried out with a dimeric rosette crystal structure **1a** and a trimeric rosette modelled structure **1b**. The detailed study indicated that the dimeric rosette assembly faced a huge energy barrier for the small movement of the Cl^- ion (Figure 2.23) compared to the trimeric rosette structure, indicating that the trimeric rosette is primarily responsible for transporting ions. Therefore, based on the experimentally evaluated Hill co-efficient (n) value, we decided to use the trimeric rosette for the MD simulation studies to understand the selectivity of the channel towards $KClO_4$ over the KCl salt.

To model the ion channel, a single ion-channel forming molecule was first optimized by using density functional theory (DFT) using ωB97X-D functional and 6-31 G(d,p) basis set.[20–22] The trimeric active rosette structure was further optimized using the same level of theory. This optimized trimeric structure was then considered for constructing the (3 × 6) ion pore by placing six trimeric layers of molecules on top of each other. The layered structure of the channel so formed was then optimized using semi-empirical quantum chemistry calculations at the PM6 level, since the size of the system was significantly large to be

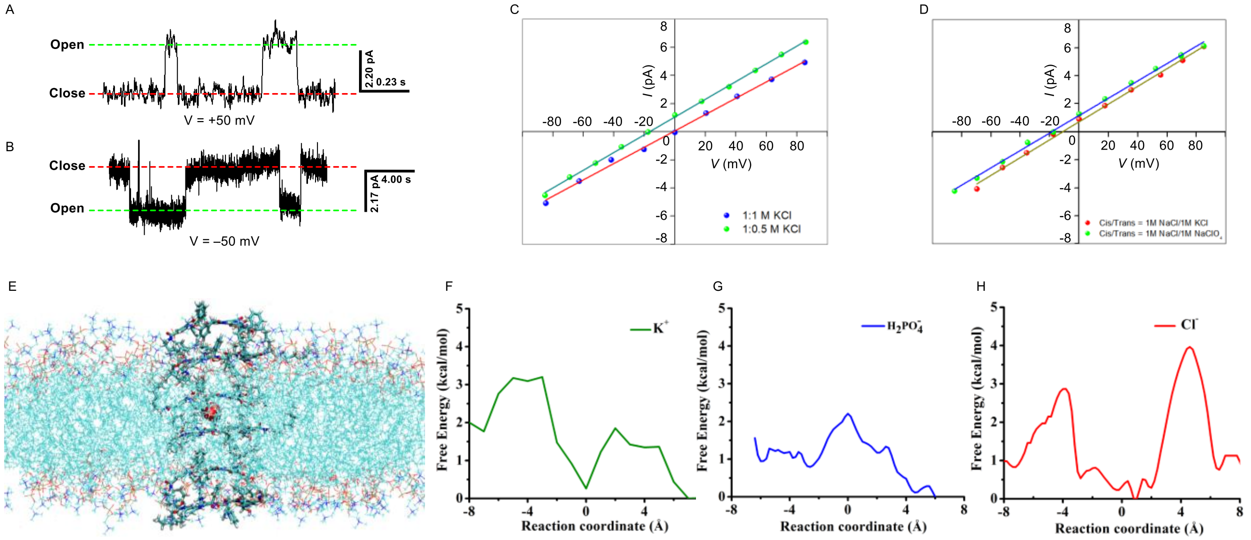

Figure 2.4 Channel opening closing event of compound **1b** (30 µM) at −50 mV (A) and +50 mV (B) under symmetrical unbuffered KCl solution; *I-V* plots of **1b** in both symmetrical and unsymmetrical unbuffered KCl solutions (C); Cation and anion selectivity of **1b** in iso-osmolar salt solutions (D); Equilibrated channel-DPPC/water system (E); calculated free energy of K^+ (F), $H_2PO_4^-$ (G) and Cl^- (H) ions during the passage through the channel cavity.

optimized using DFT.[23] The average diameter of the optimized ion channel was calculated to be about 7.1 Å, which is well in agreement with the experimental data. Further, the PM6-optimized structure was then finally embedded into the lipid bilayer for further calculation. Due to the limitation and unavailability of CHARMM General Force Field (CGenFF) parameters for ClO_4^-, structurally similar $H_2PO_4^-$ with a comparable radius of gyration was used in the MD simulation.

Upon looking at various time frames in the trimeric MD simulated channel, several non-covalent interactions between the ions and the trimeric channel were found. The ions interact with the trimeric rosette of compound **1b** through various modes, depending on the nature of the passing ions. K^+ ions interact with the carbonyl oxygen atoms and hydroxyl oxygens through electrostatic interactions (Figure 2.20). $H_2PO_4^-$ undergoes H-bonding interactions with the hydroxyl and carbonyl groups of the trimeric rosette of **1b**, the ion behaving as the H-bond acceptor and donor, respectively (Figure 2.22). Cl^- ions usually form weak H-bonds with the hydroxyl groups of the trimeric rosette of **1b** (Figure 2.21).

To quantify the possibility of the ion passage through the ion channel and the selectivity of the pore, the free energy changes were calculated for ion passage in terms of the potential of mean forces for all three ions, viz. potassium, chloride, and bi-phosphate ions. The free energy barrier encountered for potassium ion is substantially low ~ 3 kcal/mol (Figure 2.4F). On the other hand, for biphosphate ion (Figure 2.4G), the free energy barrier is about 2 kcal/mol, and the free energy lies below 1.5 kcal/mol for most of the transit path. Therefore, once it overcomes the barrier around the center of the channel, the ion can smoothly pass the rest of the length of the ion channel. The free energy barriers obtained for both potassium and biphosphate ions are, therefore, well within the diffusion-controlled limit, and therefore, it is expected that these two ions would pass through the ion channel at physiological temperatures. However, for chloride ion, two significant barriers are encountered: ~3 kcal/mol at −5 Å and ~4 kcal/mol around 5 Å (Figure 2.4H). In between these two, a local valley exists. Therefore, once the chloride ion enters the ion channel, it might get trapped within the section of the channel flanked between the two barriers, thereby blocking the entrance of other chloride ions from either end. Since the free energy barriers for chloride ion are higher compared to both potassium and biphosphate ions, and thus it is expected that the rate of ion transport would be lesser. It corroborates with the experimentally observed higher selectivity towards $KClO_4$ over KCl salt.

2.3. Conclusion

We synthesized a small molecule-based barrel rosette supramolecular ion channel capable of selective transport of cations and anions. Molecules were synthesized with varying side chains to adjust logP values. Compound **1b** exhibited superior transport activity among the synthesized series. Ion selectivity studies demonstrated its preferential transport of K^+ and ClO_4^- ions. Mechanistic investigations indicated a symport mechanism for ion transport across the bilayer. Dose-response assessments using the lucigenin assay confirmed its ability to facilitate chloride influx. The formation of ion channels was validated through cholesterol-based assays and electrophysiological studies. Electrophysiological experiments revealed a channel diameter of 6.2 ± 1 Å and a single channel conductance of 57.3 ± 1.9 pS. Selectivity studies in BLM showed that compound **1b** exhibits approximately 18.9 times greater permeability to K^+ than Cl^-. Selectivity comparisons in BLM indicated that compound **1b** has 1.5 times greater permeability for K^+ and 2 times greater for ClO_4^- compared to Na^+ and Cl^-, respectively. The selectivity of channel **1b** for $KClO_4$ over KCl salts was further supported by MD simulations, corroborating experimental results. Thus, we believe that these ion channels may offer novel insights into symporter systems with dual ion transport selectivity.

2.4. Experimental section

2.4.1. General methods

Reagents and compounds used for the synthesis were purchased from Sigma-Aldrich, Avra chemicals, Spectrochem, Alfa Aesar and used without further purification. For dry reaction MeOH, DMF, DCM, and THF were purchased from commercial suppliers and used without further purification. All the reactions were performed under nitrogen atmospheric environment using N_2 gas balloon and monitored by checking TLC, performed on pre-coated aluminum plates of silica gel 60 F254 (0.25 mm, E. Merck). Column chromatographies were performed on Merck silica gel (100–200 mesh). Egg yolk phosphatidylcholine (EYPC) was obtained from Avanti Polar Lipids as a solution in $CHCl_3$ (25 mg/mL). HEPES buffer, HPTS, Lucigenin, Triton X–100, NaOH, and inorganic salts were purchased of molecular biology grade from Sigma. Large unilamellar vesicles (LUVs) were prepared by using a mini extruder, equipped with a polycarbonate membrane of 100 nm or 200 nm pore size, purchased from Avanti Polar Lipids.

2.4.2. Physical measurements

The ^{1}H NMR spectra were recorded at 400 MHz and ^{13}C spectra at 101 MHz either in Jeol or Bruker NMR instruments. The residual (deuterium) solvent signals were considered as an internal reference (δH = 7.26 ppm for $CDCl_3$, δH = 2.50 for DMSO-d_6) to calibrate spectra. All the chemical shifts were reported in ppm. The following abbreviations were used to indicate multiplicity patterns s: singlet, d: doublet, t: triplet, q: quartet, p: pentet, m: multiplet, td: triplet of doublets. Coupling constants were measured in Hz. High-resolution mass spectra (HRMS) were recorded on electrospray ionization time-of-flight (ESI–TOF) with +ve mode. Adjustment of pH of buffer solutions was made using Hanna HI98108 PHep$^+$ pH meter. ChemBio Draw 21.0.0 software was used for drawing structures and processing figures. All buffer solutions were prepared from the autoclaved water. Fluorescence experiments were recorded on Fluoromax-4 from Jobin Yvon Edison equipped with an injector port and magnetic stirrer in a microfluorescence cuvette. The extravesicular dye was removed by performing gel chromatography using Sephadex G-50. The fluorescence studies were processed using Origin 8.5 software. Conductance measurement through ion channel was carried out in a planar bilayer lipid membrane (BLM) workstation obtained from Warner Instrument, consisting of head-stage and its corresponding amplifier BC-535, 8-pole bessel filter LPF-8, Axon CNS Digidata 1440A, and pClamp 10 software. The conductance data were analyzed in Clampfit 10.6 software.

2.4.3. Synthesis

The synthetic procedure of compound 5: Compound **5** was synthesized by using the reported procedure.[1]

The general synthetic procedure of 6a–6c: In a 25 mL round bottom flask, compound **5** (400 mg, 1.1 mmol, 1 equiv) was dissolved in dry DMF (5 mL). To the clear solution EDC·HCl (306 mg, 1.7 mmol, 1.5 equiv), HOBt (184 mg, 1.3 mmol, 1.2 equiv), and triethyl amine (396 µL, 2.8 mmol, 2.5 equiv), was added and the solution was stirred at room temperature for 30 min. A different amine (1.1 equiv) was added and stirring was continued at room temperature for 12 h. After completion of the reaction, the solution was transferred to a separating funnel with ethyl acetate (3 × 15 mL) and washed with H_2O (20 mL). The combined organic layer was then washed with brine solution (3 × 15 mL) and finally dried over the Na_2SO_4 and the solvent was evaporated on a rotary evaporator. The crude product was purified by 100-200 mesh silica gel column chromatography.

Synthesis of di-tert-butyl (5-((cyclohexylmethyl)carbamoyl)-1,3-phenylene)dicarbamate: The crude product was purified by silica gel column chromatography (Eluent: 20% ethyl acetate in petroleum ether) to obtain **6a** (Yeild = 74 %).^{1}**H NMR (400 MHz, CDCl$_3$)** δ 7.70 (t, *J* = 2.0 Hz, 1H), 7.48 (t, *J* = 2.5 Hz, 2H), 6.78 (s, 1H), 6.72 (s, 1H), 6.34 (t, *J* = 6.6 Hz, 1H), 3.26 (t, *J* = 6.5 Hz, 2H), 1.81 – 1.68 (m, 6H), 1.50 (s, 18H), 1.25 – 1.12 (m, 4H), 1.00 – 0.94 (m, 1H). ^{13}**C NMR (101 MHz, CDCl$_3$)** δ 167.11, 152.86, 139.56, 136.37, 111.35, 110.86, 81.00, 46.44, 38.14, 31.05, 28.44, 26.53, 25.96. **HRMS (ESI) m/z:** $[M+H]^+$ Calcd. for $C_{24}H_{37}N_3O_5H^+$ 448.2767; Found 448.2809.

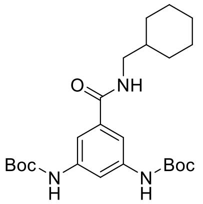

Synthesis of di-tert-butyl (5-(octylcarbamoyl)-1,3-phenylene)dicarbamate: The crude product was purified by silica gel column chromatography (Eluent: 7% ethyl acetate in petroleum ether) to obtain **6b** (Yeild = 82 %). ^{1}**H NMR (400 MHz, CDCl$_3$)** δ 7.70 (d, *J* = 2.3 Hz, 1H), 7.50 (d, *J* = 4.9 Hz, 2H), 6.84 (s, 1H), 6.74 (s, 1H), 6.29 (s, 1H), 3.41 (td, *J* = 7.3, 5.9 Hz, 2H), 1.58 (p, *J* = 7.7, 7.3 Hz, 2H), 1.50 (s, 18H), 1.35 – 1.24 (m, 10H), 0.88 (t, 3H). ^{13}**C NMR (101 MHz, CDCl$_3$)** δ 167.05, 152.91, 139.58, 136.30, 111.39, 110.87, 80.97, 40.32, 31.93, 29.78, 29.44, 29.34, 28.44, 27.15, 22.78, 14.23. **HRMS (ESI) m/z:** $[M+H]^+$ Calcd. for $C_{25}H_{41}N_3O_5H^+$ 464.3080; Found 464.3122.

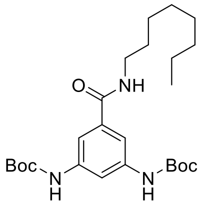

Synthesis of di-tert-butyl (5-(hexylcarbamoyl)-1,3-phenylene)dicarbamate: The crude product was purified by silica gel column chromatography (Eluent: 12% ethyl acetate in petroleum ether) to obtain **6c** (Yeild = 85 %). ^{1}**H NMR (400 MHz, CDCl$_3$)** δ 7.68 (s, 1H), 7.48 (d, *J* = 3.8 Hz, 2H), 6.71 (s, 1H), 6.63 (s, 1H), 6.27 (s, 1H), 3.44 – 3.38 (m, 2H), 1.70 – 1.62 (m, 2H), 1.60 – 1.54 (m, 2H), 1.51 (s, 18H), 1.34 – 1.29 (m, 4H), 0.88 (t, 3H). ^{13}**C NMR (101 MHz, CDCl$_3$)** δ 167.04, 152.91, 139.57, 136.28, 111.35, 110.83, 80.97, 40.30, 31.65, 29.73, 28.43, 26.80, 22.70, 14.16. **HRMS (ESI) m/z:** $[M+H]^+$ Calcd. for $C_{23}H_{37}N_3O_5H^+$ 436.2767; Found 436.2809.

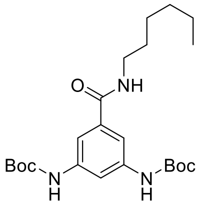

The general synthetic procedure of compound 2a–2c: In a 25 mL round bottom flask, **6a–6c** (1 equiv) was dissolved in dry DCM (3 mL) and trifluoroacetic acid (5 equiv) was added into it. The reaction mixture was kept at room temperature for 2 h. After the completion of the reaction monitored through the TLC, the solvent was evaporated under reduced pressure. The residue was extracted with ethyl acetate (3 × 20 mL), washed with $NaHCO_3$ (20 mL) and brine solution (20 mL) and finally, it was dried over Na_2SO_4.

Synthesis of 3,5-diamino-*N*-(cyclohexylmethyl)benzamide: The crude product **2a** was used in the next reaction step without any further purification (yield of crude product = 78 %). ^{1}**H NMR (400 MHz, CDCl$_3$)** δ 6.44 (d, *J* = 2.0 Hz, 2H), 6.09 (t, *J* = 2.0 Hz, 1H), 6.07 (s, 1H), 3.23 (t, *J* = 6.4 Hz, 2H), 1.78 – 1.48 (m, 6H), 1.26 – 1.13 (m, 4H), 1.01 – 0.95 (m, 1H). ^{13}**C**

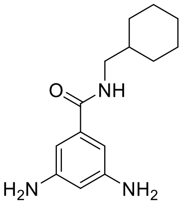

NMR (101 MHz, CDCl$_3$) δ 168.26, 147.88, 137.55, 104.40, 104.11, 46.22, 38.15, 31.03, 26.53, 25.96. **HRMS (ESI) m/z:** $[M+H]^+$ Calcd. for $C_{14}H_{21}N_3OH^+$ 248.1718; Found 248.1762.

Synthesis of 3,5-diamino-*N*-octylbenzamide: The crude product **2b** was used in the next reaction step

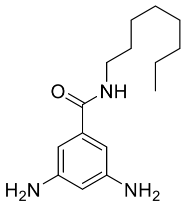

without any further purification (yield of crude product = 94 %). **^{1}H NMR (400 MHz, CDCl$_3$)** δ 6.44 (d, *J* = 2.1 Hz, 2H), 6.11 (t, *J* = 2.0 Hz, 1H), 5.97 (s, 1H), 3.63 (s, 4H), 3.39 (td, *J* = 7.2, 5.7 Hz, 2H), 1.57 (p, *J* = 7.3 Hz, 2H), 1.37 – 1.25 (m, 10H), 0.87 (t, 3H). **^{13}C NMR (101 MHz, CDCl$_3$)** δ 168.20, 147.88, 137.50, 104.40, 104.11, 40.11, 31.93, 29.78, 29.43, 29.35, 27.13, 22.77, 14.22. **HRMS (ESI) m/z:** $[M+H]^+$ Calcd. for $C_{15}H_{25}N_3OH^+$ 264.2031; Found 264.2078.

Synthesis of 3,5-diamino-*N*-hexylbenzamide: The crude product **2c** was used in the next reaction step

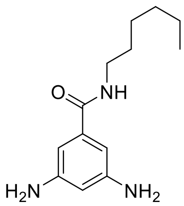

without any further purification (yield of crude product = 89 %). **^{1}H NMR (400 MHz, CDCl$_3$)** δ 6.43 (d, *J* = 1.8 Hz, 2H), 6.09 (s, 1H), 6.06 (s, 1H), 3.64 (s, 4H), 3.37 (q, *J* = 6.8 Hz, 2H), 1.56 (p, *J* = 7.2 Hz, 2H), 1.35 – 1.28 (m, 6H), 0.87 (t, 3H). **^{13}C NMR (101 MHz, CDCl$_3$)** δ 168.19, 147.87, 137.45, 104.38, 104.10, 40.09, 31.64, 29.73, 26.79, 22.70, 14.17. **HRMS (ESI) m/z:** $[M+H]^+$ Calcd. for $C_{13}H_{21}N_3OH^+$ 236.1718; Found 236.1762.

The general synthetic procedure of 3a–3c: In a 25 mL round bottom flask, (2*R*)-2-phenyl-2-((tetrahydro-2*H*-pyran-2-yl)oxy)acetic acid (2.5 equiv) was dissolved in DMF (10 mL). To the clear solution EDC·HCl (3 equiv), HOBt (2.4 equiv) and triethyl amine (7 equiv), were added and the solution was stirred at room temperature for 20 min. Compound **2a**–**2c** (1 equiv) was added to the reaction mixture and stirring was continued at room temperature for 16 h. After completion of the reaction, the solution was transferred to a separating funnel with ethyl acetate (3 × 10 mL) and washed with H_2O (15 mL). The combined organic layers were then washed with brine solution (3 × 10 mL) and finally dried over the Na_2SO_4 and the solvent was evaporated on a rotary evaporator. The crude product was **6a** was used directly for the next step without further purification.

The general synthetic procedure of 1a–1c: In a clean and dried 25 mL round bottom flask, compound **3a**–**3c** (1 equiv) was taken and dissolved in dry methanol (10 mL) and then the required amount of *p*-tolune sulfonic acid (4 equiv) was added into the reaction mixture and kept the reaction mixture for room temperature for 1.5 h. After completion of the reaction, MeOH was evaporated by using the rota evaporator. The reaction mixture was then poured into a separating funnel and the compound was extracted in EtOAc layer by washing it with H_2O (3 × 25 mL). The combined organic layers were then washed with brine solution (3 × 10 mL) and finally dried over the Na_2SO_4 and the solvent was evaporated on a rotary evaporator. The crude product was further purified through column chromatography.

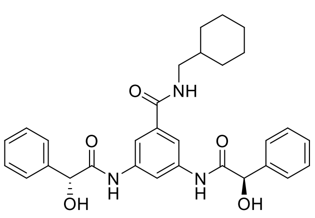

Synthesis of (2*R*,2'*R*)-*N*,*N*'-(5-((cyclohexylmethyl)carbamoyl)-1,3-phenylene)bis(2-hydroxy-2-phenylacetamide): The crude product was purified by silica gel column chromatography (Eluent: 50% ethyl acetate in petroleum ether) to obtain **1a** (Yeild = 97 %). **^{1}H NMR (400 MHz, DMSO-d_6)** δ 9.99 (s, 2H), 8.31 (t, 1H), 8.20 – 8.19 (m, 1H), 7.71 (d, *J* = 1.9 Hz, 2H), 7.52 – 7.49 (m, 4H), 7.37 – 7.32 (m, 4H), 7.30 – 7.26 (m, 2H), 6.36 (d, *J* = 1.7 Hz, 1H), 6.35 (d, *J* = 1.7 Hz, 1H), 5.11 (s, 1H), 5.09 (s, 1H), 3.04 (t, *J* = 6.4 Hz, 2H), 1.73 – 1.57 (m, 6H), 1.20 – 1.13 (m, 3H), 0.94 – 0.84 (m, 2H). **^{13}C NMR (101 MHz, DMSO-d_6)** δ 171.16, 166.39, 140.74, 138.46, 136.18, 128.06, 127.61, 126.54, 114.27, 113.73, 73.89, 45.40, 37.35, 30.50, 26.09, 25.43. **HRMS (ESI) m/z:** [M+H]$^+$ Calcd. for $C_{30}H_{33}N_3O_5H^+$ 516.2493; Found 516.2498. **IR (Neat, ν/cm^{-1}):** 3309.83, 2923.21, 2852.21, 1674.05, 1597.68, 1535.39, 1449.98, 1426.87, 1338.68, 1215.55, 1187.20, 1088.37, 1062.29, 1027.62, 872.11, 756.97, 696.00.

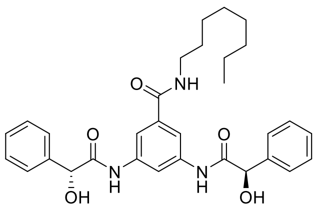

Synthesis of (2*R*,2'*R*)-*N*,*N*'-(5-(octylcarbamoyl)-1,3-phenylene)bis(2-hydroxy-2-phenyl acetamide): The crude product was purified by silica gel column chromatography (Eluent: 60% ethyl acetate in petroleum ether) to obtain **1b** (Yeild = 90 %). **^{1}H NMR (400 MHz, DMSO-d_6)** δ 9.98 (s, 2H), 8.29 (t, *J* = 5.7 Hz, 1H), 8.20 – 8.14 (m, 1H), 7.72 (d, *J* = 2.0 Hz, 2H), 7.55 – 7.47 (m, 4H), 7.39 – 7.30 (m, 4H), 7.33 – 7.23 (m, 2H), 6.35 (d, *J* = 1.8 Hz, 1H), 6.34 (d, *J* = 1.8 Hz, 1H), 5.11 (s, 1H), 5.10 (s, 1H), 3.18 (q, *J* = 6.6 Hz, 2H), 1.48 (d, *J* = 6.4 Hz, 2H), 1.26 (d, *J* = 4.6 Hz, 10H), 0.89 – 0.81 (m, 3H). **^{13}C NMR (101 MHz, DMSO-d_6)** δ 171.17, 166.20, 140.74, 138.47, 136.09, 128.07, 127.62, 126.55, 114.30, 113.84, 73.89, 39.19, 31.27, 29.06, 28.76, 28.67, 26.47, 22.10, 13.97. **HRMS (ESI) m/z:** [M+H]$^+$ Calcd. for $C_{31}H_{37}N_3O_5H^+$ 532.2806; Found 532.2805. **IR (Neat, ν/cm^{-1}):** 3310.35, 2922.25, 2851.36, 1679.67, 1597.46, 1531.87, 1452.09, 1187.58, 1062.30, 755.83, 694.86.

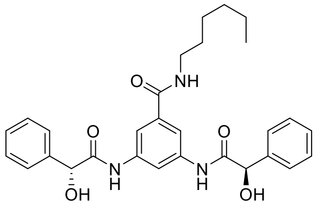

Synthesis of (2*R*,2'*R*)-*N*,*N*'-(5-(hexylcarbamoyl)-1,3-phenylene)bis(2-hydroxy-2-phenyl acetamide): The crude product was purified by silica gel column chromatography (Eluent: 62% ethyl acetate in petroleum ether) to obtain **1c** (Yeild = 93 %). **^{1}H NMR (400 MHz, DMSO-d_6)** δ 9.98 (s, 2H), 8.30 (t, *J* = 5.6 Hz, 1H), 8.17 (s, 1H), 7.72 (d, *J* = 1.9 Hz, 2H), 7.53 – 7.49 (m, 4H), 7.37 – 7.33 (m, 4H), 7.30 – 7.26 (m, 2H), 6.35 (d, *J* = 1.8 Hz, 1H), 6.34 (d, *J* = 1.8 Hz, 1H), 5.11 (s, 1H), 5.10 (s, 1H), 3.19 (q, J = 6.7 Hz, 2H), 1.47 (p, *J* = 7.3, 6.8 Hz, 2H), 1.29 – 1.25 (m, 6H), 0.85 (t, 3H). **^{13}C NMR (101 MHz, DMSO-d_6)** δ 171.17, 166.20, 140.74, 138.47, 136.09, 128.06, 127.61, 126.55, 114.30, 113.84, 73.89, 39.19, 31.03, 29.03, 26.14, 22.07, 13.95. **HRMS (ESI) m/z:** [M+H]$^+$ Calcd. for $C_{29}H_{33}N_3O_5H^+$ 504.2493; Found 504.2500. **IR (Neat, ν/cm^{-1}):** 3294.14, 2920.84, 2851.58, 1673.81, 1597.31, 1532.51, 1452.01, 1187.58, 1061.78, 757.90, 695.91.

2.4.4. Transport studies[24–26]

2.4.4.1. Determination of ion transport studies by HPTS assay

The HEPES buffer (pH = 7.0) was prepared by dissolving an appropriate amount of solid HEPES (10 mM) and NaCl (100 mM) in autoclaved water. The pH was adjusted to 7.0 by the addition of aliquots from the NaOH solution (0.5 M). HPLC grade DMSO was used for the stock solution preparation of all the derivatives.

In a clean and dried round bottom flux (10 mL), 1 mL of egg yolk phosphatidylcholine (EYPC, 25 mg/mL in $CHCl_3$) was dried by purging nitrogen gas with continuous rotation to make a thin transparent film of EYPC. Then, to remove a trace amount of $CHCl_3$, it was kept under a high vacuum for 4 h. Further, the dried thin film was hydrated with 1 mL HEPES buffer (1 mM HPTS, 10 mM HEPES, 100 mM NaCl, pH = 7.0), and resulting the suspension was vortexed for 1 h at 10 min intervals. This hydrated suspension was subjected for 21 cycles of freeze–thaw (liquid N_2 and 55 °C hot water bath) followed by extrusion through 100 nm pore size containing polycarbonate membrane for 21 times (must be an odd number), in order to achieve uniform distribution of LUVs of an average 100 nm diameter. Finally, size exclusion chromatography using gel filtration (Sephadex G-50) was carried out to remove the unentrapped extravesicular HPTS dyes with HEPES buffer (10 mM HEPES, 100 mM NaX, pH = 7.0). Collected vesicles were diluted to 6 mL to get EYPC–LUVs⊃HPTS. Final conditions: ~ 5.0 mM EYPC, Inside: 1 mM HPTS, 10 mM HEPES, 100 mM NaCl, pH = 7.0, Outside: 10 mM HEPES, 100 mM NaCl, pH = 7.0.

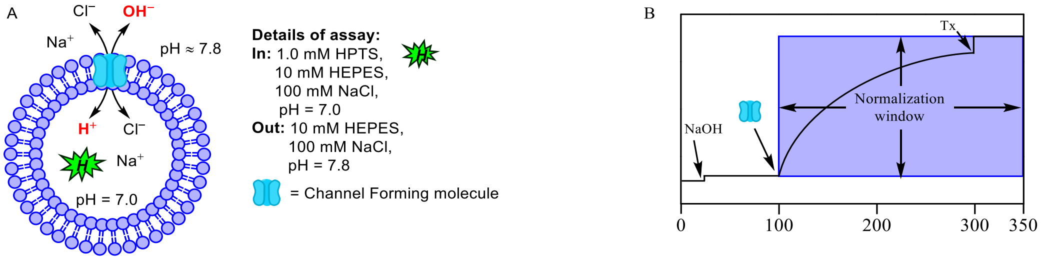

Figure 2.5 Schematic representation of ion transport activity across EYPC–LUVs⊃HPTS vesicle (A), and normalization window for same fluorescence kinetics experiment of ion transport (B).

The time axis was normalized according to Equation 1:

$$t = t - 100 \qquad \text{Equation 1}$$

where, in normalized data $t = 0$ s was the timing of compound addition during the experiment, and $t = 200$ s was the timing of Triton X–100 addition.

The time-dependent data were normalized to fractional fluorescence intensity using Equation 2

$$I_F = [(I_t - I_0) / (I_\infty - I_0)] \times 100 \qquad \text{Equation 2}$$

where, I_0 = Fluorescence intensity just before the channel forming molecule addition (at 0 s), I_∞ = Final fluorescence intensity after addition of Triton X–100, I_t = Fluorescence intensity at time t.

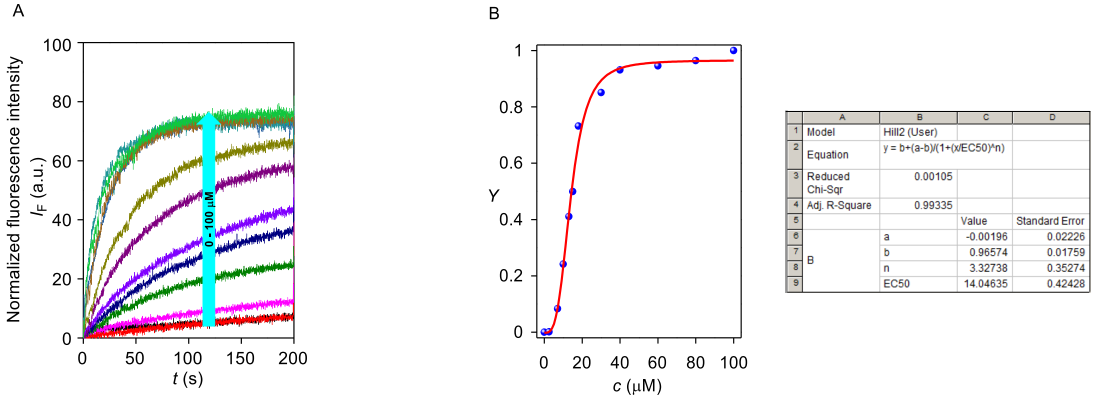

	A	B	C	D
1	Model	Hill2 (User)		
2	Equation	y = b+(a-b)/(1+(x/EC50)^n)		
3	Reduced Chi-Sqr	0.00105		
4	Adj. R-Square	0.99335		
5			Value	Standard Error
6	B	a	-0.00196	0.02226
7		b	0.96574	0.01759
8		n	3.32738	0.35274
9		EC50	14.04635	0.42428

Figure 2.6 Concentration dependent ion transport activity of compound **1a** (0–100 μM) with NaCl salt across EYPC–LUVs⊃HPTS (A), and corresponding Hill plot of compound **1a** at *t* = 190 s (B).

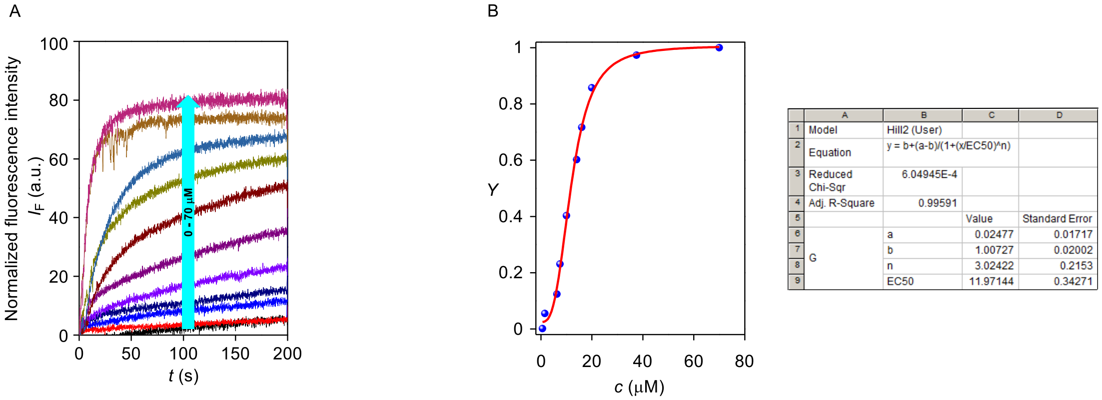

	A	B	C	D
1	Model	Hill2 (User)		
2	Equation	y = b+(a-b)/(1+(x/EC50)^n)		
3	Reduced Chi-Sqr	6.04945E-4		
4	Adj. R-Square	0.99591		
5			Value	Standard Error
6	G	a	0.02477	0.01717
7		b	1.00727	0.02002
8		n	3.02422	0.2153
9		EC50	11.97144	0.34271

Figure 2.7 Concentration dependent ion transport activity of compound **1b** (0–70 μM) with NaCl salt across EYPC–LUVs⊃HPTS (A), and corresponding Hill plot of compound **1b** at *t* = 190 s (B).

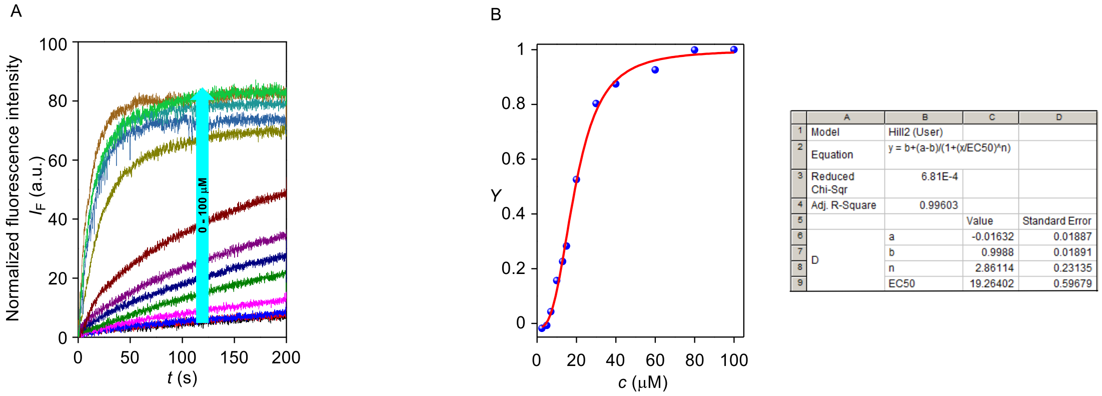

	A	B	C	D
1	Model	Hill2 (User)		
2	Equation	y = b+(a-b)/(1+(x/EC50)^n)		
3	Reduced Chi-Sqr	6.81E-4		
4	Adj. R-Square	0.99603		
5			Value	Standard Error
6	D	a	-0.01632	0.01887
7		b	0.9988	0.01891
8		n	2.86114	0.23135
9		EC50	19.26402	0.59679

Figure 2.8 Concentration dependent ion transport activity of compound **1c** (0–100 μM) with NaCl salt across EYPC–LUVs⊃HPTS (A), and corresponding Hill plot of compound **1c** at *t* = 190 s (B).

2.4.4.2. Determination of ion selectivity by HPTS assay[3,27]

HEPES buffer was prepared by dissolving an appropriate amount of solid HEPES and a salt (either of NaCl, NaBr, $NaNO_3$, $NaClO_4$, Na_2SO_4, LiCl, KCl, RbCl, and CsCl) in autoclaved water to get 10 mM HEPES and 100 mM salt (33.33 mM for Na_2SO_4), respectively. Subsequently, the pH was adjusted to 7.0 by the addition of 0.5M NaOH solution. The stock solution of most active compound **1b** was prepared in HPLC grade DMSO solution for the studies.

2.4.4.2.1. Anion selectivity by HPTS assay

The vesicles were prepared by the following same protocol as described above. Final Condition: EYPC–LUVs⊃HPTS (~ 5.0 mM EYPC), Inside: 1 mM HPTS, 10 mM HEPES, Y mM Na_mX, pH = 7.0 and Outside: 10 mM HEPES, 100 mM Na_mX, pH = 7.0 (where, m = valencey of anion, Y = 100 when X^- = Cl^-, Br^-, ClO_4^-, NO_3^- and Y= 33.33 when $X^- = SO_4^{2-}$).

In a clean fluorescence cuvette, 1975 µL of HEPES buffer (10 mM HEPES, Y mM Na_mX, at pH = 7.0; where, Y = 100 when $X^- = Cl^-$, Br^-, ClO_4^-, NO_3^- and Y= 33.33 when $X^- = SO_4^{2-}$) was added followed by addition of 25 µL of EYPC–LUVs⊃HPTS vesicle in slowly stirring condition by a magnetic stirrer equipped with the fluorescence instrument (at t = 0 s). The time-dependent HPTS emission intensity was monitored at λ_{em} = 510 nm (λ_{ex} = 450 nm) by creating a pH gradient (~0.8) between intra- and extra-vesicular system by the addition of 20 µL NaOH (0.5 M) at t = 20 s. The channel forming molecule **1b** was added at t = 100 s and at t = 300 s, 25 µL of 10% Triton X–100 was added to lyze all vesicles for the complete destruction of the pH gradient. For data analysis and comparison, time (X-axis) was normalized between the point of addition of channel forming molecule (i.e. t = 100 s was normalized to t = 0 s) and the end point of the experiment (i.e. t = 300 s was normalized to t = 200 s) using Equation 1. Fluorescence intensities (I_t) were normalized to fractional emission intensity I_F using Equation 2.

2.4.4.2.2. Cation selectivity by HPTS assay

Cation selectivity of the highest active compound **1b** was explored by changing both intravesicular and extravesicular HEPES buffer solution (10 mM HEPES, 100 mM MCl, pH = 7.0) of MCl salts (M^+ = Li^+, Na^+, K^+, Rb^+ and Cs^+). For data analysis and comparison, time (X-axis) was normalized between the point of addition of channel forming molecule (i.e. t = 100 s was normalized to t = 0 s) and the end point of the experiment (i.e. t = 300 s was normalized to t = 200 s) using Equation 1. Fluorescence intensities (I_t) were normalized to fractional emission intensity I_F using Equation 2.

In a clean fluorescence cuvette, 1975 µL of HEPES buffer (10 mM HEPES, 100 mM MCl, at pH = 7.0; where, M^+ = Li^+, Na^+, K^+, Rb^+ , and Cs^+) was added, followed by the addition of 25 µL of EYPC–

LUVs⊃HPTS vesicle in slowly stirring condition by a magnetic stirrer equipped with the fluorescence instrument (at $t = 0$ s). The time-dependent HPTS emission intensity was monitored at $\lambda_{em} = 510$ nm ($\lambda_{ex} = 450$ nm) by creating a pH gradient (~0.8) between intra- and extra-vesicular system by the addition of 20 µL NaOH (0.5 M) at $t = 20$ s. The channel forming molecule **1b** was added at $t = 100$ s and at $t = 300$ s, 25 µL of 10% Triton X–100 was added to lyze all vesicles for the destruction of pH gradient. For data analysis and comparison, time (X-axis) was normalized between the point of addition of channel forming molecule (i.e. $t = 100$ s was normalized to $t = 0$ s) and the endpoint of the experiment (i.e. $t = 300$ s was normalized to $t = 200$ s) using Equation 1. Fluorescence intensities (I_t) were normalized to fractional emission intensity I_F using Equation 2.

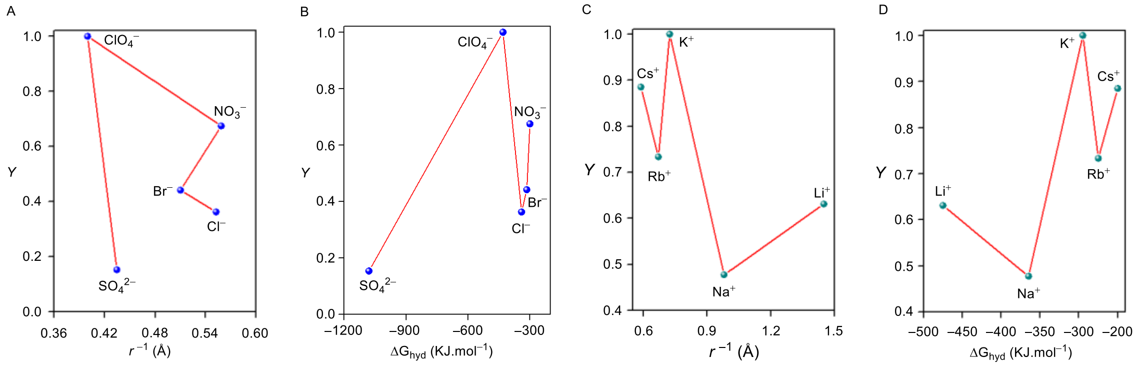

Figure 2.9 Fractional activity Y (relative to ClO_4^-) as a function of the reciprocal anion radius (A); fractional activity Y (relative to ClO_4^-) as a function of the anion hydration energy (B); fractional activity Y (relative to K^+) as a function of the reciprocal cation radius (C) and fractional activity Y (relative to K^+) as a function of the cation hydration energy (D).

2.4.4.3. Transport studies across EYPC–LUVs⊃lucigenin vesicles

2.4.4.3.1. Chloride transport activity across EYPC–LUVs⊃lucigenin vesicles[28]

HEPES buffer was prepared by dissolving an appropriate amount of solid HEPES and a $NaNO_3$ salt in autoclaved water to get 10 mM HEPES and 200 mM $NaNO_3$ salt, respectively. Subsequently, the pH was adjusted to 7.0 by the addition of 0.5 M NaOH solution. The stock solution of most active compound **1b** was prepared in HPLC grade ACN solution for the studies.

In a clean and dried small (10 mL) round bottom flask, 1 mL egg yolk phosphatidylcholine (EYPC, 25 mg/mL stock in $CHCl_3$) was added. The solution was dried by purging nitrogen with continuous rotation to form a thin transparent film of EYPC. The transparent film was kept in high vacuum for 4 h to remove all trace of $CHCl_3$ at room temperature. The resulting film was hydrated with 1 mL buffer solution (1 mM lucigenin, 10 mM HEPES and 200 mM $NaNO_3$, pH = 7.0) and resulting suspension was vortexed at 10 min intervals during 1 h. This hydrated suspension was subjected to 21 cycles of freeze-thaw (liquid N_2, 55 °C) followed by extrusion through 200 nm pore size containing polycarbonate membrane for 21 times (must be an odd number), in order to achieve the vesicles of an average 200 nm diameter. Extravesicular dyes were removed by gel filtration (using Sephadex G-50) with buffer solution (10mM HEPES and 200 mM $NaNO_3$, pH = 7.0), and diluted to 4 mL to get EYPC–LUVs⊃lucigenin. Final conditions: ~ 5 mM EYPC; Inside: 1 mM lucigenin, 10 mM HEPES, 200 mM $NaNO_3$, pH = 7.0; Outside: 10 mM HEPES, 200 mM $NaNO_3$, pH = 7.0.

In clean and dried fluorescence cuvette, 1975 µL of buffer solution (10 mM HEPES, 200 mM $NaNO_3$ and pH = 7.0) and 25 µL EYPC–LUVs⊃lucigenin were taken. This suspension was placed in a slowly stirring condition in fluorescence instrument equipped with a magnetic stirrer (at $t = 0$ s). The fluorescence intensity of lucigenin was monitored at $\lambda_{em} = 535$ nm ($\lambda_{ex} = 455$ nm) as a course of time. The chloride gradient was created by the addition of 2.0 M NaCl (33.3 µL) at $t = 20$ s between intra and extravesicular system, followed by addition of channel forming molecule **1b** at $t = 100$ s. Finally, vesicles were lysed by addition of 10% Triton X–100 (25 µL) at $t = 300$ s for the complete destruction of chloride gradient.

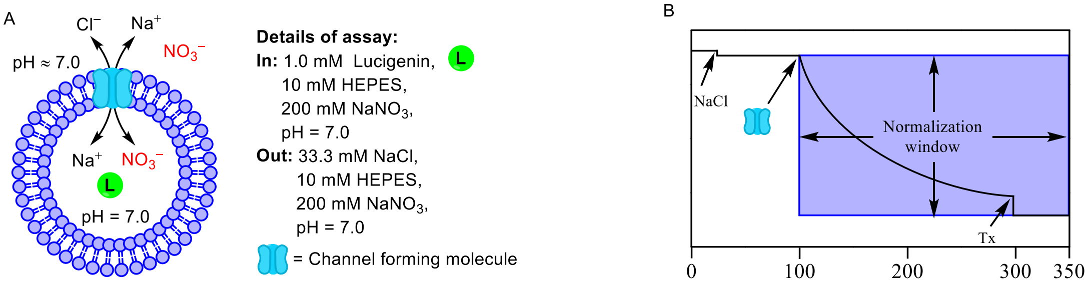

Figure 2.10 Schematic representation of ion transport activity across EYPC–LUVs⊃lucigenin vesicle (A), and normalization window for same fluorescence kinetics experiment of ion transport (B).

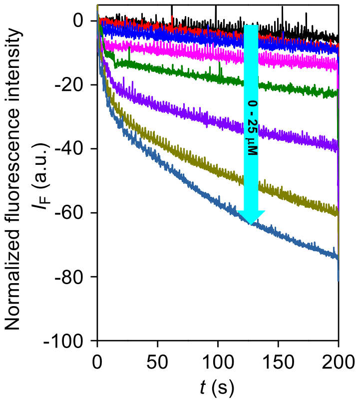

Figure 2.11 Chloride influx study across EYPC–LUVs⊃lucigenin with channel forming molecule **1b**.

Precipitation of compound **1b** restrict us to evaluate the hill-coefficient and EC_{50} value from this experiment.

The time-dependent data were normalized to fractional (in percentage) fluorescence intensity using Equation 3:

$$I_{\mathrm{F}} = [(I_{\mathrm{t}} - I_0) / (I_\infty - I_0)] \times (-100) \qquad \text{Equation 3}$$

Where, I_0 = Fluorescence intensity just before the channel forming molecule addition (at 0 s). I_∞ = Final fluorescence intensity after the addition of Triton X–100. I_{t} = Fluorescence intensity at time *t*.

For data analysis and comparison, time (X–axis) was normalized between the point of compound addition (i.e. *t* = 100 s was normalized to *t* = 0 s) and the end point of the experiment (i.e. *t* = 300 s was normalized to *t* = 200 s).

2.4.4.3.2. Cation selectivity across EYPC–LUVs⊃lucigenin vesicles

The vesicles were prepared by the same procedure as discussed above.

Details of the assay: In a clean and dried fluorescence cuvette, 1975 µL of buffer solution (10 mM HEPES, 200 mM $NaNO_3$ and pH = 7.0) and 25 µL EYPC–LUVs⊃lucigenin were taken. The suspension was kept in a slowly stirring condition in a fluorescence instrument equipped with a magnetic stirrer at t = 0 s. The quenching of fluorescence intensity of lucigenin was monitored as a course of time at λ_{em} = 535 nm (λ_{ex} = 455 nm). At *t* = 20 s, the chloride gradient was created by the addition of 2 M chloride salts (33.3 µL) of different cations MCl (M^+ = Li^+, Na^+, K^+, Rb^+ and Cs^+), followed by the addition of channel forming molecule **1b** at t = 100 s. Finally, vesicles were lysed by the addition of 10% Triton X–100 (25 µL) at *t* = 300 s to diminish the applied chloride gradient completely. The time-dependent data were normalized to fractional (in percentage) fluorescence intensity using Equation 3.

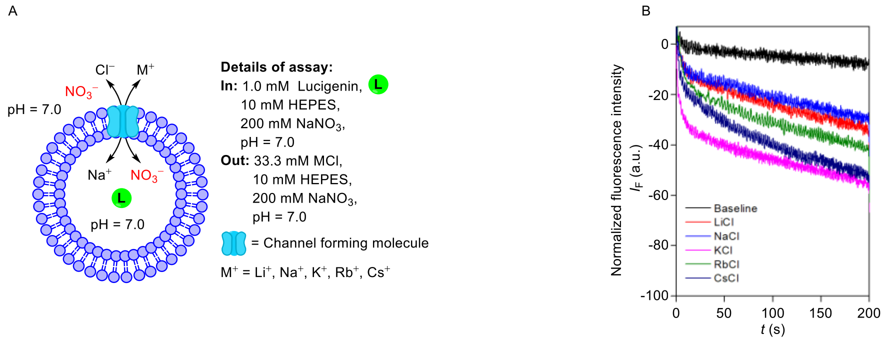

Figure 2.12 Schematic representation of cation selectivity assay across EYPC–LUVs⊃lucigenin (A), Cation selectivity of channel forming compound **1b** (19 µM) by varying extravesicular cations (B).

2.4.4.4. Mechanistic studies

2.4.4.4.1. Cl^- transport by Lucigenin assay in the presence of Valinomycin[27]

In clean and dried fluorescence cuvette, 1975 µL of buffer solution (10 mM HEPES, 200 mM $NaNO_3$, and pH = 7.0) and 25 µL EYPC–LUVs⊃lucigenin were taken and slowly stirred in a fluorescence instrument equipped with a magnetic stirrer (at $t = 0$ s). The time-dependent fluorescence intensity of lucigenin was monitored at $\lambda_{em} = 535$ nm ($\lambda_{ex} = 455$ nm). A solution of 2 M KCl (33.3 µL) was added at $t = 20$ s to create a chloride gradient between the intra- and extra-vesicular system, followed by the addition of valinomycin (0.75 µM) at $t = 50$ s and channel forming molecule **1b** (19 µM) at $t = 100$ s. Finally, the destruction of the chloride gradient was done by the addition of 10 % Triton X–100 (25 µL) at $t = 300$ s. The time-dependent data were normalized to fractional (in percentage) fluorescence intensity using Equation 3.

2.4.4.4.2. NO_3^-/SO_4^{2-} assay[9]

Buffer and stock solution preparation: HEPES buffer was prepared by dissolving an appropriate amount of solid HEPES and NaCl salt in autoclaved water to get 10 mM HEPES and 200 mM NaCl salt, respectively. Subsequently, the pH was adjusted to 7.0 by the addition of 0.5 M NaOH solution. Similarly, iso-osmolar $NaNO_3$ buffer (10 mM HEPES and 200 mM $NaNO_3$, pH = 7.0) and Na_2SO_4 (10 mM HEPES and 66.6 mM Na_2SO_4, pH = 7.0) buffer solution were prepared. The stock solution of most active compound **1b** was prepared in HPLC grade ACN solution for the studies.

Preparation of EYPC–LUVs⊃lucigenin: Lucigenin vesicles were prepared by following the same protocol as mentioned above. Final conditions: ~ 5 mM EYPC; Inside: 1 mM lucigenin, 10 mM HEPES, 200 mM NaCl, pH = 7.0; Outside: 10 mM HEPES, 200 mM NaCl, pH = 7.0.

Details of the assay: In clean and dried fluorescence cuvette 1950 µL of buffer solution (either 10 mM HEPES, 200 mM $NaNO_3$ and pH = 7.0 or 10 mM HEPES, 66.6 mM Na_2SO_4 and pH = 7.0) and 50 µL EYPC–LUVs⊃lucigenin were taken and slowly stirred in fluorescence instrument equipped with a magnetic stirrer (at $t = 0$ s). Channel-forming molecule **1b** (15 µM) was added at $t = 100$ s. The time-dependent fluorescence intensity of lucigenin was monitored at $\lambda_{em} = 535$ nm ($\lambda_{ex} = 455$ nm). Finally, the destruction of the chloride gradient was done by the addition of 10 % Triton X–100 (25 µL) at $t = 300$ s. The time-dependent data were normalized to fractional (in percentage) fluorescence intensity using Equation 2.

2.4.4.5. Evaluation of membrane stability and channel nature by ANTS–DPX assay

EYPC–LUVs were loaded with anionic fluorophore ANTS (8-aminonaphthalene-1,3,6-trisulfonic acid disodium salt) and cationic quencher DPX (1,1-[1,4-phenylenebis(methylene)]bis[pyridinium]bromide). Efflux of either ANTS or DPX through pores formed by compound **1b** was followed by an increase in ANTS fluorescence emission intensity. All buffer solutions were prepared by known method.[13] Buffer A: 12.5 mM ANTS, 45.0 mM DPX, 5 mM TES, 20 mM KCl, pH = 7.0 Buffer B: 5 mM TES, 100 mM KCl, pH = 7.0.

Prepartion of EYPC–LUVs⊃ANTS/DPX vesicles:[13] A thin film of EYPC lipid was prepared by evaporating 0.5 ml of EYPC lipid solution (25 mg/mL) in $CHCl_3$ by the flow of nitrogen and then it was kept in vacuo (4 h) to remove trace amount of $CHCl_3$. After 4 h it was hydrated with 0.5 mL buffer A, followed by vortex treatment at 10 min intervals for 1 h. This hydrated suspension was subjected to 21 cycles of freeze-thaw (liquid N_2, 55 °C) followed by extrusion through 100 nm pore size containing polycarbonate membrane 21 times (must be an odd number), in order to achieve the vesicles of an average 100 nm diameter. Extravehicular ANTS/DPX dyes were removed by gel filtration (using Sephadex G-50) with buffer B solution (5 mM TES, 100 mM KCl, pH = 7.0), and diluted with the same buffer to 3 mL to get EYPC–LUVs⊃ANTS/DPX.

ANTS/DPX assay: In clean and dried fluorescence cuvette, 1950 µL of buffer B solution (5 mM TES, 100 mM KCl, pH = 7.0) and 50 µL EYPC–LUVs⊃ANTS/DPX were taken. The suspension was kept in a slowly stirring condition in the fluorescence instrument equipped with a magnetic stirrer at $t = 0$ s. The fluorescence intensity was monitored as a course of time at $\lambda_{em} = 520$ nm ($\lambda_{ex} = 353$ nm). At $t = 100$ s channel forming molecule **1b** was added into it at different concentrations. Finally, vesicles were lysed by the addition of 10% Triton X–100 (25 µL) at $t = 300$ s for 100% efflux of ANTS/DPX dyes. The time-dependent data were normalized to fractional (in percentage) fluorescence intensity using Equation 2 and time axis (X–axis) was normalized using Equation 1.

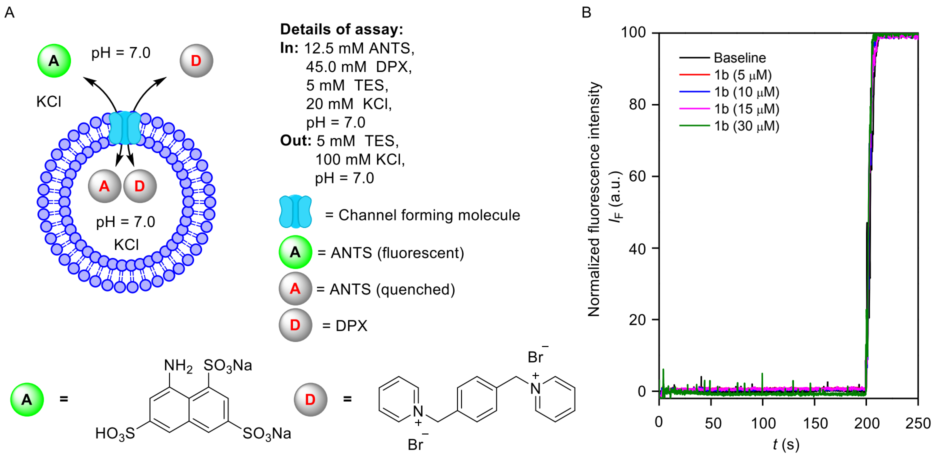

Figure 2.13 Schematic representation of ANTS/DPX assay across EYPC–LUVs⊃ANTS/DPX (A), and fluorescence kinetics experiment of channel forming compound **1b** at different concentrations (B).

2.4.4.6. Evaluation of mode of ion transport by cholesterol assay

Buffer and stock solution preparation: HEPES buffer was prepared by dissolving an appropriate amount of solid HEPES and NaCl salt in autoclaved water to get 10 mM HEPES and 100 mM NaCl, respectively.

Subsequently, the pH was adjusted to 7.0 by the addition of 0.5M NaOH solution. The stock solution of most active compound **1b** was prepared in HPLC grade DMSO solution for the studies.

Preparation of vesicles: Both EYPC–LUVs⊃HPTS and 10 mol% cholesterol based EYPC–LUVs⊃HPTS was prepared by following the above mentioned method.[16,29]

Details of the assay: In clean and well dried fluorescence cuvette, 1975 µL of HEPES buffer (10 mM HEPES, 100 mM NaCl, pH =7.0) and 25 µL of with or without cholesterol (10 mol%) based EYPC–LUVs⊃HPTS vesicle was added. The cuvette was placed in a slowly stirring condition using a magnetic stirrer equipped in the fluorescence instrument ($t = 0$ s). The time-dependent HPTS emission intensity was monitored at $\lambda_{em} = 510$ nm ($\lambda_{ex} = 450$ nm) by creating pH gradient (~ 0.8) between intra- and extra-vesicular system by the addition of 20 µL NaOH (0.5 M) at $t = 20$ s. Compound **1b** was added at $t = 100$ s. Finally, the vesicles were lysed by the addition of 10% Triton X−100 solutions (25 µL) at $t = 300$ s for destruction pH gradient.

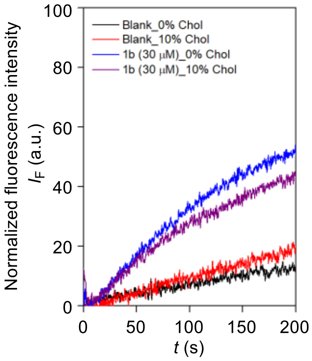

Figure 2.14 Fluorescence kinetics experiment of channel forming compound **1b**.

Experimental data revealed that with decreasing membrane fluidity ion transport activity of compound **1b** was not changed significantly, indicating that the ion transport process mainly occurred through channel formation.

2.4.5. Planar bilayer conductance measurements[27,29]

Diphytanoylphosphatidylcholine (Avanti Polar Lipids), dissolved in n-decane (20 mg/mL) was used to form a Bilayer lipid membrane (BLM) across an aperture of 150 µM diameter in a polystyrene cup (Warner Instrument, USA). Both cis and trans chambers were filled with symmetrical unbuffered 1M KCl solution. The cis chamber was connected to the BC 535 head-stage (Warner Instrument, USA) by an Ag-AgCl electrode, and the trans chamber was held at virtual ground. Compound **1b** (30 µM, stock solution prepared in DMSO) was added to the cis chamber, and the solution was stirred with a magnetic stirrer for 20 min. The addition of compound **1b** rapidly triggered the current flow with open-close transition events at different holding potentials, confirming the formation of ion channels inside the bilayer membrane.

Currents were low pass filtered at 1 kHz using pClamp9 software (Molecular Probes, USA) and an analog-to-digital converter (Digidata 1440, Molecular Probes). All data were analyzed by the software pClamp 10.7.

The average current was calculated from the trace and then conductance and other calculations were made accordingly.

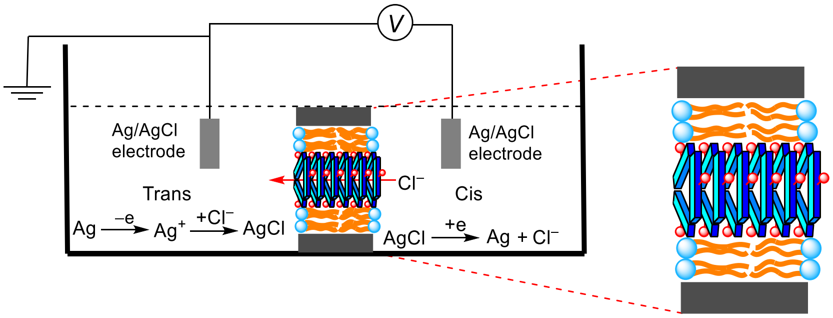

Figure 2.15 Systematic representation of bilayer lipid membrane experiment.

2.4.5.1. Channel diameter calculation

Channel diameter was calculated by using Hille's equation,

$$1/g = (l + \pi d/4) \times (4\rho/\pi d^2) \qquad \text{Equation 4}$$

Where, g = corrected conductance (obtained by multiplying measured conductance with the Sansom's correction factor), l = thickness of the membrane = 34 Å, and ρ = resistivity of 1 M KCl solution = 9.44 Ω·cm) and d = diameter of the ion channel.

2.4.5.2. Single-channel conductance calculation

Table 2.1 Table for experimentally calculated single-channel conductance of compound **1b**.

Entry	**Slope**	**G (pS)**
1	0.05801	58.01
2	0.05545	55.45
3	0.05666	56.66
4	0.05796	57.96
5	0.05874	58.74
		Average = 57.36

2.4.5.3. Anion/cation selectivity in BLM

The cis and trans chambers were filled with unsymmetrical KCl solutions. The cis chamber was filled with 1.0 M KCl solution, and the trans chamber was filled with 0.5 M KCl. The compound **1b** (30 µM) was added to the cis chamber and stirred for 20 min. The reversal potential was calculated to be –16.49 mV, and the calculated permeability ratio $P_{Cl^-}/P_{K^+} = 0.053 \pm 0.02$ (Equation 5).

The permeability ratio ($P_{\mathrm{Cl}^-}/P_{\mathrm{K}^+}$) was calculated by using Goldman-Hodgkin-Katz equation,

$$\frac{P_{Cl^-}}{P_{K^+}} = \frac{a_{K^+_{cis}} - a_{K^+_{trans}} \times \exp(-\frac{V_{rev}F}{RT})}{a_{Cl^-_{cis}} \times \exp(-\frac{V_{rev}F}{RT}) - a_{Cl^-_{trans}}} \qquad \text{Equation 5}$$

where, $\frac{P_{Cl^-}}{P_{K^+}}$ = anion/cation permeability ratio; $a_{K^+_{cis}}$ = K$^+$ activity in the cis chamber; $a_{K^+_{tras}}$ = K$^+$ activity in the trans chamber; $a_{Cl^-_{cis}}$ = Cl$^-$ activity in the cis chamber; $a_{Cl^-_{trans}}$ = Cl$^-$ activity in the trans chamber; V_{rev} = reversal potential; F = Faraday constant; R = gas constant; T = temperature (K).

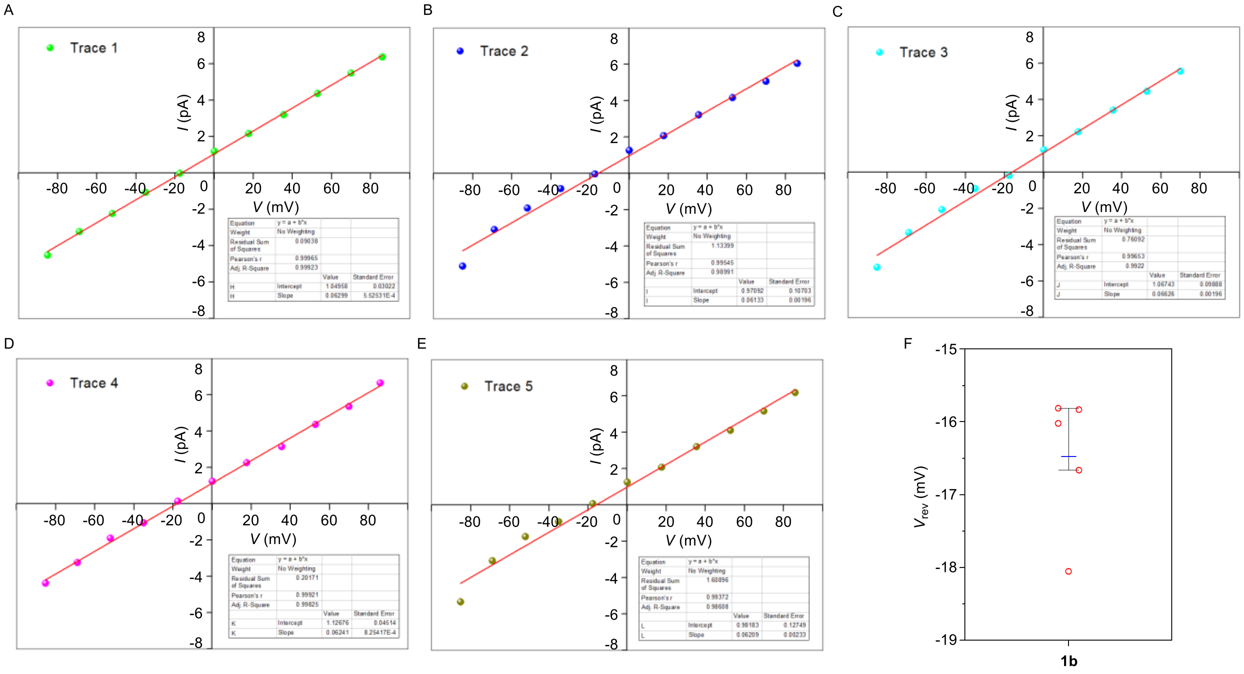

Figure 2.16 All five traces of I-V plots of **1b** in unsymmetrical (cis/trans = 1M/0.5M) KCl solutions (A, B, C, D, E); box plot of the averaged V_{rev} from five experiments (represented as red circles) (F).

From all of the five traces, the permeability ratio ($P_{\mathrm{Cl}^-}/P_{\mathrm{K}^+}$) was calculated individually. The average value of the permeability ratio ($P_{\mathrm{Cl}^-}/P_{\mathrm{K}^+}$) obtained from the five traces was represented above.

Table 2.2 Table for experimentally calculated permeability ratio of compound **1b**.

Entry	V_{rev}	P_{Cl^-}/P_{K^+}
1	-16.66	0.03138
2	-15.83	0.07223
3	-16.11	0.05822
4	-18.05	0.03162
5	-15.81	0.07324
	Average = -16.49	Average = 0.053

2.4.5.4. Cation/cation and anion/anion selectivity in BLM[19]

Table 2.3 Table for experimentally calculated permeability ratio for cation/cation and anion/anion selectivity of compound **1b**.

Cis/Trans = 1.0 M NaCl/1.0 M KCl			Cis/Trans = 1.0 M NaCl/1.0 M $NaClO_4$		
Entry	Reversal voltage V_r (mV)	$\frac{P_{K^+}}{P_{Na^+}}$	Entry	Reversal voltage V_r (mV)	$\frac{P_{ClO_4^-}}{P_{Cl^-}}$
1	– 11.152	1.5437	**1**	– 18.658	2.0679
2	– 8.301	1.3815	**2**	– 18.489	2.0544
3	– 9.574	1.5594	**3**	– 18.695	2.0709
4	– 9.757	1.4618	**4**	– 23.415	2.4888
5	– 12.188	1.6069	**5**	– 21.443	2.3048
	Average = – 10.19	Average = 1.51		Average = – 20.14	Average = 2.19

2.4.5. Single crystal X-ray diffraction study

The single crystals of **1a** were grown from acetonitrile allowing slow evaporation of the solvents with time. X-ray diffraction data on single crystals of **1a** was collected on a Bruker D8 Venture Duo X-ray diffractometer equipped with a Microfocus X-ray source (operated at 50 W; 50 kV/1 mA) and graded multilayer optics for monochromatic Mo Kα radiation (λ = 0.71073 Å) with a focused X-ray beam and a Photon 100 CMOS chip based detector system at 150 K. The crystal was mounted on nylon Cryo Loops (Hampton Research) with Paraton-N (Hampton Research). The data integration and reduction were processed with SAINT software.1 A multi-scan absorption correction was applied to the collected reflections. The structure was solved by a direct method using SHELXTL3,4 and was refined on F2 with a full-matrix least squares technique using the SHELXL 5 program package. All of the hydrogen atoms were refined anisotropically. All of the hydrogen atoms were located in successive difference fourier maps, and they were treated as riding atoms using SHELXL default parameters. The structures were examined using the Adsym subroutine in PLATON to ensure that no additional symmetries could be applied to the models.

CPK model of the dimeric crystal structure of compound **1a**, clearly indicated that it doesn't have any adequate pathway for ion passage.

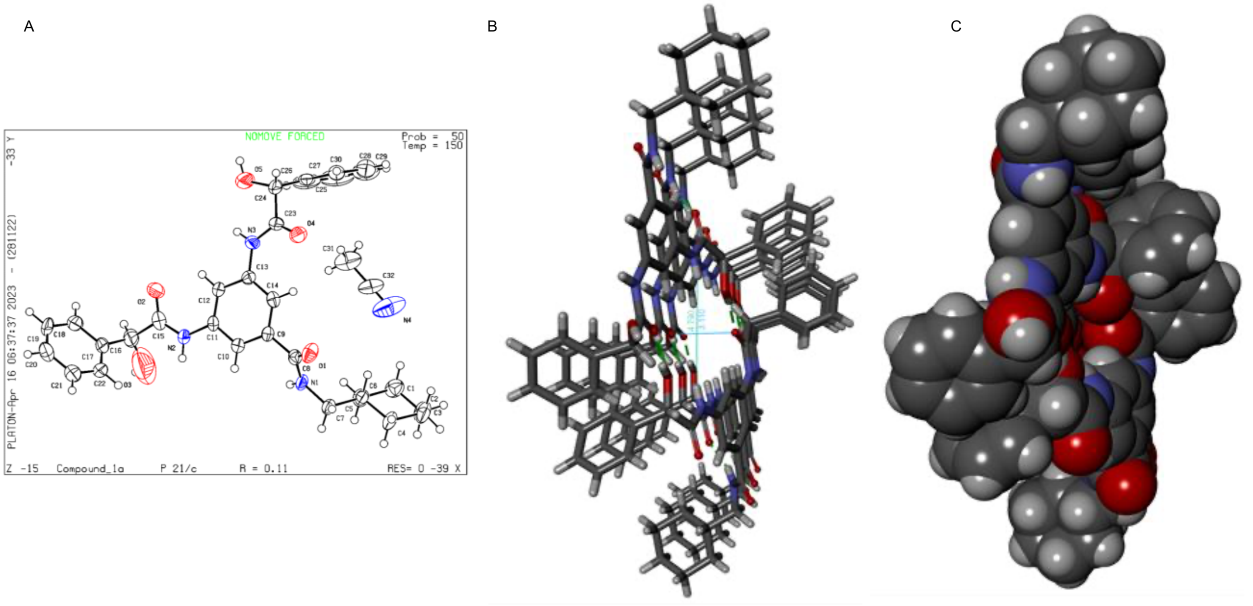

Figure 2.17 CPK (A) model of the crystal structure of compound **1a**, and self-assembled structure of compound **1a** in licorice (B) and VDW model (C).

Table 2.4 Details of the crystal structure data of compound **1a**.

Empirical formula	C32 H35 N4 O5
Formula weight	555.64
Temperature	150 K
Crystal system	Monoclinic
Space group	P 21/c
Unit cell dimensions	a = 16.068(2) Å α= 90°. b = 7.5694(11) Å β= 95.349(4)°. c = 23.663(4) Å γ = 90°
Volume	2865.4(7) Å^3
Z	4
Density (calculated)	1.288 Mg/m^3
Absorption coefficient	0.088 mm^{-1}
F(000)	1180
Theta range for data collection	2.546 to 24.675°.
CCDC No	2243918

2.4.6. Theoretical studies

Computational details:

All density functional theory and semi empirical quantum chemistry calculations for single molecules, trimers, and the layered arrangement of trimeric molecules were performed using the Gaussian16 package.[30]

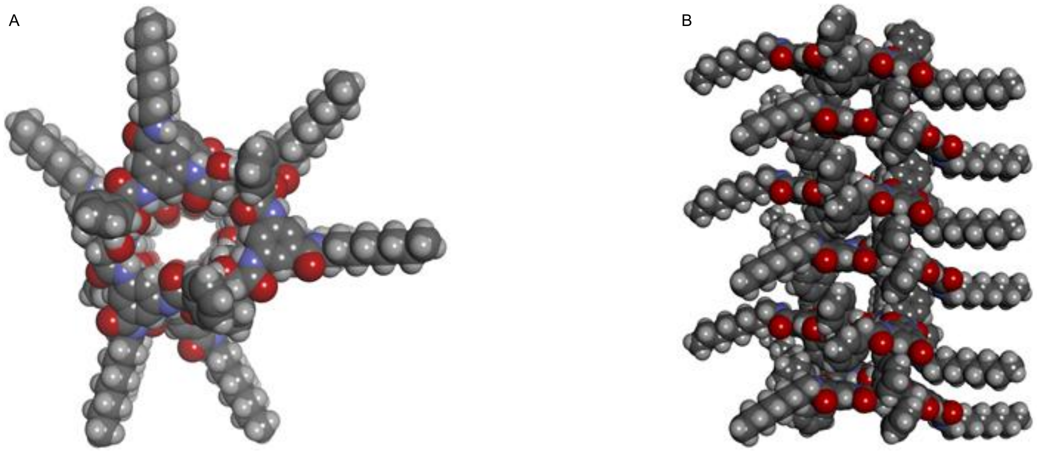

Figure 2.18 Top (A) and side (B) views of the optimized self-assembled trimeric rosette channel of compound **1b** using the Gaussview visualizer.

To create the lipid bilayer, we used the CHARMM-GUI online membrane builder placing a total of 180 1,2-dipalmitoyl-sn-phosphocholine (DPPC) molecules (90 molecules in each of the leaflets) along with 15722 water molecules having an overall box dimension of 100×100×80 Å^3.[31–33] The lipid-water system obtained from CHARMM-GUI website was separately ionized by addition of KCl and KH_2PO_4 in the form of ions, keeping the salt concentration 0.15 molar. Instead of $KClO_4$, we used potassium di-hydrogen phosphate salt in our whole simulations due to the limitation and unavailability of CHARMM General Force Field (CGenFF) parameters for ClO_4^-. The substitution of the perchlorate ions with di-hydrogen phosphate was done on the basis of their nearly same radii of gyration. The TIP3P model was used for water, CHARMM27 parameters were used for the lipid, and CGenFF parameters for the ion-pore and ions.[34,35] This system was then subjected to multistep minimization followed by equilibration in NAMD 2.12 package.[36] To this regard, we first kept the lipid molecules constrained and allowed the water molecules to minimize for 105 steps. Secondly, lipid head groups were kept constrained and lipid tails were allowed to equilibrate for 50 ns. Finally, the whole system including the lipid molecules were minimized for 106 steps by removing all the constrained forces and equilibrated for another 50 ns using the canonical ensemble (NVT) at 300 K. After that the production simulation was performed in an isothermal-isobaric ensemble (NPT) up to 500 ns at 300 K. Isothermal conditions in all of the simulations were maintained using the Langevin dynamics employing a damping coefficient of 5 ps^{-1} and we have used the Langevin piston method to maintain a constant pressure of 1 atm.[37,38] The Particle Mesh Ewald (PME) method having a 1 Å grid was used to calculate the electrostatic interactions using the periodicity of the systems and a 2 fs time step was used to integrate the classical equations of motions according to the Velocity Verlet algorithm.[39]

To introduce the constant pressure coupling, 100 fs piston period, 50 fs damping time constant and 300 K piston temperature was used. Covalent bonds involving hydrogen atoms were made rigid using the SHAKE algorithm. Non-bonded interactions were calculated employing a cut-off distance of 1.2 nm and the atomic coordinates were continuously stored after every 100 ps for visualization and trajectory analysis. All visualizations and scripting for trajectory analyses were done using VMD software.[40] In-house TCL scripts were used to remove some of the lipid molecules from the optimized lipid water system to create a nanopore at the centre of similar radius as that of the optimized ion channel. After creating the lipid-pore system, we again equilibrated the whole system using the same protocol as mentioned above and production simulation was performed for 300 ns, keeping the ion-pore harmonically constrained throughout the simulations using a mild force constant of 10 kcal/mol/Å^2.

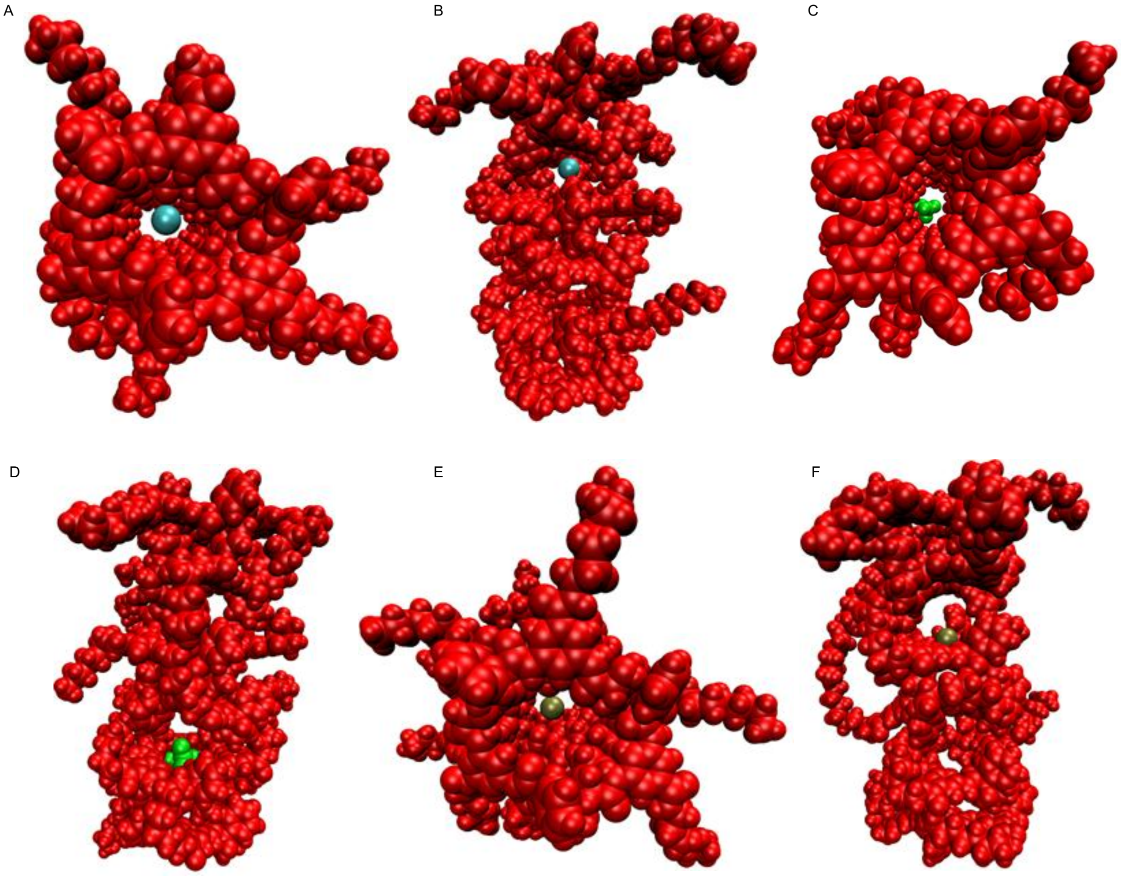

Figure 2.19 Snapshot of top and side views of the MD-simulated self-assembled trimeric rosette channel of compound **1b** with Cl^- (A and B), $H_2PO_4^-$ (C and D) and K^+ (E and F) ions receptively.

To evaluate the possibility of ion passage through the ion-channel, we have calculated the free energy profile for the transportation of the ions across the channel in terms of potential of mean force by applying the adaptive biasing force (ABF) procedure as implemented in the NAMD package.[41,42] The final structure obtained at the end of the production simulation was taken for the PMF calculations. We kept one ion first at the middle of the ion-pore and minimized the system followed by equilibration for 10 ns. After that we selected the distance between ion and bottom layer of the ion pore as the reaction coordinate which were split into several overlapping windows of width 1 Å. Each of these windows was further divided into small bins of 0.2 Å widths. A harmonic force of 100 kcal/mol/Å was applied to the upper and lower boundaries of the reaction coordinates and 20 ns production ABF simulations were performed for each window at 300 K. To reduce sampling issues and avoid memory effects, we performed each PMF calculations at least two times and the averages were reported. The central ion was then pulled along both the upper and lower side across the pore to scan the whole reaction coordinate. This procedure was followed for all the three ions namely K^+, $H_2PO_4^-$ and Cl^-. During pulling of the ions from the core of the pore, all the pore atoms were kept harmonically constrained as before.

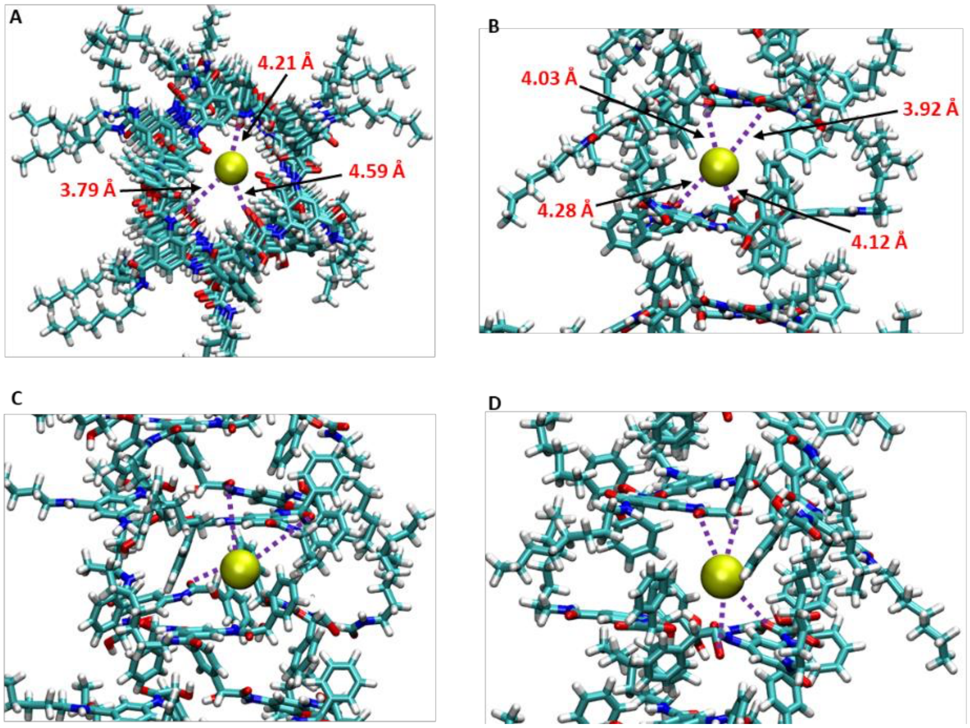

Figure 2.20 Snapshots of top view frames of MD simulated trimeric ion channel **1b** with K$^+$ ion (A); and snapshots of side view frames of MD simulated trimeric ion channel **1b** with K$^+$ ion at different time point (B, C, D).

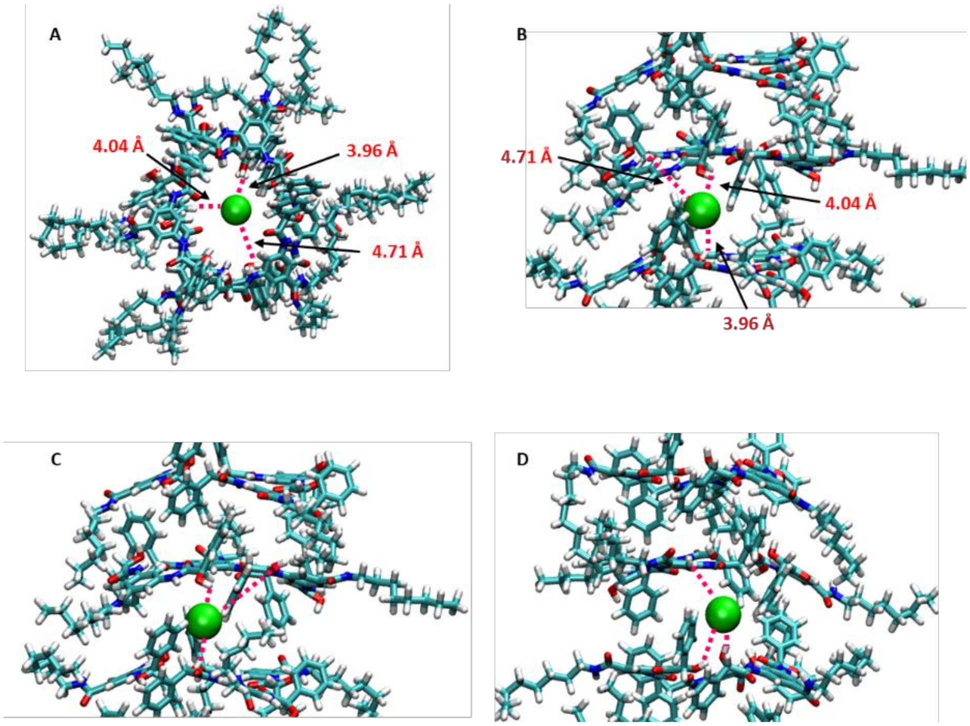

Figure 2.21 Snapshots of top view frames of MD simulated trimeric ion channel **1b** with Cl$^-$ ion (A); and snapshots of side view frames of MD simulated trimeric ion channel **1b** with Cl$^-$ ion at different time point (B, C, D).

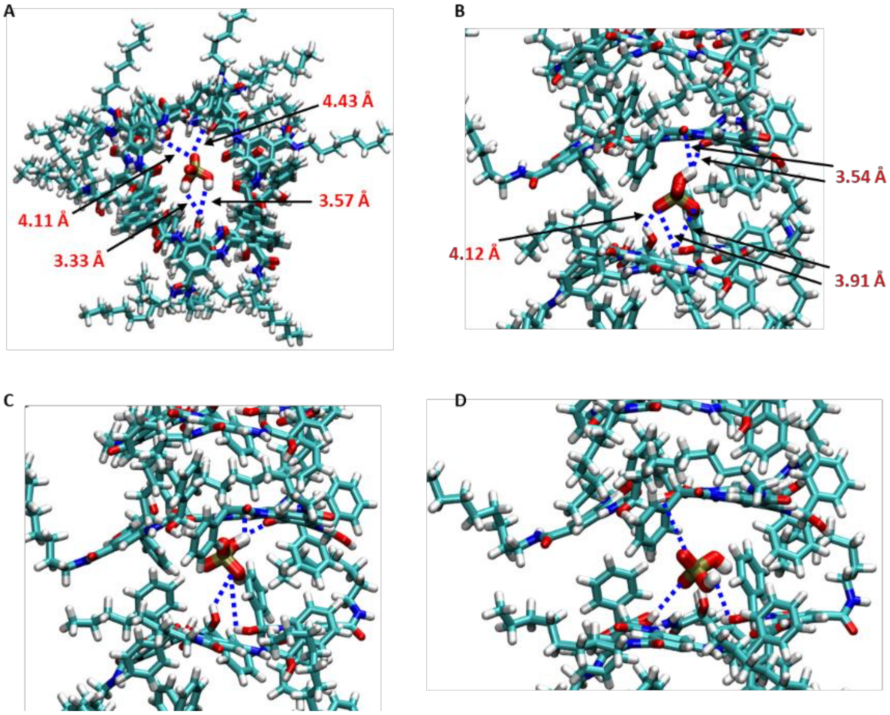

Figure 2.22 Snapshots of top view frames of MD simulated trimeric ion channel **1b** with $H_2PO_4^-$ ion (A); and snapshots of side view frames of MD simulated trimeric ion channel **1b** with $H_2PO_4^-$ ion at different time points (B, C, D).

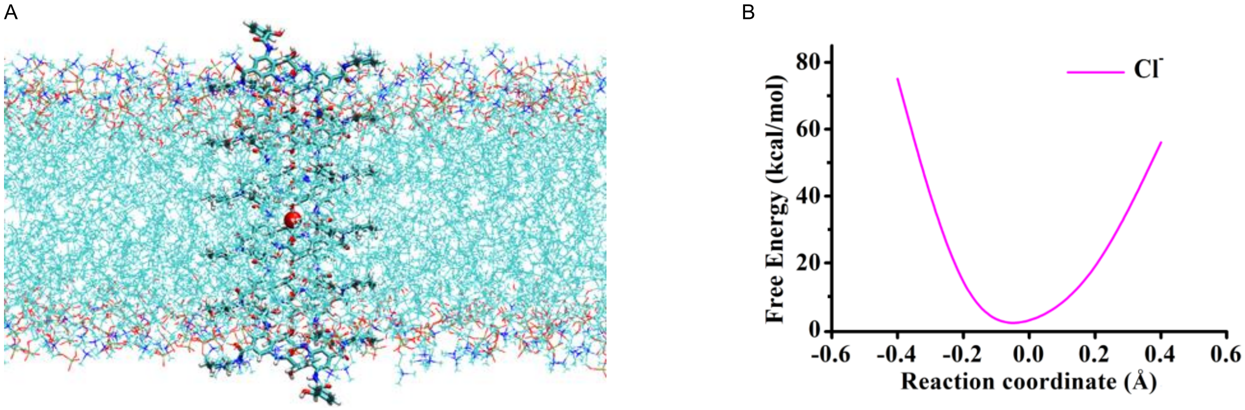

Figure 2.23 Equilibrated dimeric channel of **1a**-DPPC/water system (A); calculated free energy of Cl^- ion during the passage through the dimeric channel cavity (B).

[Note: All MD simulation studies in this chapter was carried out by Prof. Ayan Datta and associates from the Indian Association for the Cultivation of Science.]

2.5. NMR Data

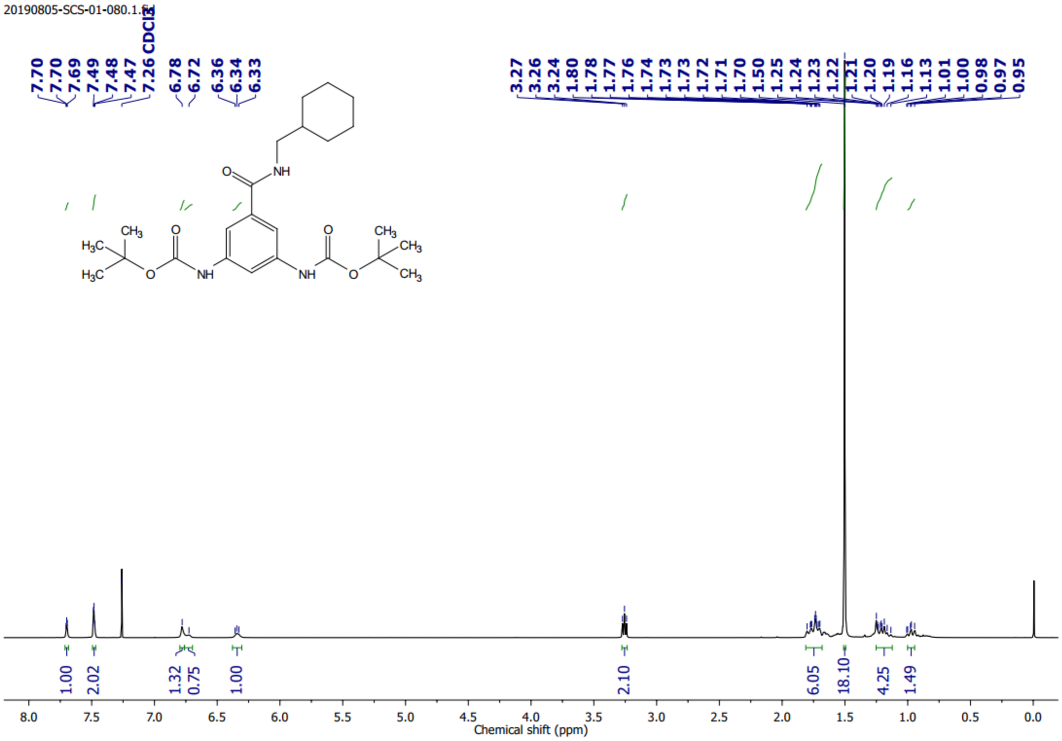

Figure 2.24 ^{1}H NMR (400 MHz) spectrum of compound **6a** in $CDCl_3$ solvent.

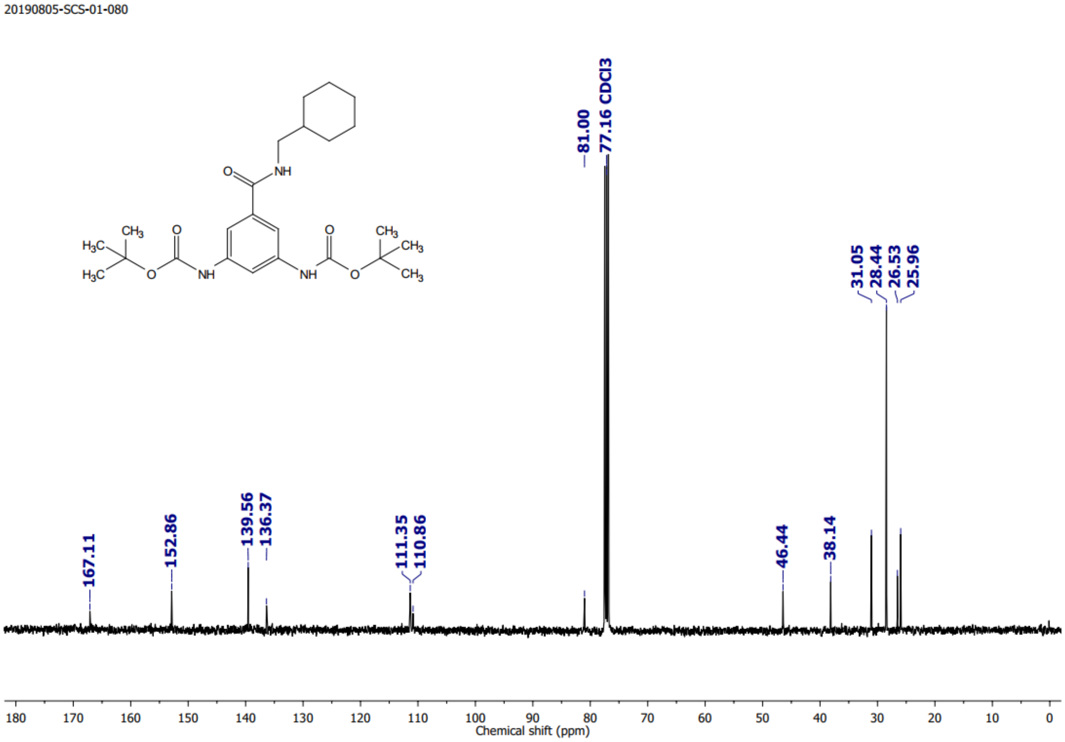

Figure 2.25 ^{13}C NMR (101 MHz) spectrum of compound **6a** in $CDCl_3$ solvent.

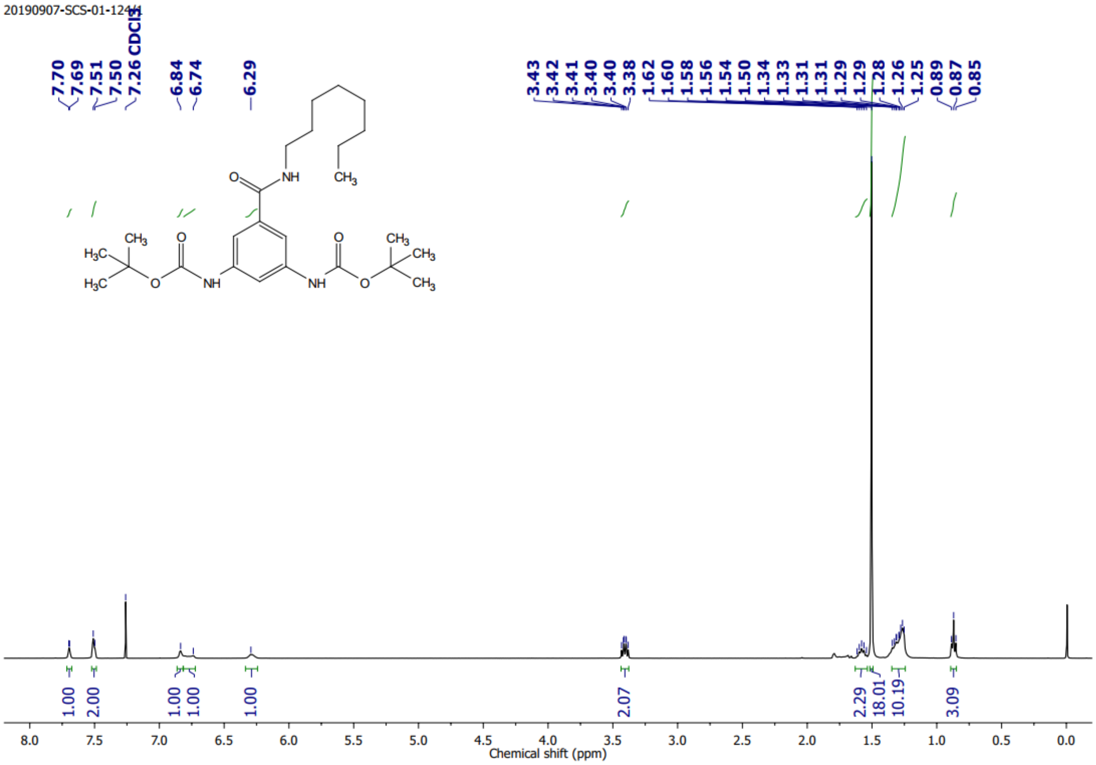

Figure 2.26 ^{1}H NMR (400 MHz) spectrum of compound **6b** in $CDCl_3$ solvent.

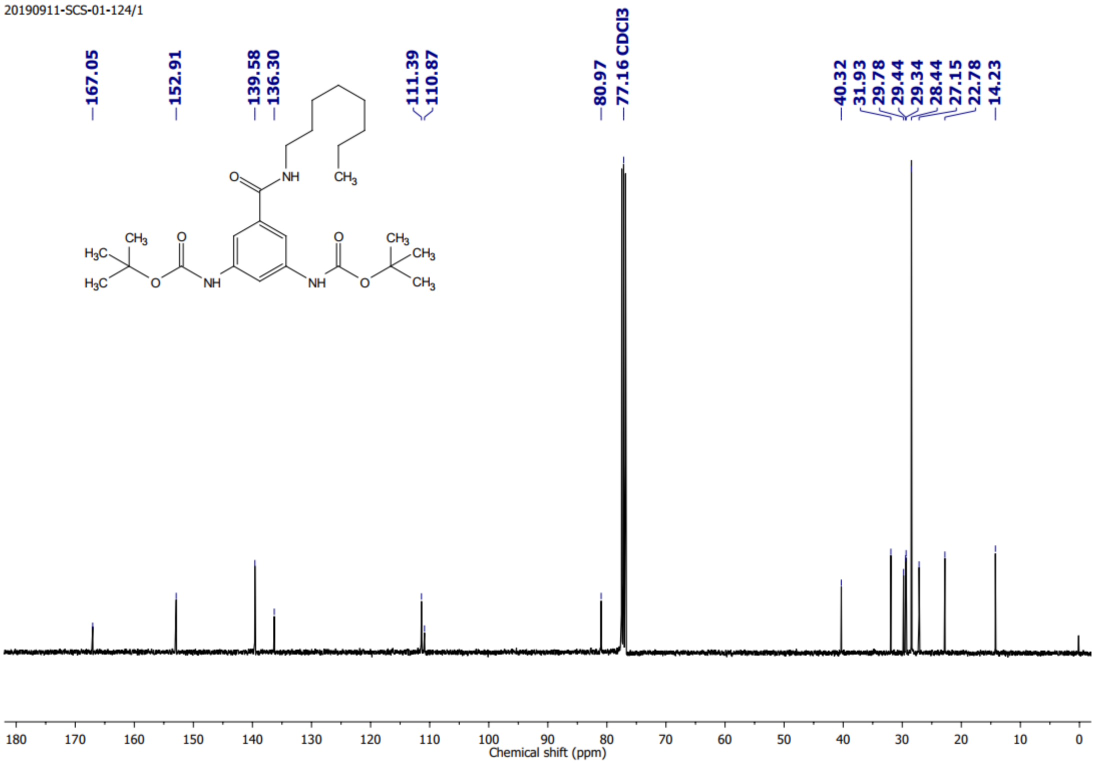

Figure 2.27 ^{13}C NMR (101 MHz) spectrum of compound **6b** in $CDCl_3$ solvent.

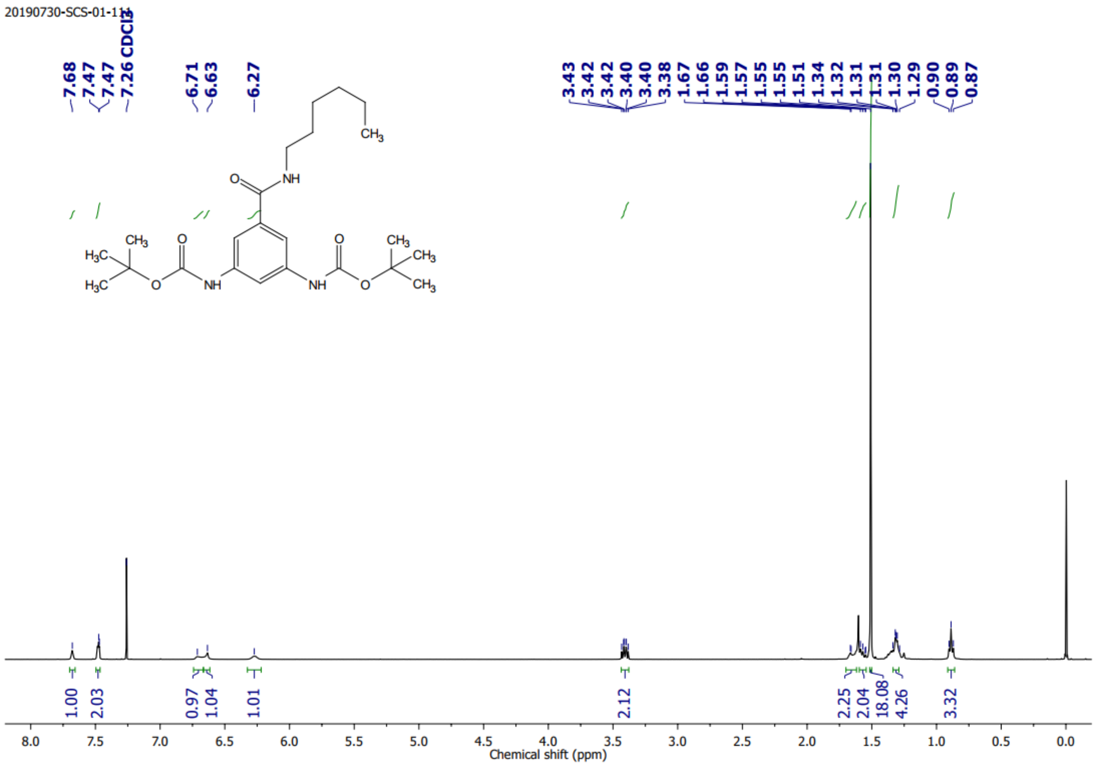

Figure 2.28 ^{1}H NMR (400 MHz) spectrum of compound **6c** in $CDCl_3$ solvent.

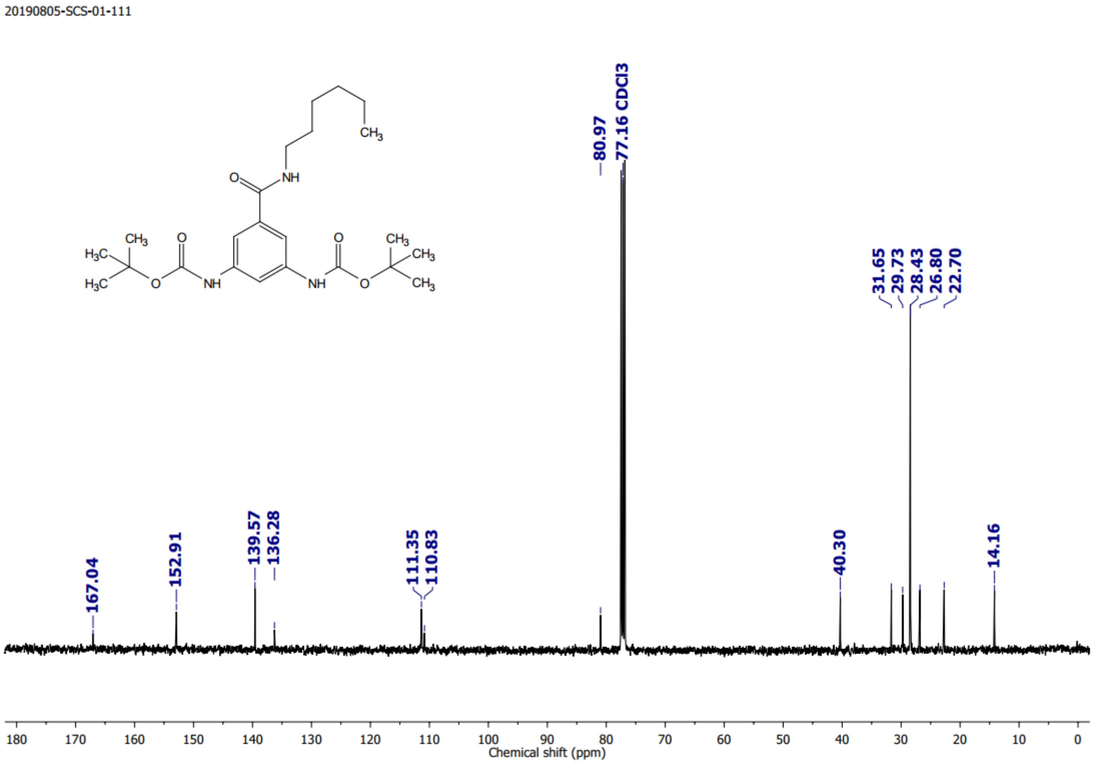

Figure 2.29 ^{13}C NMR (101 MHz) spectrum of compound **6c** in $CDCl_3$ solvent.

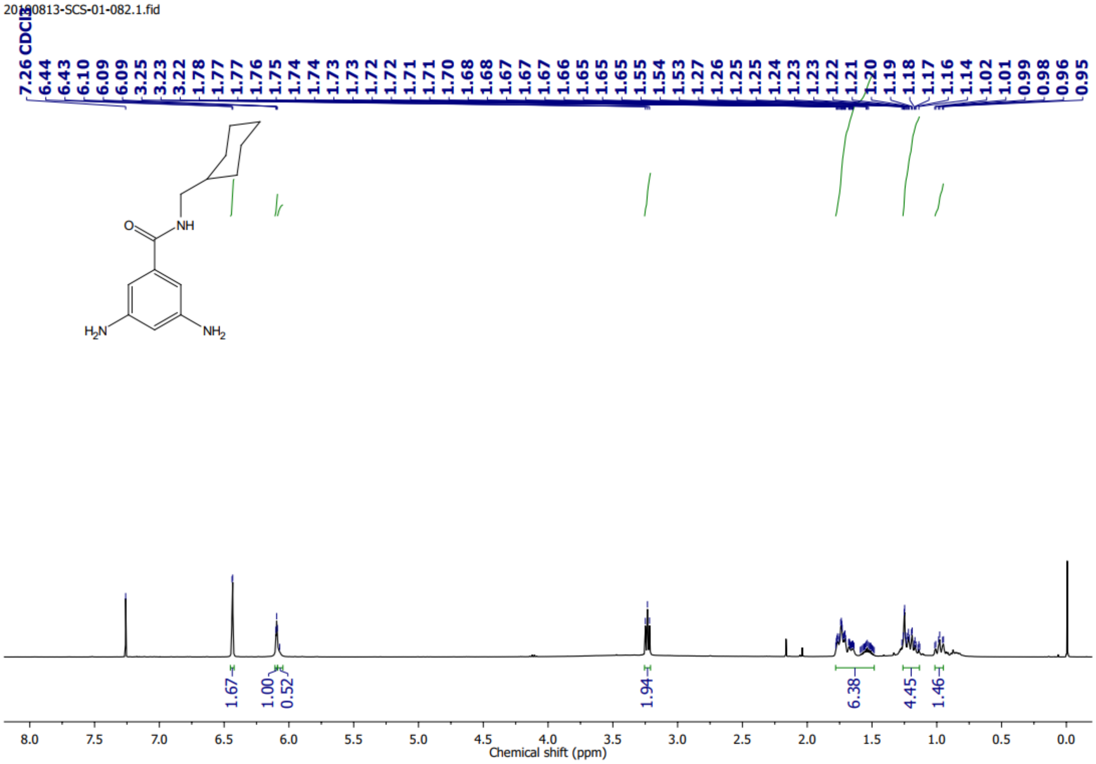

Figure 2.30 ^{1}H NMR (400 MHz) spectrum of compound **2a** in $CDCl_3$ solvent.

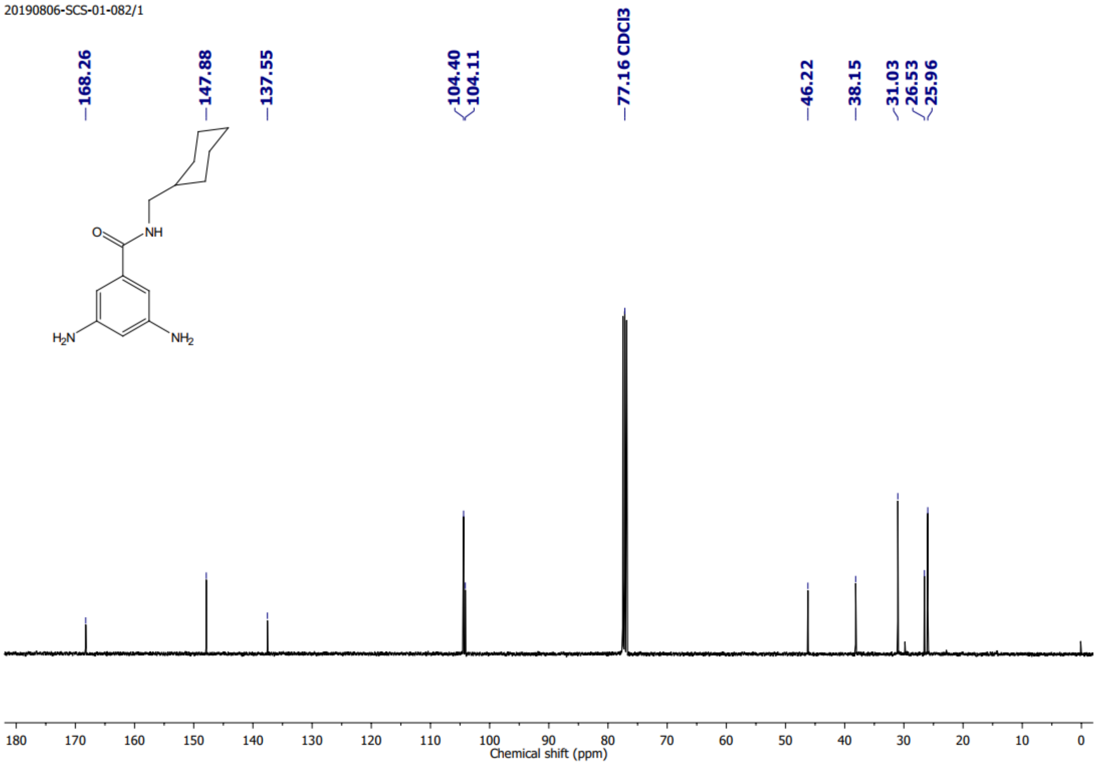

Figure 2.31 ^{13}C NMR (101 MHz) spectrum of compound **2a** in $CDCl_3$ solvent.

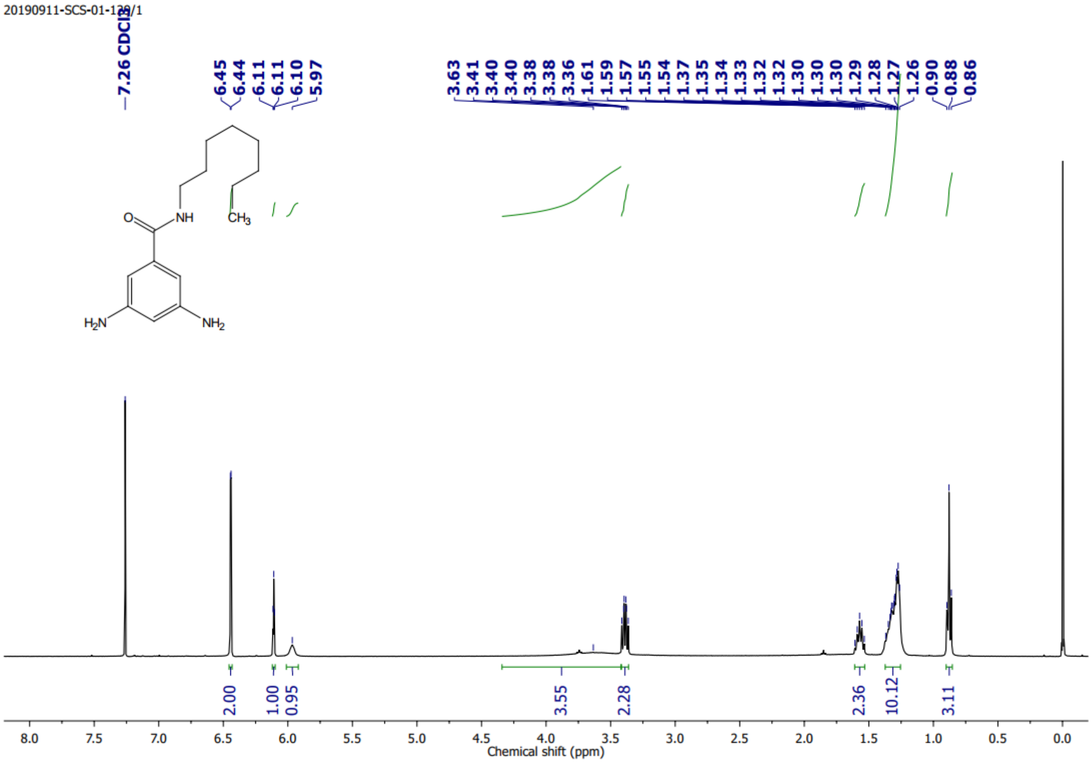

Figure 2.32 ^{1}H NMR (400 MHz) spectrum of compound **2b** in $CDCl_3$ solvent.

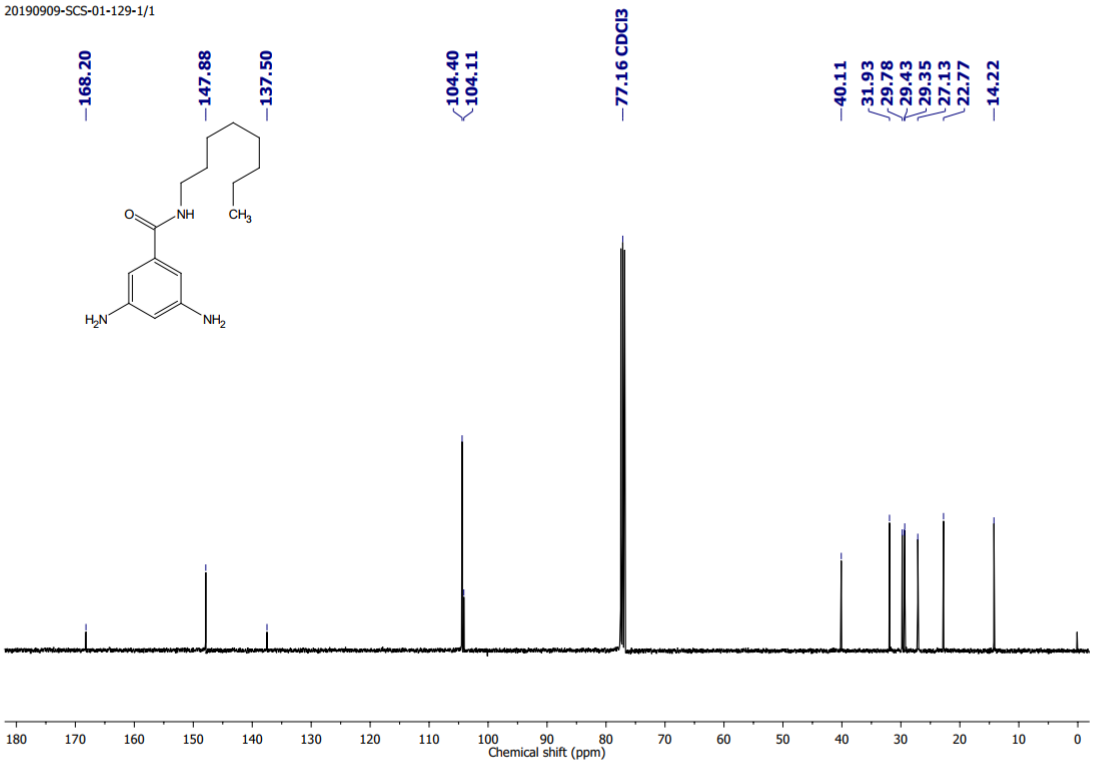

Figure 2.33 ^{13}C NMR (101 MHz) spectrum of compound **2b** in $CDCl_3$ solvent.

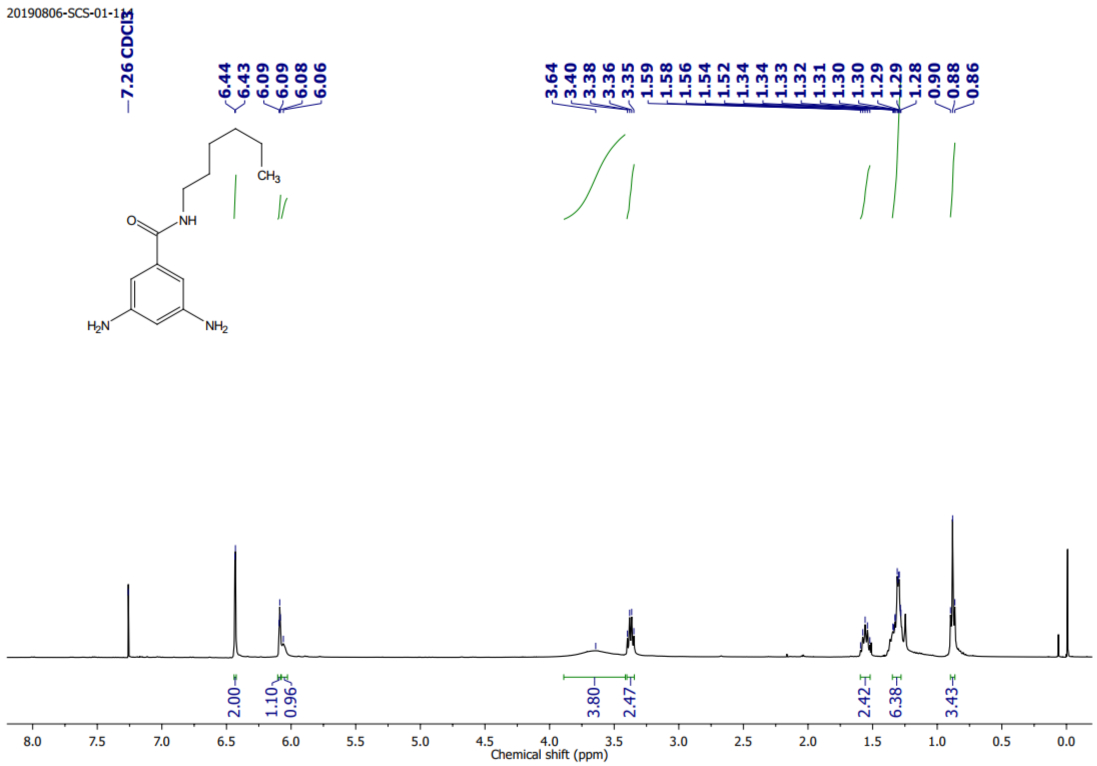

Figure 2.34 ^{1}H NMR (400 MHz) spectrum of compound **2c** in CDCl$_3$ solvent.

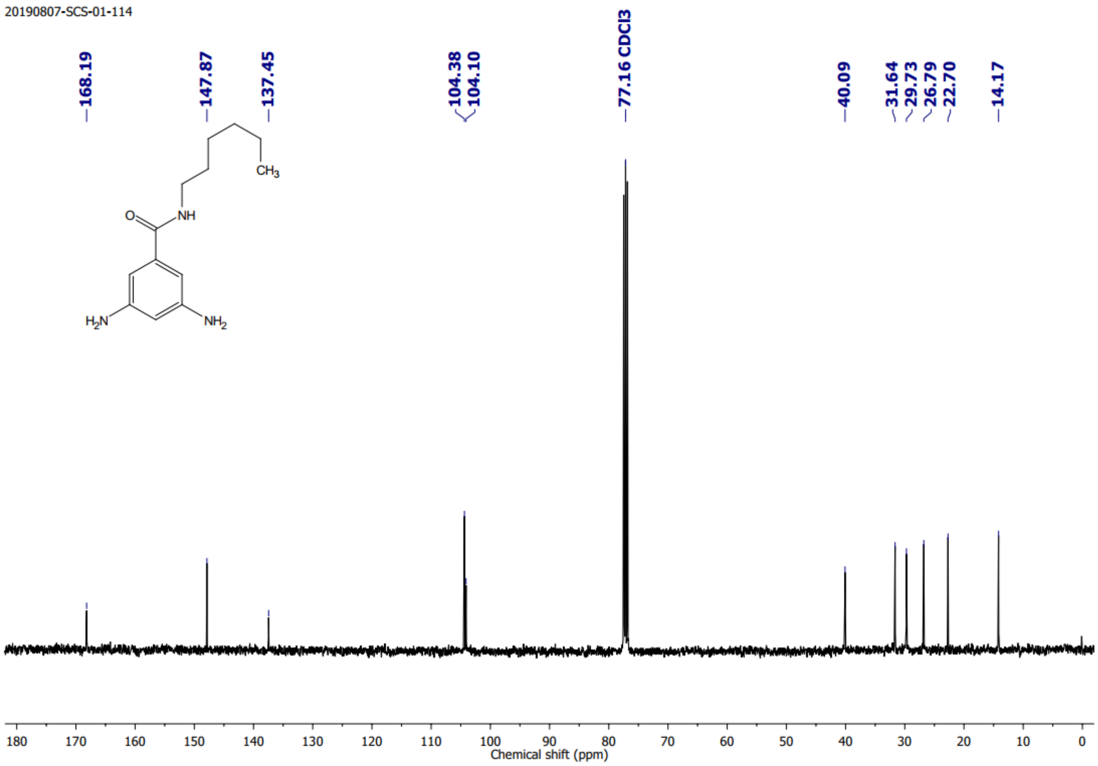

Figure 2.35 ^{13}C NMR (101 MHz) spectrum of compound **2c** in CDCl$_3$ solvent.

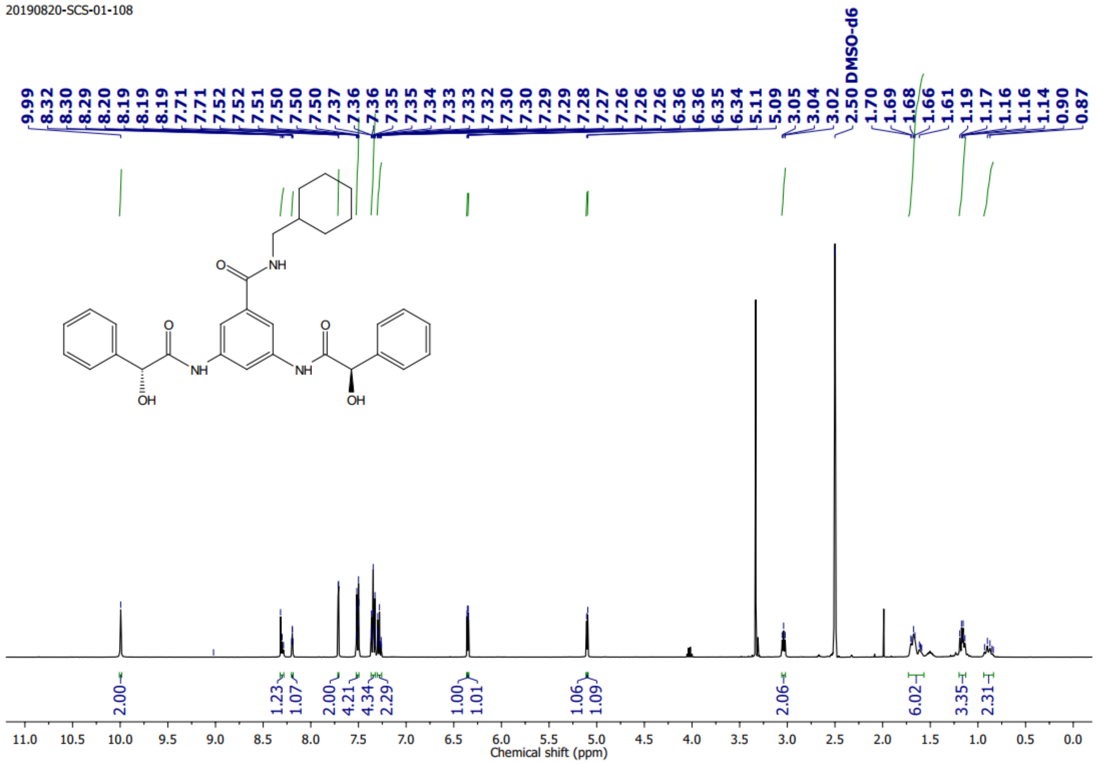

Figure 2.36 ^{1}H NMR (400 MHz) spectrum of compound **1a** in DMSO-d_6 solvent.

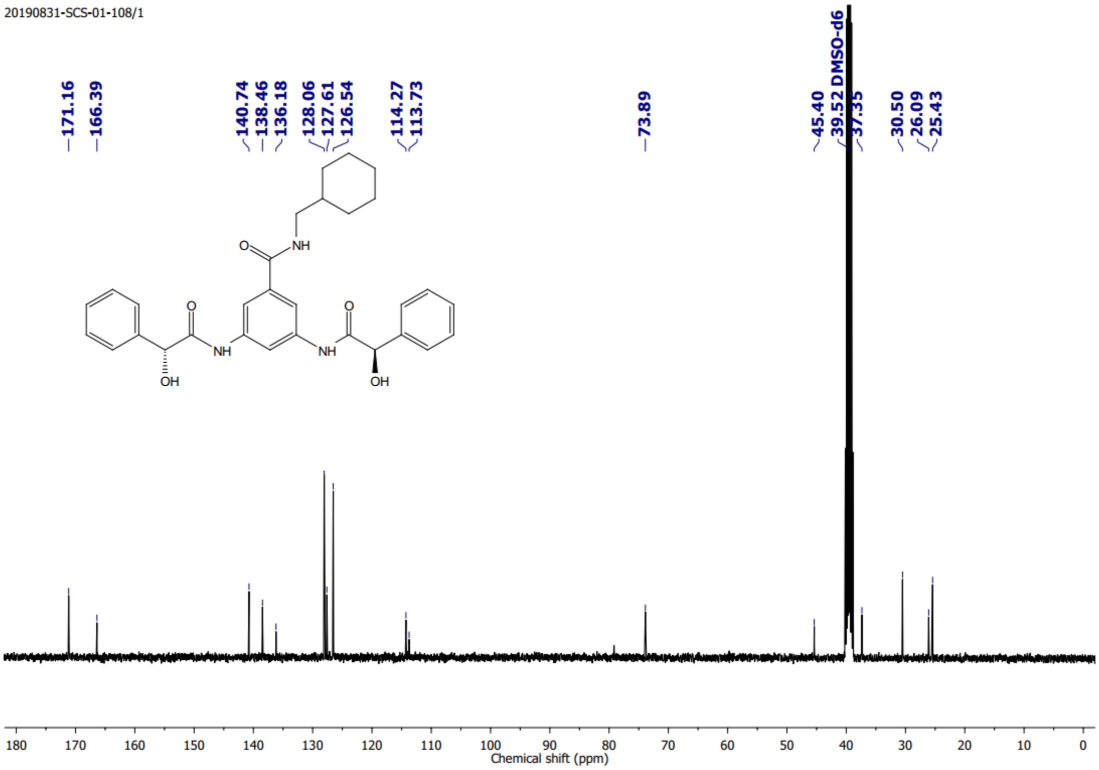

Figure 2.37 ^{13}C NMR (101 MHz) spectrum of compound **1a** in DMSO-d_6 solvent.

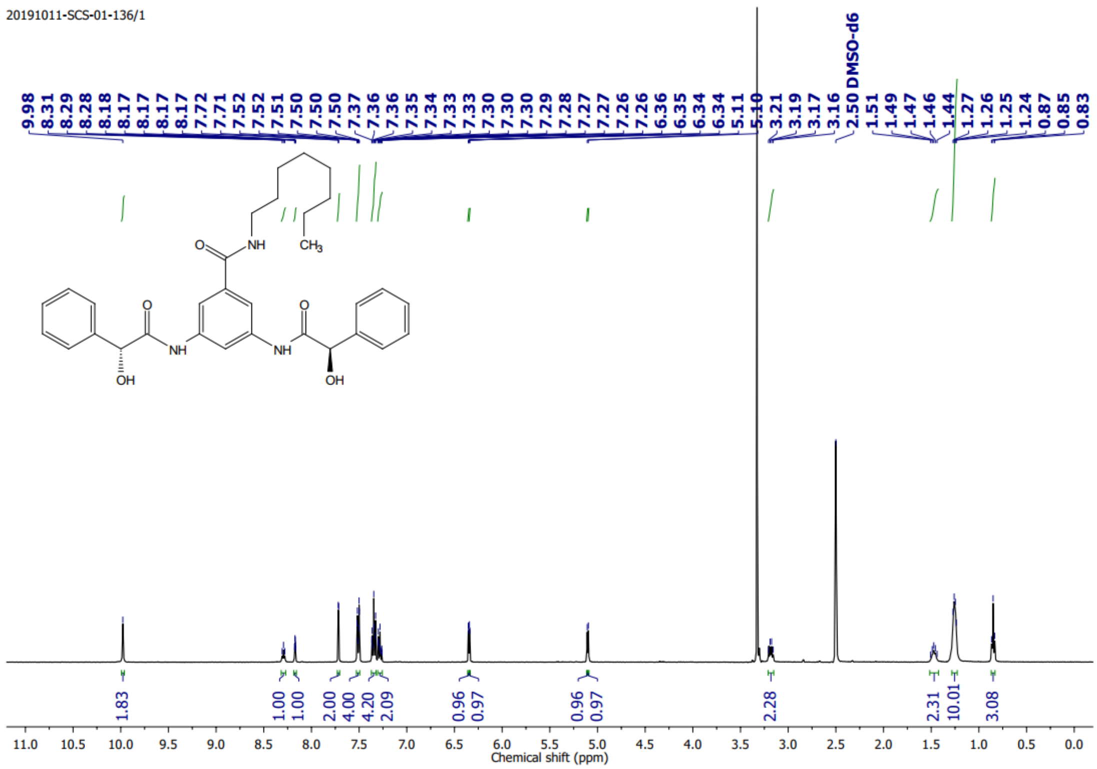

Figure 2.38 ^{1}H NMR (400 MHz) spectrum of compound **1b** in DMSO-d_6 solvent.

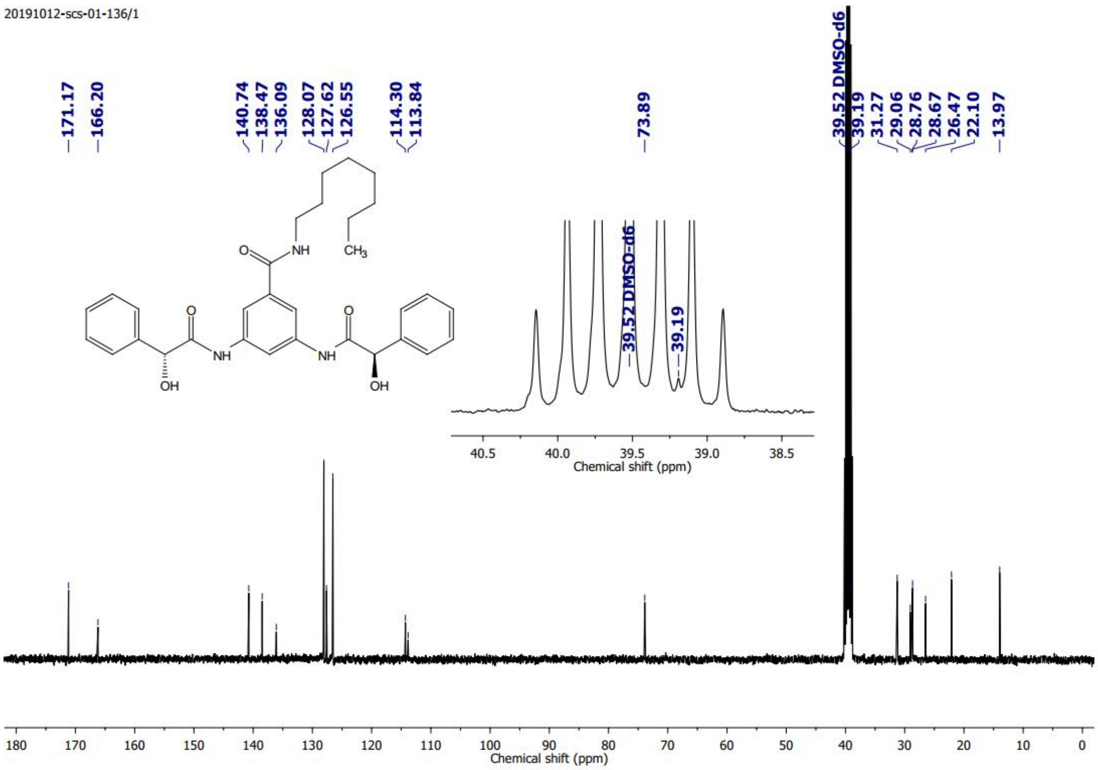

Figure 2.39 ^{13}C NMR (101 MHz) spectrum of compound **1b** in DMSO-d_6 solvent.

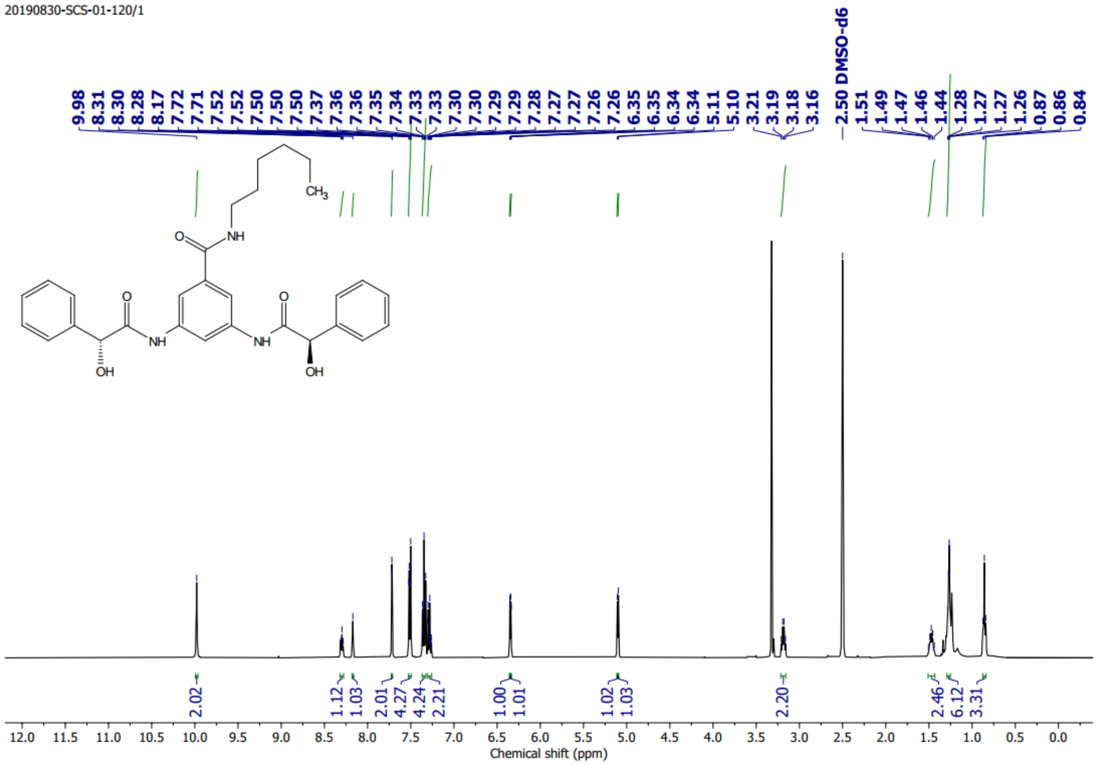

Figure 2.40 ^{1}H NMR (400 MHz) spectrum of compound **1c** in DMSO-d_6 solvent.

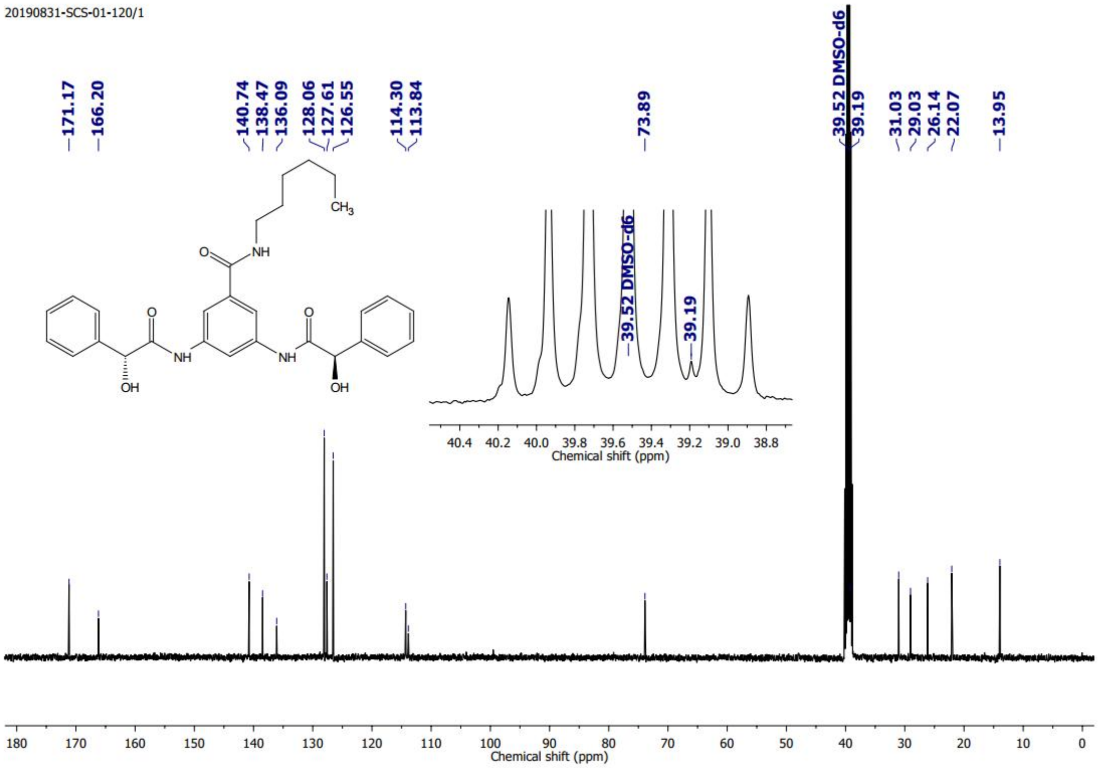

Figure 2.41 ^{13}C NMR (101 MHz) spectrum of compound **1c** in DMSO-d_6 solvent.

2.6. References

(1) Chow, H.-F.; Zhang, J. *Chem. Eur. J.* **2005**, *11*, 5817–5831.

(2) Thérien-Aubin, H.; Chen, L.; Ober, C. K. *Polymer* **2011**, *52*, 5419–5425.

(3) Ren, C.; Ding, X.; Roy, A.; Shen, J.; Zhou, S.; Chen, F.; Li, S. F. Y.; Ren, H.; Yang, Y. Y.; Zeng, H. A *Chem. Sci.* **2018**, *9*, 4044–4051.

(4) Malla, J. A.; Roy, A.; Talukdar, P. *Org. Lett.* **2018**, *20*, 5991–5994.

(5) Marcus, Y. *J. Chem. Soc., Faraday Trans.* **1991**, *87*, 2995–2999.

(6) Wright, E. M.; Diamond, J. M. *Physiol. Rev.* **1977**, *57*, 109–156.

(7) Eisenman, G.; Horn, R. *J. Membr. Biol.* **1983**, *76*, 197–225.

(8) Saha, T.; Hossain, M. S.; Saha, D.; Lahiri, M.; Talukdar, P. *J. Am. Chem. Soc.* **2016**, *138*, 7558–7567.

(9) Busschaert, N.; Wenzel, M.; Light, M. E.; Iglesias-Hernández, P.; Pérez-Tomás, R.; Gale, P. A. *J. Am. Chem. Soc.* **2011**, *133*, 14136–14148.

(10) Biwersi, J.; Tulk, B.; Verkman, A. S. *Anal. Biochem.* **1994**, *219*, 139–143.

(11) Benke, B. P.; Aich, P.; Kim, Y.; Kim, K. L.; Rohman, M. R.; Hong, S.; Hwang, I. -C.; Lee, E. H.; Roh, J. H.; Kim, K. *J. Am. Chem. Soc.* **2017**, *139*, 7432–7435.

(12) Yamnitz, C. R.; Negin, S.; Carasel, I. A.; Winter, R. K.; Gokel, G. W. *Chem. Commun.* **2010**, *46*, 2838–2840.

(13) Talukdar, P.; Sakai, N.; Sordé, N.; Gerard, D.; Cardona, V. M. F.; Matile, S. *Bioorganic Med. Chem.* **2004**, *12*, 1325–1336.

(14) Sordé, N.; Matile, S. *J. Supramol. Chem.* **2002**, *2*, 191–199.

(15) Busschaert, N.; Kirby, I. L.; Young, S.; Coles, S. J.; Horton, P. N.; Light, M. E.; Gale, P. A. *Angew. Chem., Int. Ed.* **2012**, *51*, 4426–4430.

(16) Johnson, T. G.; Sadeghi-Kelishadi, A.; Langton, M. J. *J. Am. Chem. Soc.* **2022**, *144*, 10455–10461.

(17) Saha, T.; Gautam, A.; Mukherjee, A.; Lahiri, M.; Talukdar, P. *J. Am. Chem. Soc.* **2016**, *138*, 16443–16451.

(18) Mondal, D.; Ahmad, M.; Dey, B.; Mondal, A.; Talukdar, P. *Nat. Commun.* **2022**, *13*, 6507.

(19) Huang, W. -L.; Wang, X. -D.; Ao, Y. -F.; Wang, Q. -Q.; Wang, D. -X. *J. Am. Chem. Soc.* **2020**, *142*, 13273–13277.

(20) Chai, J. -D; Head-Gordon, M. *Phys. Chem. Chem. Phys.* **2008**, *10*, 6615–6620.

(21) Herre, W. J.; Ditcrfield, R.; Pople, J. A. *J. Chem. Phys.* **1972**, *56*, 2257–2261.

(22) Francl, M. M.; Pietro, W. J.; Hehre, W. J. *J. Chem. Phys.* **1982**, *77*, 3654–3665.

(23) Stewart, J. J. P. *J. Mol. Model.* **2007**, *13*, 1173–1213.

(24) Sisson, A. L.; Shah, M. R.; Bhosale, S.; Matile, S. *Chem. Soc. Rev.* **2006**, *35*, 1269–1286.

(25) Talukdar, P.; Bollot, G.; Mareda, J.; Sakai, N.; Matile, S. *J. Am. Chem. Soc.* **2005**, *127*, 6528–6529.

(26) Saha, T.; Dasari, S.; Tewari, D.; Prathap, A.; Sureshan, K. M.; Bera, A. K.; Mukherjee, A.; Talukdar, P. *J. Am. Chem. Soc.* **2014**, *136*, 14128–14135.

(27) Malla, J. A.; Umesh, R. M.; Vijay, A.; Mukherjee, A.; Lahiri, M.; Talukdar, P. *Chem. Sci.* **2020**, *11*, 2420–2428.

(28) Shinde, S. V.; Talukdar, P. *Angew. Chem., Int. Ed.* **2017**, *56*, 4238–4242.

(29) Sharma, R.; Vijay, A.; Chattopadhayay, S.; Mukherjee, A.; Talukdar, P. *Chem. Commun.* **2023**, *59*, 3602–3605.

(30) Frisch, M. J.; Trucks, G. W.; Schlegel, H. B.; Scuseria, G. E.; Robb, M. A.; Cheeseman, J. R.; Scalmani, G.; Barone, V.; Petersson, G. A.; Nakatsuji, H.; Li, X.; Caricato, M.; Marenich, A. V.; Bloino, J.; Janesko, B. G.; Gomperts, R.; Mennucci, B.; Hratchian, H. P.; Ortiz, J. V.; Izmaylov, A. F.; Sonnenberg, J. L.; Williams-Young, D.; Ding, F.; Lipparini, F.; Egidi, F.; Goings, J.; Peng, B.; Petrone, A.; Henderson, T.; Ranasinghe, D.; Zakrzewski, V. G.; Gao, J.; Rega, N.; Zheng, G.; Liang, W.; Hada, M.; Ehara, M.; Toyota, K.; Fukuda, R.; Hasegawa, J.; Ishida, M.; Nakajima, T.; Honda, Y.; Kitao, O.; Nakai, H.; Vreven, T.; Throssell, K.; Montgomery, J. A., Jr.; Peralta, J. E.; Ogliaro, F.; Bearpark, M. J.; Heyd, J. J.; Brothers, E. N.; Kudin, K. N.; Staroverov, V. N.; Keith, T. A.; Kobayashi, R.; Normand, J.; Raghavachari, K.; Rendell, A. P.; Burant, J. C.; Iyengar, S. S.; Tomasi, J.; Cossi, M.; Millam, J. M.; Klene, M.; Adamo, C.; Cammi, R.; Ochterski, J. W.; Martin, R. L.; Morokuma, K.; Farkas, O.; Foresman, J. B.; Fox, D. J. *Gaussian 16, Revision C.01*, Gaussian, Inc., Wallingford CT, **2016**.

(31) Lee, J.; Cheng, X.; Swails, J. M.; Yeom, M. S.; Eastman, P. K.; Lemkul, J. A.; Wei, S.; Buckner, J.; Jeong, J. C.; Qi, Y.; Jo, S.; Pande, V. S.; Case, D. A.; Brooks, C. L.; MacKerell, A. D.; Klauda, J. B.; Im, W. *J. Chem. Theory Comput.* **2016**, *12*, 405–413.

(32) Wu, E. L.; Cheng, X.; Jo, S.; Rui, H.; Song, K. C.; Dávila-Contreras, E. M.; Qi, Y.; Lee, J.; Monje-Galvan, V.; Venable, R. M.; Klauda, J. B.; Im, W. *J. Comput. Chem.* **2014**, *35*, 1997–2004.

(33) Jo, S.; Kim, T.; Iyer, V. G.; Im, W. *J. Comput. Chem.* **2008**, *29*, 1859–1865.

(34) Vanommeslaeghe, K.; Hatcher, E.; Acharya, C.; Kundu, S.; Zhong, S.; Shim, J.; Darian, E.; Guvench, O.; Lopes, P.; Vorobyov, I.; MacKerell Jr., A. D. *J. Comput. Chem.* **2010**, *31*, 671–690.

(35) Jorgensen, W. L.; Chandrasekhar, J.; Madura, J. D.; Impey, R. W.; Klein, M. L. *J. Chem. Phys.* **1983**, *79*, 926–935.

(36) Kalé, L.; Skeel, R.; Bhandarkar, M.; Brunner, R.; Gursoy, A.; Krawetz, N.; Phillips, J.; Shinozaki, A.; Varadarajan, K.; Schulten, K. *J. Comput. Phys.* **1999**, *151*, 283–312.

(37) Feller, S. E.; Zhang, Y.; Pastor, R. W.; Brooks, B. R. *J. Chem. Phys.* **1995**, *103*, 4613–4621.

(38) Davidchack, R. L.; Handel, R.; Tretyakov, M. V. *J. Chem. Phys.* **2009**, *130*, 234101–234114.

(39) Andersen, H. C. *J. Comput. Phys.* **1983**, *52*, 24–34.

(40) Humphrey, W.; Dalke, A.; Schulten, K. *J. Mol. Graph.* **1996**, *14*, 33–38.

(41) Darve, E.; Pohorille, A. *J. Chem. Phys.* **2001**, *115*, 9169–9183.

(42) Darve, E.; Rodríguez-Gómez, D.; Pohorille, A. *J. Chem. Phys.* **2008**, *128*, 144120–144133.

Chapter 3

Heteroditopic “Pinakindole” [2]Catenanes as Molecular Wobbler Ion Channel for Transmembrane Transport of Ion-Pairs

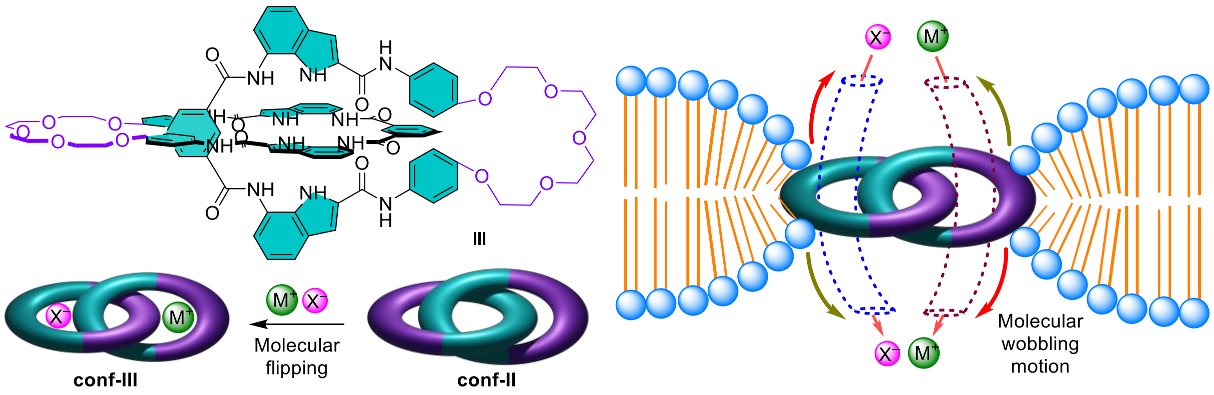

3.1. Introduction

Biomolecular machines represent extraordinarily intricate assemblies within cellular environments, executing highly regulated rotary, sliding, or walking motions that are orchestrated by noncovalent interactions. These varied motions are typically comprised of multiple substeps and entail several sequentially organized, well-defined conformational alterations, which are generally accomplished in a cooperative or coupled manner among their subunits. For example, the motion of the β-subunit in F1-ATPase helps to transform between an open to a closed state upon the binding of ATP, thereby generating the driving force necessary for the rotation of the γ-shaft.[1] Furthermore, a minimum of three distinct conformational states of myosin are present as a different phase within the actomyosin cycle.[2] The conformational dynamics of these complex assemblies, however, continue to pose significant challenges for comprehensive structural and functional understanding. In ***Chapter 2***, we successfully introduced mandelic acid as a new core motif for the engineering of a self-assembled barrel rosette ion channel which shows the prominent selectivity towards K^+ and ClO_4^- ions. The exploration of different cores for the construction of cation-anion symporting channels has consistently spurred our intellectual pursuit to devise distinctive mechanically interlocked molecules (MIMs) with the potential for the concurrent translocation of both cations and anions.

The investigation into these innovative concepts regarding the generation of an alternative synthetic scaffold propels us to enhance the structural organization of mechanically interlocked molecules (MIMs). While it is established that MIMs possess the capability to function as receptors or sensors for ion binding or catalysis, their application within the membrane context remains largely unexplored.[3,4] In order to elucidate the application of molecular machines within the membrane, in 2015, Andrea Secchi and colleagues conducted a study examining the influence of calix[6]arene-based pseudorotaxanes and rotaxanes on the transmembrane transport of ions through the lipid bilayer of liposomes.[5] Following this, Bao and collaborators,[6–8] Qu and their associates,[9] as well as López and their team,[10] also synthesized molecular shuttles designed for ion transportation across bilayer membranes. Additionally, Leigh and colleagues introduced a molecular Star of David pentafoil knot for the development of an ion channel within the bilayer membrane.[11] Recently, Beer and Langton collaboratively devised a methodology employing halogen bonding driven [2]catenane-based receptors as a chloride ion transport system.[12] It is noteworthy that the majority of the research surrounding molecular machine-based ion channels pre-dominantly centers on rotaxane-centric moieties. Although the Star of David serves as a paramount illustration of a knot-based synthetic ion channel system, within the domain of catenane-based synthetic ion transporters, the inaugural example presented by Beer and Langton functions primarily in a carrier mode for ion transport. To the best of our knowledge, there has been no report of a synthetic catenane-based cation-anion symporting ion channel system in the literature to date. Furthermore, the lack of catenane-based cation-anion symporting channels compels us to contemplate the integration of both architectural complexities into a singular construct, thereby yielding the inaugural example of Pinakindole catenane as a heteroditopic [2]catenane-based cation-anion channel system.

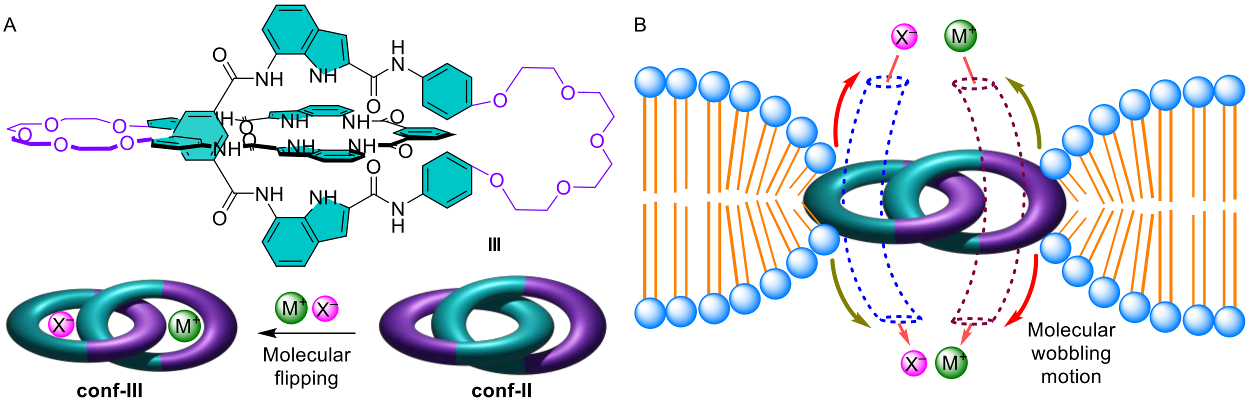

Figure 3.1 Channel structure and molecular flipping in the presence of metal-halide salt (A) and proposed model of wobbler ion channel formation by **Pinakindole catenane 1** within the bilayer membrane (B).

To fill the gap of the synthetic example of catenane-based cation-anion transporters, which can transport the ions via channel mechanism, we are continuing our search for a suitable scaffold for designing the synthetic mimic of the cation-anion transporters. Recently, our group introduced a bisindole moiety as a double helical structure in which intramolecular H-bonding stabilized the double helical structure.[13] We witnessed that it has selective chloride ion transport capability binding through the indolic core moiety. Hence, we have decided to utilize the bisindole motif as an anion binding core of our interlocked structure. To address the cation binding core in the interlocked structure, we utilized the crown ether based linker. Hence, hybridizing both the indolic core with the crown ether based linker provides both cation and anion binding sites and is expected to behave as a cation-anion channel (Figure 3.1A). We hypothesize that our designed smart supramolecular architecture, named **Pinakindole catenane 1**, has the potential to reorient them to bind both cation and anion in the respective binding motif. A wobbling motion of the molecule in the lipid bilayer membrane renders it to form a wobbler ion channel in the bilayer membrane by providing a separate ion translocation pathway for both cation and anion (Figure 3.1B).

3.2. Results and discussions

3.2.1. Synthesis

Initially compound **3** was synthesized by using the reported literature protocol.[13] Compound **3** was coupled with 4-((tert-butyldimethylsilyl)oxy)aniline in the presence of 1-(3-dimethylaminopropyl)-3-ethylcarbodiimide hydrochloride (EDC·HCl) and 1-hydroxybenzotriazole (HOBt) as a coupling agent in the presence of 4-(dimethylamino)pyridine (DMAP) in dry *N*,*N*-dimethylformamide (DMF) solvent at room temperature to obtained compound **4** with significant yield. Further nitro group of compound **4** was reduced to the amine by using H_2/Pd-C in MeOH:THF (3:1) solvent at room temperature to obtained compound **5**. Compounds **5** was further coupled with isophthaloyl dichloride by using *N*,*N*-diisopropylethylamine (DIPEA) base in acetonitrile (CH_3CN) solvent to get compound **6**. It was reacted with tetrabutylammonium fluoride (TBAF) to deprotect the TBDMS groups to obtained compound **7**. To synthesize the **Pinakindole catenane 1**, compound **7** was reacted with the 1-iodo-2-(2-(2-(2-iodoethoxy)ethoxy)ethoxy)ethane in the presence of Cs_2CO_3 as a base under 60 °C for 24 h to get the interlocked **Pinakindole catenane 1·Cs$^+$** with 31% experimental yield. To remove the Cs^+ ion from the cavity of **Pinakindole catenane 1·Cs$^+$**, it was washed thoroughly with the H_2O, which led to the formation of **Pinakindole catenane 1** with appreciable yield (Scheme 3.1).

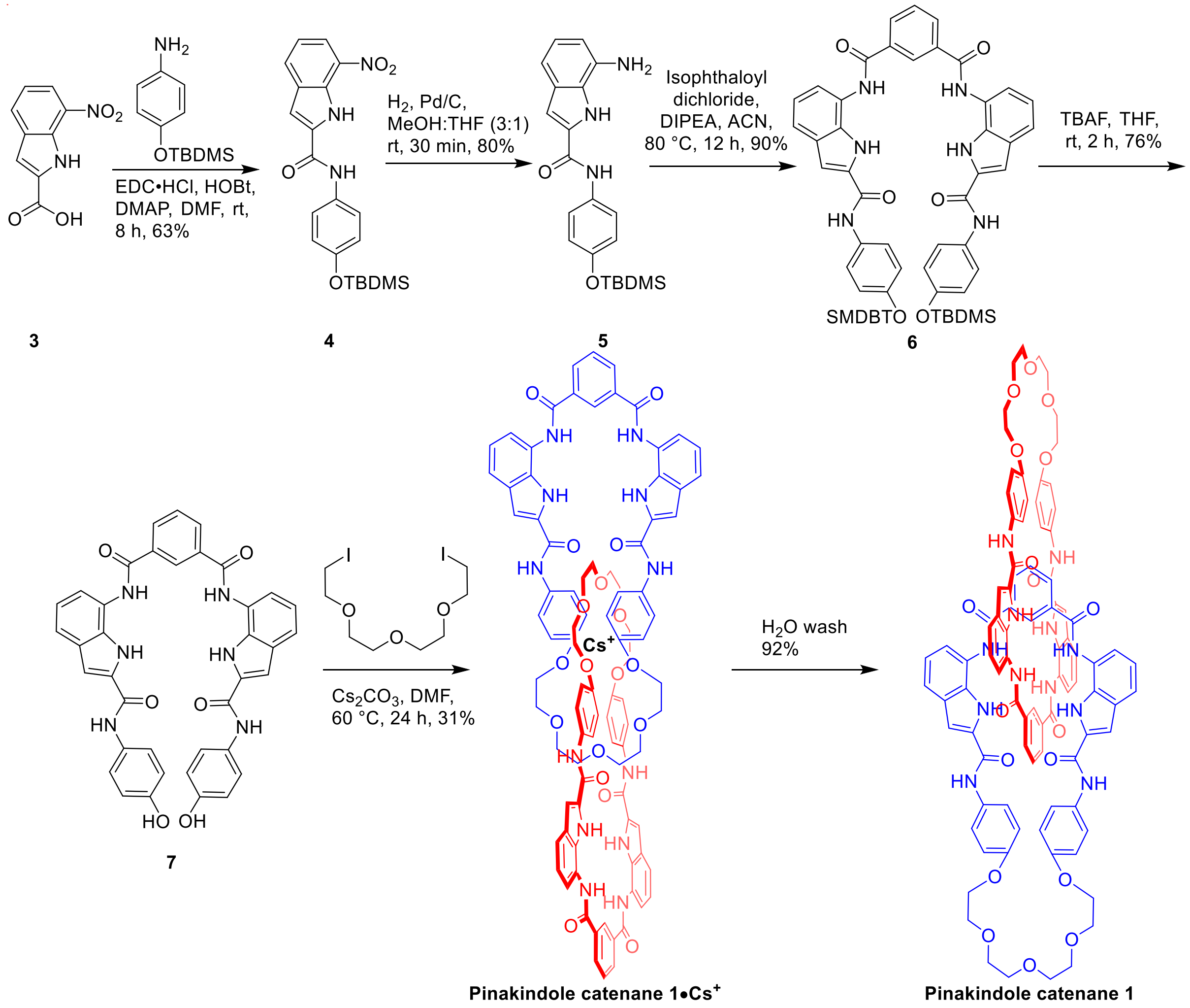

Scheme 3.1 Synthetic scheme for the **Pinakindole catenane 1**.

On the contrary, compound **7** was reacted with 1-iodo-2-(2-(2-(2-iodoethoxy)ethoxy)ethoxy)ethane at 60 °C for 72 h in the presence of Cs_2CO_3 base under high dilution technique to get a macrocyclic product **2** with 25% yield (Scheme 3.2).

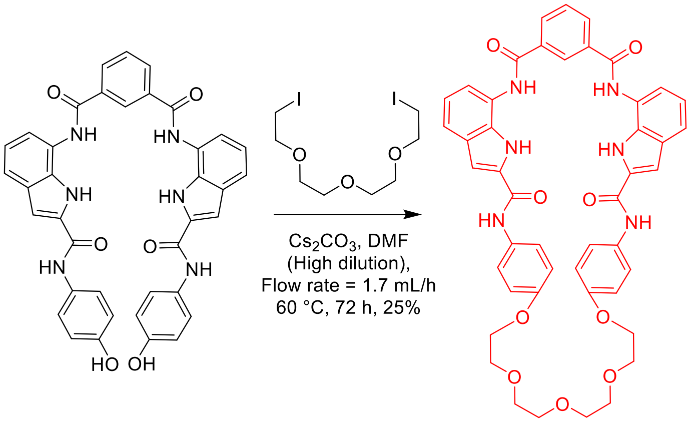

7 **Pinakindole macrocycle 2**

Scheme 3.2 Synthetic scheme for the **Pinakindole macrocycle 2**.

3.2.2. Self-assembly and membrane colocalization studies

To understand the aggregation property of **Pinakindole catenane 1**, we checked the concentration-dependent ^1H NMR in $CDCl_3$ solvent at 25 °C (Figure 3.7). If **Pinakindole catenane 1** forms an aggregation, it is expected that increasing the concentration of **Pinakindole catenane 1** will increase the downfield shift of the peak positions of N-H_a, N-$H_{a'}$, N-H_b, N-$H_{b'}$, N-H_c, and N-$H_{c'}$ protons. Whereas, if it is incapable of aggregating, then an insignificant change in the peak positions is expected. Interestingly, we noticed an indistinguishable change in the peak position of N-H_a, N-$H_{a'}$, N-H_b, N-$H_{b'}$, N-H_c, and N-$H_{c'}$ protons, clarifying that **Pinakindole catenane 1** cannot form any aggregation via the formation of intermolecular H-bonding interactions. Furthermore, in order to examine the significance of H-bonding interactions in the stabilization of the interlocked structure, a temperature-dependent ^1H NMR experiment of **Pinakindole catenane 1** was conducted at a concentration of 2 mM in $C_2D_2Cl_4$ solvent (Figure 3.8). Notably, an increase in temperature correlates with an upfield shift of the N-H_a, N-$H_{a'}$, N-H_b, N-$H_{b'}$, N-H_c, and N-$H_{c'}$ protons, suggesting that all protons participate in the formation of hydrogen bonding interactions that contribute to the stability of the interlocked structure. Moreover, the protons (N-H_a and N-$H_{a'}$), (N-H_b and N-$H_{b'}$), and (N-H_c and N-$H_{c'}$) coalesced into a single peak at higher temperatures. Thereby verifying that elevated temperatures disrupt the H-bonding interactions, resulting in the merging of the individual peaks into a singular peak.

Change in the IR spectra of egg yolk phosphatidylcholine-based large unilamellar vesicles (EYPC-LUVs) in the presence of **Pinakindole catenane 1** (5 mol% with respect to the lipid) was noted compared to the compound-free EYPC vesicles, indicating the insertion of the compound **Pinakindole catenane 1** in the lipid bilayer membrane (Figure 3.9). Moreover, the broadening and shifting of the indole N-H$_a$ stretching frequency (3294 cm^{-1} to 3268 cm^{-1}), and shifting of C=O stretching frequency (1740 cm^{-1} to 1738 cm^{-1} and 1631 cm^{-1} to 1660 cm^{-1}) of **Pinakindole catenane 1** in the absence and presence of EYPC vesicles confirmed that the **Pinakindole catenane 1** can efficiently inserted in the bilayer membrane.

3.2.3. Molecular orientation in the presence of salt

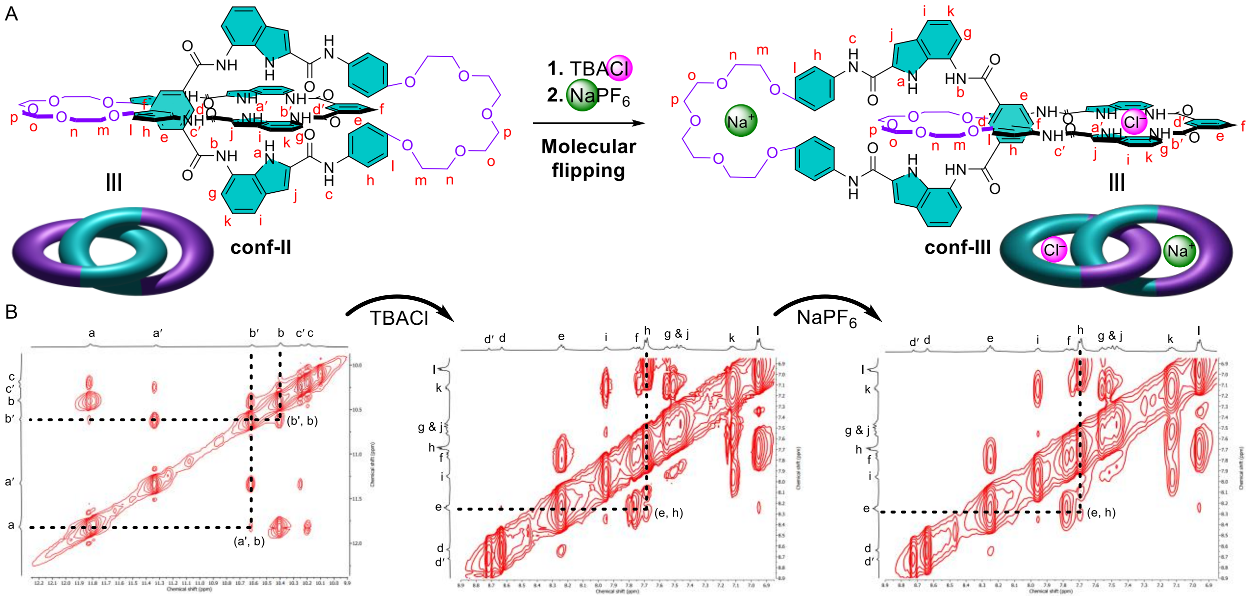

Figure 3.2 Change in the molecular orientation of **Pinakindole catenane 1** upon sequential addition of 1 equiv TBACl and 1 equiv NaPF$_6$ (A). Zoom version of NOESY spectra before and after sequential addition of 1equiv TBACl and 1 equiv NaPF$_6$ salt.

To understand the molecular orientation in the presence of different salts, both DOSY and NOESY spectra were taken before and after the sequential addition of 1 equiv of TBACl and 1 equiv of NaPF$_6$ salts. Before the addition of any salt, NOESY spectra of **Pinakindole catenane 1** (Figure 3.2B, 3.11) showed the correlation between the (a, b') and (b, b') protons, validating it stays in the **conf-II**, and DOSY spectra (Figure 3.12) confirmed the presence of a single molecular entity with a diffusion coefficient of 1.52 (± 0.01) × 10^{-6} cm^2/s. It is expected that the addition of TBACl salt will open the anion-binding cavity by reorienting it in such a way that it can form the **conf-III**. The further addition of 1 equiv of NaPF$_6$ salt is anticipated to have no effect on the structural orientation, as it has already been reoriented in a manner that allows for the accessibility of both the cation and anion binding sites. Interestingly, the addition of 1 equiv of TBACl salt diminished the (a, b') and (b, b') proton correlations and generated a set of new (e, h), (a, o), and (a, p) proton correlations in the NOESY spectra (Figure 3.2B, 3.13), conforming to the orientation of the **Pinakindole catenane 1** from **conf-II** to **conf-III**. Alongside, in the DOSY spectra (Figure 3.14), two different distinct correlations were observed, validating the presence of both free catenane **1** and [**1**+Cl$^-$]

complex with a diffusion coefficient of 1.46 (± 0.01) × 10^{-6} cm^2/s. Noteworthy, further addition of the 1 equiv $NaPF_6$ into it did not change any NOESY signals (Figure 3.2B, 3.15), giving a conformation of no further change in the molecular orientation of the catenane. Whereas a change in the DOSY spectra (Figure 3.16) was observed having a single correlation with diffusion coefficient 1.81 (± 0.01) × 10^{-6} cm^2/s. This data indicated all of the free catenane transformed the [**1**+NaCl] complex. Therefore, these experimental data validated that **Pinakindole catenane 1** has the capability of reorienting itself to bind both cation and anion in their respective ion binding sites.

3.2.4. Ion transport studies

Initial screening of the transport activity of **Pinakindole catenane 1** and **Pinakindole macrocycle 2** was evaluated across pH-sensitive 8-hydroxypyrene-1,3,6-trisulfonic acid trisodium salt (HPTS, $pK_a = 7.2$) dyes entrapped egg yolk phosphatidylcholine large unilamellar vesicles (EYPC–LUVs). Concentration-dependent studies divulged that **Pinakindole catenane 1** has the lowest half maximal effective concentration (EC_{50}) value (18.7 ± 2.7 nM, 0.0276 mol% with respect to the lipid) compared to EC_{50} (99.5 ± 19.6 nM, 0.147 mol% with respect to the lipid) of the **Pinakindole macrocycle 2**, indicating **Pinakindole catenane 1** has the superior transport activity compared to the **Pinakindole macrocycle 2**. Hill analysis also divulged that for both of the compounds the Hill coefficient (n) ≈ 1, indicating a single monomer can help in the permeation of the ions across the bilayer membrane. Subsequently, ion selectivity studies[14,15] were carried out by varying the extravesicular salts. Cation selectivity demonstrated that **Pinakindole catenane 1** has selectivity towards cation with an activity sequence $Na^+ > K^+ > Rb^+ > Cs^+ > Li^+$ (Figure 3.3A, B). Anion selectivity also confirmed that **Pinakindole catenane 1** has selectivity towards the anion with an activity sequence $Cl^- > Br^- >> F^- \approx SCN^- \approx OAC^- \approx ClO_4^-$ (Figure 3.3C, D).

To understand the transport mechanism by the **Pinakindole catenane 1**, initially, a valinomycin assay[16] was conducted across EYPC–LUVs by entrapping the 1 mM lucigenin along with 200 mM $NaNO_3$ salt with pH = 7.0. In the presence of an externally added KCl ionic gradient, **Pinakindole catenane 1** will initiate the chloride influx across EYPC–LUVs. If the transport process is mediated via an antiport mechanism, it is expected that in the presence of valinomycin (a K^+ ion transporter), **Pinakindole catenane 1** will influx more amount of Cl^- ion, which will be reflected as the enhancement in the lucigenin fluorescence quenching. On the contrary, if the transport process happens via the symport mechanism, then **Pinakindole catenane 1** will not couple with the externally added valinomycin, and hence, the fluorescence quenching of the lucigenin is expected to remain unaltered. During the experiment, we noticed an insignificant change in the lucigenin fluorescence quenching (Figure 3.3C), providing an initial confirmation of the symport mechanism by **Pinakindole catenane 1**. For further confirmation of the mechanistic pathway, NO_3^-/SO_4^{2-} assay[16] was conducted. During the assay, vesicles were entrapped with

1 mM lucigenin and 200 nM NaCl salt, keeping intravesicular pH 7.0. In the presence of the intravesicular NaCl salt, lucigenin remains in a fully fluorescence quenching state. During the experiment, the isoosmolar $NaNO_3$ and Na_2SO_4 salts were used as extravesicular buffer medium (200 mM $NaNO_3$ or 66.6 mM Na_2SO_4, 10 mM HEPES, pH = 7.0). Due to the higher charge density present over SO_4^{2-} ion, it is difficult to translocate across the bilayer membrane. Hence fluorescence activity gaining of lucigenin dye will be affected if the transporter transports the ion via the antiport mechanism, whereas it is expected to remain unaltered if the transport process happens via the symport mechanism. Noteworthy, during the experiment an insignificant change in the lucigenin fluorescence activity was observed (Figure 3.3D), validating **Pinakindole catenane 1** follows the symport mechanism during the transport process.

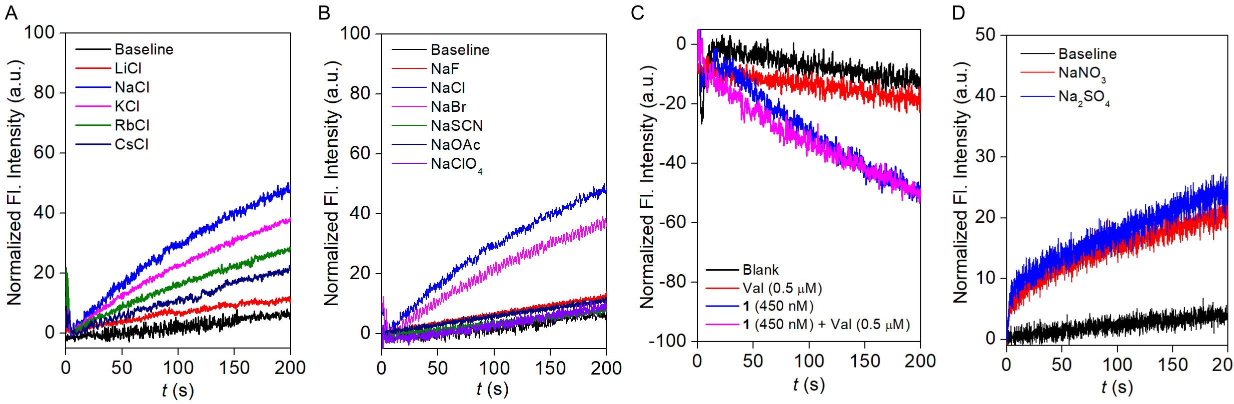

Figure 3.3 Anion (A) and cation (B) selectivity of **Pinakindole catenane 1** across EYPC–LUVs⊃HPTS at 20 nM concentration. Change in Cl^- influx by **Piankindole catenane 1** in the presence and absence of valinomycin across EYPC−LUVs⊃lucigenin (C). Change in Cl^- efflux by **Piankindole catenane 1** in the presence of intravesicular Cl^- and either SO_4^{2-} or NO_3^- as an iso-osmolar extravesicular anion across EYPC−LUVs⊃lucigenin.

Moreover, to understand the capability of the **Pinakindole catenane 1** towards the transport of the physiologically relevant Cl^- ion, a halide sensitive lucigenin dye was used. For this experiment, EYPC–LUVs were by entrapping the 1 mM lucigenin dye (a halide sensitive dye) and 200 mM $NaNO_3$ salt with pH =7.0. During the assay, an anionic gradient was created by the exogenous addition of the 20 µL of 2 M NaCl salt. If transporter **Pinakindole catenane 1** influx the Cl^- ion, the lucigenin fluorescence quenching activity is expected to be enhanced. A prominent increment in the lucigenin fluorescence quenching with increasing the concentration of **Pinakindole catenane 1** (Figure 3.22), demonstrated that it can efficiently influx the Cl^- ion across the bilayer membrane. Alongside, the variation of the extravesicular MCl salts (M^+ = Li^+, Na^+, K^+, Rb^+, and Cs^+) during the lucigenin assay, changes the fluorescence quenching of the lucigenin dye. This data reconfirmed that **Pinakindole catenane 1** is selective towards cations (Figure 3.23B), and the observed selectivity pattern follows the same trend as observed during the HPTS cation selectivity assay.

Before investigating the mode of the transport process, the effect of the **Pinakindole catenane 1** on the membrane was assessed utilizing a 5(6)-carboxyfluorescein (CF) leakage assay.[16] CF is a self-quenching dye, and hence, under the membrane-entrapped condition at its high concentration, it will remain in a fluorescence-quenched state. Whereas if the added external compound forms any large pore or disintegrates the membrane, then it can leak out CF dye and enhance its fluorescence activity. It is noteworthy that even at different concentrations of **Pinakindole catenane 1**, an insignificant enhancement of the CF fluorescence activity was observed (Figure 3.26B). This data confirmed that **Pinakindole catenane 1** neither induces the formation of large pores nor disrupts the integrity of the membrane.

To address the mode of the ion transport (carrier or channel) by **Pinakindole catenane 1**, initially cholesterol based assay was conducted.[17] Cholesterol loading makes the membrane rigid, and hence, other than the exception, it is expected that it will decrease the to and fro movement of a carrier across the bilayer membrane; thereby, a significant decrease in ion transport activity is expected. Whereas, for the channel mode of ion transport is expected to remain unaltered. Interestingly, insignificant changes in the transport activity both in the presence of 10% cholesterol and absence of cholesterol (Figure 3.27) preliminary confirmed the channel mode of ion transport by **Pinakindole catenane 1**. To understand the real-time ion channel formation by **Pinakindole catenane 1**, the electrophysiological experiment was carried out by using the unbuffered 1 M KCl solution in both cis and trans chambers by using diphytanoyl phosphatidylcholine (diPhyPC) bilayer lipid membrane (BLM).[14] The addition of **Pinakindole catenane 1** (4 μM) in the cis chamber rapidly triggered square-top shaped current flow with open-close transitions at different holding potentials (Figure 3.4A, B), confirming the formation of ion channels inside the bilayer membrane with an average channel diameter of 4.5 ± 1 Å. The average single-channel conductance was evaluated to be 530 ± 2 pS (Figure 3.4C, 3.30), indicating our channel has superior ion fluxing capability across the bilayer.

To understand the selectivity of **Pinakindole catenane 1** towards anion in comparison with cation, the permeability ratio P_{Cl^-}/P_{K^+} was calculated by using the Goldman-Hodgkin-Katz equation with unsymmetrical KCl solutions (i.e. KCl_{cis} = 1 M and KCl_{trans} = 0.5 M). It was observed that **Pinakindole catenane 1** is approximately 1.43 times (Figure 3.4C, Table 3.2) more permeable towards the K^+ ion than the Cl^- ion. The moderate permeability ratio during cation/anion selectivity also justifies the simultaneous transport of both cation and anion. However, $P_{K^+}/P_{Cl^-} > 1$ verified our developed channel slightly prefers to permeate K^+ ion over Cl^- ion through the ion permeation pathway. Further anion/anion and cation/cation selectivities were also evaluated in BLM to get a better visualization of ion selectivity.[18] The ion selectivity of **Pinakindole catenane 1** towards Na^+ ion over K^+ ion was investigated with cis/trans = 1 M KCl/ 1 M NaCl setup (Figure 3.4D). Investigation indicated our channel is approximately 3.54 times more permeable towards the Na^+ ion over the K^+ ion (Table 3.3). Further validation of Cl^- ion selectivity was addressed by using the 1 M NaCl/ 1 M NaBr cis/trans setup (Figure 3.4D). A distinct negative reversible voltage was observed which was used to calculate the permeability ratio. The calculation indicates our channel has 1.48 times (Table 3.4) higher permeability towards the Cl^- ion over the Br^- ion, divulging the prominent selectivity towards the Cl^- ion compared to the relatively larger Br^- ion. Selectivity towards Na^+ and Cl^- ions from BLM also corroborates with the ion selectivity data achieved from the fluorescence assay.

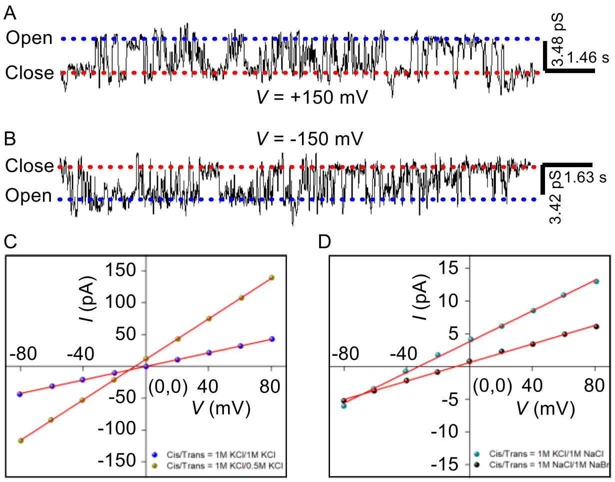

Figure 3.4 Ion channel opening-closing event of **Piankindole catenane 1** (4 µM) at +150 mV (A) and −150 mV (B) holding potential with symmetrical 1M KCl buffer solution. *I-V* plot of **Pinakindole catenane 1** with symmetrical and unsymmetrical buffered KCl solution (C). *I-V* plot of **Pinakindole catenane 1** for anion/anion (cis/trans = 1M NaCl/1M NaCl) and cation/cation (cis/trans = 1M KCl/1M NaCl) selectivity (D).

3.2.5. Theoretical calculations

After successfully addressing the ion transport process, it becomes essential to delve into the ion channel formation inside the bilayer membrane and understand the ion binding process during ion transport. Based on the experimentally obtained interlocked structure, we initially geometrically optimized the **conf-I** (Figure 3.36), **conf-II** (Figure 3.37), and **conf-III** (Figure 3.38) by using the Gaussian 09 program package using B3LYP functional and 6–311G(d,p) basis set.[19] Optimization data indicated that **conf-II** exhibits superior conformational stability compared to **conf-I** and **conf-III** (Table 3.5). It was observed that the stabilization of all conformational orientations is facilitated by the establishment of intermolecular H-bonding interactions, which contribute to the stabilization of the interlocked structure. This finding further supports the data obtained from the temperature-dependent ^{1}H NMR experiment. **Conf-I** and **conf-III** are stabilized by the formation of H-bonding interaction between the crown ether and the indolic core. Whereas, **conf-II** formed intermolecular bifurcated H-bonding interactions between the indole core moiety. It is noteworthy that **conf-II** does not have any void space for binding with the ion (Figure 3.5, 3.37B). Hence, it is less likely to be the responsible conformational orientation that is responsible for both cation and anion binding. Even though **conf-I** has void space for cation binding (Figure 3.36), the lack of availability of both cation and anion binding sites in a single entity of **conf-I** rules out the possibility of the responsible conformational orientation for simultaneous cation and anion binding. Interestingly, in **conf-III**, we noticed the presence of both cation and anion-binding sites (Figure 3.5, 3.38B), indicating that **conf-III** might be responsible for the conformational orientation for the simultaneous binding of both cation and anion.

The presence of sufficient void space in the **conf-I** and **conf-III** promoted us to understand the Cs^+ and Na^+Cl^- ion binding process, respectively. For **conf-I**, geometry optimization was carried out by using the Gaussian 09 program package using B3LYP functional with 6-311G(d,p) basis set for C, H, N, and O atoms and LanL2DZ basis set for Cs atom. An optimized structure indicated that Cs^+ ion can perfectly be fitted between the crown ether core (Figure 3.5). Cs^+ ion formed electrostatic interactions with the O-atom of the crown ether core ($O\cdots Cs^+ = 3.320$ Å) and two C=O groups ($C{=}O\cdots Cs^+ = 3.185$ Å and 3.336 Å). Alongside the cation-π intersections (π-surface$\cdots Cs^+ = 2.073$ Å and 1.909 Å) also help it to stabilize the Cs^+ ion inside the cavity of **conf-I** (Figure 3.39). Similarly, geometry optimization of **conf-III** with NaCl salt discloses that both Na^+ and Cl^- ions can bind within the crown ether and indole core, respectively. Cl^- ion is found to interact with the acidic N-H_a protons ($N\text{-}H_a\cdots Cl^- = 2.467$ Å and 2.299 Å), N-H_b protons ($N\text{-}H_b\cdots Cl^- = 2.412$ Å), and aromatic C-H_d protons ($C\text{-}H_d\cdots Cl^- = 2.856$ Å), whereas Na^+ ion showed the electrostatic interaction with the O-atoms of the crown ether core ($O\cdots Na^+ = 2.267$ Å and 2.313 Å) and C=O group ($C{=}O\cdots Na^+ = 2.197$ Å) (Figure 3.5, 3.40). Interestingly, we noticed that the [$\mathbf{1}_{\textbf{conf-III}}$+NaCl] complex has lower energy than that of the most stable conformational orientation $\mathbf{1}_{\textbf{conf-II}}$ (Table 3.5). The lowering in energy may be providing the driving force to reorient the molecule from **conf-II** to comparatively higher energy containing **conf-III**, which ultimately gives an energetically more stable [$\mathbf{1}_{\textbf{conf-III}}$+NaCl] complex than **conf-II**. Hence, we hypothesized that **conf-III** might be the responsible conformational orientation that can translocate both cation and anion during the ion transport process.

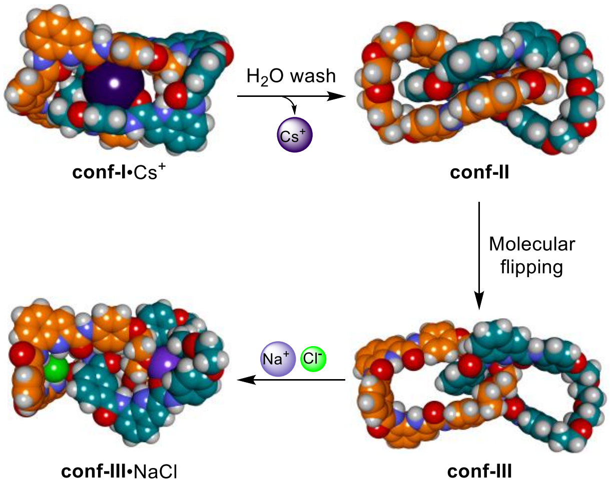

Figure 3.5 Geometry optimized structures of **Pinakindole catenane 1** and changes of the molecular orientation in the presence of the NaCl salt.

3.3. Conclusion

In conclusion, here we introduced Pinakindole catenane as the first example of the catenane-based synthetic ion channel system. Ion transport comparison clarifies the emerging ion transport activity of **Pinakindole catenane 1** compared to the macrocyclic analog **2**. Detailed transport studies verify that **Pinakindole catenane 1** selectively transports Na^+ and Cl^- ions across the bilayer membrane by following the symport as a transport mechanism. Cholesterol-based assay and electrophysiological experiments revealed that **Pinakindole catenane 1** formed an ion channel in the membrane with a single channel conductance of 530 ± 2 pS and an average channel diameter of 4.5 ± 1 Å. Further selectivity studies confirmed that **Pinakindole catenane 1** is 3.54 times more permeable towards Na^+ ion over K^+ ion, and it has 1.48 times higher permeability towards Cl^- ion over Br^- ion. Finally, geometrical optimization of different conformational orientations (**conf-I**, **conf-II**, and **conf-III**) were carried out to understand the responsible conformational orientation for cation-anion transport. Even though **conf-II** is a more energetically stable conformational orientation, **conf-III** is more susceptible to cation-anion transport due to the presence of both cation and anion binding sites in itself. We hypothesize that **conf-III** follows the wobbler motion in the bilayer membrane to provide a translocating path for both cation and anion by forming an ion channel. Hence, we believe that our decorated **Pinakindole catenane 1** can enlighten a pathway for generating more interesting interlocked catenane channel structures for different applications within the biological membrane.

3.4. Experimental section

3.4.1. General methods

Reagents and compounds used for the synthesis were purchased from Sigma-Aldrich, Avra Chemicals, Spectrochem, and BLDpharm and used without further purification. For dry reaction CH_3CN, DMF, MeOH, and THF were purchased from commercial suppliers and used without further purification. All the reactions were performed under nitrogen atmospheric environment using N_2 gas balloon and monitored by checking TLC, performed on pre-coated aluminum plates of silica gel 60 F254 (0.25 mm, E. Merck). Column chromatographies were performed on Merck silica gel (100–200 mesh). Egg yolk phosphatidylcholine (EYPC) was obtained from Avanti Polar Lipids as a solution in $CHCl_3$ (25 mg/mL). HEPES buffer, HPTS, Lucigenin, Triton X–100, NaOH, and inorganic salts were purchased of molecular biology grade from Sigma. Large unilamellar vesicles (LUVs) were prepared by using a mini extruder, equipped with a polycarbonate membrane of 100 nm or 200 nm pore size, purchased from Avanti Polar Lipids.

3.4.2. Physical measurements

The ^1H NMR spectra were recorded at 400 MHz and ^{13}C spectra at 101 MHz either in Jeol or Bruker NMR instruments. The residual (deuterium) solvent signals were considered as an internal reference ($\delta H = 7.26$

ppm for $CDCl_3$, δH = 2.50 for DMSO-d_6) to calibrate spectra. All the chemical shifts were reported in ppm. The following abbreviations were used to indicate multiplicity patterns; s: singlet, d: doublet, t: triplet, m: multiplet, dd: doublet of doublets. Coupling constants were measured in Hz. High-resolution mass spectra (HRMS) were recorded on electrospray ionization time-of-flight (ESI–TOF) with +ve mode. Adjustment of pH of buffer solutions was made using Hanna HI98108 PHep$^+$ pH meter. ChemBio Draw 21.0.0 software was used for drawing structures and processing figures. All buffer solutions were prepared from the autoclaved water. Fluorescence experiments were recorded on Fluoromax-4 and Fluoromax+ from Jobin Yvon Edison equipped with an injector port and magnetic stirrer in a microfluorescence cuvette. The extravesicular dye was removed by performing gel chromatography using Sephadex G-50. The fluorescence studies proceeded using Origin 8.5 software. Conductance measurement through ion channel was carried out in a planar bilayer lipid membrane (BLM) workstation obtained from Warner Instrument, consisting of head-stage and its corresponding amplifier BC-535, 8-pole bessel filter LPF-8, Axon CNS Digidata 1440A, and pClamp 10 software. The conductance data were analyzed in Clampfit 10.6 software.

3.4.3. Synthetic procedures

The synthetic procedure of compound 3: Compound **3** was synthesized by using the reported literature procedure.[13]

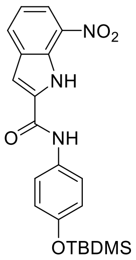

Synthesis of *N*-(4-((tert-butyldimethylsilyl)oxy)phenyl)-7-nitro-1*H*-indole-2-carboxamide (4): In a 50 mL round bottom flask, compound **3** (600 mg, 2.9 mmol, 1 equiv) was dissolved in dry DMF (10 mL). To the clear solution EDC·HCl (725 mg, 3.78 mmol, 1.3 equiv), HOBt (433 mg, 3.2 mmol, 1.1 equiv), and 4-Dimethylaminopyridine (1.78 g, 14.5 mmol, 5 equiv), was added and the reaction mixture was stirred at room temperature for 30 min under N_2 atmosphere. 4-((tert-butyldimethylsilyl)oxy)aniline (650mg, 2.9 mmol, 1 equiv) was added to the reaction mixture by dissolving it with 5 mL DMF and continued the stirring at room temperature for 12 h. After completion of the reaction, excess water was added to it. The yellowish precipitate was obtained, which was filtered to get a pure compound **4** (753 mg, Yield = 63 %). **^{1}H NMR (400 MHz, $CDCl_3$)** δ 10.60 (s, 1H), 8.29 (dd, *J* = 8.1, 1.0 Hz, 1H), 8.03 (d, *J* = 7.8 Hz, 1H), 7.81 (s, 1H), 7.51 (d, *J* = 8.8 Hz, 2H), 7.29 (t, *J* = 8.0 Hz, 1H), 7.11 (s, 1H), 6.89 – 6.85 (m, 2H), 1.00 (s, 9H), 0.21 (s, 6H).**^{13}C NMR (101 MHz, $CDCl_3$)** δ 158.25, 153.13, 133.67, 133.65, 131.38, 130.79, 130.29, 129.60, 122.00, 121.86, 120.73, 120.35, 103.39, 25.82, 18.36, -4.29. **HRMS (ESI) m/z:** [M+H]$^+$ Calcd. for $C_{21}H_{25}N_3O_4SiH^+$ 412.1688; Found 412.1689. **IR (Neat, ν/cm^{-1}):** 3294, 2955, 2929, 2888, 2858, 1643, 1602, 1548, 1508, 1403, 1339, 1318, 1290, 1250, 1169, 1110, 986, 915, 836, 804, 781, 729, 699, 627, 564.

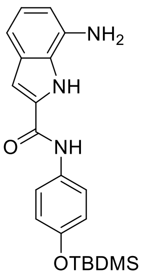

Synthesis of 7-amino-*N*-(4-((tert-butyldimethylsilyl)oxy)phenyl)-1*H*-indole-2-carboxamide (5): In a 50 mL round bottom flask, compound **4** (740 mg, 1.8 mmol, 1 equiv) was dissolved in dry 16 mL MeOH:THF (3:1 *V*/*V*) solvent and degassed it properly for 30 min. After degassing, Pd/C (64 mg, 0.5 mmol, 0.3 equiv) was added to it, and H_2 gas was purged into it. After completion of the H_2 purging, the reaction mixture was kept at room temperature for 30 min under stirring conditions. After completion of the reaction, it was passed through the celite bed to remove the Pd/C from the solution by washing it with MeOH. The solvent was evaporated by a rota evaporator to get the pure compound **5** (550 mg, Yield = 78 %). **^{1}H NMR (400 MHz, DMSO-*d*$_6$)** δ 11.31 (s, 1H), 10.03 (s, 1H), 7.69 – 7.65 (m, 2H), 7.27 (d, *J* = 2.1 Hz, 1H), 6.88 – 6.84 (m, 3H), 6.79 (t, *J* = 7.6 Hz, 1H), 6.38 (dd, *J* = 7.3, 1.1 Hz, 1H), 5.39 (s, 2H), 0.96 (s, 9H), 0.20 (s, 6H). **^{13}C NMR (101 MHz, DMSO-*d*$_6$)** δ 159.62, 151.02, 134.53, 132.84, 130.46, 127.89, 126.53, 121.67, 121.20, 119.79, 109.18, 105.90, 103.84, 25.61, 17.96, -4.51. **HRMS (ESI) m/z:** $[M+H]^+$ Calcd. for $C_{21}H_{27}N_3O_2SiH^+$ 382.1946; Found 382.1951. **IR (Neat, ν/cm^{-1}):** 3355, 2956, 2930, 2857, 2362, 2338, 1725, 1710, 1692, 1658, 1642, 1600, 1589, 1548, 1511, 1468, 1441, 1426, 1410, 1353, 1330, 1253, 914, 839, 781, 731, 655.

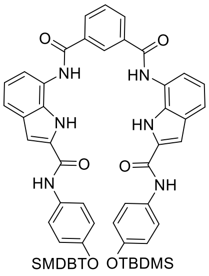

Synthesis of *N*1,*N*3-bis(2-((4-((tert-butyldimethylsilyl)oxy)phenyl)carbamoyl)-1*H*-indol-7-yl)isophthalamide (6): In a clean and dry 50 mL round bottom flask, compound **5** (517 mg, 1.3 mmol, 1.1 equiv) was dissoled in dry 7 mL CH_3CN solvent along with the *N*,*N*-Diisopropylethylamine base (0.5 mL, 3.1 mmol, 2.5 equiv) and reaction mixture was kept at 80 °C for 20 min. A dissolved CH_3CN solution (5 mL) of isophthaloyl dichloride (250 mg, 1.2 mmol, 1 equiv) was dropwise added to the reaction mixture over 15 min. After complete addition, the reaction mixture was kept for 12 h under starring conditions at 80 °C, maintaining the N_2 atmosphere. After completion of the reaction, the solution was transferred to a separating funnel with ethyl acetate (3 × 15 mL) and washed with H_2O (15 mL). The combined organic layers were then washed with brine solution (3 × 10 mL) and finally dried over the Na_2SO_4, and the solvent was evaporated on a rotary evaporator. The crude product **6** was purified by silica gel column chromatography (Eluent: 1% MeOH/$CHCl_3$) to obtain pure compound **6** (990 mg, Yield = 90 %). **^{1}H NMR (400 MHz, $CDCl_3$)** δ 11.79 (s, 2H), 9.46 (s, 2H), 8.34 (dd, *J* = 5.6, 3.2 Hz, 2H), 7.98 (s, 1H), 7.85 (s, 2H), 7.63 (dd, *J* = 7.6, 1.6 Hz, 2H), 7.14 (t, *J* = 7.6 Hz, 1H), 6.96 (s, 2H), 6.94 (d, *J* = 2.5 Hz, 2H), 6.77 (d, *J* = 1.9 Hz, 2H), 6.71 (d, *J* = 8.8 Hz, 4H), 6.31 (d, *J* = 8.8 Hz, 4H), 0.96 (s, 18H), 0.16 (s, 6H), 0.13 (s, 6H). **^{13}C NMR (101 MHz, $CDCl_3$)** δ 166.90, 160.90, 152.60, 135.11, 131.47, 129.25, 129.11, 128.85, 128.46, 128.36, 123.92, 123.53, 121.94, 120.49, 119.82, 119.31, 115.79, 105.31, 25.82, 18.34, -4.34. **HRMS (ESI) m/z:** $[M+H]^+$ Calcd. for $C_{50}H_{56}N_6O_6Si_2H^+$ 893.3873; Found 893.3878. **IR (Neat, ν/cm^{-1}):** 3306, 2956, 2929, 2857, 1657, 1622, 1603, 1538, 1508, 1463, 1435, 1409, 1336, 1306, 1296, 1264, 1243, 1168, 1018, 1007, 985, 915, 837, 780, 758, 731, 696, 658.

Synthesis of *N*1,*N*3-bis(2-((4-hydroxyphenyl)carbamoyl)-1*H*-indol-7-yl)isophthalamide (7): In a clean and dry 50 mL round bottom flask, compound **6** (965 mg, 1 mmol, 1 equiv) was dissoled in dry 12 mL THF solvent and required amount of TBAF (847 mg, 3.2 mmol, 3 equiv) was added in the reaction mixture. The reaction mixture was stirred at room temperature for 2 h. After completion of the reaction, THF was evaporated using a rota evaporator. It was transferred to a separating funnel with ethyl acetate (3 × 15 mL) and washed with H_2O (15 mL). The combined organic layers were then washed with brine solution (3 × 10 mL) and finally dried over the Na_2SO_4, and the solvent was evaporated on a rotary evaporator. The crude product **7** was purified by silica gel column chromatography (Eluent: 12% MeOH/$CHCl_3$) to obtain pure compound **7** (546 mg, Yield = 76 %). **^{1}H NMR (400 MHz, DMSO-*d*$_6$)** δ 11.77 (s, 2H), 10.38 (s, 2H), 10.08 (s, 2H), 9.27 (s, 2H), 8.63 (t, *J* = 1.8 Hz, 1H), 8.25 (dd, *J* = 7.8, 1.8 Hz, 2H), 7.95 (d, *J* = 7.7 Hz, 2H), 7.78 (t, *J* = 7.7 Hz, 1H), 7.57 – 7.53 (m, 4H), 7.51 (d, *J* = 7.9 Hz, 2H), 7.44 (d, *J* = 2.0 Hz, 2H), 7.12 (t, *J* = 7.8 Hz, 2H), 6.78 – 6.73 (m, 4H). **^{13}C NMR (101 MHz, DMSO-*d*$_6$)** δ 165.63, 159.12, 153.76, 135.28, 131.78, 130.97, 130.29, 128.84, 128.77, 128.52, 127.58, 124.12, 122.15, 120.11, 118.11, 116.09, 115.11, 103.88. **HRMS (ESI) m/z:** $[M+H]^+$ Calcd. for $C_{38}H_{28}N_6O_6H^+$ 665.2124; Found 665.2148. **IR (Neat, ν/cm^{-1}):** 3480, 3293, 2961, 2920, 2877, 1630, 1585, 1546, 1513, 1434, 1415, 1357, 1311, 1264, 1243, 1170, 828, 781, 731.

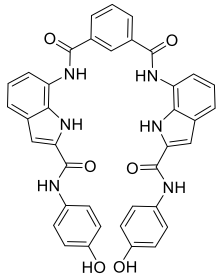

Synthesis of Pinakindole catenane 1·Cs$^+$: In a well dry and clean 25 mL two-necked round bottom flask, 1-iodo-2-(2-(2-(2-iodoethoxy)ethoxy)ethoxy)ethane (62.3 mg, 0.15 mmol, 1 equiv) was dissolved in 3 mL well dried DMF. The required amount of Cs_2CO_3 (147 mg, 0.45 mmol, 3 equiv) was added to the reaction mixture, and it was kept at 60 °C for 30 min. Compound **7** was added to the reaction mixture dropwise over a time period of 1 h as DMF solution (2 mL), and the reaction mixture continued starting for 24 h at room temperature. After completion of the reaction, ice-cooled HPLC $CHCl_3$ was added to the reaction to form a precipitate. Finally, the precipitate was filtered by using the Bruckner funnel and washed with ice-cold HPLC MeOH to get the pure compound of catenane **1**. (93 mg, Yield = 31 %). **^{1}H NMR (600 MHz, DMSO-*d*$_6$)** δ 11.85 (s, 2H), 11.51 (s, 2H), 10.67 (s, 2H), 10.43 (s, 2H), 10.27 (s, 2H), 10.22 (s, 2H), 8.72 (s, 1H), 8.65 (s, 1H), 8.29 – 8.18 (m, 4H), 7.95 (s, 2H), 7.80 – 7.73 (m, 4H), 7.73 – 7.64 (m, 8H), 7.58 – 7.42 (m, 8H), 7.17 – 7.07 (m, 4H), 7.01 – 6.83 (m, 8H), 4.05 (s, 8H), 3.73 (s, 8H), 3.59 (s, 8H), 3.56 (s, 8H). **^{133}Cs NMR (53 MHz, $CDCl_3$)** δ 77.42.**^{13}C NMR (151 MHz, DMSO-*d*$_6$)** δ 165.70, 159.30, 159.24, 154.77, 151.90, 139.22, 135.30, 135.11, 131.98, 131.92, 131.68, 131.62, 131.14, 131.08, 131.04, 129.34, 128.97, 128.77, 128.56, 127.60, 127.20, 124.19, 124.01, 122.15, 121.85, 120.20, 118.54, 118.20, 116.92, 116.24, 115.15, 114.49, 114.44, 110.64, 104.29, 104.22, 70.04, 69.94, 69.84, 69.80, 69.69, 69.01, 68.94, 67.29. **MALDI-TOF m/z:** $[M]^+$ Calcd. for

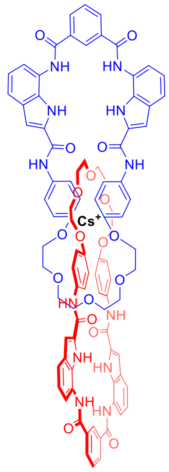

$C_{92}H_{84}N_{12}O_{18}Cs^+$ 1777.5076 (100.0%), 1778.5110 (99.5%), 1779.5143 (49.0%); Found 1778.124 and 1779.133. **HRMS (ESI) m/z:** Calcd. for $C_{92}H_{84}N_{12}O_{18}Cs^+$ $[M+Cs]^+$ = 1777.5076 and $[M/2+Cs]^+$ = 955.2063; Found $[M+Cs]^+$ = 1777.5188 and $[M/2+Cs]^+$ = 955.2076. **IR (Neat, ν/cm^{-1}):** 3026, 2969, 2954, 2923, 2851, 2365, 2340, 1739, 1672, 1636, 1628, 1600, 1541, 1509, 1459, 1439, 1369, 1302, 1229, 1217, 1130, 1101, 1093, 1020, 820, 799, 785, 732, 719, 707.9, 681, 663, 638, 625, 604, 579.

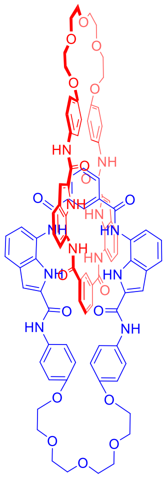

Synthesis of Pinakindole catenane 1: To obtain the **Pinakindole catenane 1** from the **Pinakindole catenane 1·Cs$^+$** (85 mg) compound was properly washed with the H_2O to remove the entrapped Cs^+ ion from the cavity of the **Pinakindole catenane 1·Cs$^+$**. After multiple times washing with the H_2O, it was filtered through the Buchner funnel, and the precipitate was collected and dried overnight in the desiccator to obtain a pure brown solid of the **Pinakindole catenane 1** (72 mg, Yield = 92 %). **^{1}H NMR (600 MHz, DMSO-*d$_6$*)** δ 11.82 (s, 2H), 11.33 (s, 2H), 10.61 (s, 2H), 10.40 (s, 2H), 10.24 (s, 2H), 10.19 (s, 2H), 8.64 (s, 2H), 8.24 (t, *J* = 9.7 Hz, 4H), 7.96 (s, 2H), 7.80 – 7.74 (m, 4H), 7.71 – 7.66 (m, 8H), 7.57 – 7.51 (m, 4H), 7.49 – 7.44 (m, 4H), 7.15 – 7.09 (m, 4H), 6.98 – 6.92 (m, 8H), 4.07 (s, 8H), 3.74 (s, 8H), 3.59 (s, 8H), 3.56 (s, 8H). **^{133}Cs NMR (53 MHz, DMSO-*d$_6$*)** no signal found. **^{13}C NMR (151 MHz, DMSO-*d$_6$*)** δ 165.65, 165.60, 159.27, 159.20, 154.77, 151.88, 135.30, 135.04, 131.95, 131.86, 131.65, 131.53, 131.10, 130.97, 130.30, 129.19, 129.02, 128.93, 128.77, 128.52, 127.60, 127.22, 124.16, 123.95, 122.16, 121.85, 121.81, 120.16, 118.59, 118.16, 116.86, 116.18, 115.12, 114.50, 114.44, 104.10, 70.03, 69.93, 69.83, 69.78, 69.67, 68.99, 68.92, 67.26. **MALDI-TOF m/z:** $[M+2Na]^{2+}$ Calcd. for $C_{92}H_{84}N_{12}O_{18}Na_2^{2+}$ 845.2906 (100.0%), 845.7922 (99.5%); Found 845.5800. **HRMS (ESI) m/z:** $[M+H]^+$ Calcd. for $C_{92}H_{84}N_{12}O_{18}H^+$ 1645.6100; Found 1645.6127. $[(M/2)+H]^+$ Calcd. for $C_{46}H_{42}N_6O_9H^+$ 823.3087 or $[(M+2H)]^+/2$ Calcd. for $C_{92}H_{84}N_{12}O_{18}H_2^{2+}$ 823.3086; Found 823.3085. **IR (Neat, ν/cm^{-1}):** 3312, 3296, 3279, 2955, 2925, 2871, 2856, 1741, 1726, 1654, 1630, 1603, 1542, 1510, 1436, 1420, 1377, 1364, 1342, 1302, 1300, 1262, 1236, 1175, 1100, 1082, 1020, 968, 944, 907, 894, 884, 822, 780, 731, 694, 672, 663, 576, 562.

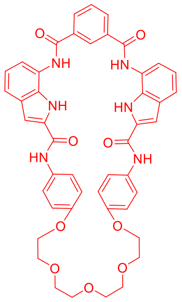

Synthesis of Pinakindole macrocycle 2: In a clean and dry 500 mL two naked round bottom flask, 1-iodo-2-(2-(2-(2-iodoethoxy)ethoxy)ethoxy)ethane (62.3 mg, 0.15 mmol, 1 equiv) was dissolved in 170 mL well dry DMF. Required amount of Cs_2CO_3 (147 mg, 0.45 mmol, 3 equiv) was added to the reaction mixture, and it was kept at 60 °C for 30 min. Compound **7** (100 mg, 0.15 mmol, 1 equiv) dissolved in 30 mL of dry DMF was added to the reaction mixture by using a syringe pump with a flow rate of 1.7 mL/h. After the complete addition of compound **7**, the reaction mixture continued starting for a further 72 h. After completion of the reaction, DMF was evaporated in the rota evaporator, and the reaction mixture was then poured into a separating funnel. The compound was extracted in the EtOAc layer by washing it with H_2O (3×25 mL).

The combined organic layers were then washed with brine solution (3 × 10 mL) and finally dried over the Na_2SO_4, and the solvent was evaporated on a rotary evaporator. The crude product was purified by silica gel column chromatography (Eluent: 8% MeOH/$CHCl_3$) to obtain macrocycle **2** (31 mg, Yield = 25 %). **^{1}H NMR (600 MHz, DMSO-*d$_6$*)** δ 11.80 (s, 2H), 10.38 (s, 2H), 10.18 (s, 2H), 8.63 (s, 1H), 8.25 (d, 2H), 7.95 (s, 2H), 7.73 – 7.66 (m, 4H), 7.56 – 7.44 (m, 4H), 7.12 (s, 2H), 6.95 (s, 4H), 6.76 (s, 1H), 4.07 (s, 4H), 3.74 (s, 4H), 3.59 (s, 4H), 3.56 (s, 13H). **^{133}Cs NMR (53 MHz, DMSO-*d$_6$*)** no signal found. **^{13}C NMR (151 MHz, DMSO-*d$_6$*)** δ 165.64, 159.25, 154.75, 135.30, 131.93, 131.63, 130.96, 128.74, 128.51, 124.15, 122.14, 121.80, 120.12, 118.15, 115.10, 114.49, 114.40, 104.05, 69.92, 69.82, 68.98, 67.25. **HRMS (ESI) m/z:** $[M+Na]^+$ Calcd. for $C_{46}H_{42}N_6O_9Na^+$ 845.2906; Found 845.2835 and $[M+H]^+$ Calcd. for $C_{46}H_{42}N_6O_9H^+$ 823.3087; Found 823.3076. **IR (Neat, ν/cm^{-1}):** 3322, 2949, 2922, 2837, 1658, 1643, 1633, 1547, 1536, 1511, 1479, 1462, 1450, 1412, 1243, 1114, 1018, 824, 731.

3.4.4. Comparison of ^{1}H NMR of Pinakindole catenane 1·Cs$^+$, 1 and macrocycle 2

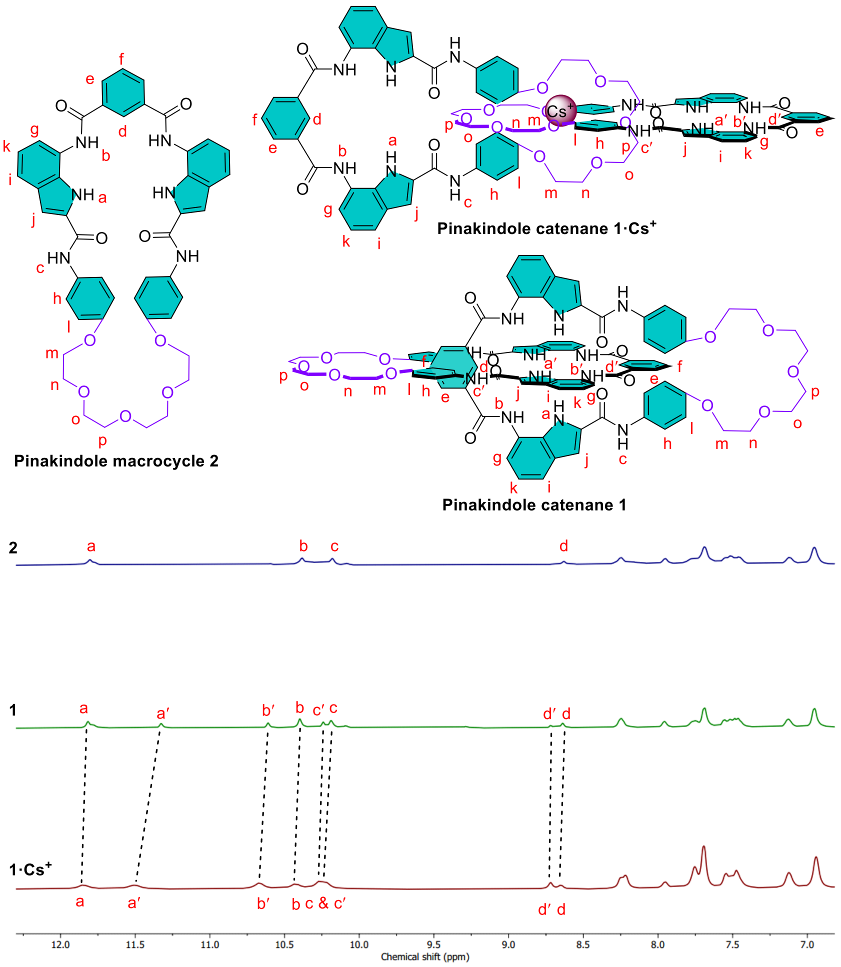

Figure 3.6 Comparison of ^{1}H NMR (600 MHz) spectrum of **Pinakindole catenane 1·Cs$^+$, 1, and macrocycle 2** in DMSO-*d$_6$* solvent at 25 °C with 2μM concentration.

3.4.5. Concentration-dependent NMR experiment

To investigate the self-assembly property of the **Pinakindole catenane 1**, a concentration-dependent ^{1}H NMR was taken in $CDCl_3$ solvent at 25 °C. If the **Pinakindole catenane 1** can assemble through the formation of the π- π stacking interaction by the formation of the intermolecular H-bonding, then the respective peak positions are expected to be shifted with an increase in the concentration of the **Pinakindole catenane 1**.

During the experiment, no significant change in the position of the peak was observed with an increase in the concentration of the **Pinakindole catenane 1**, validating that our catenane is unable to form any self-assembled structure by the formation of intermolecular H-bonding.

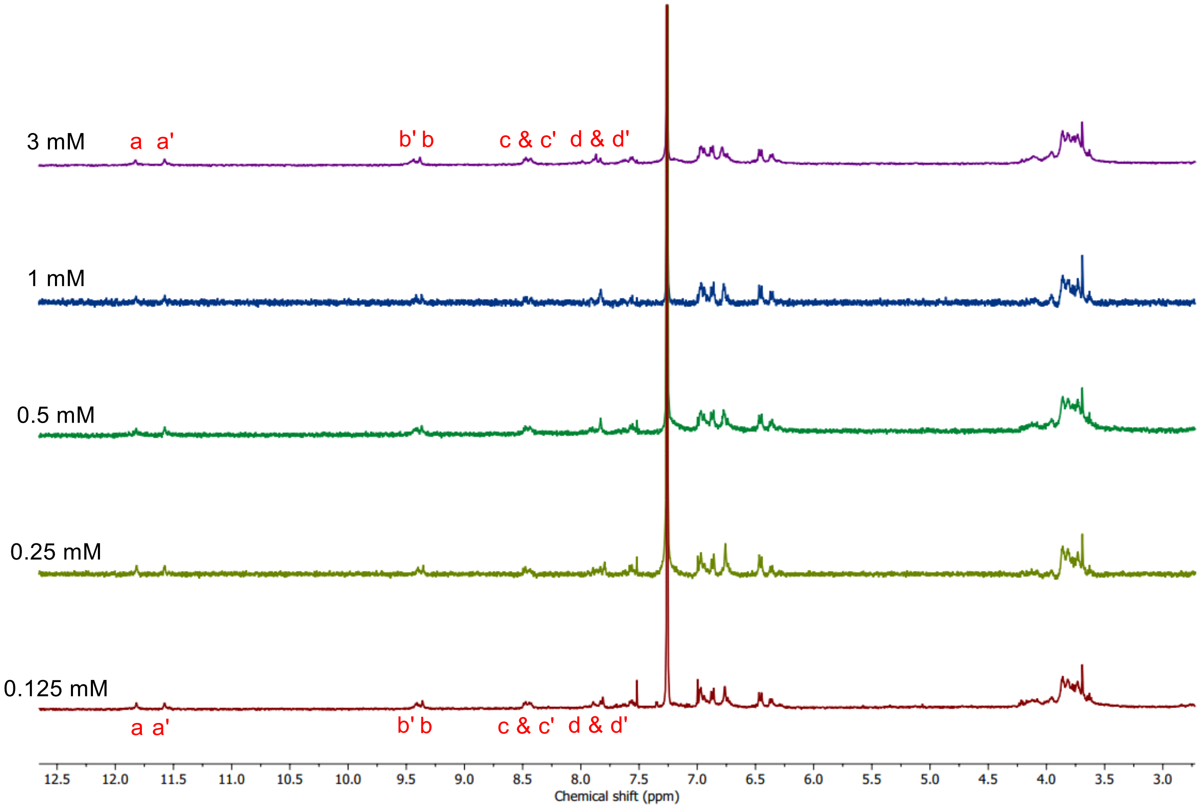

Figure 3.7 Concentration-dependent ^{1}H NMR of **Pinakindole catenane 1** in $CDCl_3$ solvent at 25 °C.

3.4.6. Temperature-dependent ^{1}H NMR experiment[20]

To envisage the role of H-bonding as a stabilization of the interlocked structure of the **Pinakindole catenane 1**, a 2 mM solution of the **Pinakindole catenane 1** was prepared by dissolving it in $C_2D_2Cl_4$ solvent in an NMR tube and ^{1}H NMR was recorded at different temperature.

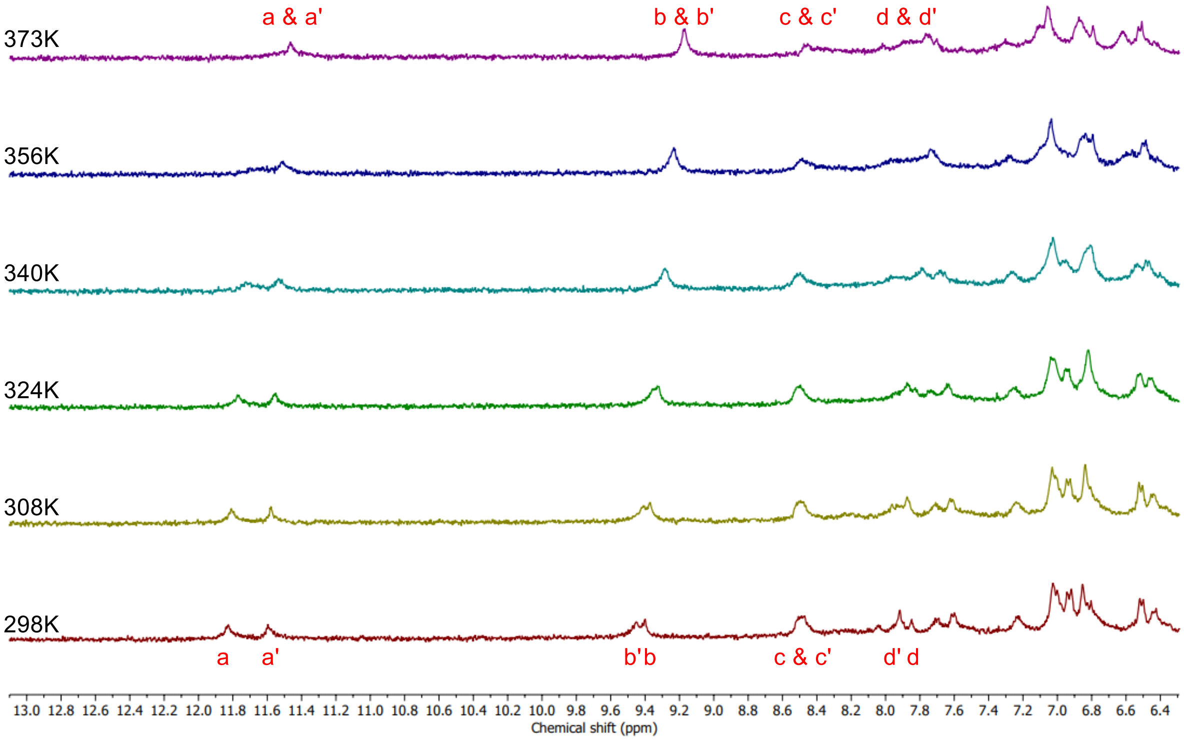

Figure 3.8 Temperature-dependent ^{1}H NMR of **Pinakindole catenane 1** in $C_2D_2Cl_4$ solvent.

A significant upfield shift of the a, a', b, b', c, c', d, and d' peaks were observed with an increase in the temperature. At elevated temperatures, (a and a'), (b and b'), (c and c'), and (d, d') merge into a single peak. This data confirmed that H-bonding stabilized in the interlock structure, which breaks at the elevated temperature and, therefore, individual identity of (a and a'); (b and b'); (c and c'); (d, d') diminished.

3.4.7. Membrane colocalization of Pinakindole catenane 1 by IR experiment[21]

A. Preparation of vesicles: In a clean and dry round-bottomed flask (10 mL), 12.5 mg of EYPC lipid was taken. It was hydrated with HEPES buffer (10 mM HEPES, pH 7.0) solution, and the mixture was vortexed 4-5 times over a period of 1 h. Then, the hydrated vesicle suspension was subjected to 23 freeze-thaw cycles (liquid nitrogen and 55 °C temperature water bath), and extrusions were done 23 times (must be an odd number) using a 200 nm polycarbonate membrane at 25 °C. The extruded vesicle suspension was then collected and used for the IR sample preparation.

B. Sample preparation for IR experiment: A stock solution (20 μL in DMSO) of **Pinakindole catenane 1** was added (5 mol% with respect to the lipid) to the vesicle suspension to prepare channel-incorporated vesicles. The vesicle solution was then subjected to centrifuge with 10000 rpm rotational speed for 1 h at 25 °C. The upper buffer layer was removed, and the process was repeated three times using HEPES buffer as washing solvent (10 mM HEPES, pH 7.0) to remove the unincorporated **Pinakindole catenane 1**. The resulting compound incorporated lipid membrane was collected from the bottom of the centrifuge tube. It was then dried under a high vacuum and used for IR spectroscopic studies.

C. IR experiment: The IR spectra were recorded for the channel-forming molecule **Pinakindole catenane 1**, only the lipid membrane, and the lipid membrane with incorporated channel-forming molecule **Pinakindole catenane 1**. All data were compared to understand the insertion of the channel-forming molecule **Pinakindole catenane 1** in the bilayer membrane. Interestingly, the peaks corresponding to **Pinakindole catenane 1** were noticed in the IR spectra of the **Pinakindole catenane 1**-incorporated lipid membrane. Additionally, the broadening and shifting of the indole N-H peak (3294 cm^{-1} to 3268 cm^{-1}) as well as C=O peaks (1740 cm^{-1} to 1738 cm^{-1} and 1631 cm^{-1} to 1660 cm^{-1}) confirming the colocalization of the **Pinakindole catenane 1** in the lipid bilayer membrane.

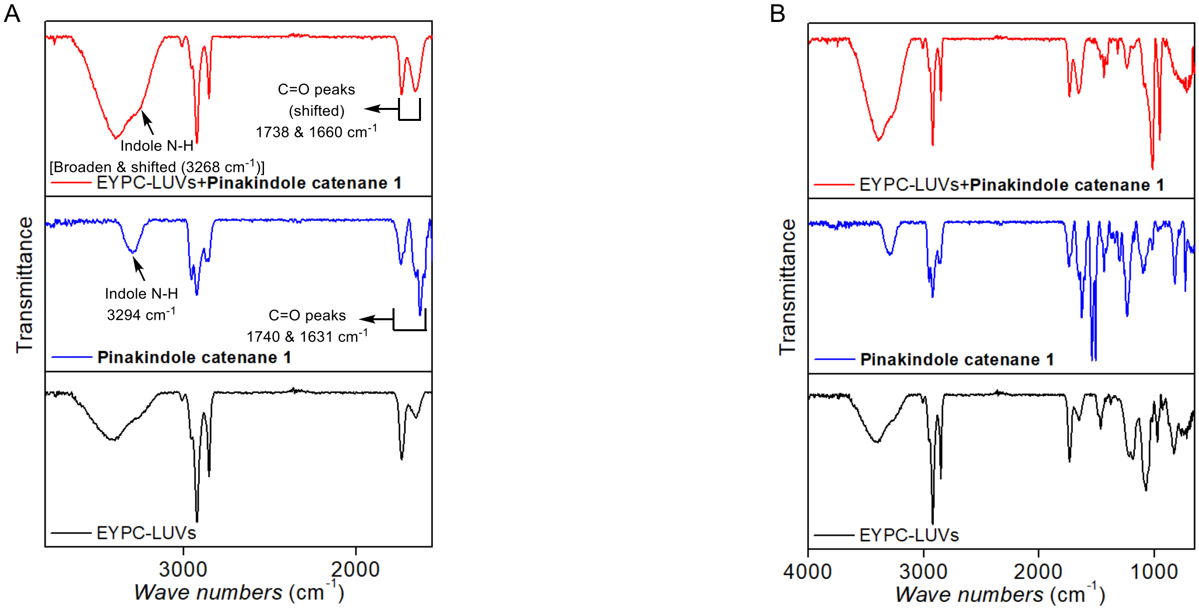

Figure 3.9 Zoom (A) and full (B) IR spectra of the **Pinakindole catenane 1**, EYPC-lipid vesicles, and **Pinakindole catenane 1** incorporated EYPC-lipid vesicles (5 mol% with respect to lipid) at 25 °C.

3.4.8. Conformational orientation of the Pinakindole catenane 1 in the presence of salt

The change in the conformational orientation of **Pinakindole catenane 1** was investigated by using NOESY and DOSY spectra. A 2 mM stock solution of **Pinakindole catenane 1** was prepared in DMSO-d_6 solvent in an NMR tube. Both NOESY and DOSY spectra were recorded before the addition of any salt. A 1 equiv of TBACl and 1 equiv $NaPF_6$ salts were added into the NMR tube sequentially. After each addition of the salt, NOESY and DOSY spectra were recorded. Interestingly, we noticed a change in the NOESY spectra after the addition of the 1 equiv of TBACl salt, conforming to the reorientation of **Pinakindole catenane 1** from **conf-II** to **conf-III** for effective binding with the Cl^- ion the anion binding cavity. Whereas DOSY spectra show the two signals, confirming the presence of both free catenane **1** and the [**1**+Cl⁻] complex. Moreover, further addition of the 1 equiv of $NaPF_6$ into it does not further change in the NOESY spectra, indicating that no further conformational change is happening upon the addition of the $NaPF_6$ salt. Noteworthy, in DOSY NMR only one signal was observed validating all of the free catenane convert to the [**1**+NaCl] complex.

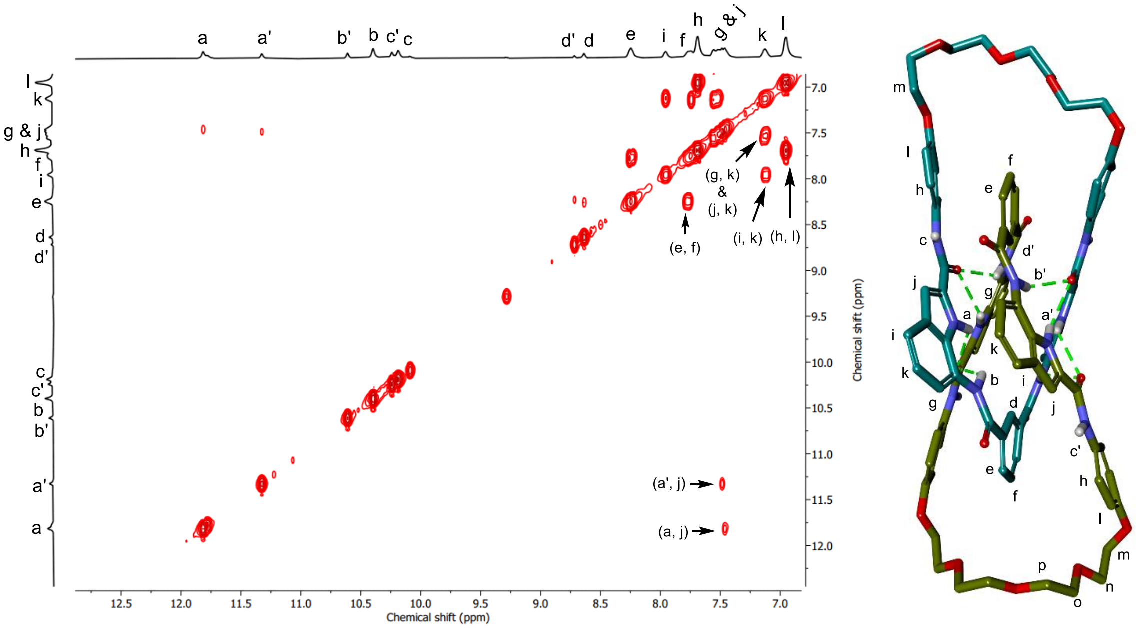

Figure 3.10 ^1H-^1H COSY NMR (600 MHz) spectrum of **Pinakindole catenane 1** (2 mM) in DMSO-d_6 solvent at 25 °C.

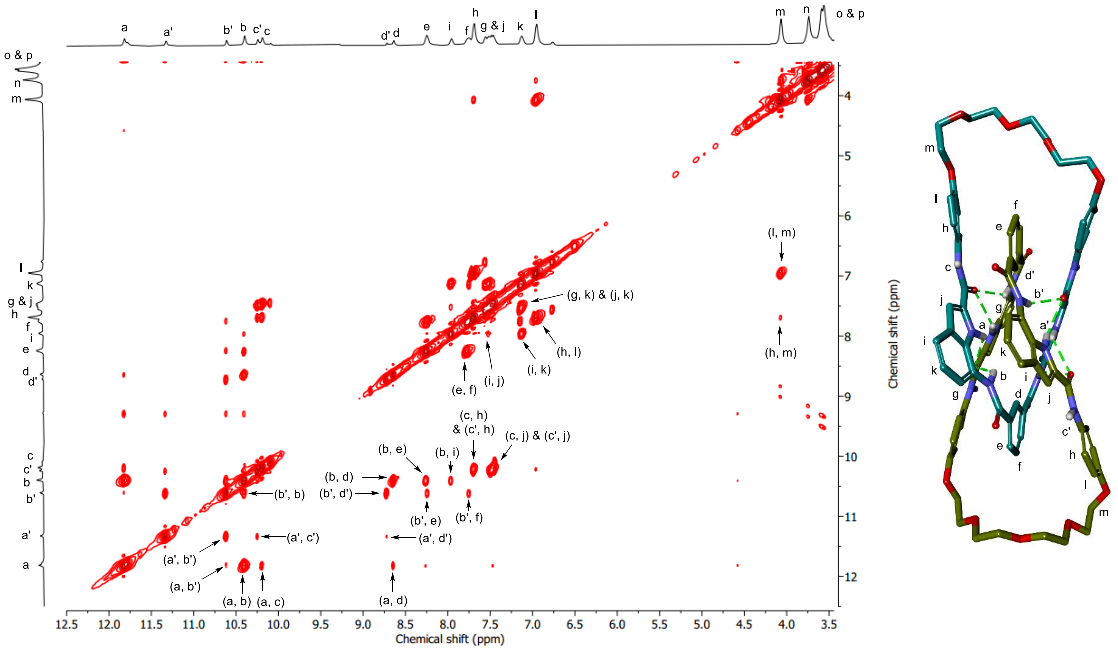

Figure 3.11 ^1H-^1H NOESY NMR (600 MHz) spectrum of **Pinakindole catenane 1** (2 mM) in DMSO-d_6 at 25 °C before the addition of any salt.

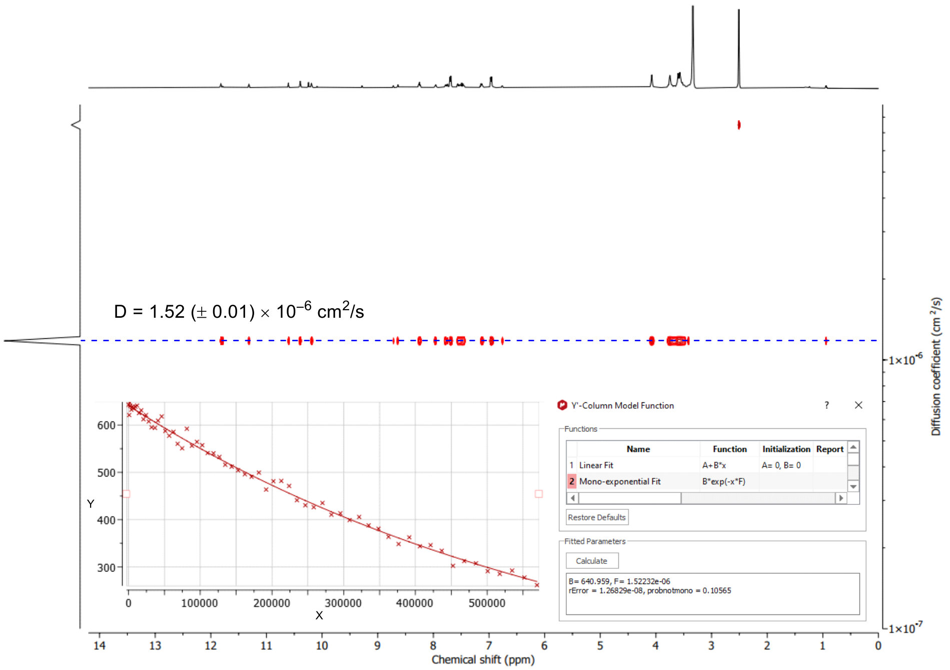

	Name	Function	Initialization	Report
1	Linear Fit	A+B*x	A= 0, B= 0	
2	Mono-exponential Fit	B*exp(-x*F)		

```
B= 640.959, F= 1.52232e-06
rError = 1.26829e-08, probnotmono = 0.10565
```

Figure 3.12 The DOSY NMR spectrum of **Pinakindole catenane 1** (2 mM) in DMSO-d_6 at 25 ºC before the addition of any salt. Two sub-figures in the bottom sections are the screenshots of the processed data. The calculated diffusion coefficient value for this compound in the above-mentioned condition is 1.52 (± 0.01) × 10^{-6} cm^2/s.

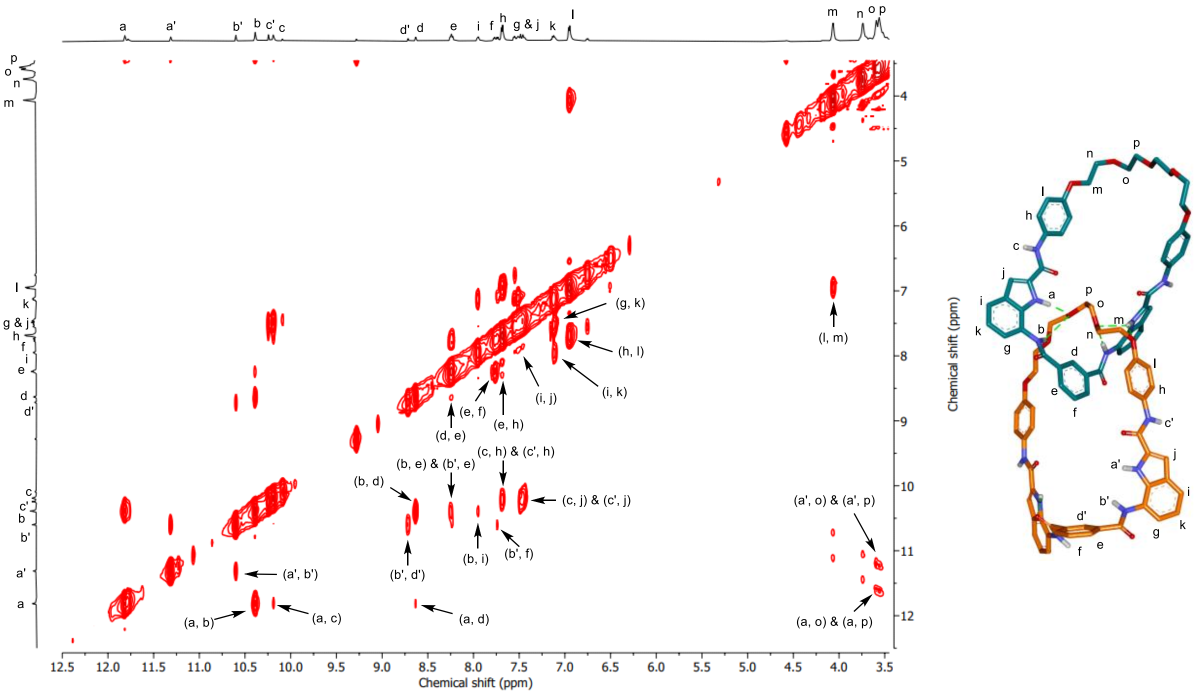

Figure 3.13 ^{1}H-^{1}H NOESY NMR (600 MHz) spectrum of **Pinakindole catenane 1** (2 mM) in DMSO-d_6 solvent at 25 °C after the addition of 1 equiv TBACl salt.

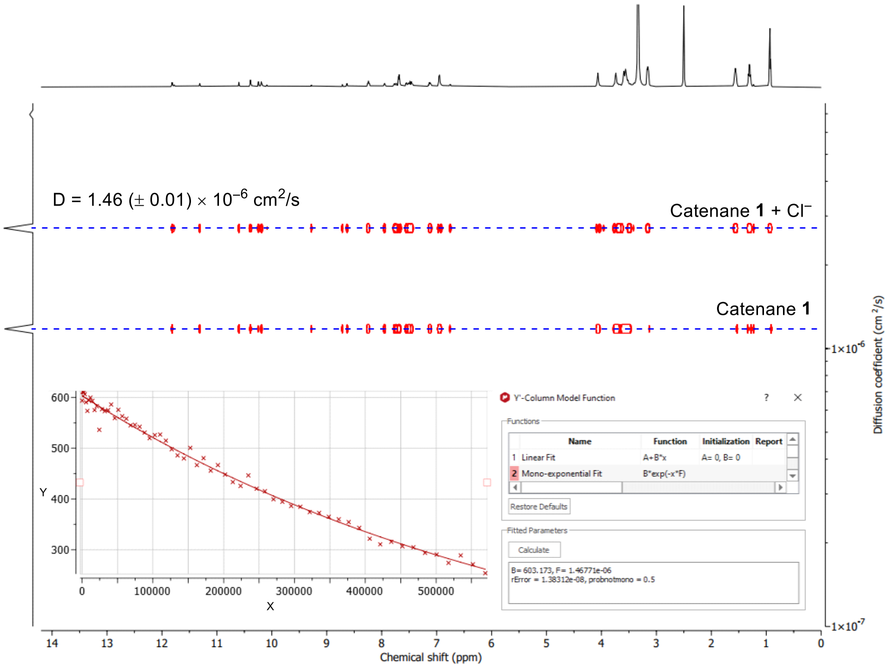

	Name	Function	Initialization	Report
1	Linear Fit	A+B*x	A= 0, B= 0	
2	Mono-exponential Fit	B*exp(-x*F)		

```
B= 603.173, F= 1.46771e-06
rError = 1.38312e-08, probnotmono = 0.5
```

Figure 3.14 The DOSY NMR spectrum of **Pinakindole catenane 1** (2 mM) in DMSO-d_6 at 25 ºC after addition of 1 equiv TBACl salt. Two sub-figures in the bottom sections are the screenshots of the processed data. The calculated diffusion coefficient value for this compound in the above-mentioned condition is 1.46 (± 0.01) × 10^{-6} cm²/s.

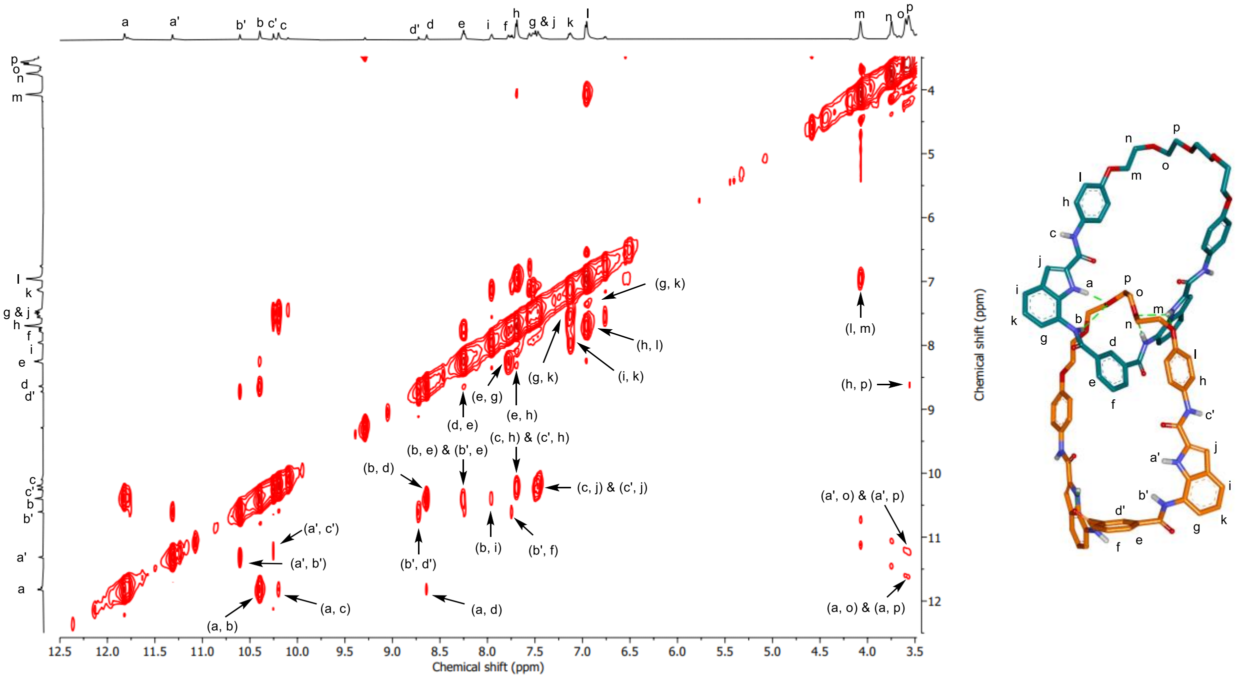

Figure 3.15 ^{1}H-^{1}H NOESY NMR (600 MHz) spectrum of **Pinakindole catenane 1** (2 mM) in DMSO-d_6 solvent at 25 °C after sequential addition of 1 equiv TBACl and 1 equiv NaPF$_6$ salt.

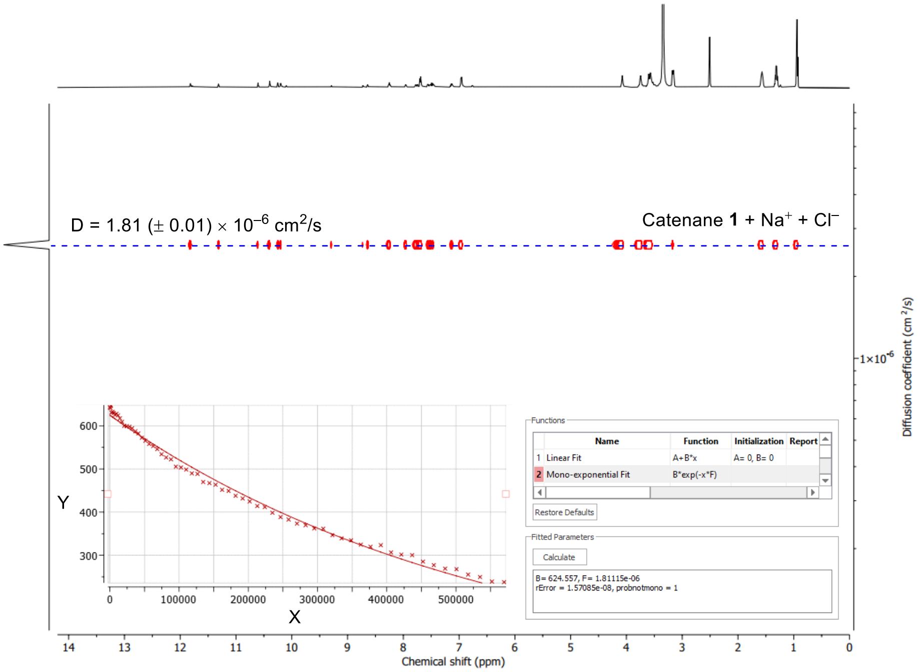

	Name	Function	Initialization	Report
1	Linear Fit	A+B*x	A= 0, B= 0	
2	Mono-exponential Fit	B*exp(-x*F)		

```
B= 624.557, F= 1.81115e-06
rError = 1.57085e-08, probnotmono = 1
```

Figure 3.16 The DOSY NMR spectrum of **Pinakindole catenane 1** (2 mM) in DMSO-d_6 at 25 ºC after sequential addition of 1 equiv TBACl salt and 1 equiv $NaPF_6$ salt. Two sub-figures in the bottom sections are the screenshots of the processed data. The calculated diffusion coefficient value for this compound in the above-mentioned condition is 1.81 (± 0.01) × 10^{-6} cm^2/s.

3.4.9. Ion Transport Studies

3.4.9.1. Ion transporting activity studies across EYPC–LUVs⊃HPTS

Preparation of HEPES buffer and stock solutions: The HEPES buffer (pH = 7.0) was prepared by dissolving an appropriate amount of solid HEPES (10 mM) and NaCl (100 mM) in autoclaved water. The pH was adjusted to 7.0 by the addition of aliquots from the NaOH solution (0.5 M). HPLC grade DMSO was used for the stock solution preparation of all the derivatives.

Preparation of EYPC–LUVs⊃HPTS with NaCl: In a dry and clean round bottom flux (10 mL), 1 mL of egg yolk phosphatidylcholine (EYPC, 25 mg/mL in $CHCl_3$) was dried by purging nitrogen gas with continuous rotation to make a thin transparent film of EYPC. Then to remove a trace amount of $CHCl_{3,}$ it was kept under a high vacuum for 4 h. Further, the dried thin film was hydrated with 1 mL HEPES buffer (1 mM HPTS, 10 mM HEPES, 100 mM NaCl, pH = 7.0), and resulting the suspension was vortexed for 1 h at 10 min intervals. This hydrated suspension was subjected for 23 cycles of freeze–thaw (liquid N_2 and 55 °C hot water bath) followed by extrusion through 100 nm pore size containing polycarbonate membrane for 23 times (must be an odd number), in order to achieve uniform distribution of LUVs of an average 100 nm diameter. Finally, size exclusion chromatography using gel filtration (Sephadex G-50) was carried out to remove the unentrapped extravesicular HPTS dyes with HEPES buffer (10 mM HEPES, 100 mM NaCl, pH = 7.0). Collected vesicles were diluted to 6 mL to get EYPC–LUVs$\supset$HPTS. Final conditions: ~ 5.0 mM EYPC, Inside: 1 mM HPTS, 10 mM HEPES, 100 mM NaCl, pH = 7.0, Outside: 10 mM HEPES, 100 mM NaCl, pH = 7.0.

Ion transport activity by HPTS assay: In clean and well-dry fluorescence cuvette, 1975 µL of HEPES buffer (10 mM HEPES, 100 mM NaCl, pH =7.0) and 25 µL of EYPC–LUVs$\supset$HPTS vesicle was added. The cuvette was placed in slowly stirring condition using a magnetic stirrer equipped in the fluorescence instrument (t = 0 s). The time-dependent HPTS emission intensity was monitored at λ_{em} = 510 nm (λ_{ex} = 450 nm) by creating pH gradient (~ 0.8) between the intra- and extra-vesicular system by the addition of 20 µL NaOH (0.5 M) at t = 20 s. Then different concentrations of channel forming molecules in DMSO were added at t = 100 s. Finally, the vesicles were lysed by the addition of 10% Triton X–100 solutions (25 µL) at t = 300 s for destruction pH gradient.

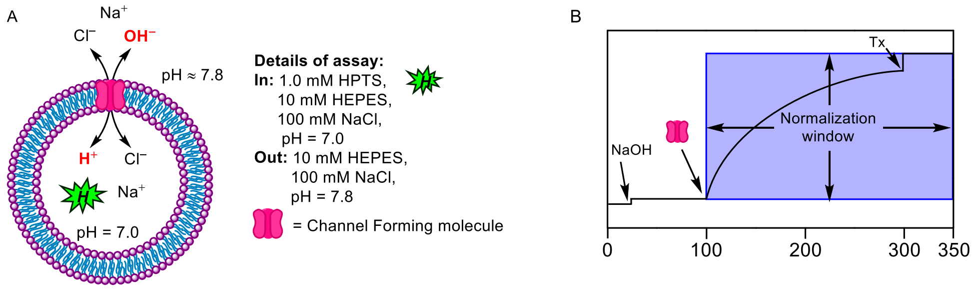

Figure 3.17 Schematic representation of ion transport activity across EYPC–LUVs$\supset$HPTS vesicle (A), and normalization window for same fluorescence kinetics experiment of ion transport (B).

The time axis was normalized according to Equation 1:

$$t = t - 100$$ Equation 1

Where, in normalized data t = 0 s was the timing of compound addition during the experiment, and t = 200 s was the timing of Triton X–100 addition. The time-dependent data were normalized to fractional fluorescence intensity (in percentage) using Equation 2

$$I_F = [(I_t - I_0) / (I_\infty - I_0)] \times 100$$ Equation 2

where, I_0 = Fluorescence intensity just before the channel forming molecule addition (at 0 s), I_∞ = Final fluorescence intensity after addition of Triton X–100, I_t = Fluorescence intensity at time t.

Dose-response activity in EYPC–LUVs$\supset$HPTS: The fluorescence kinetics of each channel-forming molecule at different concentrations was studied over the course of time. The concentration profile data were evaluated at t = 290 s to get effective concentration, EC_{50} (i.e. the concentration of transporter needed to achieve 50% ion efflux activity) using Hill equation (Equation 3):

$$Y = Y_\infty + (Y_0 - Y_\infty) / [1 + (c/EC_{50})^n] \qquad \text{Equation 3}$$

Where, Y_0 = Fluorescence intensity just before the addition of channel forming molecule (at t = 0 s), Y_∞ = Fluorescence intensity with excess compound concentration, c = concentration of channel forming molecule, and n = Hill coefficient (i.e. indicative for the number of monomers needed to form an active supramolecule).

Dose-response activity of compounds 1 and 2 with NaCl salt

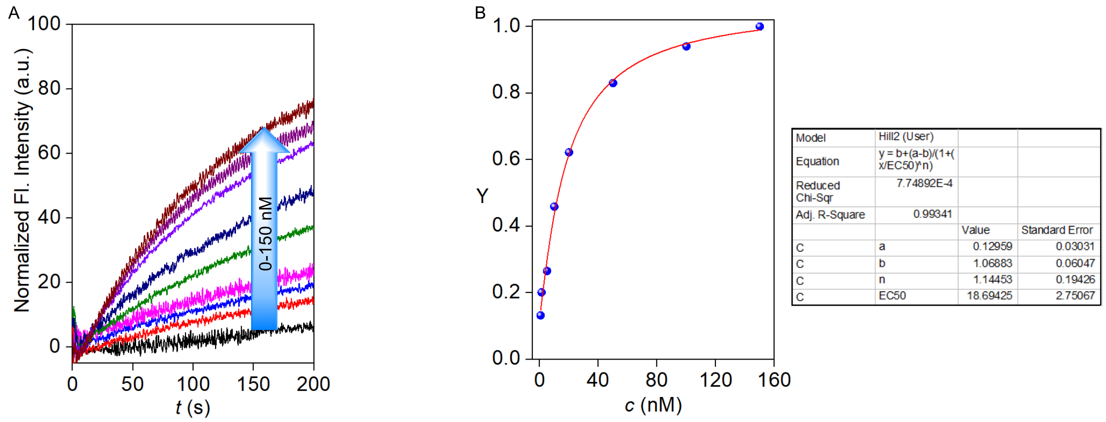

Model	Hill2 (User)		
Equation	y = b+(a-b)/(1+(x/EC50)^n)		
Reduced Chi-Sqr	7.74892E-4		
Adj. R-Square	0.99341		
		Value	Standard Error
C	a	0.12959	0.03031
C	b	1.06883	0.06047
C	n	1.14453	0.19426
C	EC50	18.69425	2.75067

Figure 3.18 Concentration-dependent ion transport activity of **Pinakindole catenane 1** (0–150 nM) with NaCl salt across EYPC–LUVs⊃HPTS (A), and corresponding Hill plot of **Pinakindole catenane 1** at t = 190 s (B).

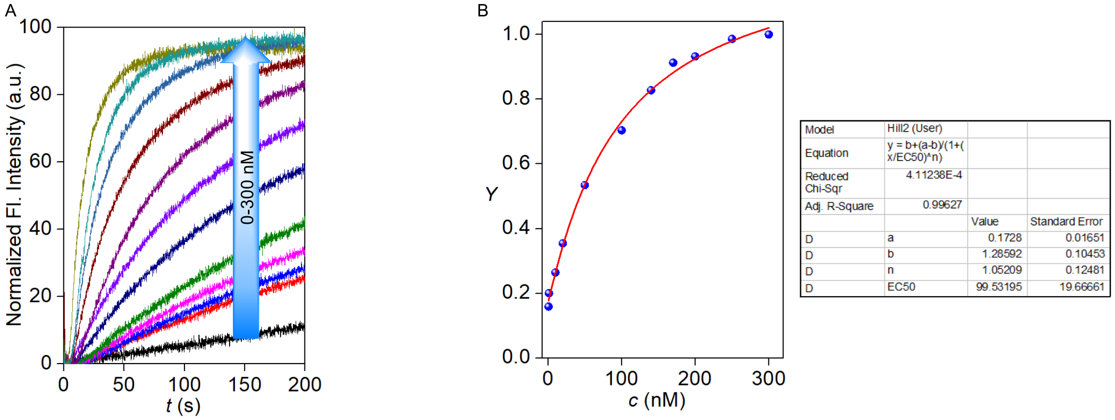

Model	Hill2 (User)		
Equation	y = b+(a-b)/(1+(x/EC50)^n)		
Reduced Chi-Sqr	4.11238E-4		
Adj. R-Square	0.99627		
		Value	Standard Error
D	a	0.1728	0.01651
D	b	1.28592	0.10453
D	n	1.05209	0.12481
D	EC50	99.53195	19.66661

Figure 3.19 Concentration-dependent ion transport activity of **Pinakindole macrocycle 2** (0–300 nM) with NaCl salt across EYPC–LUVs⊃HPTS (A), and corresponding Hill plot of **Pinakindole macrocycle 2** at t = 190 s (B).

3.4.9.2. Ion selectivity studies across EYPC–LUVs⊃HPTS

Buffer and stock solution preparation: HEPES buffer was prepared by dissolving an appropriate amount of solid HEPES and a salt (either of NaF, NaCl, NaBr, NaSCN, NaOAc, $NaClO_4$, LiCl, KCl, RbCl, and CsCl) in autoclaved water to get 10 mM HEPES and 100 mM salt respectively. Subsequently, the pH was adjusted to 7.0 by the addition of 0.5 M NaOH solution. The stock solution of **Pinakindole catenane 1** was prepared in HPLC grade DMSO solution for the studies.

Preparation of EYPC–LUVs⊃HPTS for anion selectivity: The vesicles were prepared by the following same protocol as described above. Final Condition: EYPC–LUVs⊃HPTS (~ 5.0 mM EYPC), Inside: 1 mM HPTS, 10 mM HEPES, 100 mM NaCl, pH = 7.0 and Outside: 10 mM HEPES, 100 mM 100 mM NaX, pH = 7.0 (where, $X^- = F^-$, Cl^-, Br^-, SCN^-, OAc^-, ClO_4^-).

Anion selectivity assay: In a clean fluorescence cuvette, 1975 μL of HEPES buffer (10 mM HEPES, 100 mM NaX, at pH = 7.0 (where, $X^- = F^-$, Cl^-, Br^-, SCN^-, OAc^-, ClO_4^-) was added, followed by addition of 25 μL of EYPC–LUVs⊃HPTS vesicle in slowly stirring condition by a magnetic stirrer equipped with the fluorescence instrument (at $t = 0$ s). The time-dependent HPTS emission intensity was monitored at λ_{em} = 510 nm (λ_{ex} = 450 nm) by creating a pH gradient (~ 0.8) between intra- and extra-vesicular system by the addition of 20 μL NaOH (0.5 M) at $t = 20$ s. The channel-forming molecule **Pinakindole catenane 1** was added at $t = 100$ s, and at $t = 300$ s, 25 μL of 10% Triton X–100 was added to lyze all vesicles for the complete destruction of the pH gradient. For data analysis and comparison, time (X-axis) was normalized between the point of addition of channel forming molecule (i.e., $t = 100$ s was normalized to $t = 0$ s) and the endpoint of the experiment (i.e., $t = 300$ s was normalized to $t = 200$ s) using Equation 1. Fluorescence intensities (I_t) were normalized to fractional emission intensity I_F using Equation 2.

Preparation of EYPC–LUVs⊃HPTS for cation selectivity: Similarly, the cation selectivity of **Pinakindole catenane 1** was explored by changing the extravesicular HEPES buffer solution (10 mM HEPES, 100 mM MCl, pH = 7.0) of MCl salts ($M^+ = Li^+$, Na^+, K^+, Rb^+, and Cs^+). For data analysis and comparison, time (X-axis) was normalized between the point of addition of channel forming molecule (i.e., $t = 100$ s was normalized to $t = 0$ s) and the end point of the experiment (i.e., $t = 300$ s was normalized to $t = 200$ s) using Equation 1. Fluorescence intensities (I_t) were normalized to fractional emission intensity I_F using Equation 2.

Cation selectivity assay: In a clean fluorescence cuvette, 1975 μL of HEPES buffer (10 mM HEPES, 100 mM MCl, at pH = 7.0; where, $M^+ = Li^+$, Na^+, K^+, Rb^+, and Cs^+) was added, followed by addition of 25 μL of EYPC–LUVs⊃HPTS vesicle in slowly stirring condition by a magnetic stirrer equipped with the fluorescence instrument (at $t = 0$ s). The time-dependent HPTS emission intensity was monitored at λ_{em} = 510 nm (λ_{ex} = 450 nm) by creating a pH gradient (~ 0.8) between the intra- and extra-vesicular system by the addition of 20 μL NaOH (0.5 M) at $t = 20$ s. The channel forming molecule **Pinakindole catenane 1** was added at $t = 100$ s, and at $t = 300$ s, 25 μL of 10% Triton X–100 was added to lyze all vesicles for the complete destruction of the pH gradient. For data analysis and comparison, time (X-axis) was normalized between the point of addition of channel forming molecule (i.e., $t = 100$ s was normalized to $t = 0$ s) and the endpoint of the experiment (i.e., $t = 300$ s was normalized to $t = 200$ s) using Equation 1. Fluorescence intensities (I_t) were normalized to fractional emission intensity I_F using Equation 2.

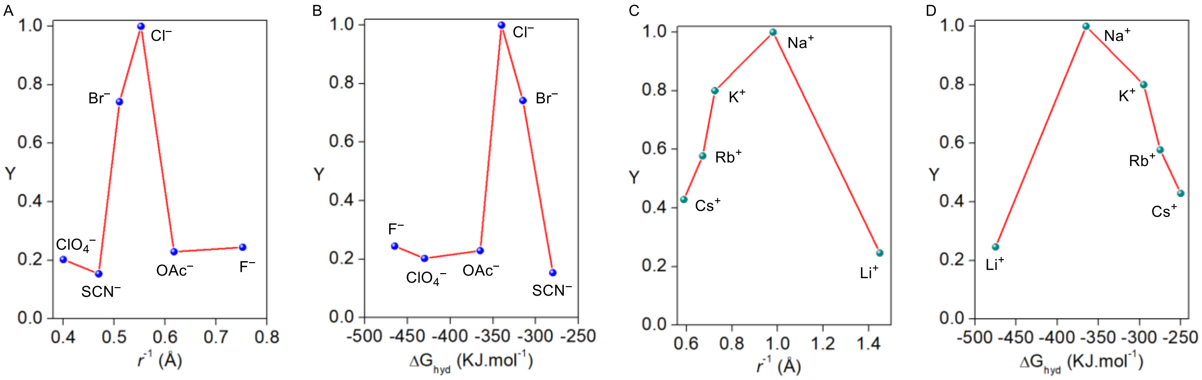

Figure 3.20 Fractional activity *Y* (relative to Cl⁻) as a function of the reciprocal anion radius (A); fractional activity *Y* (relative to Cl⁻) as a function of the anion hydration energy (B); fractional activity *Y* (relative to Na⁺) as a function of the reciprocal cation radius (C); and fractional activity *Y* (relative to Na⁺) as a function of the cation hydration energy (D).

3.4.9.3. Chloride transport activity across EYPC–LUVs⊃lucigenin vesicles

Buffer and stock solution preparation: HEPES buffer was prepared by dissolving an appropriate amount of solid HEPES and a $NaNO_3$ salt in autoclaved water to get 10 mM HEPES and 200 mM $NaNO_3$ salt, respectively. Subsequently, the pH was adjusted to 7.0 by adding 0.5 M NaOH solution. The stock solution of **Pinakindole catenane 1** was prepared using HPLC grade DMF solution for the studies.

Preparation of EYPC–LUVs⊃lucigenin: In a clean and dry small (10 mL) round bottom flask, 1 mL egg yolk phosphatidylcholine (EYPC, 25 mg/mL stock in $CHCl_3$) was added. The solution was dried by purging nitrogen with continuous rotation to form a thin transparent film of EYPC. The transparent film was kept in a high vacuum for 4 h to remove all traces of $CHCl_3$ at room temperature. The resulting film was hydrated with 1 mL buffer solution (1 mM lucigenin, 10 mM HEPES, and 200 mM $NaNO_3$, pH = 7.0), and the resulting suspension was vortexed at 10 min intervals for 1 h. This hydrated suspension was subjected to 21 cycles of freeze-thaw (liquid N_2, 55 °C) followed by extrusion through 200 nm pore size containing polycarbonate membrane for 21 times (must be an odd number), in order to achieve the vesicles of an average 200 nm diameter. Extravesicular dyes were removed by gel filtration (using Sephadex G-50) with buffer solution (10 mM HEPES and 200 mM $NaNO_3$, pH = 7.0), and diluted to 4 mL to get EYPC–LUVs⊃lucigenin. Final conditions: ~ 5 mM EYPC; Inside: 1 mM lucigenin, 10 mM HEPES, 200 mM $NaNO_3$, pH = 7.0; Outside: 10 mM HEPES, 200 mM $NaNO_3$, pH = 7.0.

Dose dependent Cl⁻ transport by lucigenin assay: In clean and dry fluorescence cuvette, 1975 µL of buffer solution (10 mM HEPES, 200 mM $NaNO_3$ and pH = 7.0) and 25 µL EYPC–LUVs⊃lucigenin were taken. This suspension was placed in a slowly stirring condition in the fluorescence instrument equipped with a magnetic stirrer (at t = 0 s). The fluorescence intensity of lucigenin was monitored at λ_{em} = 535 nm

(λ_{ex} = 455 nm) as a course of time. The chloride gradient was created by the addition of 2.0 M NaCl (33.3 μL) at t = 20 s between intra and extravesicular system, followed by addition of channel forming molecule **Pinakindole catenane 1** at t = 100 s. Finally, vesicles were lysed by the addition of 10% Triton X–100 (25 μL) at t = 300 s for the complete destruction of the chloride gradient.

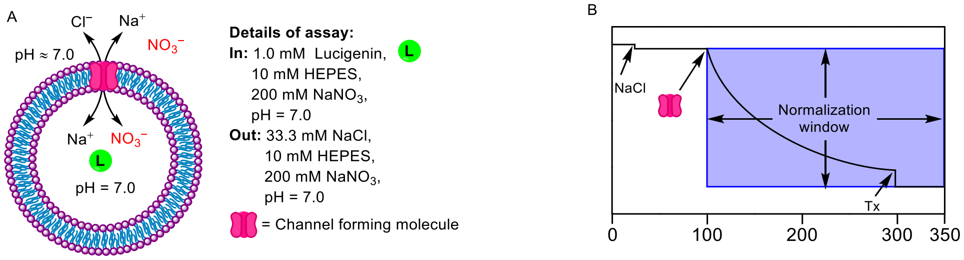

Figure 3.21 Schematic representation of ion transport activity across EYPC–LUVs⊃lucigenin vesicle (A), and normalization window for same fluorescence kinetics experiment of ion transport (B).

The time-dependent data were normalized to fractional (in percentage) fluorescence intensity using Equation 4:

$$I_F = [(I_t - I_0) / (I_\infty - I_0)] \times (-100) \qquad \text{Equation 4}$$

Where, I_0 = Fluorescence intensity just before the channel forming molecule addition (at 0 s). I_∞ = Final fluorescence intensity after the addition of Triton X–100. I_t = Fluorescence intensity at time t.

For data analysis and comparison, time (X–axis) was normalized between the point of compound addition (i.e., t = 100 s was normalized to t = 0 s) and the endpoint of the experiment (i.e., t = 300 s was normalized to t = 200 s).

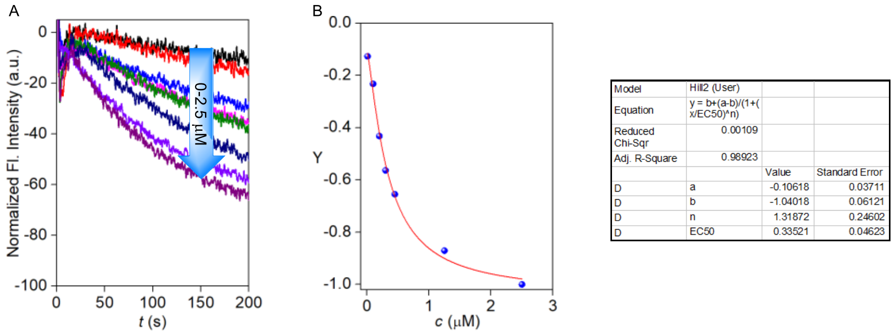

Model	Hill2 (User)		
Equation	y = b+(a-b)/(1+(x/EC50)^n)		
Reduced Chi-Sqr	0.00109		
Adj. R-Square	0.98923		
		Value	Standard Error
D	a	-0.10618	0.03711
D	b	-1.04018	0.06121
D	n	1.31872	0.24602
D	EC50	0.33521	0.04623

Figure 3.22 Concentration-dependent chloride influx study across EYPC–LUVs⊃lucigenin with **Pinakindole catenane 1** (A), and corresponding Hill plot of **Pinakindole catenane 1** at t = 190 s (B).

Cation selectivity assay across EYPC–LUVs⊃lucigenin vesicles: The vesicles were prepared by following the same procedure as discussed above.

Details of the assay: In a clean and dry fluorescence cuvette, 1975 μL of buffer solution (10 mM HEPES, 200 mM $NaNO_3$, and pH = 7.0) and 25 μL EYPC–LUVs⊃lucigenin were taken. The suspension was kept in a slow stirring condition in the fluorescence instrument equipped with a magnetic stirrer at *t* = 0 s. The quenching of fluorescence intensity of lucigenin was monitored as a course of time at λ_{em} = 535 nm (λ_{ex} = 455 nm). At *t* = 20 s, the chloride gradient was created by the addition of 2 M chloride salts (33.3 µL) of different cations MCl (M^+ = Li^+, Na^+, K^+, Rb^+, and Cs^+), followed by the addition of channel forming molecule **Pinakindole catenane 1** at *t* = 100 s. Finally, vesicles were lysed by adding 10% Triton X–100 (25 µL) at *t* = 300 s to completely disrupt the applied chloride gradient. The time-dependent data were normalized to fractional (in percentage) fluorescence intensity using Equation 4.

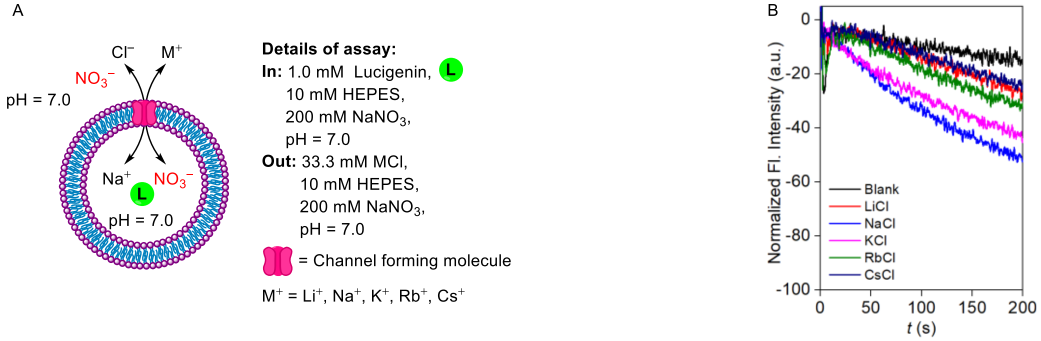

Figure 3.23 Schematic representation of cation selectivity assay across EYPC–LUVs⊃lucigenin (A), Cation selectivity of channel forming molecule **Pinakindole catenane 1** (450 nM) by varying extravesicular cations (B).

3.4.9.4. Mechanistic study of ion transport across EYPC–LUVs⊃Lucigenin

Cl^- transport by Lucigenin assay in the presence of Valinomycin: In clean and dry fluorescence cuvette 1975 µL of buffer solution (10 mM HEPES, 200 mM $NaNO_3$ and pH = 7.0) and 25 µL EYPC–LUVs⊃lucigenin were taken and slowly stirred in fluorescence instrument equipped with a magnetic stirrer (at *t* = 0 s). The time-dependent fluorescence intensity of lucigenin was monitored at λ_{em} = 535 nm (λ_{ex} = 455 nm). A solution of 2 M KCl (33.3 µL) was added at *t* = 20 s to create a chloride gradient between the intra- and extra-vesicular system, followed by the addition of valinomycin (0.5 µM) at *t* = 50 s and channel forming molecule **Pinakindole catenane 1** (450 nM) at *t* = 100 s. Finally, the disruption of chloride gradient was achived by the addition of 10% Triton X–100 (25 µL) at *t* = 300 s. The time-dependent data were normalized to fractional (in percentage) fluorescence intensity using Equation 4.

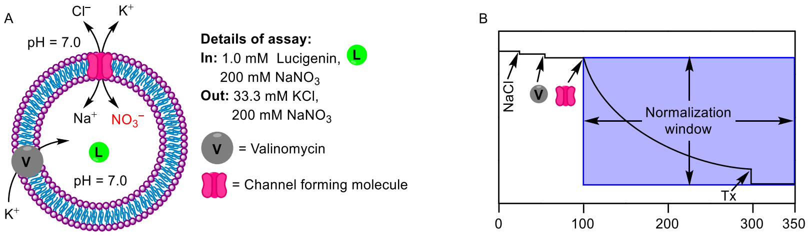

Figure 3.24 Schematic representation of valinomycin assay across EYPC–LUVs⊃lucigenin (A), and normalization window for same fluorescence kinetics experiment of ion transport (B).

NO_3^-/SO_4^{2-} assay

Buffer and stock solution preparation: HEPES buffer was prepared by dissolving an appropriate amount of solid HEPES and NaCl salt in autoclaved water to get 10 mM HEPES and 200 mM NaCl salt, respectively. Subsequently, the pH was adjusted to 7.0 by adding 0.5 M NaOH solution. Similarly, iso-osmolar $NaNO_3$ buffer (10 mM HEPES and 200 mM $NaNO_3$, pH = 7.0) and Na_2SO_4 (10 mM HEPES and 66.6 mM Na_2SO_4, pH = 7.0) buffer solution were prepared. The stock solution of **Pinakindole catenane 1** was prepared using HPLC grade DMF solution for the studies.

Preparation of EYPC–LUVs⊃lucigenin: Lucigenin vesicles were prepared by following the same protocol as mentioned above. Final conditions: ~ 5 mM EYPC; Inside: 1 mM lucigenin, 10 mM HEPES, 200 mM NaCl, pH = 7.0; Outside: 10 mM HEPES, 200 mM NaCl, pH = 7.0.

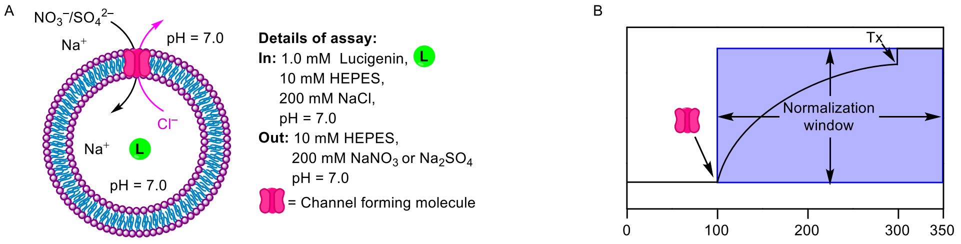

Figure 3.25 Schematic representation of NO_3^-/SO_4^{2-} assay across EYPC–LUVs⊃lucigenin (A), and normalization window for same fluorescence kinetics experiment of ion transport (B).

Details of the assay: In clean and dry fluorescence cuvette 1950 μL of buffer solution (either 10 mM HEPES, 200 mM $NaNO_3$ and pH = 7.0 or 10 mM HEPES, 66.6 mM Na_2SO_4 and pH = 7.0) and 50 μL EYPC–LUVs⊃lucigenin were taken and slowly stirred in fluorescence instrument equipped with a magnetic stirrer (at $t = 0$ s). Channel-forming molecule **Pinakindole catenane 1** (20 μM) was added at $t = 100$ s. The time-dependent fluorescence intensity of lucigenin was monitored at $\lambda_{em} = 535$ nm ($\lambda_{ex} = 455$ nm). Finally, the destruction of the chloride gradient was done by the addition of 10% Triton X–100 (25 μL) at $t = 300$ s. The time-dependent data were normalized to fractional (in percentage) fluorescence intensity using Equation 2.

3.4.9.5. Evaluation of membrane stability and channel nature by CF assay

Preparation of EYPC-LUVs⊃CF vesicles: In a clean and dry small (10 mL) round bottom flask, 0.5 mL egg yolk phosphatidylcholine (EYPC, 25 mg/mL stock in $CHCl_3$) was added. A thin lipid film was prepared by evaporating a solution of EYPC lipid by purging the N_2 flow and keeping it for the high vacuum for 4 h to remove a trace amount of $CHCl_3$. After that lipid film was hydrated with 0.5 mL buffer (10 mM HEPES, 10 mM NaCl, 50 mM CF, pH 7.0) for 1 h with occasional vortexing of 4-5 times and then subjected to freeze-thaw cycle (≥ 20 times). The vesicle solution was extruded through a polycarbonate membrane with

200 nm pores 23 times (has to be an odd number. The extracellular dye was removed size exclusion chromatography (Sephadex G-50) with HEPES buffer (10 mM HEPES, 100 mM NaCl, pH 7.0). Final concentration: ~ 2.5 mM EYPC lipid; intravesicular solution: 10 mM HEPES, 10 mM NaCl, 50 mM CF, pH 7.0; extravesicular solution: 10 mM HEPES, 100 mM NaCl, pH 7.0.

CF assay details: In clean and dry fluorescence cuvette, 1950 μL of HEPES buffer solution (10 mM HEPES, 100 mM NaCl, pH 7.0) and 50 μL EYPC–LUVs⊃CF were taken. The suspension was kept in a slow stirring condition in the fluorescence instrument equipped with a magnetic stirrer at t = 0 s. The fluorescence intensity was monitored as a course of time at λ_{em} = 517 nm (λ_{ex} = 492 nm). At t = 100 s channel forming molecule **Pinakindole catenane 1** was added to it at different concentrations. Finally, vesicles were lysed by the addition of 10% Triton X–100 (25 μL) at t = 300 s for 100% efflux of CF dyes. The time-dependent data were normalized to fractional (in percentage) fluorescence intensity using Equation 2 and time axis (X–axis) was normalized using Equation Equation 1.

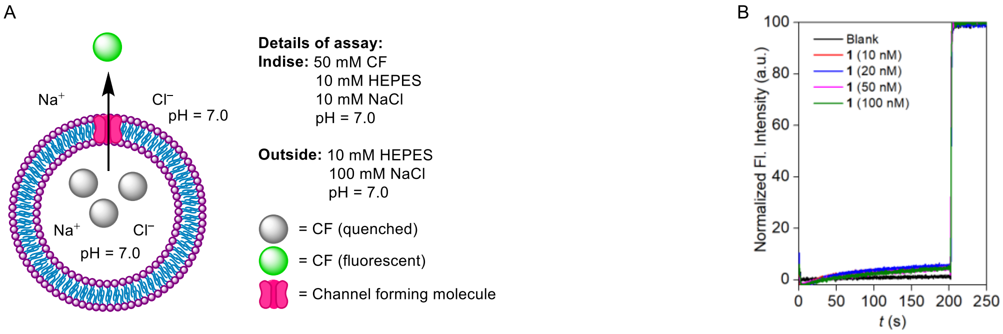

Figure 3.26 Schematic representation of CF assay across EYPC–LUVs⊃CF (A), and fluorescence kinetics experiment of channel forming compound **Pinakindole catenane 1** at different concentrations (B).

3.4.9.6. Evaluation of mode of ion transport by cholesterol assay

Buffer and stock solution preparation: HEPES buffer was prepared by dissolving appropriate amount of solid HEPES and a NaCl salt in autoclaved water to get 10 mM HEPES and 100 mM NaCl, respectively. Subsequently, the pH was adjusted to 7.0 by addition of 0.5 M NaOH solution. Stock solution of **Pinakindole catenane 1** was prepared in HPLC grade DMSO solution for the studies.

Preparation of vesicles: Both EYPC–LUVs⊃HPTS and 10 mol% cholesterol based EYPC–LUVs⊃HPTS was prepared by following the above mentioned method.[15]

Details of the assay: In clean and well dry fluorescence cuvette, 1975 μL of HEPES buffer (10 mM HEPES, 100 mM NaCl, pH =7.0) and 25 μL of with or without cholesterol (10 mol%) based EYPC–LUVs⊃HPTS vesicle was added. The cuvette was placed in a slowly stirring condition using a magnetic stirrer equipped in the fluorescence instrument (t = 0 s). The time-dependent HPTS emission intensity was monitored at λ_{em} = 510 nm (λ_{ex} = 450 nm) by creating pH gradient (~ 0.8) between intra- and extra-vesicular system by the addition of 20 µL NaOH (0.5 M) at *t* = 20 s. **Pinakindole catenane 1** was added at *t* = 100 s. Finally, the vesicles were lysed by the addition of 10% Triton X–100 solutions (25 µL) at *t* = 300 s for destruction pH gradient.

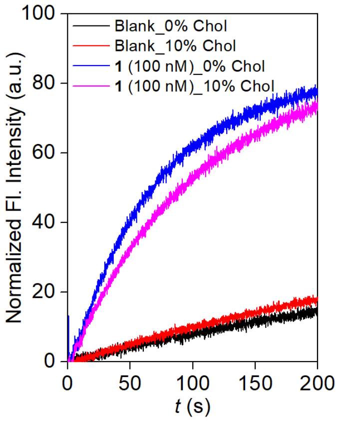

Figure 3.27 Fluorescence kinetics experiment of the channel-forming compound **Pinakindole catenane 1**.

Experimental data revealed that decreasing membrane fluidity due to the presence of the cholesterol did not change the significant ion transport activity of **Pinakindole catenane 1**. This data indicated that the ion transport process primarily occurred through channel formation.

3.4.10. Planar Bilayer Conductance Measurements

Diphytanoylphosphatidylcholine (Avanti Polar Lipids), dissolved in n-decane (20 mg/mL) was used to form a Bilayer lipid membrane (BLM) across an aperture of 150 µM diameter in a polystyrene cup (Warner Instrument, USA). Both cis and trans chambers were filled with symmetrical unbuffered 1 M KCl solution. The cis chamber was connected to the BC 535 head-stage (Warner Instrument, USA) by an Ag-AgCl electrode, and the trans chamber was held at virtual ground. **Pinakindole catenane 1** (4 µM, stock solution prepared in DMSO) was added to the cis chamber, and the solution was stirred with a magnetic stirrer for 10 min. The addition of **Pinakindole catenane 1** rapidly triggered the current flow with open-close transition events at different holding potentials, confirming the formation of ion channels inside the bilayer membrane. Currents were low pass filtered at 1 kHz using pClamp9 software (Molecular Probes, USA) and an analog-to-digital converter (Digidata 1440, Molecular Probes). All data were analyzed by the software pClamp 10.7.

The average current was calculated from the trace, and then conductance and other calculations were made accordingly.

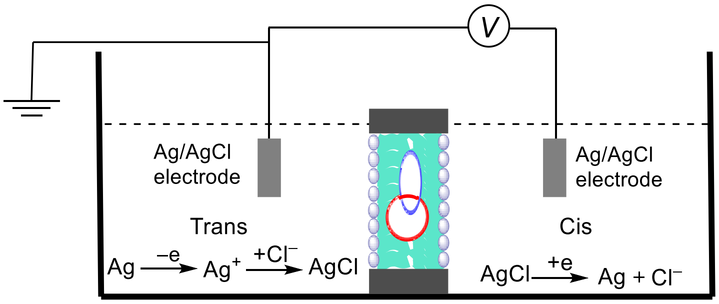

Figure 3.28 Systematic representation of bilayer lipid membrane experiment.

3.4.10.1. Channel diameter calculation

Channel diameter was calculated by using Hille's equation,

$$1/g = (l + \pi d/4) \times (4\rho/\pi d^2) \qquad \text{Equation 5}$$

where, g = corrected conductance (obtained by multiplying measured conductance with the Sansom's correction factor), l = thickness of the membrane = 34 Å, and ρ = resistivity of 1 M KCl solution = 9.44 Ω·cm) and d = diameter of the ion channel.

The experimentally evaluated average channel diameter = 4.5 ± 1 Å.

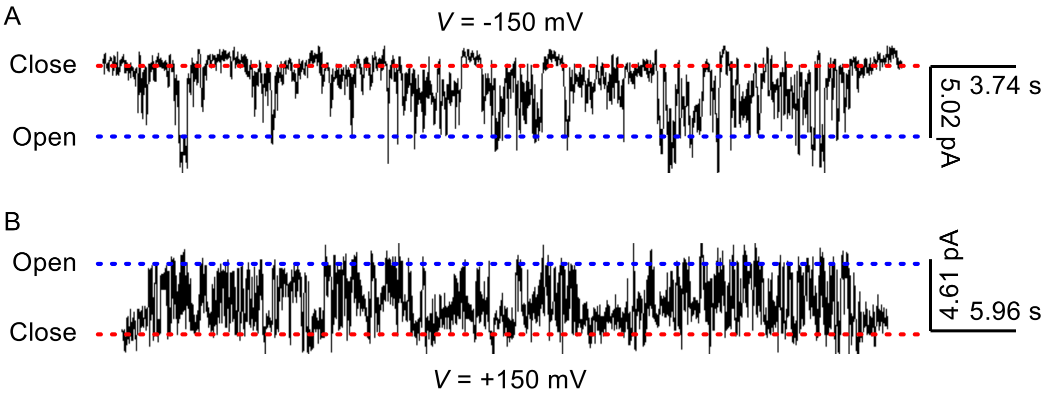

Figure 3.29 Opening-closing events of **Pinakindole catenane 1** under symmetric unbuffered 1 M KCl solution.

3.4.10.2. Single-channel conductance calculation

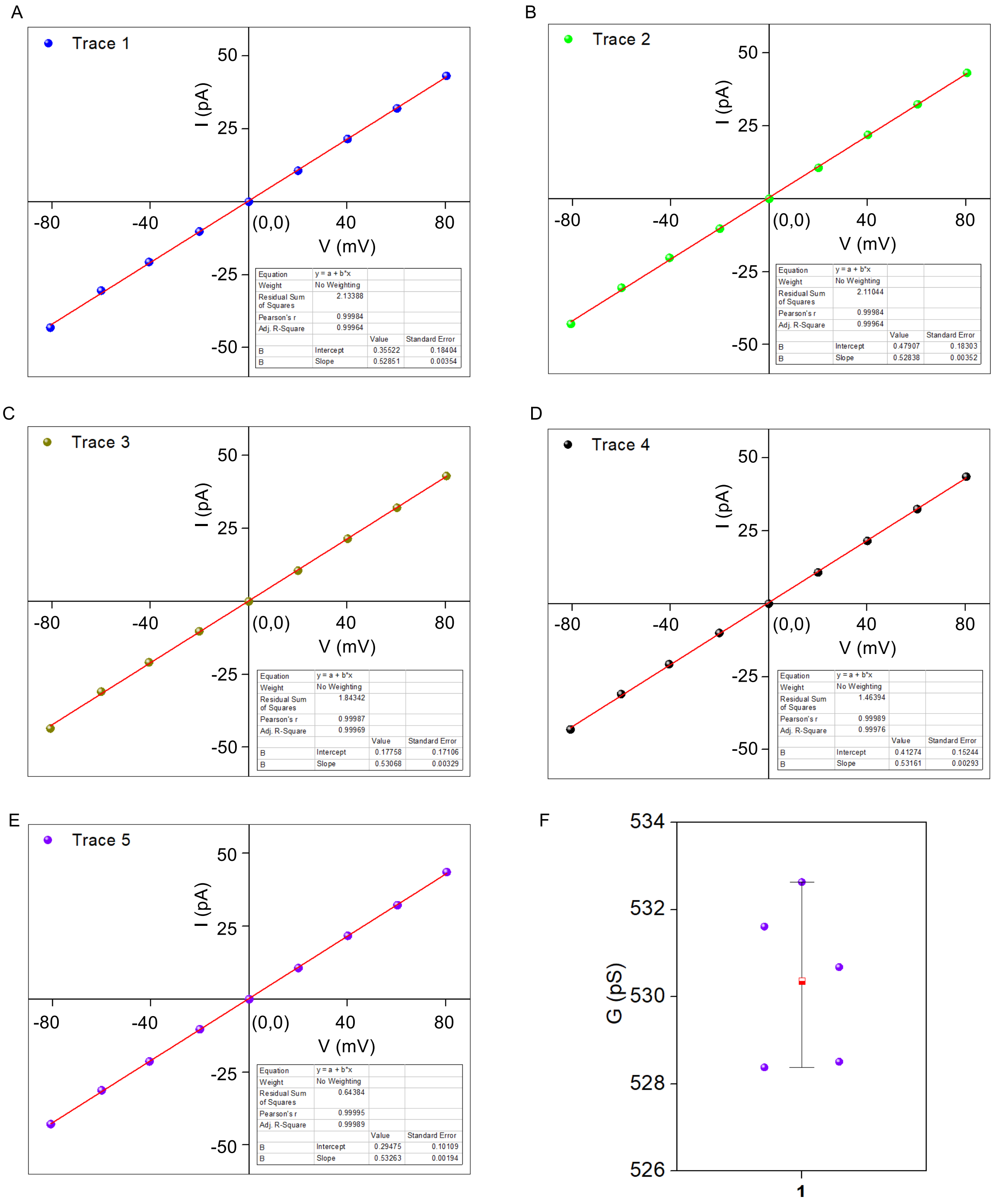

Equation	y = a + b*x		
Weight	No Weighting		
Residual Sum of Squares	2.13388		
Pearson's r	0.99984		
Adj. R-Square	0.99964		
		Value	Standard Error
B	Intercept	0.35522	0.18404
B	Slope	0.52851	0.00354

Equation	y = a + b*x		
Weight	No Weighting		
Residual Sum of Squares	2.11044		
Pearson's r	0.99984		
Adj. R-Square	0.99964		
		Value	Standard Error
B	Intercept	0.47907	0.18303
B	Slope	0.52838	0.00352

Equation	y = a + b*x		
Weight	No Weighting		
Residual Sum of Squares	1.84342		
Pearson's r	0.99987		
Adj. R-Square	0.99969		
		Value	Standard Error
B	Intercept	0.17758	0.17106
B	Slope	0.53068	0.00329

Equation	y = a + b*x		
Weight	No Weighting		
Residual Sum of Squares	1.46394		
Pearson's r	0.99989		
Adj. R-Square	0.99976		
		Value	Standard Error
B	Intercept	0.41274	0.15244
B	Slope	0.53161	0.00293

Equation	y = a + b*x		
Weight	No Weighting		
Residual Sum of Squares	0.64384		
Pearson's r	0.99995		
Adj. R-Square	0.99989		
		Value	Standard Error
B	Intercept	0.29475	0.10109
B	Slope	0.53263	0.00194

Figure 3.30 All five traces of *I*-*V* plots of **Pinakindole catenane 1** in symmetrical cis/trans = 1 M KCl /1 M KCl (A, B, C, D, E); box plot of the averaged V_{rev} from five experiments (represented as dark violet circles) (F).

Table. 3.1. Table for experimentally calculated single-channel conductance of **Pinakindole catenane 1**.

Entry	Slope	G (pS)
1	0.52851	528.51
2	0.52838	528.38
3	0.53068	530.68
4	0.53161	531.61
5	0.53263	532.63
		Average = 530.36

3.4.10.3. Anion/cation selectivity in BLM

The cis and trans chambers were filled with unsymmetrical KCl solutions. The cis chamber was filled with 1.0 M KCl solution, and the trans chamber was filled with 0.5 M KCl. Pinakindole (4 µM) was added to the cis chamber and stirred for 10 minutes. The average reversal potential was calculated to be −7.12 mV, and the calculated permeability ratio was $P_{Cl^-}/P_{K^+} = 0.7 \pm 0.3$ (Equation 6).

The permeability ratio ($P_{\mathrm{Cl}^-}/P_{\mathrm{K}^+}$) was calculated by using the Goldman-Hodgkin-Katz equation,

$$\frac{P_{Cl^-}}{P_{K^+}} = \frac{a_{K^+_{cis}} - a_{K^+_{trans}} \times \exp(-\frac{V_{rev}F}{RT})}{a_{Cl^-_{cis}} \times \exp(-\frac{V_{rev}F}{RT}) - a_{Cl^-_{trans}}} \qquad \text{Equation 6}$$

where, $\frac{P_{Cl^-}}{P_{K^+}}$ = anion/cation permeability ratio; $a_{K^+_{cis}}$ = K^+ activity in the cis chamber; $a_{K^+_{tras}}$ = K^+ activity in the trans chamber; $a_{Cl^-_{cis}}$ = Cl^- activity in the cis chamber; $a_{Cl^-_{trans}}$ = Cl^- activity in the trans chamber; V_{rev} = reversal potential; F = Faraday constant; R = gas constant; T = temperature (K).

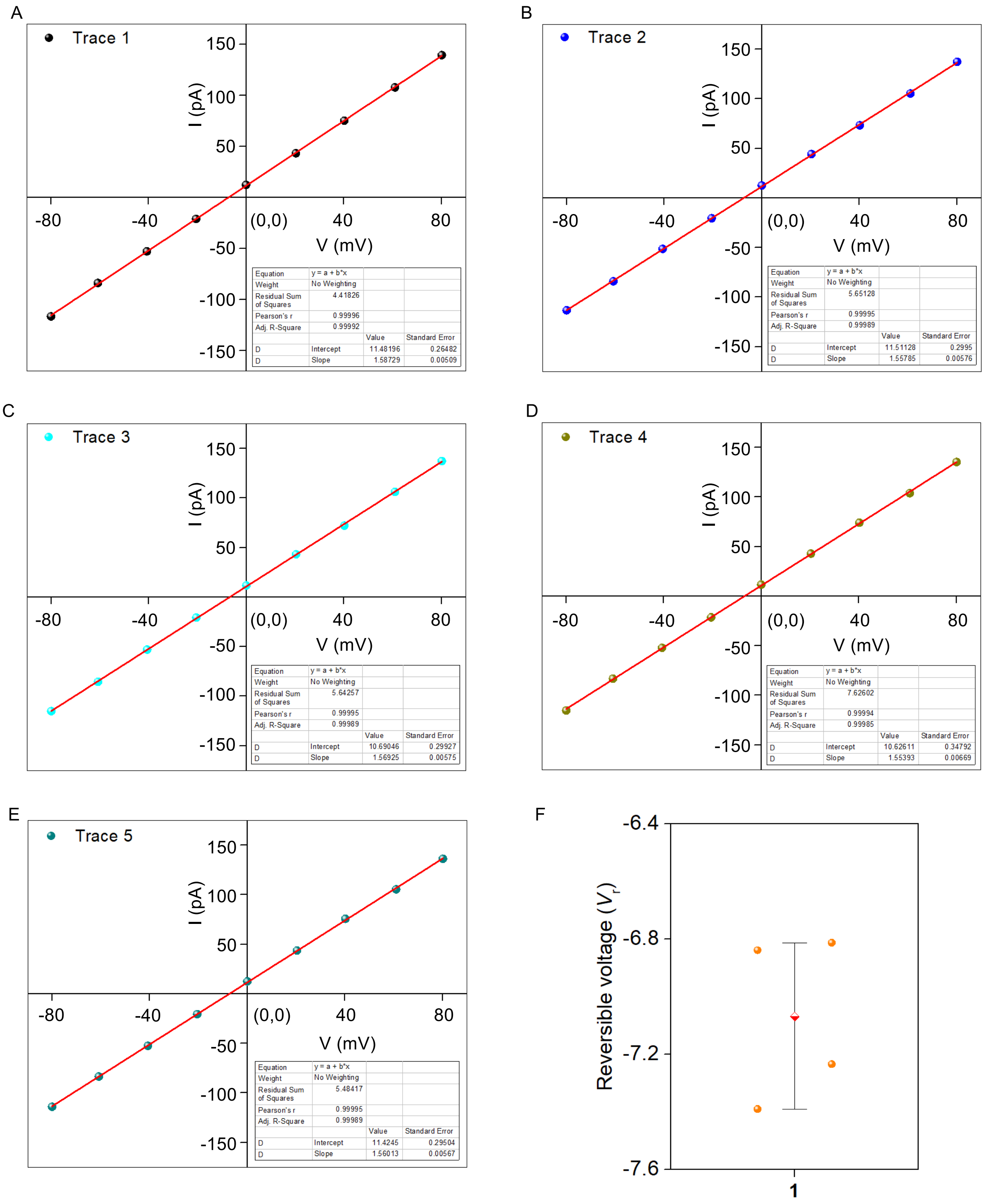

Figure 3.31 All five traces of *I-V* plots of **Pinakindole catenane 1** in symmetrical cis/trans = 1 M KCl /0.5 M KCl (A, B, C, D, E); box plot of the averaged V_{rev} from five experiments (represented as orange circles) (F).

Table. 3.2 Table for experimentally calculated permeability ratio for anion/cation selectivity of **Pinakindole catenane 1**.

Cis/Trans = 1.0 M KCl/0.5 M KCl		
Entry	Reversal voltage V_r (mV)	$\frac{P_{Cl^-}}{P_{K^+}}$
1	– 7.234	0.69
2	– 7.389	0.67
3	– 6.812	0.73
4	– 6.838	0.73
5	– 7.323	0.68
	Average = – 7.12	Average = 0.7

3.4.10.4. Cation/cation selectivity in BLM[18]

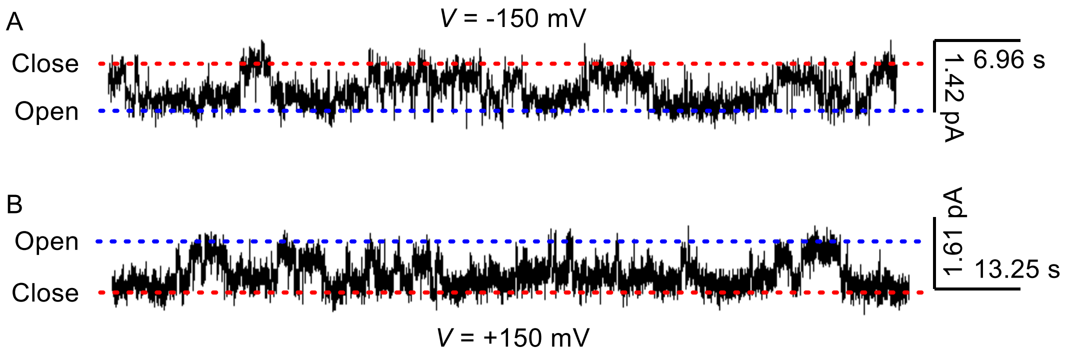

Figure 3.32 Opening-closing events of **Pinakindole catenane 1** under symmetrical unbuffered cis/trans = 1 M KCl/ 1 M NaCl solution.

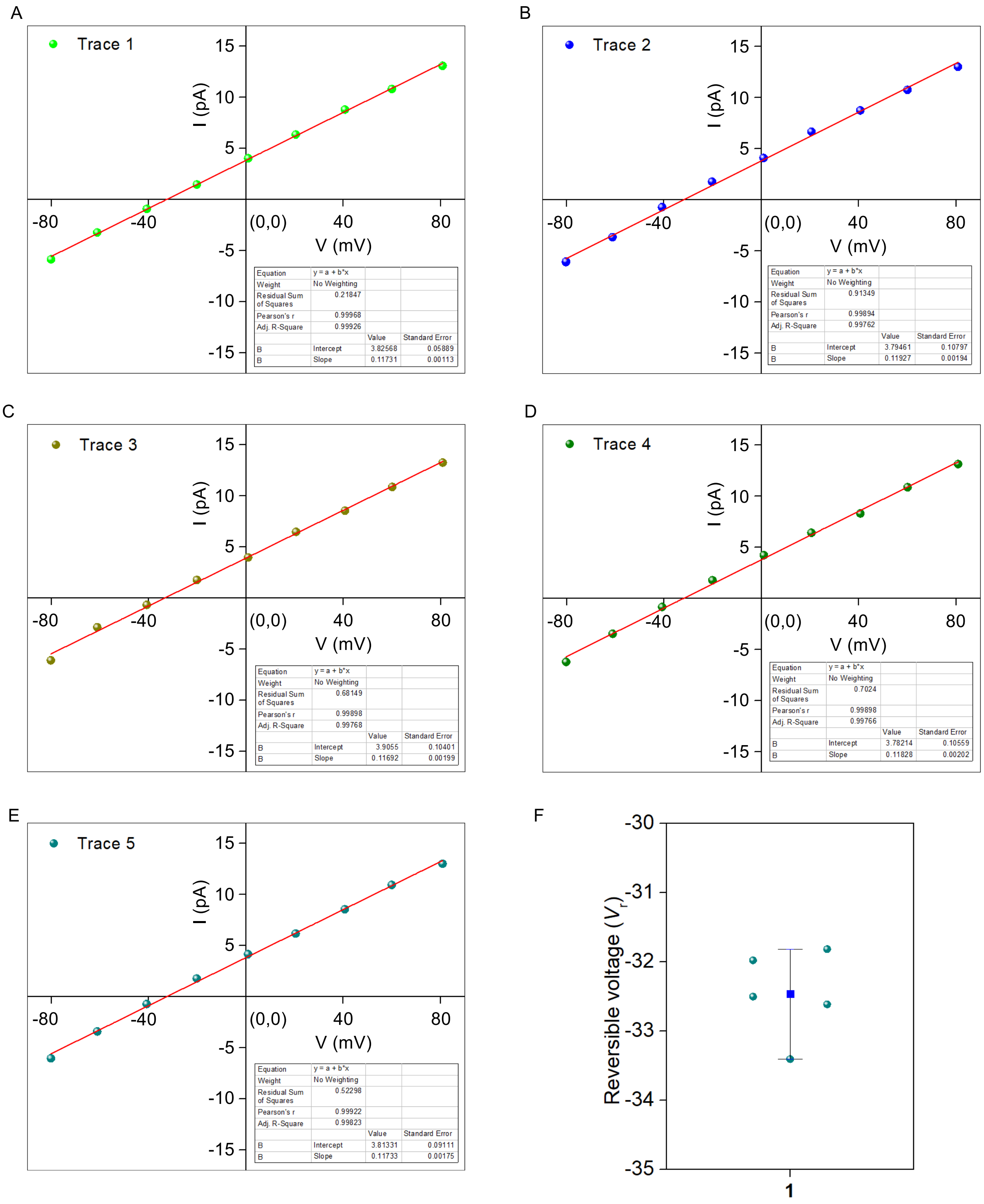

Figure 3.33 All five traces of *I*-*V* plots of **Pinakindole catenane 1** in symmetrical cis/trans = 1 M KCl /1 M NaCl (A, B, C, D, E); box plot of the averaged V_{rev} from five experiments (represented as dark cyan circles) (F).

Table. 3.3 Table for experimentally calculated permeability ratio for cation/cation selectivity of **Pinakindole catenane 1**.

Cis/Trans = 1.0 M KCl/1.0 M NaCl		
Entry	Reversal voltage V_r (mV)	$\frac{P_{Na^+}}{P_{K^+}}$
1	– 32.612	3.56
2	– 31.815	3.45
3	– 33.403	3.67
4	– 31.976	3.47
5	– 32.500	3.54
	Average = – 32.46	Average = 3.54

3.4.10.5. Anion/anion selectivity in BLM[18]

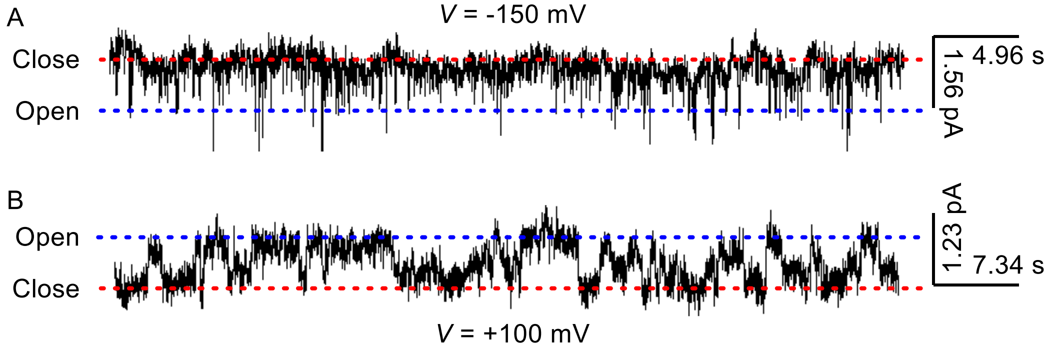

Figure 3.34 Opening-closing events of **Pinakindole catenane 1** under symmetrical unbuffered cis/trans = 1 M NaCl/ 1 M NaBr solution.

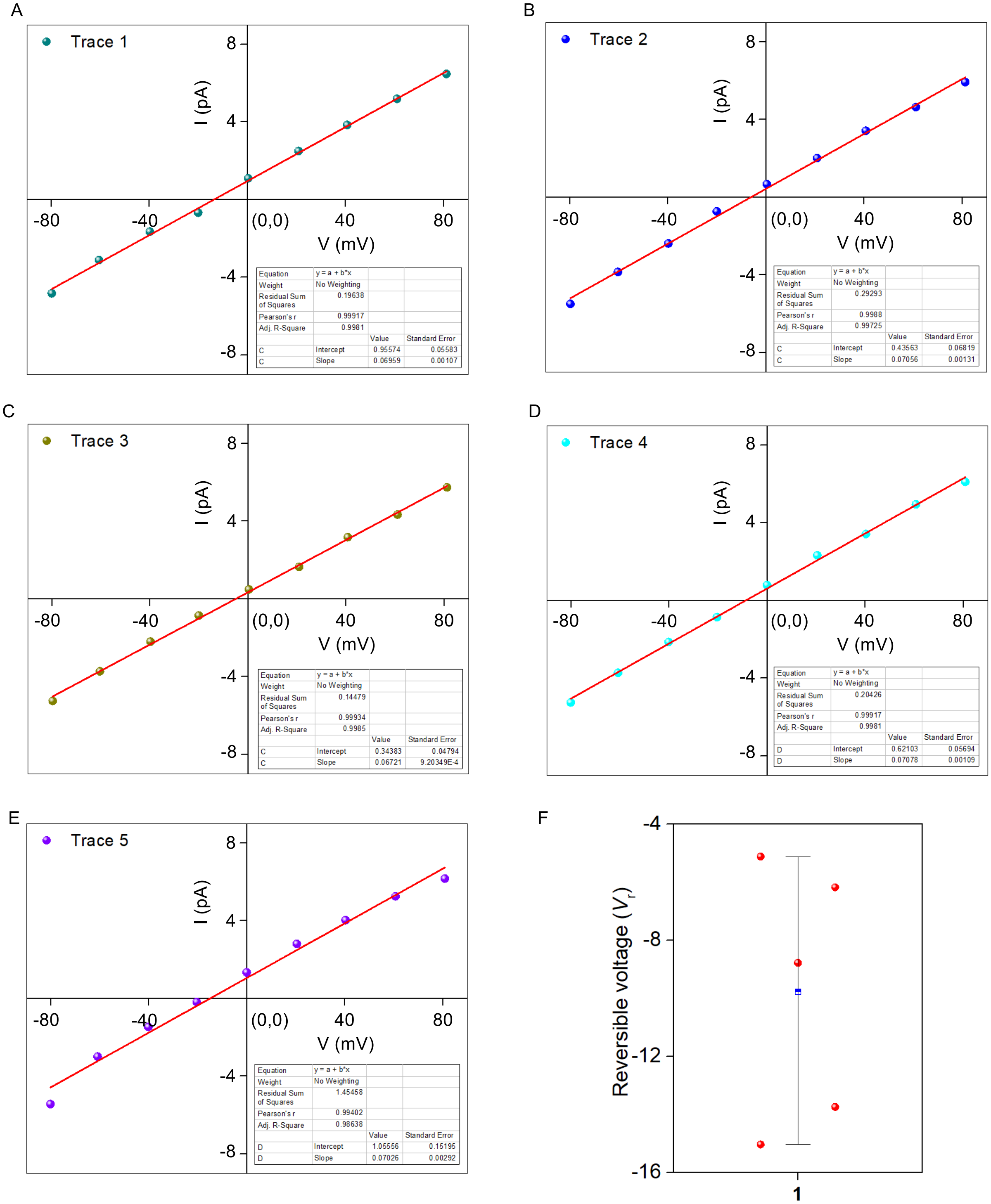

Figure 3.35 All five traces of *I*-*V* plots of **Pinakindole catenane 1** in symmetrical cis/trans = 1 M NaCl /1 M NaBr (A, B, C, D, E); box plot of the averaged V_{rev} from five experiments (represented as red circles) (F).

Table. 3.4 Table for experimentally calculated permeability ratio for anion/anion selectivity of **Pinakindole catenane 1**.

Cis/Trans = 1.0 M NaCl/1.0 M NaBr		
Entry	Reversal voltage V_r (mV)	$\frac{P_{Cl^-}}{P_{Br^-}}$
1	– 13.734	1.71
2	– 6.174	1.27
3	– 5.116	1.22
4	– 8.774	1.41
5	– 15.023	1.79
	Average = – 9.76	Average = 1.48

3.4.11. Theoretical studies

Computational details

All geometry optimizations were carried out by using the Gaussian 09 package.[19]

To understand the structural orientation of the **Pinakindole catenane 1**, initially, four possible conformations (**conf-I**, **conf-II**, and **conf-III**) were geometrically optimized. All geometry optimizations were performed in the Gaussian 09 package using B3LYP functional and 6-311G(d,p) basis set. During the geometry optimization, no imaginary frequencies were shown, which indicated that all of the optimized structures of **conf-I**, **conf-II**, and **conf-III** were in the ground state minima.

The geometry-optimized CPK models of all of the possible conformers confirmed that **conf-II** does not have any void space to bind with the ions. Hence, **conf-II** cannot be the responsible conformer that binds with the cation and anion. Even though **conf-I** have void space for binding with the cation and anion respectively, the lack of the presence of both the cation and anion binding pocket in the same conformer ruled out the involvement of these consumers in the cation-anion transport process. Interestingly, **conf-III** has both cation and anion binding cavity in itself, which indicates that **conf-III** might be the responsible conformer for the transport of both cation and anion at a same time.

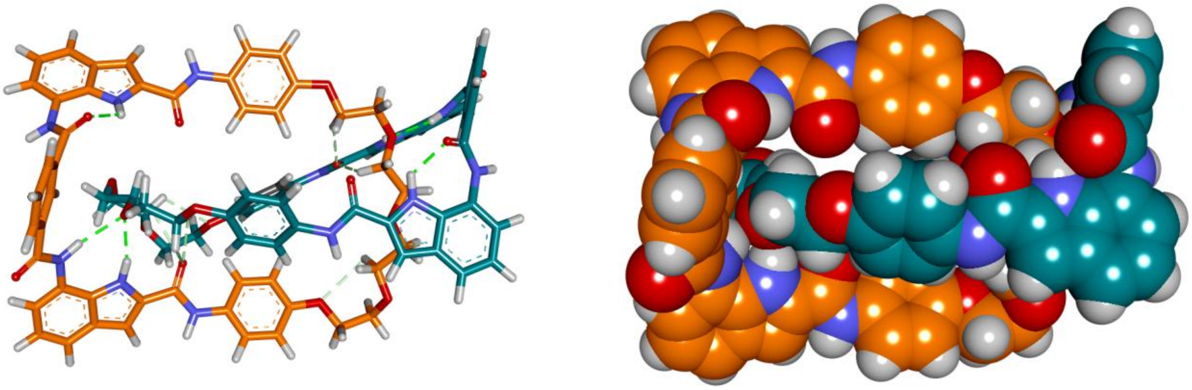

Figure 3.36 Geometry optimized structure of **conf-I** of **Pinakindole catenane 1** with the stick (A) and CPK (B) model.

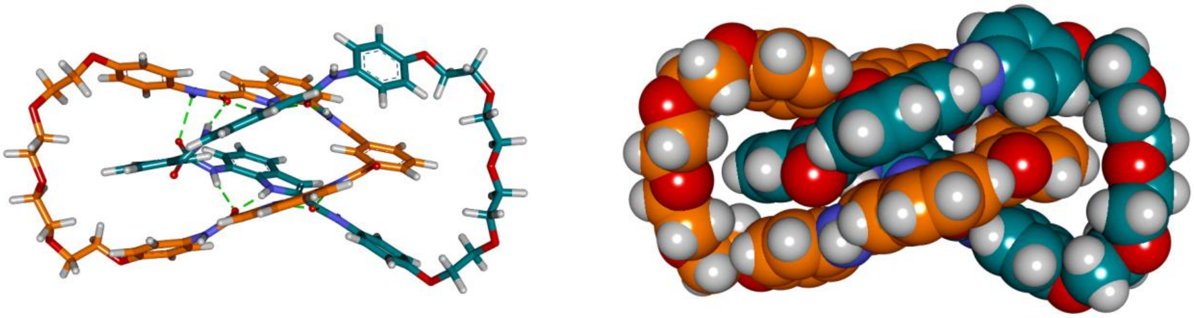

Figure 3.37 Geometry optimized structure of **conf-II** of **Pinakindole catenane 1** with the stick (A) and CPK (B) model.

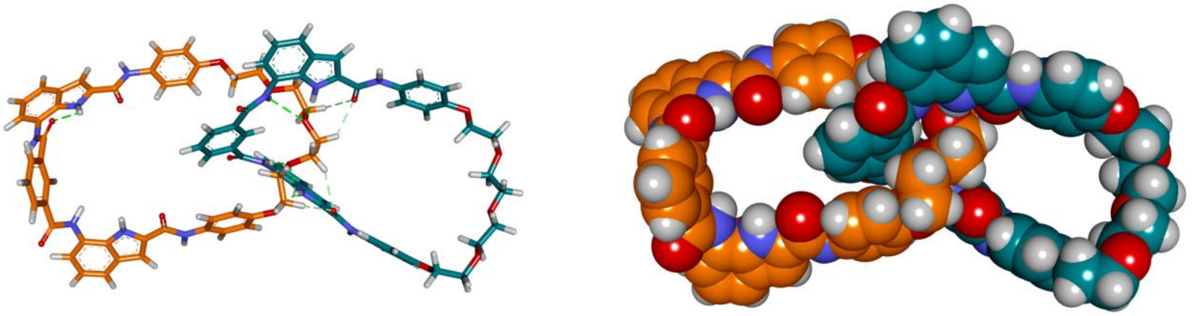

Figure 3.38 Geometry optimized structure of **conf-III** of **Pinakindole catenane 1** with the stick (A) and CPK (B) model.

To understand the encapsulation of the Cs$^+$ ion in the **conf-I**, **conf-I** was geometrically optimized with the Gaussian 09 package using B3LYP functional with 6-311G(d,p) basis set for C, H, N, and O atoms and LanL2DZ basis set for Cs atom. The optimized structure indicated that the Cs$^+$ ion can easily encapsulate inside the cavity if the interlocked structure of the **conf-I** gets stabilized by the electrostatic interactions with the O-atom of the TEG linker (O···Cs$^+$ = 3.320 Å) and two C=O groups (C=O···Cs$^+$ = 3.185 Å and 3.336 Å). Alongside the cation-π intersections (π-surface···Cs$^+$ = 2.073 Å and 1.909 Å) also help it to stabilize inside the cavity.

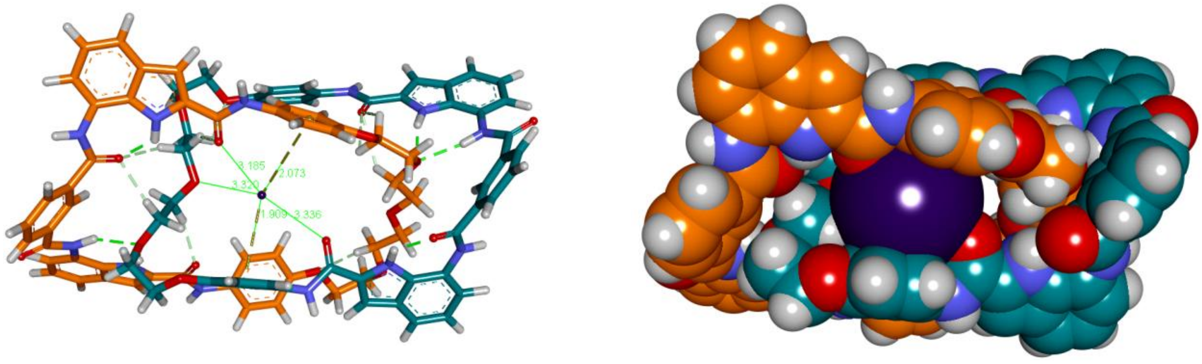

[$\mathbf{1}_{\text{conf-I}}$+Cs$^+$]

Figure 3.39 Geometry optimized structure of [$\mathbf{1}_{\text{conf-I}}$+Cs$^+$] complex with the stick (A) and CPK (B) model.

Since the geometry optimization divulged that **conf-III** has sufficient void space to bind both cation and anion at the same time, we further optimized the **conf-III** along with the NaCl salt by sing the Gaussian 09 package using B3LYP functional and 6-311G(d,p) basis set. As expected we noticed both Na$^+$ and Cl$^-$ ions are fitted in the corresponding ion binding cavity. Cl$^-$ ion formed H-bonding interactions with the acidic N-H and aromatic C-H groups whereas Na$^+$ ion showed the electrostatic interaction with the O-atoms of the TEG linker and C=O groups. Hence it clear that **conf-III** can hold both of the Na$^+$ and Cl$^-$ ions in the respective ion binding cavity and have the potential of translocating across the membrane.

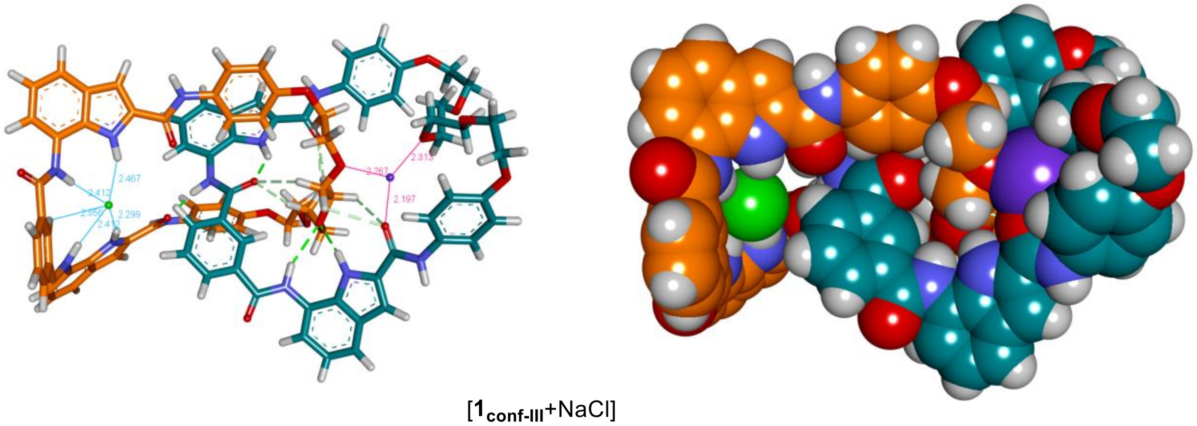

[$\mathbf{1}_{\text{conf-III}}$+NaCl]

Figure 3.40 Geometry optimized structure of [$\mathbf{1}_{\text{conf-III}}$+NaCl] complex with the stick (A) and CPK (B) model.

An energy screening of all of the conformers is listed below in the tabular format.

Table. 3.5 Table for calculated energy values of the different conformational orientations of **Pinakindole catenane 1**.

Conformational orientation	Electronic energy in Hartree (HF)	Zero point energy in Hartree (ZPE)	HF+ZPE (Hartree)	Energy difference (Hartree) compared to conf-II	Energy difference (KJ/mol) compared to conf-II
conf-I	-5568.948349	1.640522	-5567.307827	0.00665	17.459575
conf-II	-5568.956502	1.642024	-5567.314477	0	0
conf-III	-5568.949499	1.640129	-5567.30937	0.005107	13.4084285
[conf-III+NaCl]	-6191.574171	1.642983	-6189.931188	-622.616711	-1634680.175

Geometry optimization validates that **conf-II** has the lowest energy among the three conformational orientations. **Conf-I** and **conf-III** are approximately 17.459 KJ/mol and 13.408 KJ/mol higher in energy compared to the **conf-II**.

3.5. NMR Data

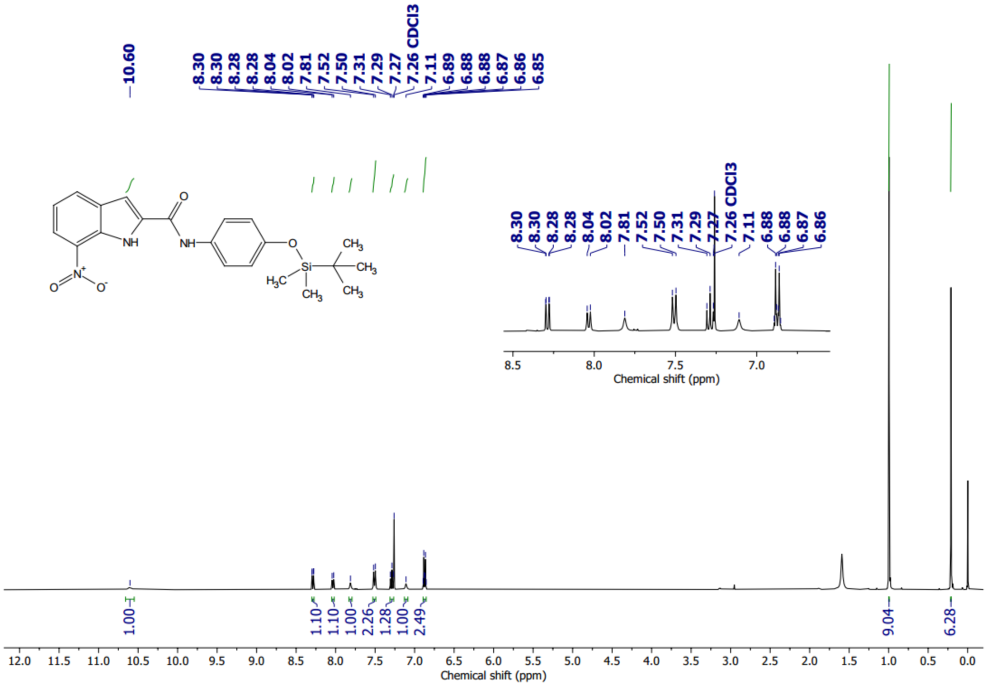

Figure 3.41 ^{1}H NMR (400 MHz) spectrum of compound **4** in CDCl$_3$ solvent.

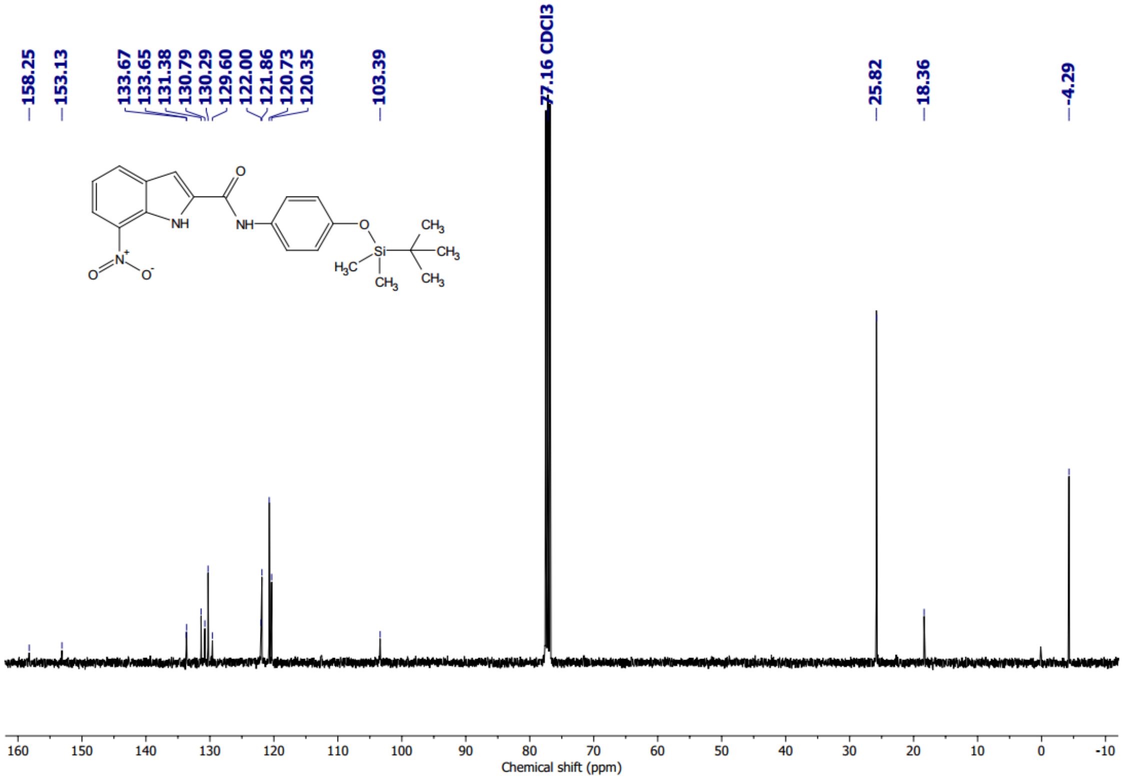

Figure 3.42 ^{13}C NMR (101 MHz) spectrum of compound **4** in CDCl$_3$ solvent.

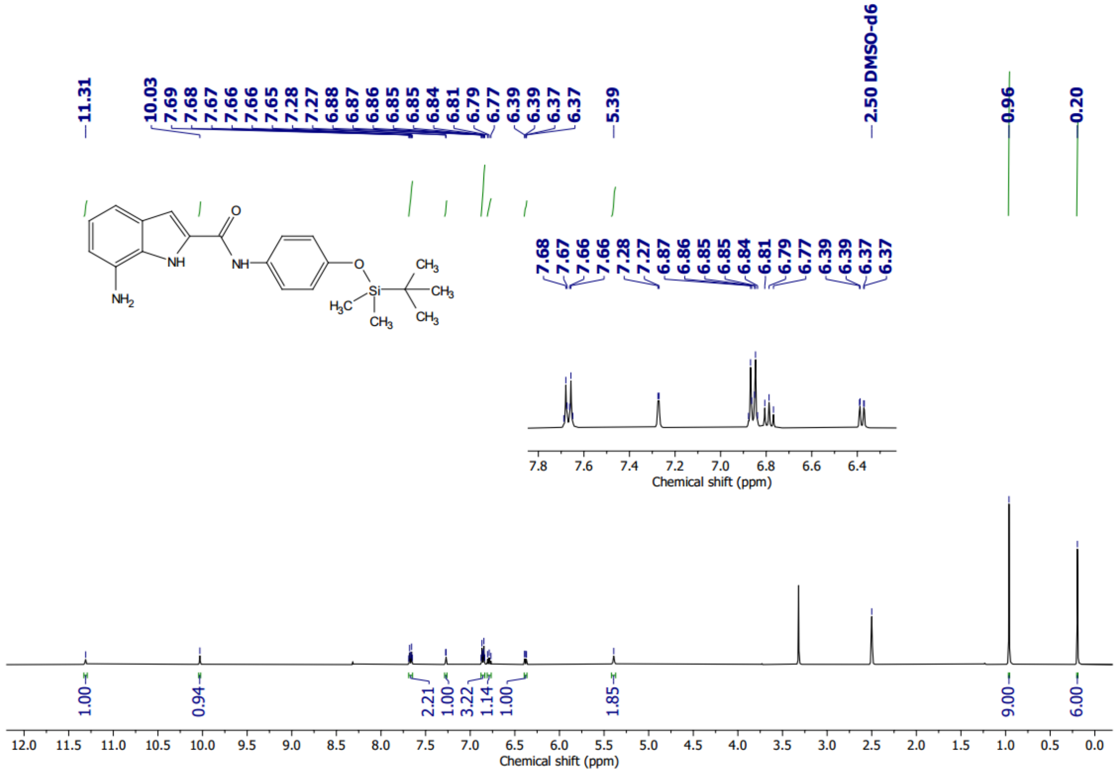

Figure 3.43 ^{1}H NMR (400 MHz) spectrum of compound **5** in DMSO-d_6 solvent.

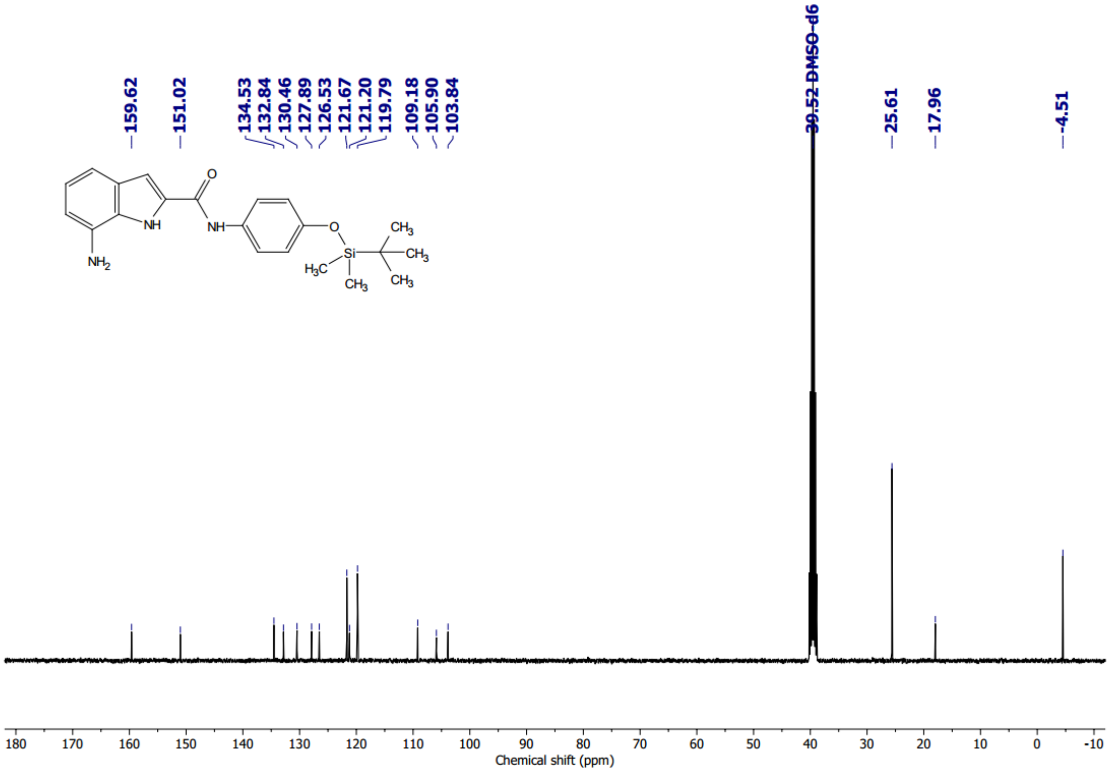

Figure 3.44 ^{13}C NMR (101 MHz) spectrum of compound **5** in DMSO-d_6 solvent.

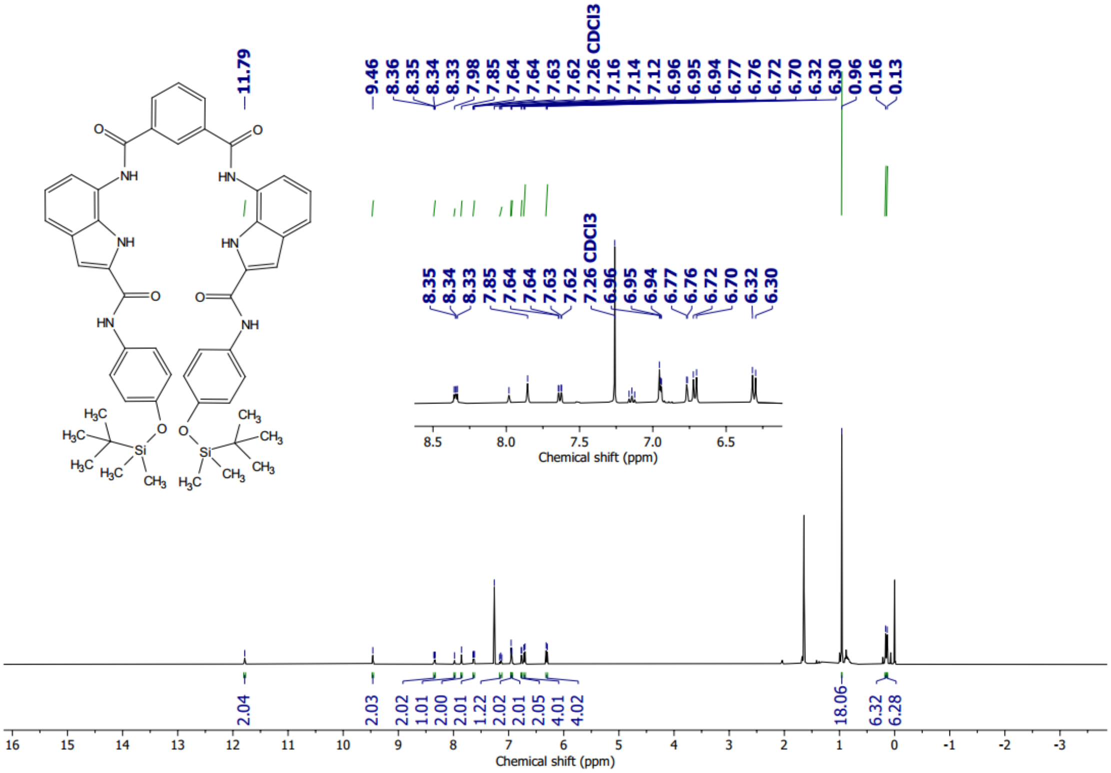

Figure 3.45 ^{1}H NMR (400 MHz) spectrum of compound **6** in CDCl$_3$ solvent.

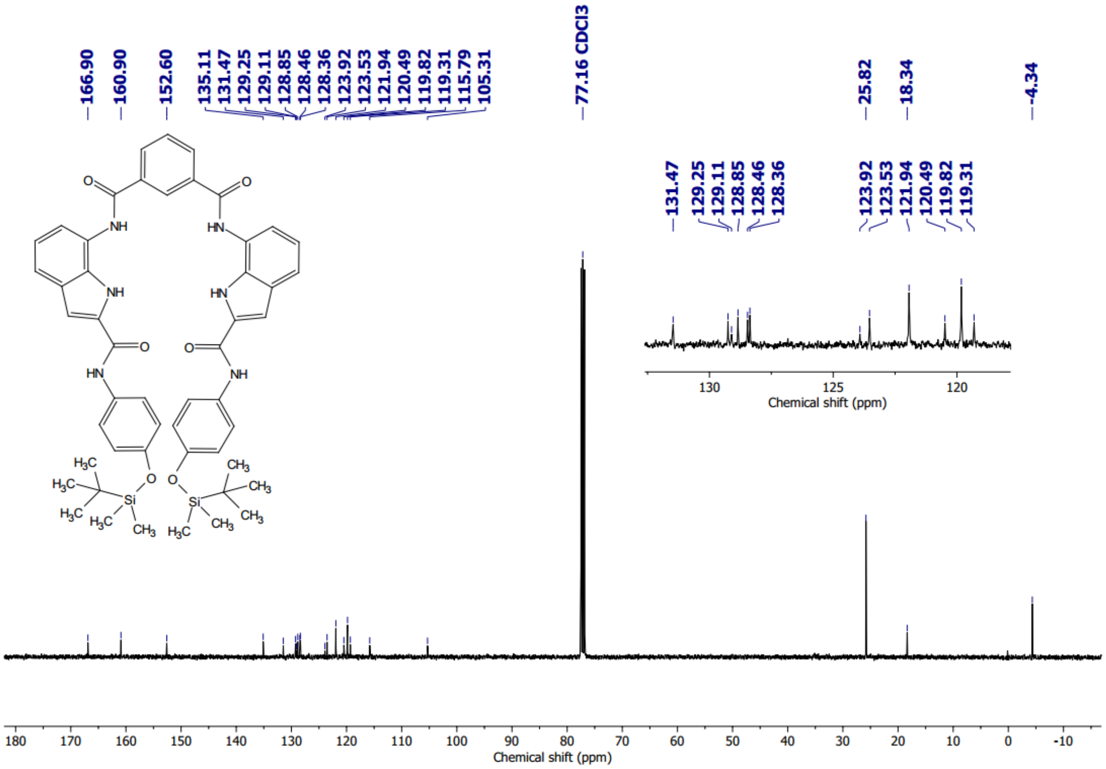

Figure 3.46 ^{13}C NMR (101 MHz) spectrum of compound **6** in $CDCl_3$ solvent.

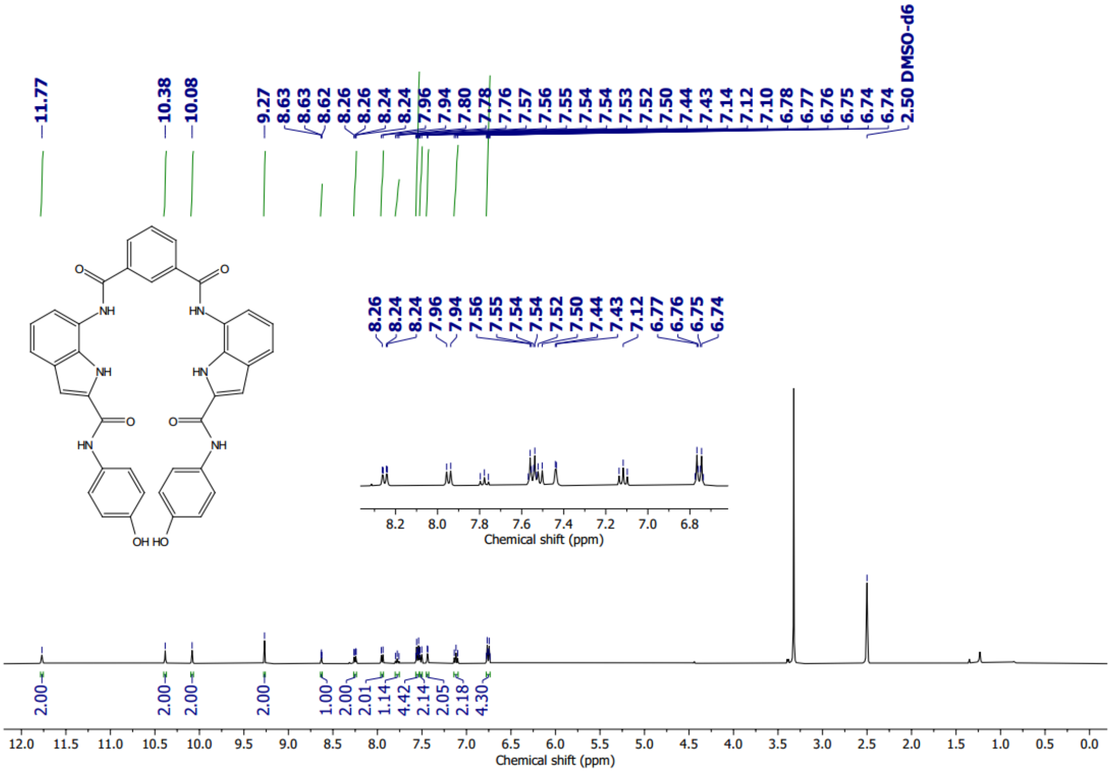

Figure 3.47 ^{1}H NMR (400 MHz) spectrum of compound **7** in DMSO-d_6 solvent.

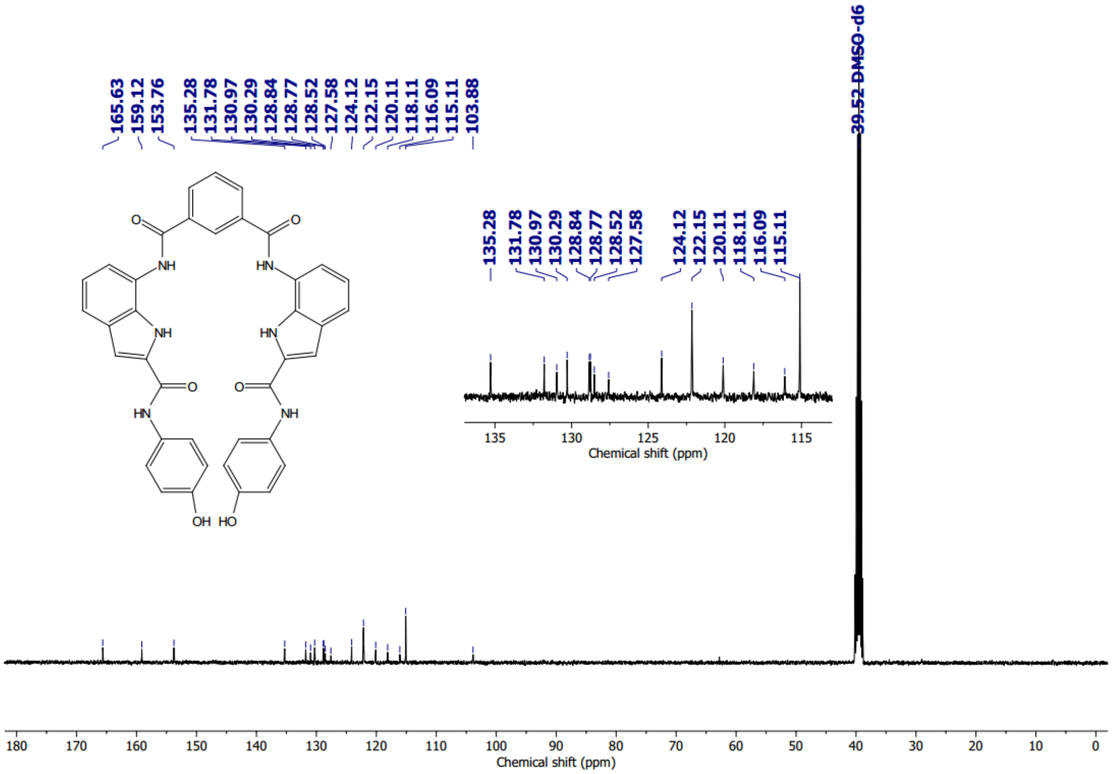

Figure 3.48 ^{13}C NMR (101 MHz) spectrum of compound **7** in DMSO-d_6 solvent.

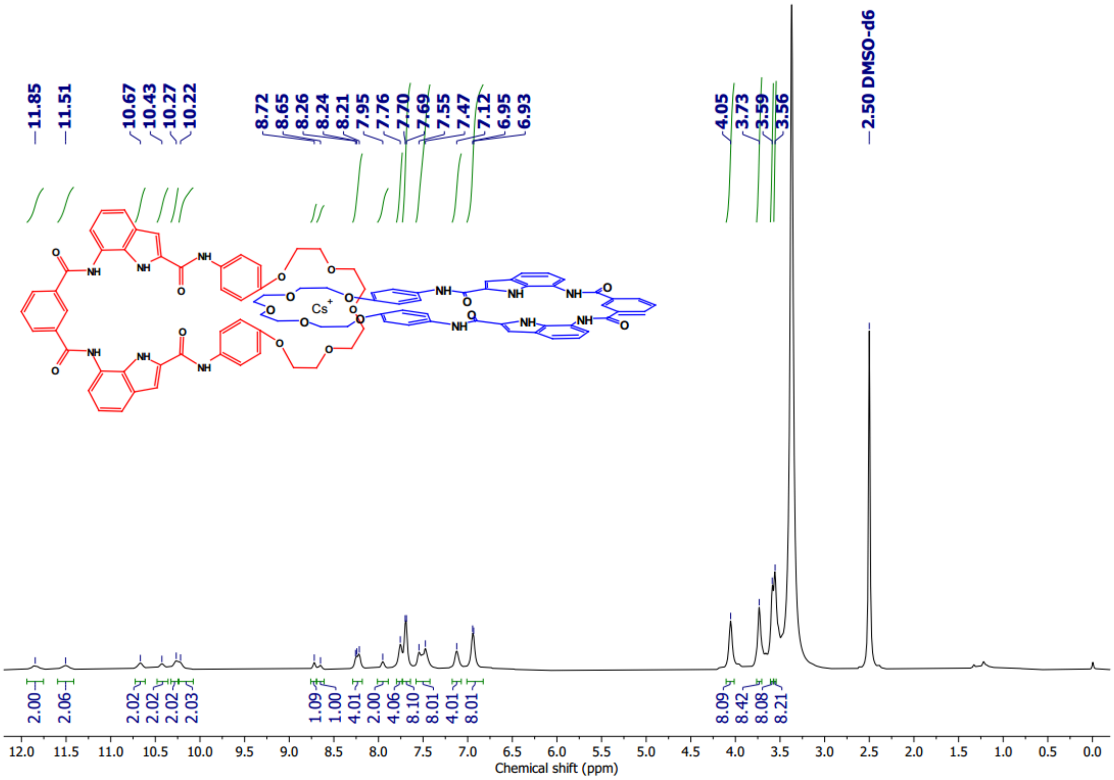

Figure 3.49 ^{1}H NMR (400 MHz) spectrum of **Pinakindole catenane 1·Cs^{+}** in DMSO-d_6 solvent.

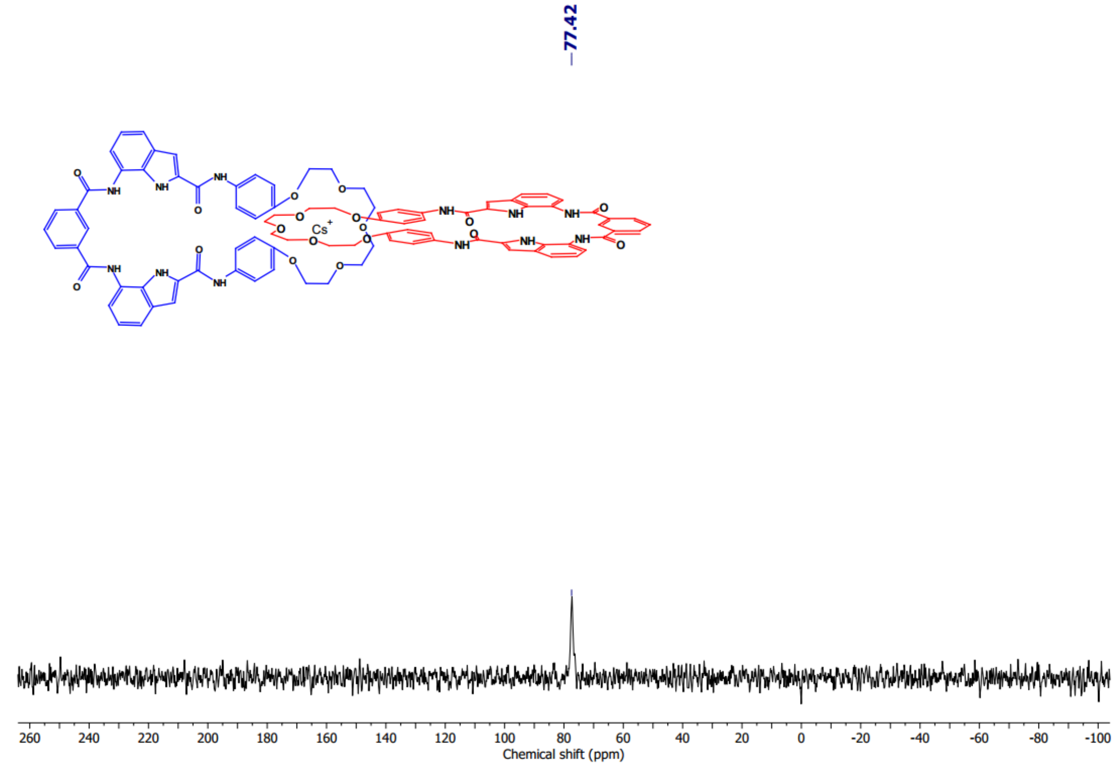

Figure 3.50 ^{133}Cs NMR (53 MHz) spectrum of **Pinakindole catenane 1·Cs$^+$** in CDCl$_3$ solvent.

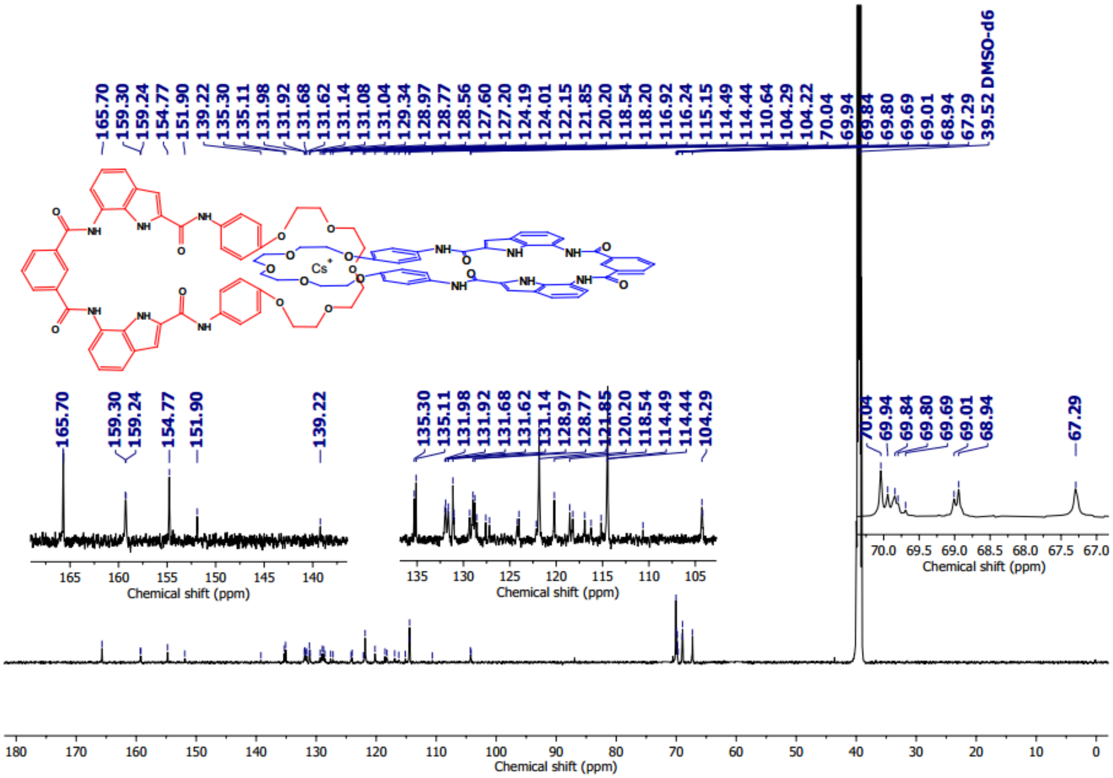

Figure 3.51 ^{13}C NMR (101 MHz) spectrum of **Pinakindole catenane 1·Cs$^+$** in DMSO-d_6 solvent.

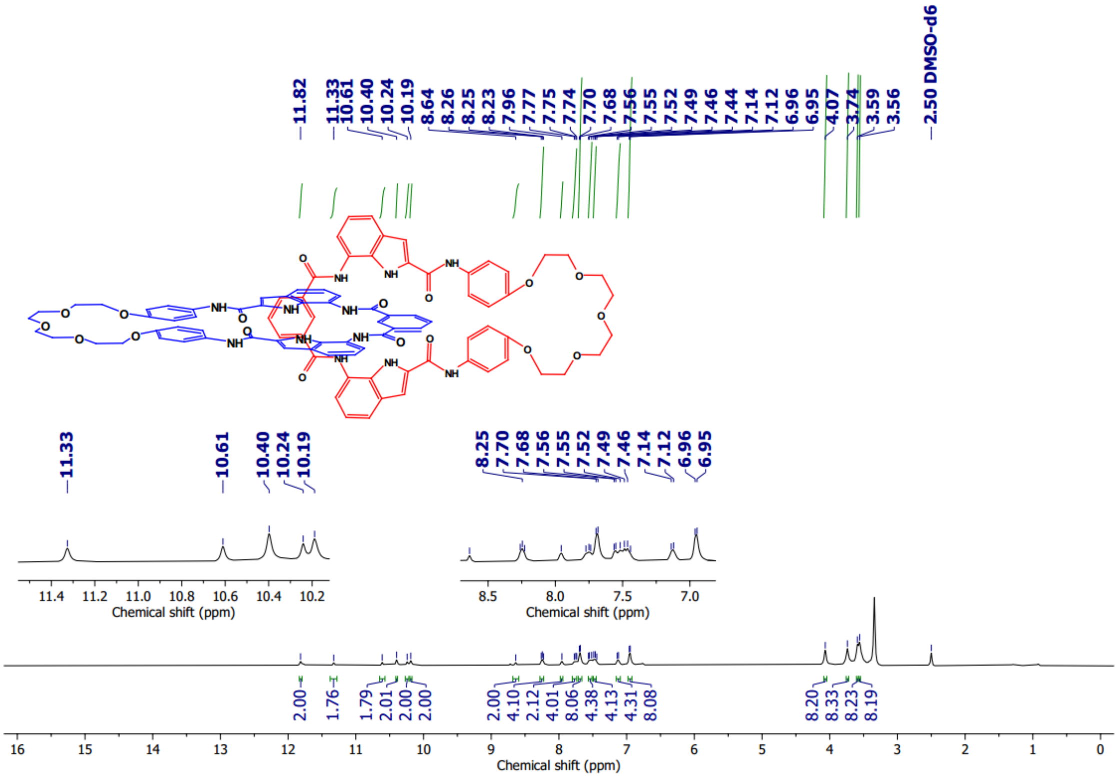

Figure 3.52 ^{1}H NMR (600 MHz) spectrum of compound **Pinakindole catenane 1** in DMSO-d_6 solvent.

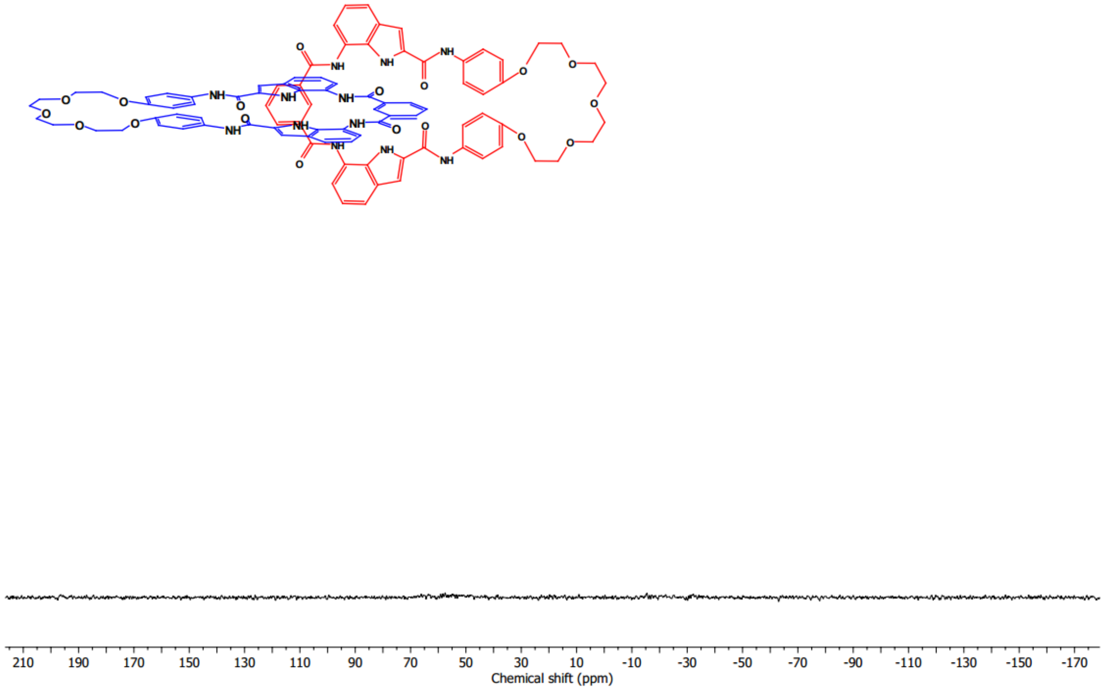

Figure 3.53 ^{133}Cs NMR (53 MHz) spectrum of **Pinakindole catenane 1** in DMSO-d_6 solvent.

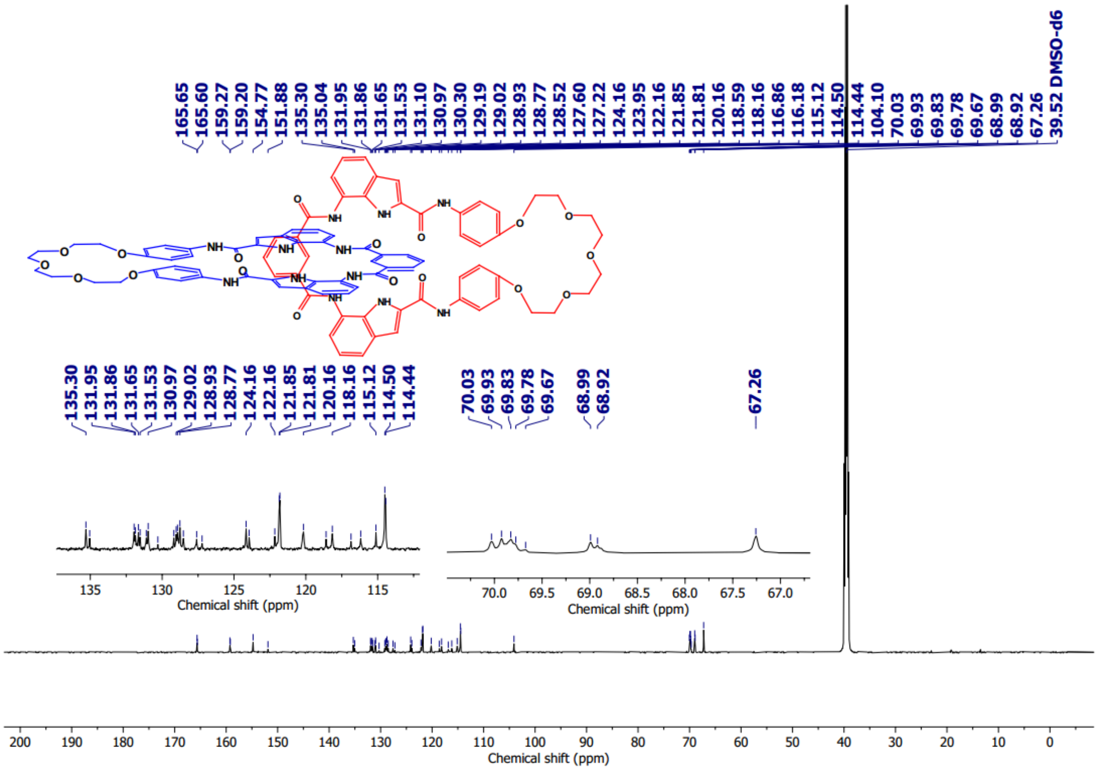

Figure 3.54 ^{13}C NMR (101 MHz) spectrum of **Pinakindole catenane 1** in DMSO-d_6 solvent.

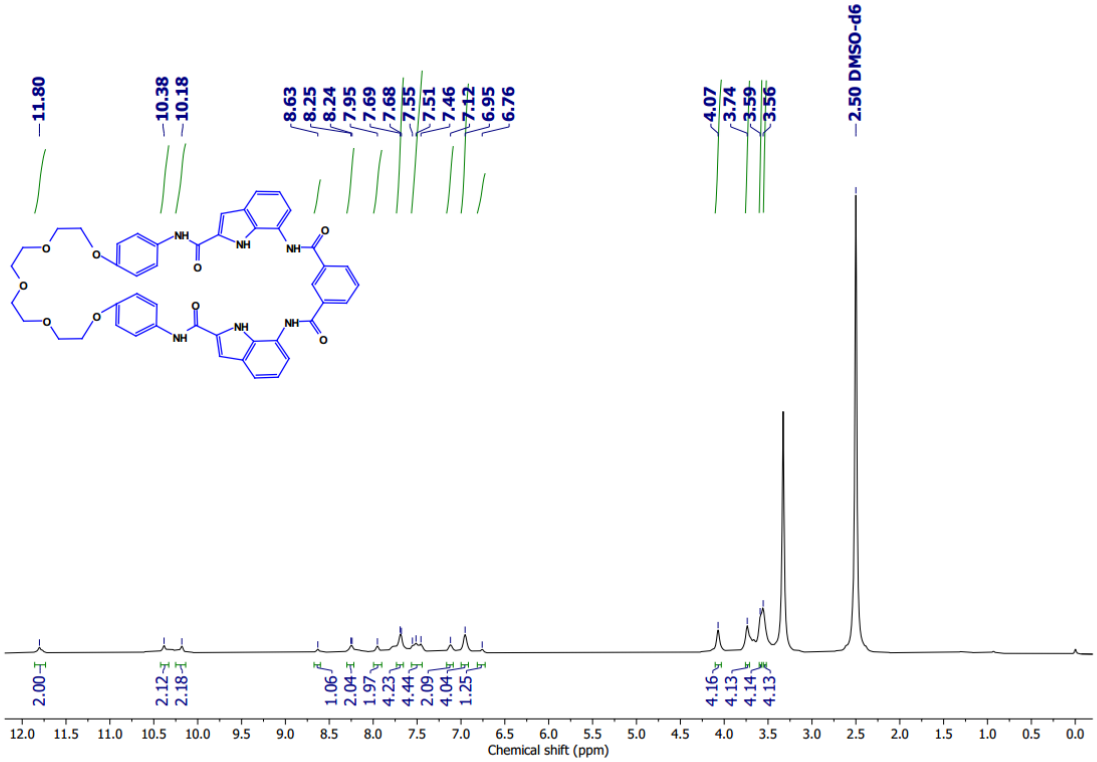

Figure 3.55 ^{1}H NMR (400 MHz) spectrum of **Pinakindole macrocycle 2** in DMSO-d_6 solvent.

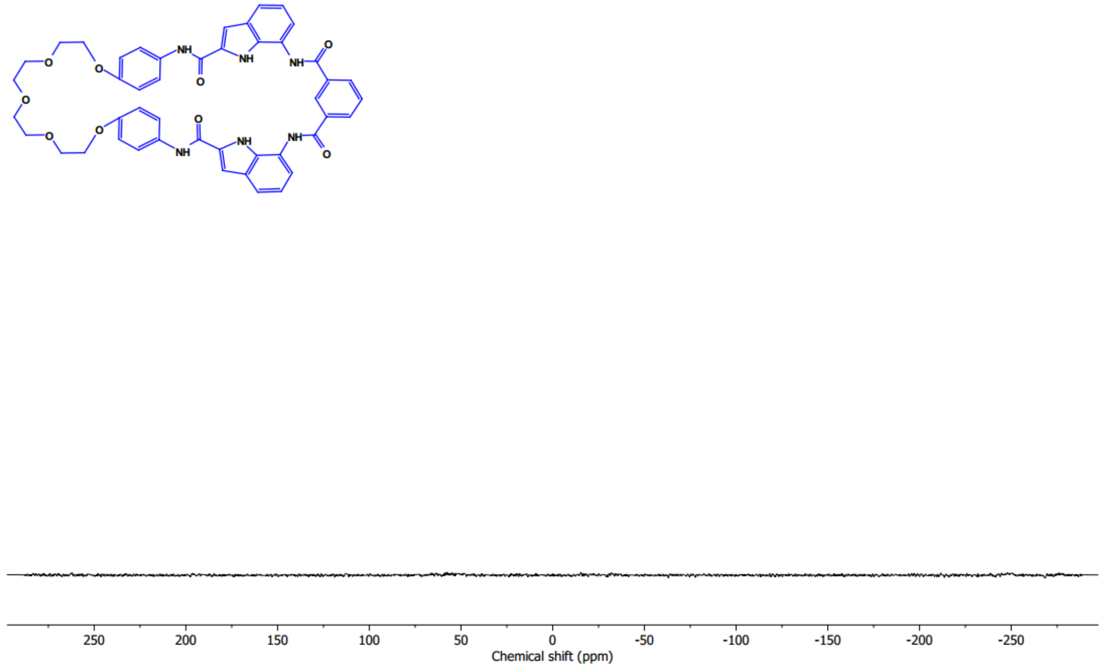

Figure 3.56 ^{133}Cs NMR (53 MHz) spectrum of **Pinakindole macrocycle 2** in DMSO-d_6 solvent.

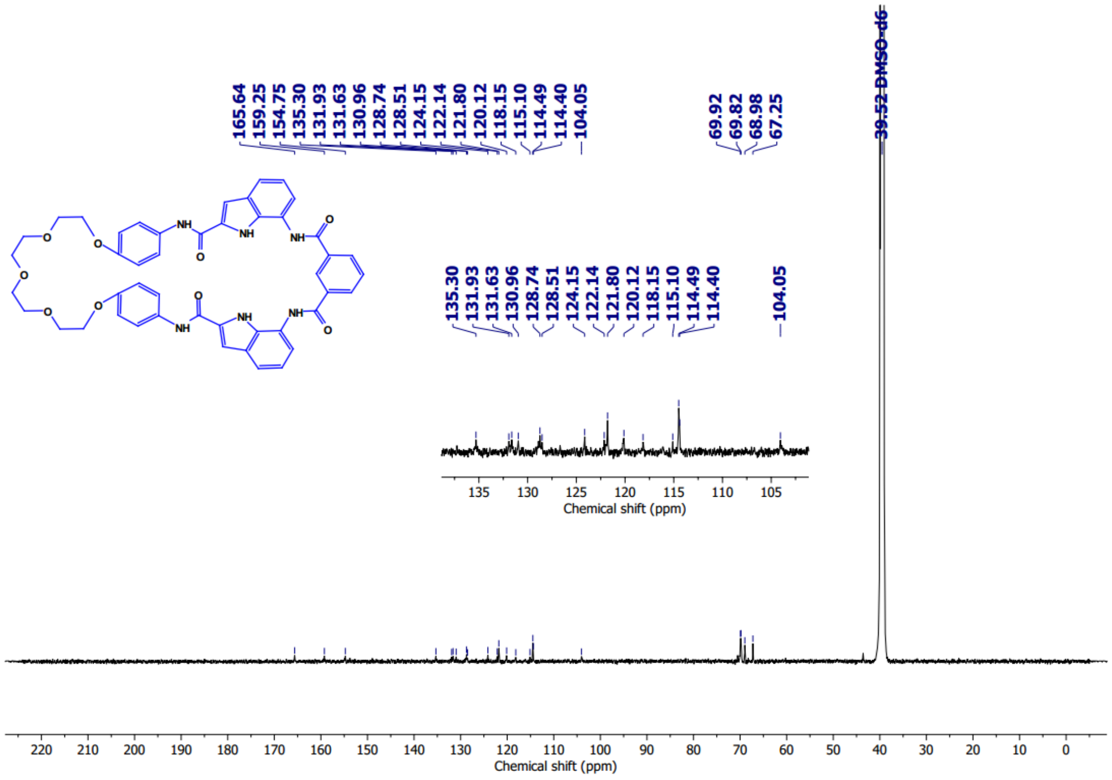

Figure 3.57 ^{13}C NMR (151 MHz) spectrum of **Pinakindole macrocycle 2** in DMSO-d_6 solvent.

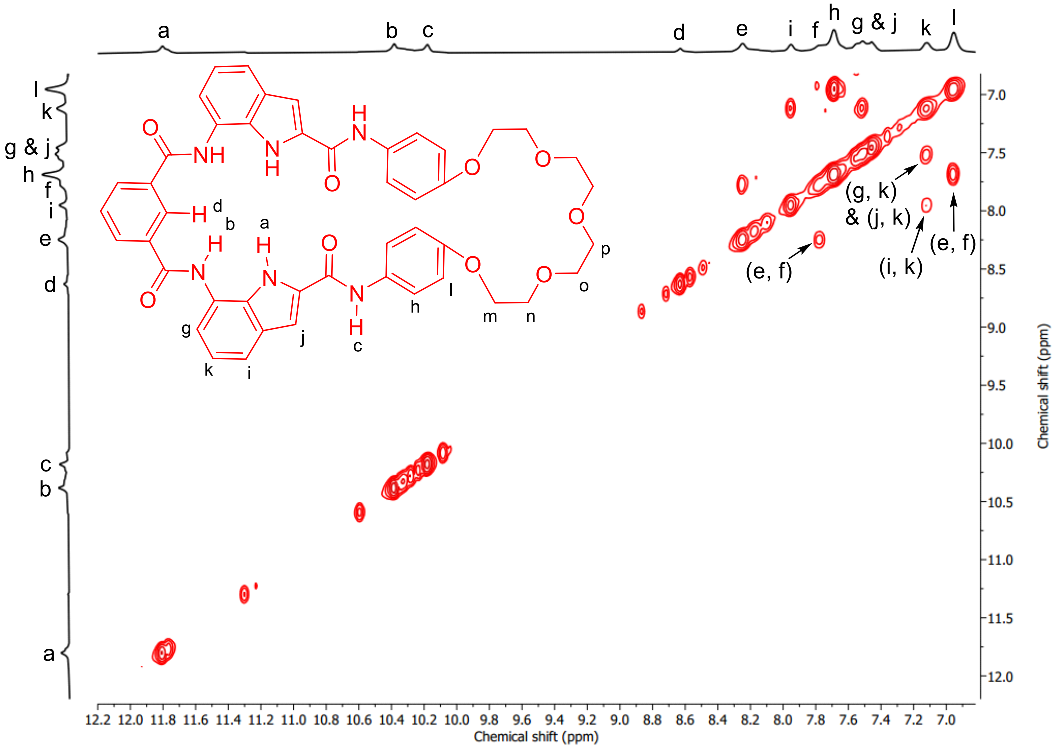

Figure 3.58 ^{1}H-^{1}H COSY NMR (600 MHz) spectrum of **Pinakindole macrocycle 2** (2 mM) in DMSO-d_6 solvent at 25 °C.

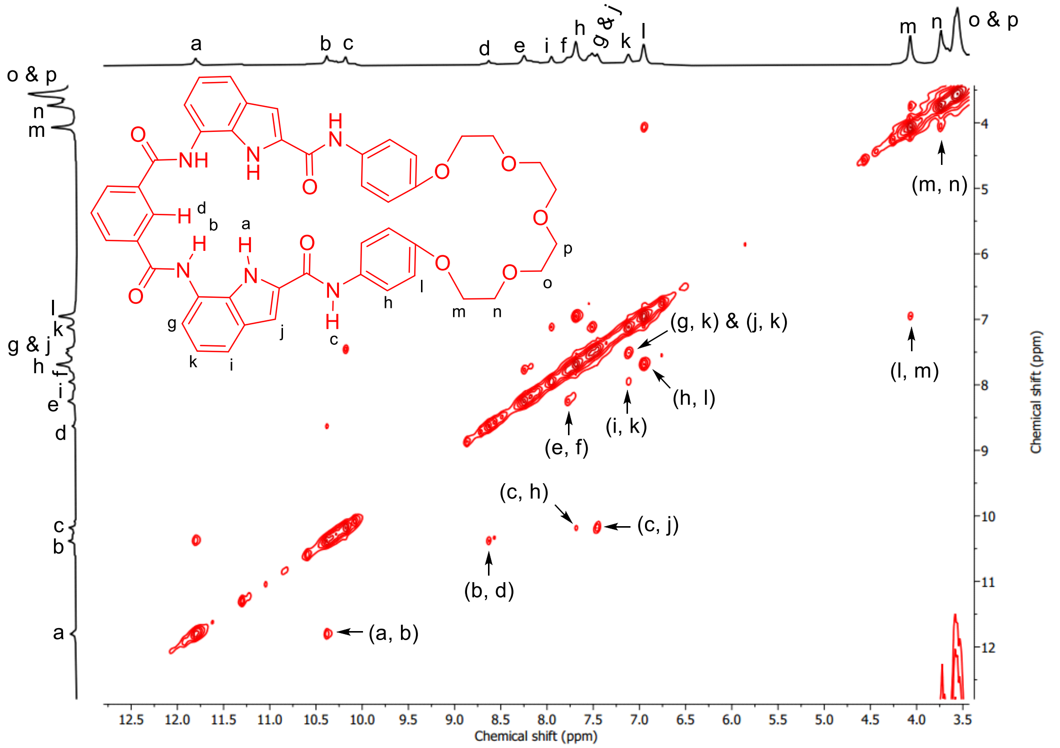

Figure 3.59 ^{1}H-^{1}H NOESY NMR (600 MHz) spectrum of **Pinakindole macrocycle 2** (2 mM) in DMSO-d_6 solvent at 25 °C.

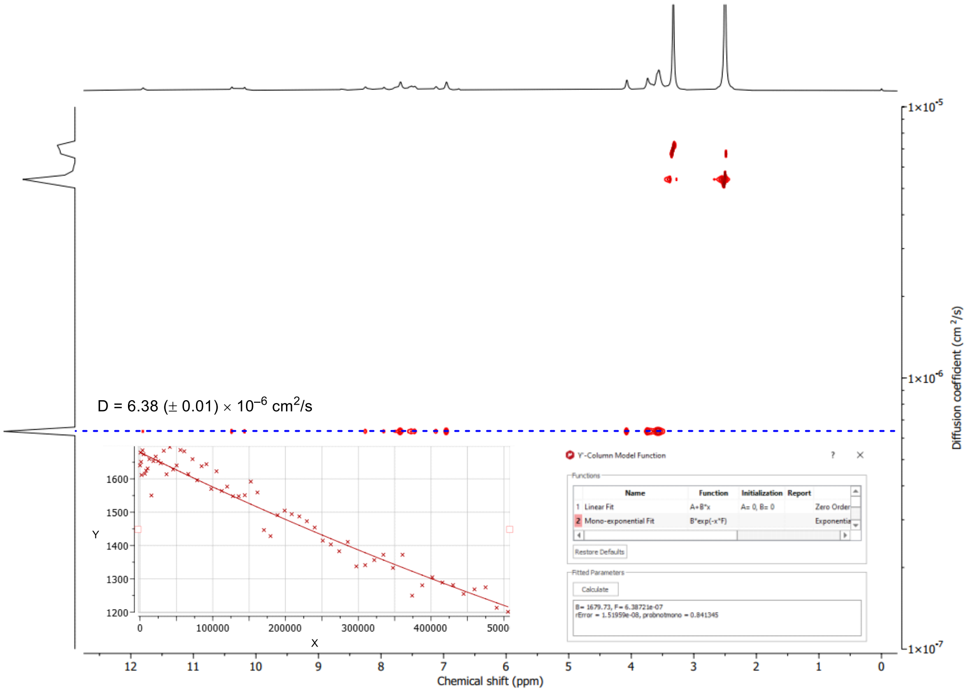

	Name	Function	Initialization	Report	
1	Linear Fit	A+B*x	A= 0, B= 0		Zero Order
2	Mono-exponential Fit	B*exp(-x*F)			Exponentia

```
B= 1679.73, F= 6.38721e-07
rError = 1.51959e-08, probnotmono = 0.841345
```

Figure 3.60 DOSY NMR (600 MHz) spectrum of **Pinakindole macrocycle 2** (2 mM) in DMSO-d_6 solvent at 25 °C.

3.6. References

(1) Ito, Y.; Oroguchi, T.; Ikeguchi, M. *J. Am. Chem. Soc.* **2011**, *133*, 3372–3380.

(2) Houdusse, A.; Szent-Györgyi, A. G.; Cohen, C. *Proc. Natl. Acad. Sci. U. S. A.* **2000**, *97*, 11238–11243.

(3) Heard, A. W.; Goldup, S. M. *ACS Cent. Sci.* **2020**, *6*, 117–128.

(4) Lewis, J. E. M.; Galli, M.; Goldup, S. M. *Chem. Commun.* **2017**, *53*, 298–312.

(5) Zappacosta, R.; Fontana, A.; Credi, A.; Arduini, A.; Secchi, A. *Asian J. Org. Chem.* **2015**, *4*, 262–270.

(6) Ye, K.; Zhang, Z.; Yan, Z.; Pang, S.; Yang, H.; Sun, X.; Liu, C.; Zhu, L.; Lian, C.; Bao, C. *Sci. China Chem.* **2023**, *66*, 2300–2308.

(7) Chen, S.; Wang, Y.; Nie, T.; Bao, C.; Wang, C.; Xu, T.; Lin, Q.; Qu, D. -H.; Gong, X.; Yang, Y.; Zhu, L.; Tian, H. *J. Am. Chem. Soc.* **2018**, *140*, 17992–17998.

(8) Pang, S.; Sun, X.; Yan, Z.; Wang, C.; Ye, K.; Ma, S.; Zhu, L.; Bao, C. *Chem. Commun.* **2023**, *59*, 3866–3869.

(9) Wang, C.; Wang, S.; Yang, H.; Xiang, Y.; Wang, X.; Bao, C.; Zhu, L.; Tian, H.; Qu, D. -H. *Angew. Chem., Int. Ed.* **2021**, *60*, 14836–14840.

(10) Akhtar, N.; Conthagamage, U. N. K.; Bucher, S. P.; Abdulsalam, Z. A.; Davis, M. L.; Beavers, W. N.; García-López, V. *Mater. Adv.* **2024**, *5*, 8534–8545.

(11) August, D. P.; Borsley, S.; Cockroft, S. L.; della Sala, F.; Leigh, D. A.; Webb, S. J. *J. Am. Chem. Soc.* **2020**, *142*, 18859–18865.

(12) Tay, H. M.; Johnson, T. G.; Docker, A.; Langton, M. J.; Beer, P. D. *Angew. Chem., Int. Ed.* **2023**, *62*, e202312745.

(13) Mondal, D.; Ahmad, M.; Dey, B.; Mondal, A.; Talukdar, P. *Nat. Commun.* **2022**, *13*, 6507.

(14) Saha, T.; Gautam, A.; Mukherjee, A.; Lahiri, M.; Talukdar, P. *J. Am. Chem. Soc.* **2016**, *138*, 16443–16451.

(15) Chattopadhayay, S.; Banzal, K. V.; Talukdar, P. *Angew. Chem., Int. Ed.* **2024**, e202414354.

(16) Malla, J. A.; Umesh, R. M.; Vijay, A.; Mukherjee, A.; Lahiri, M.; Talukdar, P. *Chem. Sci.* **2020**, *11*, 2420–2428.

(17) Johnson, T. G.; Sadeghi-Kelishadi, A.; Langton, M. J. *J. Am. Chem. Soc.* **2022**, *144*, 10455–10461.

(18) Huang, W. -L.; Wang, X. -D.; Ao, Y. -F.; Wang, Q. -Q.; Wang, D. -X. *J. Am. Chem. Soc.* **2020**, *142*, 13273–13277.

(19) Frisch, M. J.; Trucks, G. W.; Schlegel, H. B.; Scuseria, G. E.; Robb, M. A.; Cheeseman, J. R.; Scalmani, G.; Barone, V.; Petersson, G. A.; Nakatsuji, H.; Li, X.; Caricato, M.; Marenich, A. V.; Bloino, J.; Janesko, B. G.; Gomperts, R.; Mennucci, B.; Hratchian, H. P.; Ortiz, J. V.; Izmaylov, A. F.; Sonnenberg, J. L.; Williams-Young, D.; Ding, F.; Lipparini, F.; Egidi, F.; Goings, J.; Peng, B.; Petrone, A.; Henderson, T.; Ranasinghe, D.; Zakrzewski, V. G.; Gao, J.; Rega, N.; Zheng, G.; Liang, W.; Hada, M.; Ehara, M.; Toyota, K.; Fukuda, R.; Hasegawa, J.; Ishida, M.; Nakajima, T.; Honda, Y.; Kitao, O.; Nakai, H.; Vreven, T.; Throssell, K.; Montgomery, J. A., Jr.; Peralta, J. E.; Ogliaro, F.; Bearpark, M. J.; Heyd, J. J.; Brothers, E. N.; Kudin, K. N.; Staroverov, V. N.; Keith, T. A.; Kobayashi, R.; Normand, J.; Raghavachari, K.; Rendell, A. P.; Burant, J. C.; Iyengar, S. S.; Tomasi, J.; Cossi, M.; Millam, J. M.; Klene, M.; Adamo, C.; Cammi, R.; Ochterski, J. W.; Martin, R. L.; Morokuma, K.; Farkas, O.; Foresman, J. B.; Fox, D. J. *Gaussian 16, Revision C.01*, Gaussian, Inc., Wallingford CT, **2016**.

(20) Marrs, C. N.; Evans, N. H. *Org. Biomol. Chem.* **2015**, *13*, 11021–11025.

(21) Li, Y.; Dong, J.; Gong, W.; Tang, X.; Liu, Y.; Cui, Y.; Liu, Y. *J. Am. Chem. Soc.* **2021**, *143*, 20939–20951.

Chapter 4

Ligand-Gated *Meta*-Dipropynylbenzene-Based Trimeric Barrel-Rosette Ion Channel for Cation-Anion Cotransport

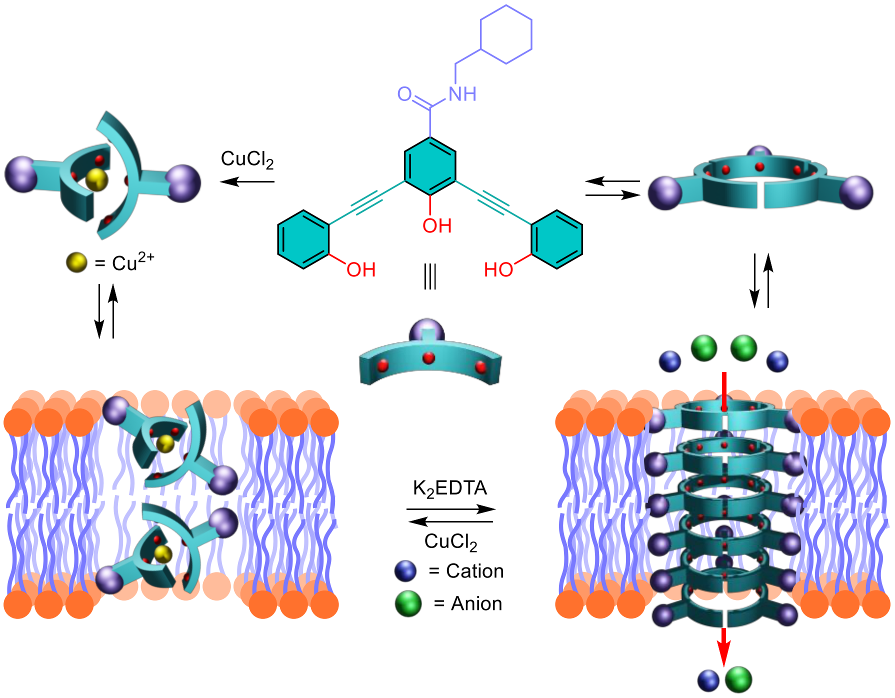

4.1. Introduction

The gating of ion channels is a common phenomenon for natural transmembrane proteins to regulate precise control over the ion transport process. In ***Chapters 2*** and ***3***, even though we successfully introduced different core motifs to decorate the cation-anion symporter ion channels, its transport activity cannot be controlled by using any stimulus. Cation-anion cotransport (CAC) is one class of trans-membrane proteins ubiquitous in our physiological systems for regulating versatile physiological functions.[1–5] Due to the complexity of the structure and function of these cotransporters, it now becomes a challenging task to decorate a synthetic mimic of cation-anion ion channels, which need precise and adequate binding sites that simultaneously hold cations and anions and translocate them across the bilayer membrane. For accurate and appropriate ion fluxes, nature-endowed gating mechanisms in the ionotropic receptors have various triggering mechanisms, including ligand-gated,[6,7] mechanosensitive,[8–10] chemosensitive,[11,12] etc. These ligand-gated ion channels mediate fast responses, affecting and maintaining the appropriate membrane potential. However, overwork or underwork of these transmembrane proteins obstruct ion translocation across the cellular membrane and create different diseases, collectively known as channelopathies.[13] Hence, decorating a synthetic alternation of these natural channels can be an alternative approach to providing a path for biomedical utilization of these synthetic ion channel systems.

Motivated by the fast and reversible response of these natural ligand-gated ion channels, Matile and coworkers devised an inaugural example of the synthetic ligand-gated ion channel.[14] They introduced the addition of the ligand, which triggered the cation transport process by forming the aggregation of the monomers. Subsequently, in 2005, they introduced an alternate strategy of ligand-gated activation of an ion channel system.[15] Where transport inactive helix–barrel undergoes a topological change upon intercalation of dialkoxynaphthalene (DAN) donors to form an open barrel stave ion channel. Although the examples mentioned above provide a direction for developing the ligand-gated ion channels, the irreversible nature remains a significant limitation. In 2006, Futaki and coworkers came up with an approach to decorating reversible ligand-gated response of a semisynthetic peptide ion channel.[16] Here, the addition of Fe(III) will bind with the extramembrane diiminoacetic acid derivatives of lysine (Ida) residues and destabilize the helix formation of the extramembrane peptide to provide a fast ion transport. The removal of the Fe(III) ion by adding EDTA helped the extramembrane peptide in regaining helical conformation and provided slow ion transport. Further, Webb and coworkers,[17,18] as well as Kinbara and coworkers,[19] introduced reversible ON-OFF ligand-gated ion channels by introducing different strategies. Although reversibility in the ion transport was achieved, the attempt was carried out either with cation or anion channels. In an effort to make a stimuli-activated cation-anion channel, in 2020, our group invented a vintage strategy of utilising GSH[20] and esterase[21] to activate the cation-anion cotransport. Even though we successfully developed a ligand-responsive and enzyme-responsive cation-anion channel, this activation process remains irreversible.

On the contrary, an acylhydrazone-based ion Na^+Cl^- cotransporter was reported from our group in which we successfully made an OFF-ON transport response in the presence of light.[22] Although a successful attempt was made to make a reversible stimuli-responsive cation-anion cotransport system, it emerges as a carrier.

To the best of our knowledge, till now, none of the reversibly stimuli-gated responses have been achieved with the cation-anion channels. Hence, the unavailability of the reversible stimuli-gated cation-anion channel continuously stimulates us to decorate a synthetic mimic in which the reversible OFF-ON transport activity can be achieved.

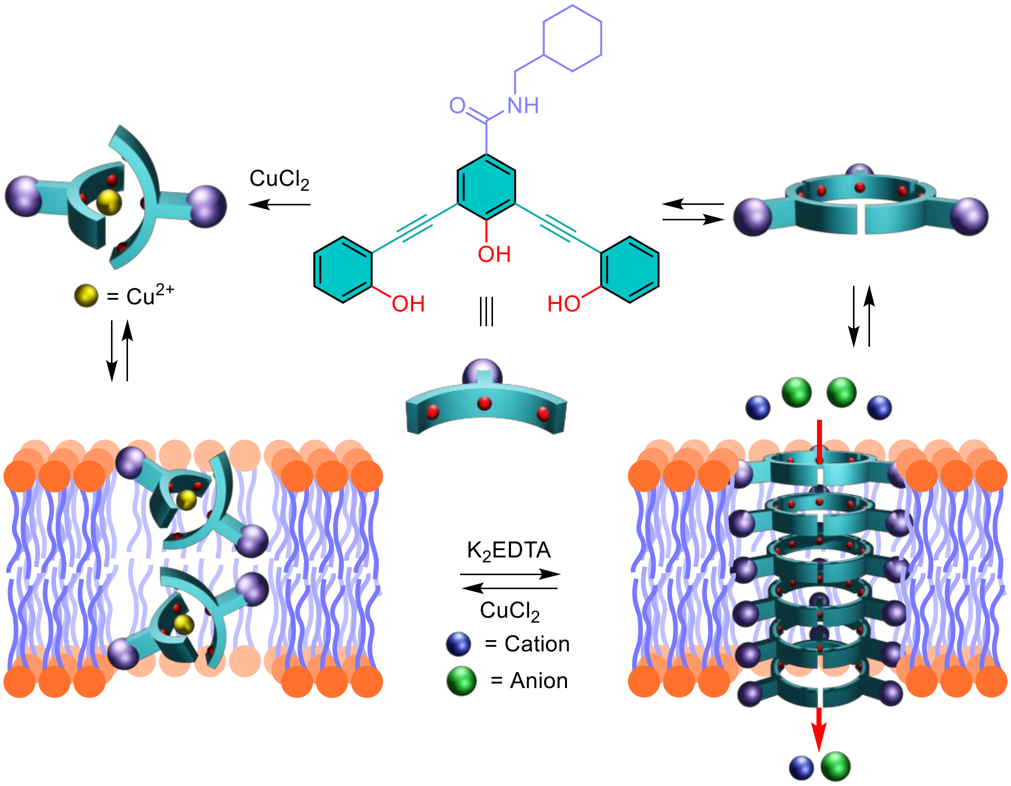

Figure 4.1 Structure of channel-forming compound **1** and its ligand-gated reversible OFF-ON cotransport activity in the presence of $CuCl_2$ and K_2EDTA across the bilayer membrane.

Herein, for the first time, we introduced a reversible ligand-gated *meta*-dipropynylbenzene-based barrel rosette ion channel having reversible OFF-ON cation-anion transport properties across the bilayer membrane (Figure 4.1). The dual binder triphenolic core was installed in the selectivity filter to bind cation and anion. A rigid acetylene unit was connected to make the molecule more reorganized. Installing an amide linker will help form an efficient aggregation to enhance the self-assembly of the molecule by forming the intermolecular H-bonding. It is expected that the addition of $CuCl_2$ with compound **1** gives a dimeric $Cu^{2+}\cdot(\mathbf{1})_2$ complex and blocks their ion binding sites, and hence, it will not form any assembled channel in the bilayer membrane. The addition of dipotassium ethylenediaminetetraacetic acid (K_2EDTA) will remove the Cu^{2+} from $Cu^{2+}\cdot(\mathbf{1})_2$ complex and generate the free compound **1**, which can assembled in the bilayer to give rise to a self-assembled barrel-rosette ion channel. Hence, it is expected the sequential addition of $CuCl_2$ and K_2EDTA can reversibly OFF-ON the transport activity of compound **1** in the bilayer membrane.

4.2. Results and discussions

4.2.1. Synthesis

Initially, compound **2** was coupled with cyclohexylmethanamine in the presence of the EDC·HCl and HOBt as coupling agents in the presence of NEt_3 base and DMF solvent to obtain compound **3**. Sonogashira coupling was carried out on compound **3** and trimethylsilylacetylene in the presence of the $PdCl_2(PPh_3)_2$ and CuI catalyst in *N*,*N*-Diisopropylethylamine (DIPEA) as a solvent under 60 °C to obtain the compound **4**. Desilylation was further carried out by reacting compound **4** with tetra-n-butylammonium fluoride in MeOH solvent to obtain compound **5**. Compound **5** was further coupled with the 1-iodo-2-methoxybenzene at room temperature by using the Sonogashira coupling utilizing $PdCl_2(PPh_3)_2$ and CuI catalysts in triethylamine (NEt_3) as a solvent to synthesize compound **6**. Finally, the demethylation of all three methyl groups in compound **6** with 1 M BBr_3 solution in dichloromethane (DCM) provided our desired compound **1** with a significant yield.

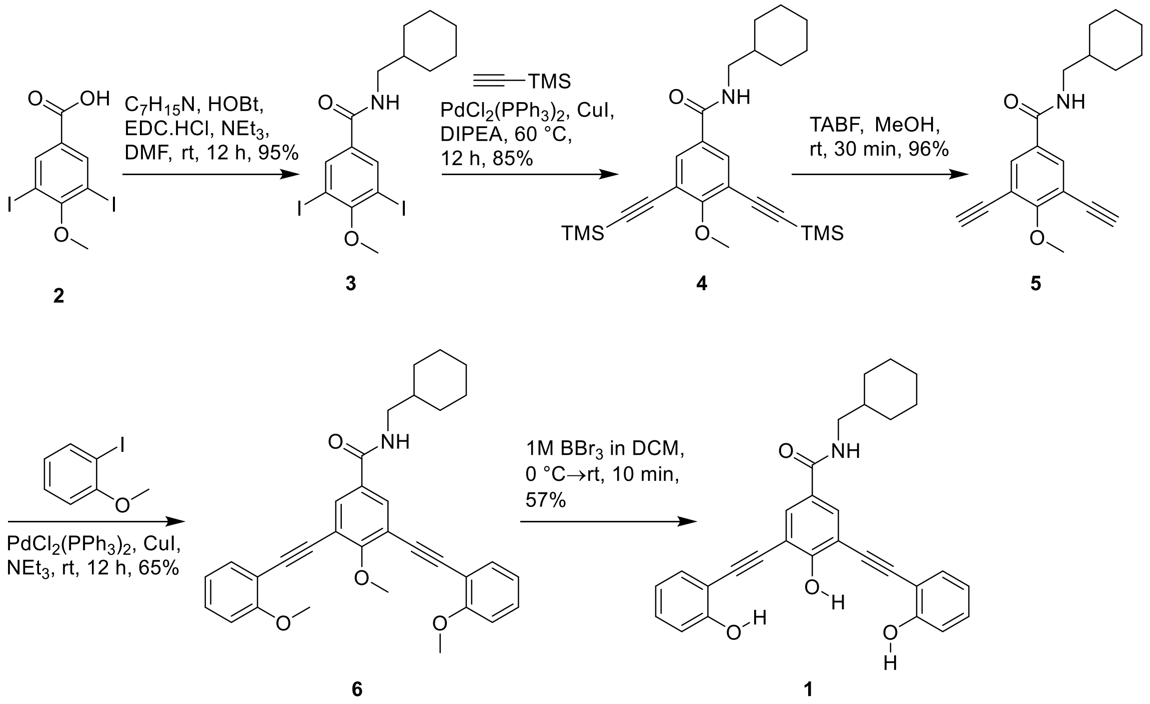

Scheme 4.1 Synthetic scheme for the compound **1**.

4.2.2. Self-assembly and morphological studies

To understand the self-assembly of compound **1**, concentration-dependent ^{1}H NMR was taken in $CHCl_3$ solvent at 25 °C. Increasing the concentration of **1** increases the downfield shift of the H_a proton and increases the upfield shift of H_b, H_c, H_d, and H_f protons (Figure 4.5). This data indicated the formation of the self-aggregated structure via the formation of intermolecular H-bonding and π-π stacking interactions. Further, Field emission scanning electron microscopy (FESEM) was utilized to investigate the morphological pattern of channel **1** at different concentrations. Compound **1** formed a helical fibril morphology (Figure 4.6), which divulged that compound **1** has strong aggregation due to the formation of intermolecular H-bonding and π-π stacking interactions.

4.2.3. Ion transport studies

Initially, the transport activity of compound **1** was investigated using HPTS assay by entrapping the pH-sensitive 8-hydroxypyrene-1,3,6-trisulfonic acid trisodium salt (HPTS, $pK_a = 7.2$) dyes in egg yolk phosphatidylcholine large unilamellar vesicles (EYPC–LUVs).[23,24] Concentration-dependent studies of compound **1** indicated the efficient transport activity of compound **1** across the vesicular membranes. Hill analysis (Figure 4.8B) validated compound **1** has a half-maximal effective concentration (EC_{50}) value (4.57 ± 0.1 µM, 6.74 mol% with respect to the lipid) and Hill coefficient (n) ≈ 3, validating the involvement of the three monomeric units to form an active rosette structure in the membrane. An ion selectivity study[25,26] by varying the extravesicular anions or cations validates the involvements of both cations and anions in the transport process. The cation selectivity studies validate the activity sequence of $K^+ > Rb^+ > Cs^+ > Na^+ > Li^+$ (Figure 4.2A), and anion selectivity also confirms the activity sequence $Cl^- > Br^- > NO_3^- > I^- > ClO_4^-$ (Figure 4.2B). The observed selectivity demonstrated both the hydration energy and the size overall governed the ion selectivity of compound **1** (Figure 4.11). To delve into the mechanistic insight of the transport process, both Valinomycin[27] (Figure 4.2C) and NO_3^-/SO_4^{2-} assay[28] (Figure 4.2D) were conducted by entrapping the halide-sensitive lucigenin dye. These two mechanistic studies concluded that compound **1** primarily follows the symport mechanism during the transmembrane transport.

To understand the physiologically relevant Cl^- ion transport by compound **1**, a lucigenin assay was conducted by entrapping the lucigenin in egg yolk phosphatidylcholine large unilamellar vesicles (EYPC–LUVs). A concentration-dependent study with compound **1** confirmed its ability to flux the Cl^- ions across the membrane. Hill analysis provided compound **1** has $EC_{50} = 6.29 \pm 0.67$ µM and Hill coefficient (n) ≈ 3, which corroborated with the HPTS assay. Further cation selectivity by varying the extravesicular cations across EYPC–LUVs⊃Lucigenin reconfirmed the involvement of the cation in the overall transport process. Additionally, the ^{39}K NMR was used to quantify the rate of the K^+ ion transport across the EYPC–LUVs in

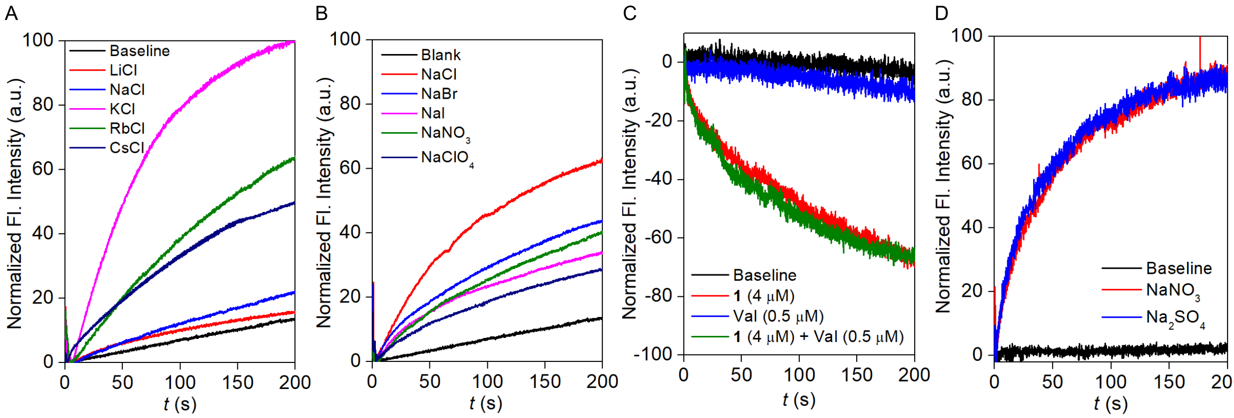

Figure 4.2 Cation (A) and anion (B) selectivity of compound **1** across EYPC–LUVs⊃HPTS. Change in Cl^- influx by compound **1** in the presence and absence of valinomycin across EYPC−LUVs⊃lucigenin (C). Change in Cl^- efflux by compound **1** in the presence of intravesicular Cl^- and either SO_4^{2-} or NO_3^- as an iso-osmolar extravesicular anion across EYPC−LUVs⊃lucigenin (D).

the presence of a $Na_7Dy(P_3O_{10})_2 \cdot 3NaCl$ shift regent (Figure 4.17).[29–31] A change in the line width of the external K^+ ion peak was monitored in the presence of the different concentrations of compound **1**. The K^+ ion transport rate measurement through line width alteration confirmed that compound **1** effectively facilitates K^+ ion translocation across the membrane.

Realizing the presence of the phenolic hydroxyl (–OH) groups in the selectivity filter, pH-dependent cation selectivity was investigated by varying the extravesicular MCl salts ($M^+ = Na^+, K^+$) across EYPC−LUVs⊃lucigenin with a different range of extravesicular pH = 4.0–8.0.[32] Interestingly, an increase or decrease in pH diminished the cation selectivity of channel **1**, whereas, in the physiological pH range (pH = 7.0–7.4), channel **1** retains its cation selectivity (Figure 4.3A). This data justifies the pH-dependent ion transport behaviour and possesses the cation selectivity pattern under the physiological pH range (pH = 7.0-7.4). Hence, compound **1** can behave as a cation-anion channel under the physiological pH range.

Electrophysiological experiments were carried out to get insight into the mode of ion transport by compound **1**.[20] A real-time opening-closing event at different holding potentials was observed in the presence of a symmetrical 1 M KCl solution (10 mM HEPES, 1 M KCl, pH = 7.0) with compound **1** (5 μM), confirming the formation of an ion channel in the membrane during the ion transport process. The calculated average diameter of channel **1** was found to be 6.7 ± 1 Å, and the average single channel conductance was 375.5 pS (Table 4.1). Moreover, the ion selectivity studies of compound **1** with cis/trans = 1 M KCl/ 0.5 M KCl, confirmed that even though channel **1** transports both K^+ and Cl^- ions slightly preferential permeability towards the K^+ ion ($P_{Cl^-}/P_{K^+} = 0.35 \pm 0.9$) (Figure 4.22, Table 4.2). Furthermore, evaluation of the anion/anion and cation/cation selectivity validated the permeability ratio $P_{K^+}/P_{Na^+} = 3.5 \pm 0.8$ (Table 4.3) and $P_{Cl^-}/P_{Br^-} = 2.6 \pm 0.4$ (Table 4.4) with cis/trans = 1.0 M NaCl/1.0 M KCl cis/trans = 1.0 M NaCl/1.0 M NaBr setup respectively. Both ion selectivity validated that channel **1** has preferential selectivity towards the K^+ and Cl^- ions over the Na^+ and Br^- ions, respectively.

Before investigation of its ligand-gated response towards the ion transport process, UV-vis absorption spectra of the compound **1** (60 µM) were checked in the CH_3CN:HEPES (3:2, v/v, pH = 7.4) solution to understand the stoichiometric ratio of the host-guest complex. A prominent change in the UV-vis absorption spectra in the presence of the sequential addition of the $CuCl_2$ solution validated its effective binding with the Cu^{2+} ion. Change in the absorbance at $\lambda = 288$ nm was used for the Job's plot (Figure 4.18B), which confirmed the formation of the 2:1 host:guest complex between the compound **1** and Cu^{2+} ion. Cu^{2+} binding

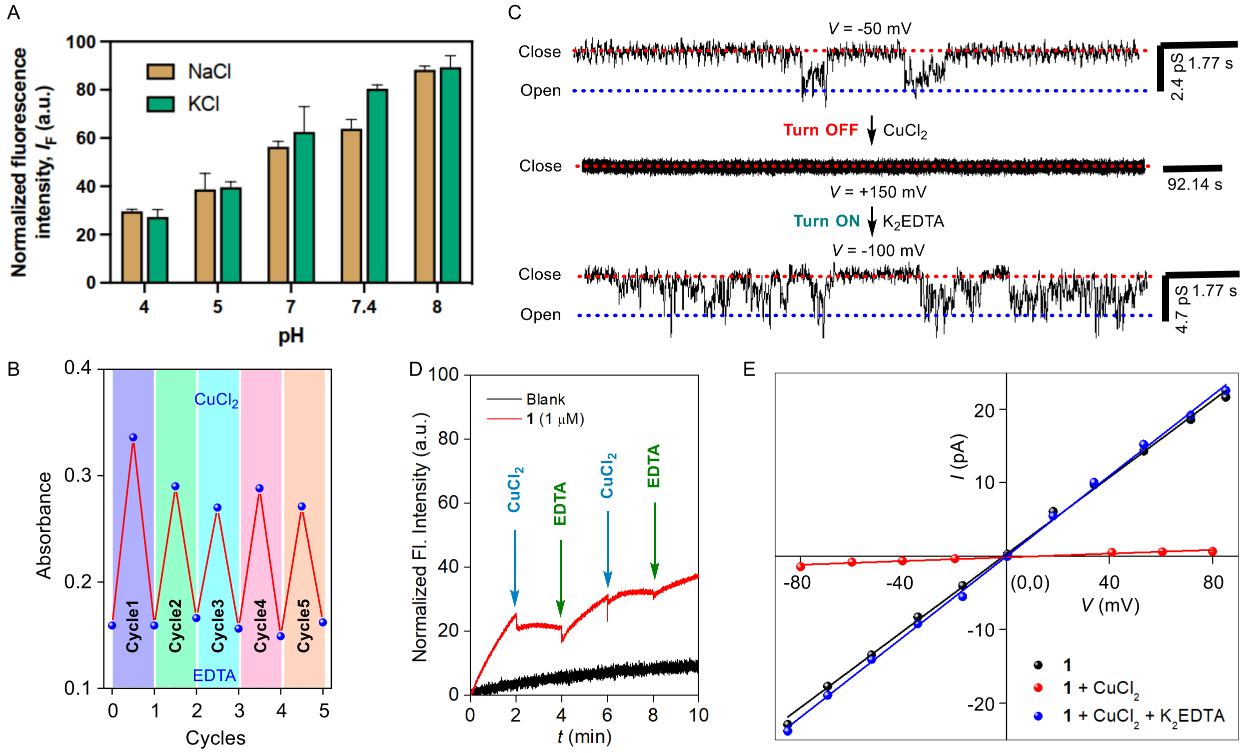

Figure 4.3 Cation selectivity of channel **1** (10 µM) at different pH ranges 4.0–8.0 (A). Ligand binding and unbinding cycles with the sequential addition of $CuCl_2$ and K_2EDTA in CH_3CN:HEPES (3:2 v/v, pH = 7.0) solution (B). Ligand-gated reversible OFF-ON opening-closing events of channel forming compound **1** in the presence of the $CuCl_2$ and K_2EDTA under symmetric 1 M KCl buffer (10 mM HEPES, 1 M KCl, pH = 7.0) (C). Reversible OFF–ON transport activity of channel **1** across EYPC–LUVs⊃HPTS with sequential addition of $CuCl_2$ and EDTA (D). Change in the *I*-*V* plot of channel forming compound 1 in the presence of the $CuCl_2$ and K_2EDTA under symmetric 1 M KCl buffer (10 mM HEPES, 1 M KCl, pH = 7.0) (E).

and unbinding cycles was further evaluated with the sequential addition of $CuCl_2$ (1 equiv) and K_2EDTA (1.1 equiv) in CH_3CN:HEPES (3:2 v/v, pH = 7.0) solution. Interestingly, even after five cycles, efficient Cu^{2+} binding and unbinding were noticed, validating its reversible response towards the ligands (Figure 4.3B). The effect of the reversible ligand binding in the ion transport process was further investigated by entrapping KCl salt and HPTS dye across EYPC–LUVs. A prominent increment in the HPTS fluorescence activity after the addition of the base pulse validated its efficient ion transport activity across the membrane. Interestingly, the addition of the $CuCl_2$ halts the ion transport activity (OFF state) due to the formation of the $Cu^{2+}\cdot(\mathbf{1})_2$ complex, whereas the addition of the K_2EDTA rapidly turns ON the ion transport activity by decomplexation of the channel-forming compound **1** from the $Cu^{2+}\cdot(\mathbf{1})_2$ complex (Figure 4.3D). This data indicated compound **1** can be utilized as a reversible ligand-gated ion channel system. Moreover, the real OFF-ON of the channel activity of compound **1** was investigated by using the bilayer lipid membrane (BLM) experiment (Figure 4.3C). The addition of compound **1** (5 μM) in the cis chamber rapidly triggered the opening-closing events, validating the efficient insertion of channel **1** in the membrane. Further, 1 equiv of the $CuCl_2$ was added in the cis chamber, and opening-closing events were monitored at different holding potentials. Interestingly, no opening-closing events were observed after the addition of the $CuCl_2$, validating Cu^{2+} disassembling the channel by forming the $Cu^{2+}\cdot(\mathbf{1})_2$ complex, which shows the OFF state of the channel formation. To regain its channel formation ability 1.1 equiv of K_2EDTA was added. Notably, the addition of the K_2EDTA instantaneously turns ON the opening-closing events by decomplexing the channel forming molecule **1** from the $Cu^{2+}\cdot(\mathbf{1})_2$ complex. Additionally, the change in the *I-V* plot before and after adding the $CuCl_2$ and K_2EDTA ligands was investigated (Figure 4.3E). It is noteworthy that before the addition of $CuCl_2$, the channel-forming compound **1** could efficiently flux the ions, and as a result, a prominent change in the current was noticed with a change in the voltage. However, after the addition of $CuCl_2$, a negligible change in the current was observed, with a change in the voltage validating its OFF state. The addition of the K_2EDTA rapidly enhances the current flux with the voltage, which is comparable with the initial *I-V* plot. This data indicated that the addition of the K_2EDTA turned ON the transport process, and hence, the change in the current with the voltage reached a comparable value to its initial state.

4.2.4. Theoretical calculations

Finally, molecular dynamics (MD) simulation of the trimeric rosette was investigated with the K^+Cl^- salts to understand the channel formation by compound **1** and the selectivity pattern. The detailed MD simulation studies revealed the efficient transport of K^+ and Cl^- through the translocation pathway of the trimeric rosette of compound **1** (Figure 4.4A) under a favourable H_2O rich environment (Figure 4.26A). Quantitative estimation of K^+ and Cl^- ion transport suggests the transport of more cations compared to that of the anions through the channel (Figure 4.4B, C), most likely attributed to the smaller size of the K^+ ions relative to the larger Cl⁻ ions. This data corroborated with experimentally observed selectivity data. Additionally, in an in-depth investigation of mechanistic insights into ion transport, it was noticed that both ions pass through the channel by making favourable contact with the channel residues (Figure 4.26B). Interestingly, it was noticed that the number of ion and channel contacts is higher in the case of the K^+ ion over the Cl^- ion, which might be the controlled parameter of reflecting the higher K^+ ion permeation over the Cl^- ion permeation.

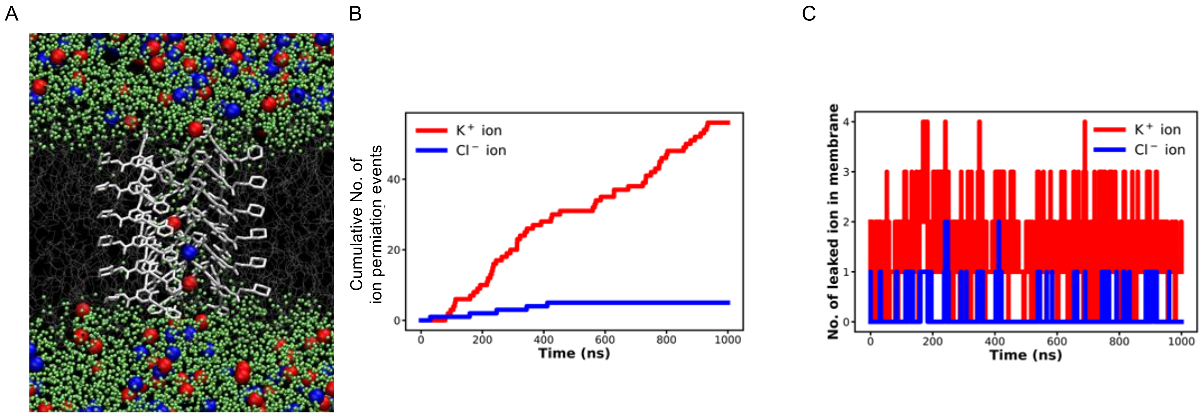

Figure 4.4 A representative snapshot depicting the transport of K^+ and Cl^- ions (shown in red and blue spheres, respectively) and water (represented by green spheres) through the synthetic channel embedded within the membrane separating the two aqueous compartments containing 1 M KCl salt (A). The count of K^+ (red) and Cl^- (blue) ions permeation events through the channel embedded in membrane from one compartment to the other during the course of simulation. The count of leaked K^+ (red) and Cl^- (blue) ions in membrane through the channel structure.

4.3. Conclusion

In conclusion, here we introduced the first example of a reversible ligand-gated cation-anion symporting barrel rosette ion channel. Scrutinizing the ion selectivity and mechanistic study with compound **1** confirmed its selectivity towards cations and anions with promising selectivity towards K^+ and Cl^- ions and follows a symport mechanism. The rate of K^+ transport by compound **1** was further evaluated using the ^{39}K NMR, conforming to the increment of the rate of K^+ transport with an increase in the concentration of compound **1**. A concentration-dependent study in lucigenin assay confirmed its ability to transport Cl^- ion across the vesicular membrane. Detailed electrophysiological experiments divulged the formation of an ion channel inside the bilayer with an average diameter of 6.7 ± 1 Å and an average single channel conductance of 375.5 pS. An investigation of the ion selectivity confirmed that compound **1** has approximately 2.8 times higher permeability towards K^+ ion than Cl^- ion. Further, cation/cation and anion/anion selectivity validated channel **1** is approximately 3.5 times and 2.6 times higher permeable towards the K^+ and Cl^- ions over the Na^+ and Br^- ions, respectively. pH-dependent cation selectivity confirmed that compound **1** showed the cation selectivity at physiological pH ranges. In contrast, the cation selectivity was lost at lower or higher pH values, validating channel **1** showed cation-action transport under physiological pH (7.0-7.4) ranges. Ligand-gated chelation studies confirmed channel **1** formed a 2:1 complex with Cu^{2+} ion, and the addition of K_2EDTA removed the chelated Cu^{2+} ion from the complex and regenerated free channel **1**. A reversible chelation-deceleration upon sequential addition of $CuCl_2$ and K_2EDTA conformed channel **1** showed efficient complexation and decomplexation even after five cycles. The ligand-gated reversible OFF-ON ion transport process was checked sequentially adding $CuCl_2$ and K_2EDTA using fluorescence and electrophysiological experiments, confirming that compound **1** can be utilized as a reversible ligand-gated cation-anion channel. Finally, molecular dynamics simulation was investigated with the hexameric layer of the trimeric rosette to unveil the ion translocation pathways and investigate the reason for the higher permeability of the channel towards K^+ ion compared to the Cl^- ion, which showed well agreement with the experimental results. Hence, we believe the development of this ligand-gated reversible OFF-ON cation-anion symporter ion channel can pave a new avenue for generating synthetic reversible stimuli-gated cation-anion synthetic channel systems.

4.4. Experimental section

4.4.1. General methods

Reagents and compounds used for the synthesis were purchased from Sigma-Aldrich, Avra Chemicals, Spectrochem, BLDpharm and used without further purification. For dry reaction MeOH, DMF, and DCM, were purchased from commercial suppliers and used without further purification. All the reactions were performed under a nitrogen atmospheric environment using an N_2 gas balloon and monitored by checking TLC, performed on pre-coated aluminum plates of silica gel 60 F254 (0.25 mm, E. Merck). Column chromatographies were performed on Merck silica gel (100–200 mesh). Egg yolk phosphatidylcholine (EYPC) was obtained from Avanti Polar Lipids as a solution in $CHCl_3$ (25 mg/mL). HEPES buffer, HPTS, Lucigenin, Triton X–100, NaOH, and inorganic salts were purchased of molecular biology grade from Sigma. Large unilamellar vesicles (LUVs) were prepared by using a mini extruder, equipped with a polycarbonate membrane of 100 nm or 200 nm pore size, purchased from Avanti Polar Lipids.

4.4.2. Physical measurements

The ^{1}H NMR spectra were recorded at 400 MHz and ^{13}C spectra at 101 MHz in Bruker NMR instruments. The residual (deuterium) solvent signals were considered as an internal reference (δH = 7.26 ppm for $CDCl_3$, δH = 2.50 for DMSO-d_6) to calibrate spectra. All the chemical shifts were reported in ppm. The following abbreviations were used to indicate multiplicity patterns s: singlet, d: doublet, t: triplet, q: quartet, m: multiplet, dd: doublet of doublets, ddd: doublet of doublet of doublets, td: triplet of doublets, dt: doublet of triplets. Coupling constants were measured in Hz. High-resolution mass spectra (HRMS) were recorded on electrospray ionization time-of-flight (ESI–TOF) with +ve mode. Adjustment of pH of buffer solutions was made using Hanna HI98108 PHep$^+$ pH meter. ChemBio Draw 21.0.0 software was used to draw structures and process figures. All buffer solutions were prepared from the autoclaved water. Fluorescence experiments were recorded on Fluoromax-4 from Jobin Yvon Edison, equipped with an injector port and magnetic stirrer in a microfluorescence cuvette. The extravesicular dye was removed by performing gel chromatography using Sephadex G-50. The fluorescence studies have proceeded using Origin 8.5 software. Conductance measurement through ion channel was carried out in a planar bilayer lipid membrane (BLM) workstation obtained from Warner Instrument, consisting of head-stage and its corresponding amplifier BC-535, 8-pole bessel filter LPF-8, Axon CNS Digidata 1440A, and pClamp 10 software. The conductance data were analyzed using Clampfit 10.6 software.

4.4.3. Synthetic procedures

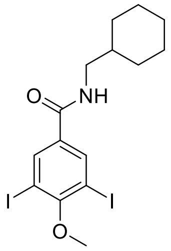

Synthesis of *N*-(cyclohexylmethyl)-3,5-diiodo-4-methoxybenzamide (3): In a 25 mL round bottom flask, compound **2** (600 mg, 1.49 mmol, 1 equiv) was dissolved in dry DMF (8 mL). To the clear solution, EDC·HCl (427 mg, 2.23 mmol, 1.5 equiv), HOBt (241 mg, 1.78 mmol, 1.2 equiv) and triethyl amine (621 µL, 4.46 mmol, 3 equiv), was added and the solution was stirred at room temperature for 30 min. Cyclohexylmethanamine (194 µL, 1.49 mmol, 1 equiv) was added, and stirring was continued at room temperature for 12 h. After completion of the reaction, the solution was transferred to a separating funnel with ethyl acetate (3 × 15 mL) and washed with H_2O (20 mL). The combined organic layer was then washed with brine solution (3 × 15 mL) and finally dried over the Na_2SO_4. The crude product was purified by 100–200 mesh silica gel column chromatography (Eluent: 14% EtOAc/PE) to obtain pure compound **3** (Yield = 707 mg, 95%). **^{1}H NMR (400 MHz, $CDCl_3$)** δ 8.13 (s, 2H), 6.04 (s, 1H), 3.88 (s, 3H), 3.27 (dd, *J* = 6.9, 6.0 Hz, 2H), 1.79 – 1.72 (m, 4H), 1.68 (dt, *J* = 10.4, 1.7 Hz, 1H), 1.32 – 1.11 (m, 4H), 1.04 – 0.92 (m, 2H). **^{13}C NMR (101 MHz, $CDCl_3$)** δ 164.23, 161.45, 138.67, 134.36, 90.66, 77.16, 60.93, 46.62, 38.12, 31.04, 26.48, 25.92. **HRMS (ESI) m/z:** $[M+H]^+$ Calcd. for $C_{15}H_{19}I_2NO_2H^+$ 499.9585; Found 499.9583. **IR (Neat, ν/cm^{-1}):** 3277, 3081, 2920, 2845, 1634, 1580, 1550, 1528, 1456, 1411, 1368, 1306, 1253, 1150, 1056, 992, 893, 745, 697, 641.

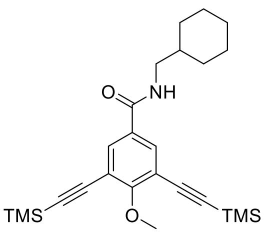

Synthesis of *N*-(cyclohexylmethyl)-4-methoxy-3,5-bis((trimethylsilyl)ethynyl)benzamide (4): In a clean and dry 25 mL round bottom flask, compound **3** (700 mg, 1.4 mmol, 1 equiv) was dissolved in 18 mL *N*,*N*-Diisopropylethylamine (DIPEA). Then $PdCl_2(PPh_3)_2$ (59 mg, 0.08 mmol, 0.06 equiv) and CuI (16 mg, 0.08 mmol, 0.06 equiv) were added into it and kept at room temperature under stirring conditions for 20 min. Trimethylsilylacetylene (0.6 µL, 4.21 mmol, 3 equiv) was added to the reaction mixture and kept the reaction mixture at 60 °C for 12 h. After completion of the reaction, the solution was filtered through the celite bed and washed properly with EtOAc. The filtrate was the concentrate, and the crude product was purified by 100–200 mesh silica gel column chromatography (Eluent: 5% EtOAc/PE) to obtain pure compound **3** (Yield = 371 mg, 60%). **^{1}H NMR (400 MHz, CDCl$_3$)** δ 7.75 (s, 2H), 6.03 (t, *J* = 5.4 Hz, 1H), 4.09 (s, 3H), 3.26 (dd, *J* = 6.9, 6.0 Hz, 2H), 1.78 – 1.72 (m, 4H), 1.68 (d, *J* = 10.3 Hz, 1H), 1.22 (ddd, *J* = 22.6, 10.6, 3.1 Hz, 4H), 0.99 (td, *J* = 11.1, 10.5, 2.2 Hz, 2H), 0.26 (s, 18H). **^{13}C NMR (101 MHz, CDCl$_3$)** δ 165.68, 164.74, 132.80, 129.90, 117.22, 100.56, 99.97, 77.16, 61.15, 46.47, 38.15, 31.04, 26.51, 25.94, -0.07. **HRMS (ESI) m/z:** [M+H]$^+$ Calcd. for $C_{25}H_{37}NO_2Si_2H^+$ 440.2436; Found 440.2431. **IR (Neat, ν/cm^{-1}):** 3292, 2923, 2852, 2159, 1635, 1547, 1466, 1416, 1327, 1248, 1005, 840, 758, 699, 651.

Synthesis of *N*-(cyclohexylmethyl)-3,5-diethynyl-4-methoxybenzamide (5): In a cleaned and dry round bottom flask, compound **4** (350 mg, 0.8 mmol, 1 equiv) was dissolved in 7 mL dry MeOH. Then, the required amount of TBAF (625 mg, 2.4 mmol, 3 equiv) was added to it, and the reaction mixture was kept under stirring conditions at room temperature for 30 min. After completion of the reaction, the reaction mixture was poured into a separating funnel with ethyl acetate (3 × 15 mL) and washed with H_2O (15 mL). The combined organic layers were then washed with brine solution (3 × 10 mL) and finally dried over the Na_2SO_4, and the solvent was evaporated on a rotary evaporator. The crude product **5** was purified by 100–200 mesh silica gel column chromatography (Eluent: 16% EtOAc/PE) to obtain pure compound **5** (Yield = 225 mg, 96%). **^{1}H NMR (400 MHz, CDCl$_3$)** δ 7.84 (s, 2H), 6.06 (s, 1H), 4.12 (s, 3H), 3.33 (s, 2H), 3.28 (dd, *J* = 6.9, 6.0 Hz, 2H), 1.80 – 1.71 (m, 4H), 1.71 – 1.65 (m, 1H), 1.27 – 1.16 (m, 4H), 1.00 (td, *J* = 11.8, 3.2 Hz, 2H). **^{13}C NMR (101 MHz, CDCl$_3$)** δ 165.50, 165.09, 133.60, 130.16, 116.27, 82.92, 78.78, 77.16, 61.64, 46.50, 38.11, 31.03, 26.49, 25.93. **HRMS (ESI) m/z:** [M+H]$^+$ Calcd. for $C_{19}H_{21}NO_2H^+$ 296.1645; Found 296.1650. **IR (Neat, ν/cm^{-1}):** 3294, 3076, 2923, 2851, 1638, 1592, 1547, 1467, 1324, 1232, 1182, 1000, 762.

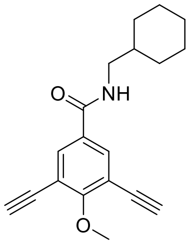

Synthesis of *N*-(cyclohexylmethyl)-4-methoxy-3,5-bis((2-methoxyphenyl)ethynyl) benzamide (6): In a clean and dry 25 mL round bottom flask, 1-iodo-2-methoxybenzene (499 mg, 2.1 mmol, 3 equiv) was dissolved in 15 mL triethylamine. Then $PdCl_2(PPh_3)_2$ (30 mg, 0.04 mmol, 0.06 equiv) and CuI (8 mg, 0.04 mmol, 0.06 equiv) were added into it and kept at room temperature under stirring conditions for 20 min. Compound **5** (210 mg, 0.7 mmol, 1 equiv) was added to the reaction mixture, and the reaction mixture was kept at room temperature for 12 h. After completion of the reaction, the solution was filtered through the celite bed and washed properly with EtOAc. The filtrate was the concentrate, and the crude product was purified by 100–200 mesh silica gel column

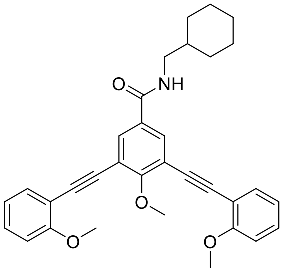

chromatography (Eluent: 12% EtOAc/PE) to obtain pure compound **3** (Yield = 235 mg, 65%). **^{1}H NMR (400 MHz, DMSO-d_6)** δ 8.59 (t, J = 5.7 Hz, 1H), 7.99 (s, 2H), 7.51 (dd, J = 7.5, 1.7 Hz, 2H), 7.43 (ddd, J = 8.4, 7.4, 1.7 Hz, 2H), 7.12 (dd, J = 8.5, 1.0 Hz, 2H), 7.01 (td, J = 7.5, 1.0 Hz, 2H), 4.17 (s, 3H), 3.88 (s, 6H), 3.14 – 3.07 (m, 2H), 1.74 – 1.62 (m, 4H), 1.59 – 1.49 (m, 1H), 1.28 – 1.08 (m, 4H), 0.92 (q, J = 10.9, 9.6 Hz, 2H). **^{13}C NMR (101 MHz, DMSO-d_6)** δ 164.06, 162.69, 159.85, 132.97, 132.09, 130.78, 130.01, 120.57, 116.62, 111.47, 111.01, 91.03, 88.37, 60.98, 55.74, 45.59, 39.52, 37.34, 30.54, 26.06, 25.43. **HRMS (ESI) m/z:** $[M+H]^+$ Calcd. for $C_{33}H_{33}NO_4H^+$ 508.2482; Found 508.2487. **IR (Neat, ν/cm^{-1}):** 3313, 2923, 2850, 2214, 1637, 1544, 1493, 1464, 1435, 1413, 1357, 1275, 1247, 1180, 1111, 1046, 1024, 1000, 898, 798, 693.

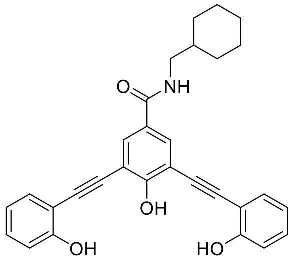

Synthesis of *N*-(cyclohexylmethyl)-4-hydroxy-3,5-bis((2-hydroxyphenyl)ethynyl)benzamide (1): In a 25 mL round bottom flask, compound **6** (50 mg, 0.1 mmol, 1 equiv) was dissolved in 1 mL dry DCM and kept it at 0 °C for 10 min. A BBr_3 in 1 M DCM solution (1 mL, 0.1 mmol, 10 equiv) was added to the reaction mixture at 0 °C and continued stirring for 10 min. After completion of the reaction, ice-cold water (3-4 mL) was slowly added to the reaction mixture. The solution was transferred to a separating funnel with ethyl acetate (3 × 15 mL) and washed with H_2O (20 mL). The combined organic layer was then washed with brine solution (3 × 15 mL) and dried over the Na_2SO_4. The crude product was purified by 100–200 mesh silica gel column chromatography (Eluent: 2% MeOH/$CHCl_3$) to obtain pure compound **1** (Yield = 26 mg, 57%). [**NOTE:** During the synthesis of compound **1**, a maximum of 50 mg of compound **6** was used, and yield was calculated accordingly]. **^{1}H NMR (400 MHz, DMSO-d_6)** δ 10.07 (s, 1H), 9.97 (s, 2H), 8.47 (t, J = 5.7 Hz, 1H), 7.94 (s, 2H), 7.46 (dd, J = 7.7, 1.7 Hz, 2H), 7.24 (ddd, J = 8.6, 7.4, 1.8 Hz, 2H), 6.93 (dd, J = 8.3, 1.1 Hz, 2H), 6.85 (td, J = 7.5, 1.1 Hz, 2H), 3.09 (t, J = 6.3 Hz, 2H), 1.74 – 1.64 (m, 4H), 1.61 – 1.53 (m, 1H), 1.26 – 1.11 (m, 4H), 0.96 – 0.84 (m, 2H). **^{13}C NMR (101 MHz, DMSO-d_6)** δ 164.41, 159.52, 158.17, 132.98, 131.79, 130.26, 126.26, 119.19, 115.65, 111.30, 109.77, 91.44, 88.18, 45.51, 39.52, 37.38, 30.57, 26.10, 25.44. **HRMS (ESI) m/z:** $[M+H]^+$ Calcd. for $C_{30}H_{27}NO_4H^+$: 466.2013, Found 466.2018. **IR (Neat, ν/cm^{-1}):** 3346, 2923, 2852, 1632, 1584, 1449, 1285, 1243, 1103, 1033, 749.

4.4.4. Self-assembly and morphological studies

4.4.4.1. Concentration-dependent ^{1}H NMR study

Self-assembly studies of compound **1** was investigated through the concentration-dependent ^{1}H NMR in $CDCl_3$ solvent at 25 °C in Bruker 400 MHz NMR instrument. An increase in the concentration of the compound increases the downfield shift of the N-H_a proton, indicating the formation of the intermolecular H-bonding with an increase in the concentration of compound **1**. Moreover, the upfield shift of the aromatic

C–H_b, C–H_c, C–H_d, C–H_e, and C–H_f protons also validates the presence of the π-π stacking during the assembly process.

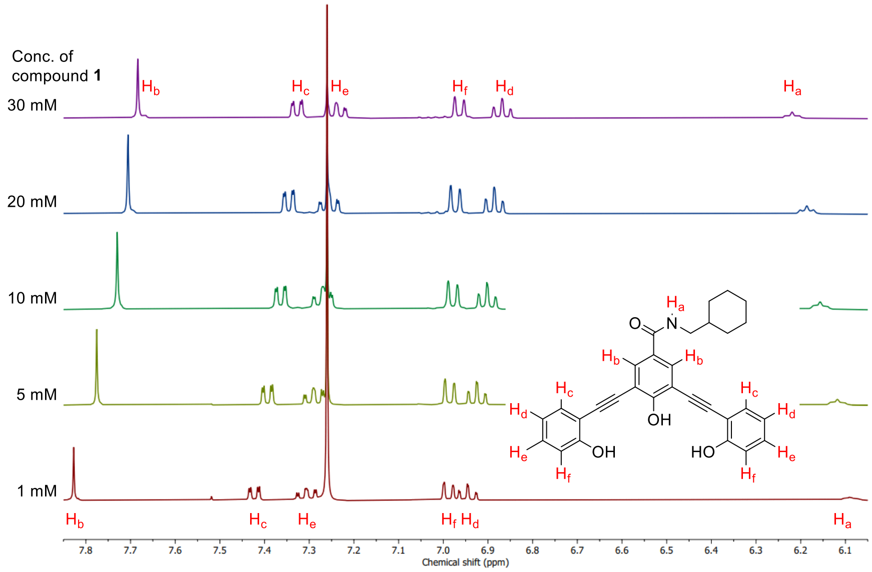

Figure 4.5 Concentration-dependent ^{1}H NMR (400 MHz) of compound **1** in $CDCl_3$ solvent at 298 K.

4.4.4.2. Morphological study with field emission scanning electron microscopy (FESEM)

Compound **1** with different concentrations (10 µM and 20 µM) in $CHCl_3$ solvent was drop-casted carefully on a silicon wafer, and dried over the surface morphology of the compound in the solid state was examined by FESEM studies.

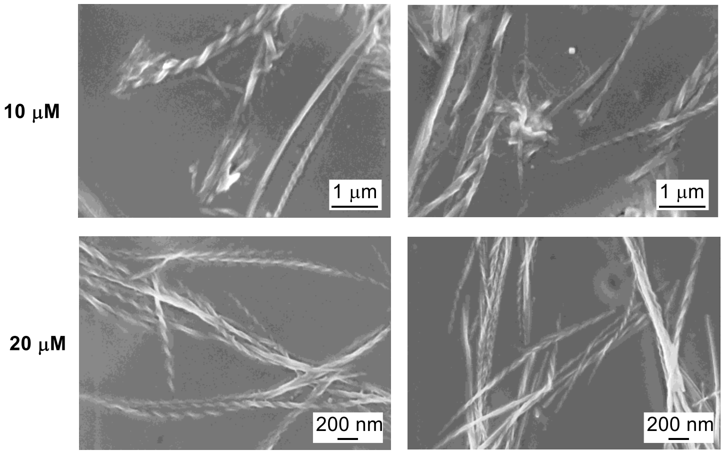

Figure 4.6 Concentration-dependent FESEM images of compound **1** in $CHCl_3$ solvent at 298 K.

4.4.5. Ion transport studies

4.4.5.1. Ion transporting activity studies across EYPC–LUVs⊃HPTS[33,34]

Buffer and stock solution preparation: HEPES buffer (10 mM HEPES, 100 mM NaCl, pH = 7.0) was prepared by dissolving an accurate amount of solid HEPES in autoclaved water. Then, the required amount of solid NaCl salt was dissolved into it, and finally, the pH was maintained at 7.0 by the addition of NaOH solution. All stock solutions of compound **1** were prepared in HPLC grade DMSO solvent for HPTS-based transport studies.

Preparation of EYPC-LUVs⊃HPTS: Vesicles were prepared according to the reported protocol.[35]

Ion transport activity: In a clean and dry fluorescence cuvette, 1975 μL of NaCl buffer (10 mM HEPES, 100 mM NaCl, pH = 7.0) was taken with 25 μL of vesicles and placed on the fluorescence instrument (t = 0 s) equipped with a magnetic stirrer. At t = 20 s, 20 μL of 0.5 M NaOH solution was added to create a pH gradient between the intravesicular and extravesicular medium. The fluorescence emission intensity of HPTS dye (F_t) was monitored at λ_{em} = 510 nm (λ_{ex} = 450 nm) after the addition of the transporter molecule at t = 100 s. Finally, at t = 300 s, 25 μL of 10% Triton X-100 was added to the cuvette to lyze the vesicles in order to achieve 100 % fluorescence activity of HPTS dye.

The time axis was normalized according to Equation 1

$$t = t - 100 \qquad \text{Equation 1}$$

The time-dependent data were normalized to percent change in fluorescence intensity using Equation 2

$$I_F = [(I_t - I_0) / (I_\infty - I_0)] \times 100 \qquad \text{Equation 2}$$

where, I_0 is the initial intensity, I_t is the intensity at time t, and I_∞ is the final intensity after the addition of Triton X-100.

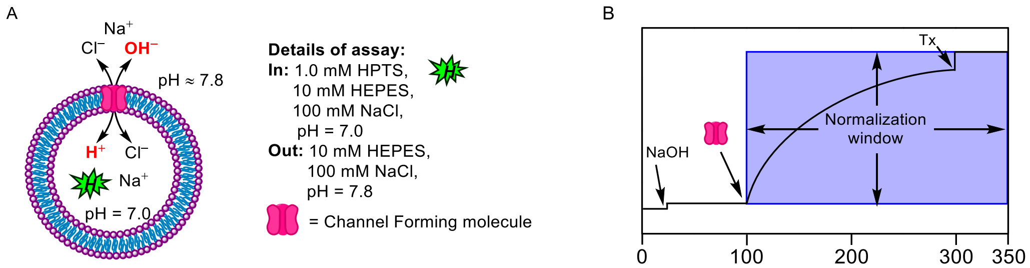

Figure 4.7 Schematic illustration of ion transport activity using EYPC–LUVs⊃HPTS (A), representative fluorescence kinetics experiment of ion transport (B).

Concentration-dependent study

The fluorescence kinetics was investigated with different concentrations of transporter molecules over the course of time. Hill plot was analyzed at t = 190 s to get effective concentration (EC_{50}, i.e. the concentration of transporter required to achieve 50% transport activity) and Hill coefficient (n) by using the Hill equation.

$$Y = Y_\infty + (Y_0 - Y_\infty) / [1 + (c/EC_{50})^n] \qquad \text{Equation 3}$$

where, Y_0 = fluorescence intensity just before the channel addition (t = 0 s), Y_∞ = fluorescence intensity with excess channel concentration, c = concentration of channel compound, and n = Hill coefficient.

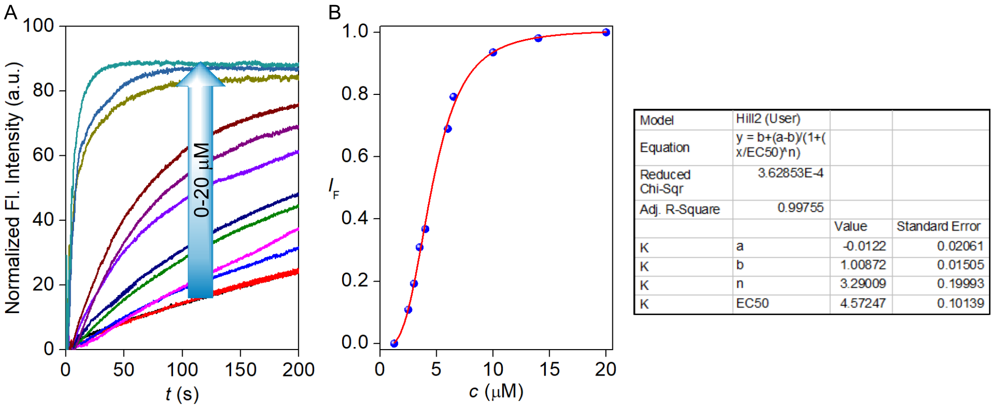

Model	Hill2 (User)		
Equation	y = b+(a-b)/(1+(x/EC50)^n)		
Reduced Chi-Sqr	3.62853E-4		
Adj. R-Square	0.99755		
		Value	Standard Error
K	a	-0.0122	0.02061
K	b	1.00872	0.01505
K	n	3.29009	0.19993
K	EC50	4.57247	0.10139

Figure 4.8 Concentration-dependent study of compound **1** across EYPC–LUVs⊃HPTS (A), and Hill plot analysis of compound **1** at t = 190 s (B).

4.4.5.2. Ion selectivity study across EYPC–LUVs⊃HPTS

4.4.5.2.1. Anion selectivity study across EYPC–LUVs⊃HPTS

Buffer and stock solution preparation: Different NaX (where, X^- = Cl^-, Br^-, I^-, NO_3^-, and ClO_4^-) buffer (10 mM HEPES, 100 mM NaX, pH = 7.0) was prepared by dissolving an accurate amount of solid HEPES in autoclaved water. Then, the required amount of solid NaX salt was dissolved into it, and finally, the pH was maintained at 7.0 by the addition of NaOH solution. All stock solutions of compound **1** were prepared in HPLC grade DMSO solvent for ion selectivity studies.

Anion selectivity assay: In a clean and dry fluorescence cuvette, 1975 µL of NaX buffer and 25 µL of vesicles were taken and placed on the fluorescence instrument (t = 0 s) equipped with a magnetic stirrer. At t = 20 s, 20 µL of 0.5 M NaOH solution was added to it to create a pH gradient across the lipid bilayer membrane (pH_{in} = 7.0 and pH_{out} = 7.8). Channel-forming compound **1** (6.25 µM) was added at t =100 s, and the fluorescence emission intensity of HPTS was monitored at λ_{em} = 510 nm (λ_{ex} = 450 nm) over the course of time. Finally, at t = 300 s 25 µL of 10%, Triton X-100 was added to lyze the vesicle for the complete distraction of pH gradient across the lipid bilayer.

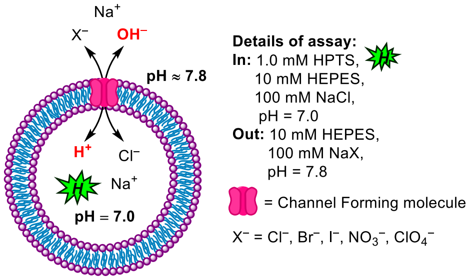

Figure 4.9 Schematic illustration of anion selectivity assay using EYPC–LUVs⊃HPTS.

4.4.5.2.2. Cation selectivity study across EYPC–LUVs⊃HPTS

Buffer and stock solution preparation: Different MCl ($M^+ = Li^+$, Na^+, K^+, Rb^+, and Cs^+) buffer (10 mM HEPES, 100 mM MCl, pH = 7.0) was prepared by dissolving an accurate amount of solid HEPES in autoclaved water. Then, the required amount of solid MCl salt was dissolved into it, and finally, the pH was maintained at 7.0 by the addition of NaOH solution. All stock solutions of compound **1** were prepared in HPLC grade DMSO solvent for ion selectivity studies.

Cation selectivity assay: In a clean and dry fluorescence cuvette, 1975 µL of MCl buffer and 25 µL of vesicles were taken and placed on the fluorescence instrument ($t = 0$ s) equipped with a magnetic stirrer. At $t = 20$ s, 20 µL of 0.5 M NaOH solution was added to it to create a pH gradient across the lipid bilayer membrane ($pH_{in} = 7.0$ and $pH_{out} = 7.8$). Channel-forming compound **1** (1.75 µM) was added at $t = 100$ s, and the fluorescence emission intensity of HPTS was monitored at $\lambda_{em} = 510$ nm ($\lambda_{ex} = 450$ nm) over the course of time. Finally, at $t = 300$ s 25 µL of 10%, Triton X-100 was added to lyze the vesicle for the complete distraction of pH gradient across the lipid bilayer.

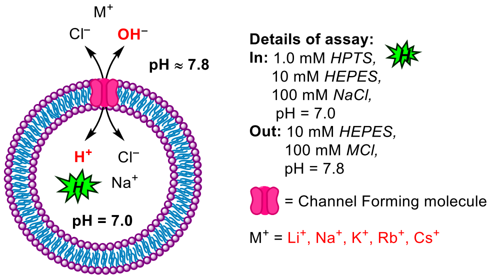

Figure 4.10 Schematic illustration of cation selectivity assay using EYPC–LUVs⊃HPTS.

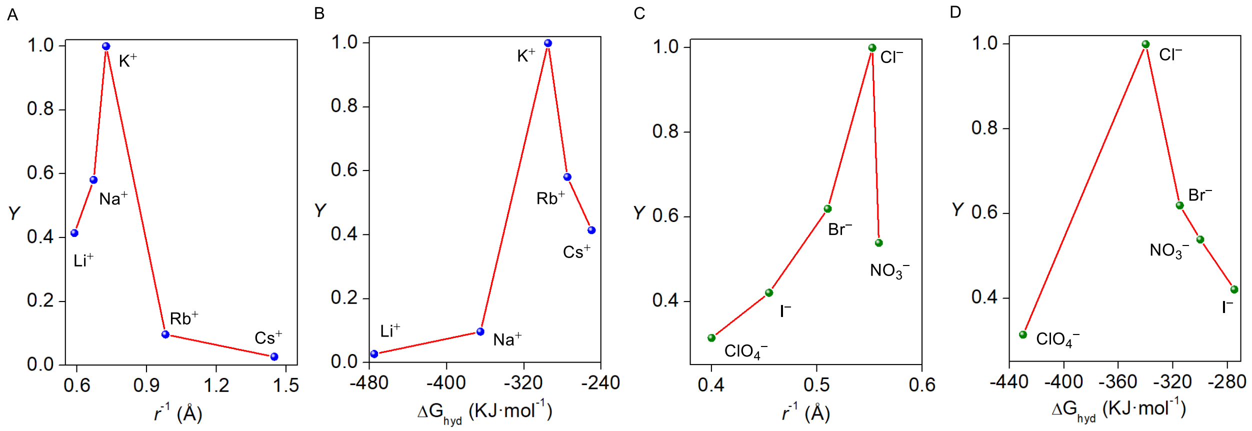

Figure 4.11 Fractional activity Y (relative to K^+) as a function of the reciprocal anion radius (A); fractional activity Y (relative to K^+) as a function of the anion hydration energy (B); fractional activity Y (relative to Cl^-) as a function of the reciprocal cation radius (C); and fractional activity Y (relative to Cl^-) as a function of the cation hydration energy (D).

4.4.5.3. Transport assays across EYPC–LUVs⊃Lucigenin[22]

Buffer and stock solution preparation: $NaNO_3$ buffer (10 mM HEPES, 200 mM $NaNO_3$, pH = 7.0) was prepared by dissolving an accurate amount of solid HEPES in autoclaved water. Then, the required amount of solid $NaNO_3$ salt was dissolved into it, and finally, the pH was maintained at 7.0 by the addition of NaOH solution. All stock solutions of compound **1** were prepared in HPLC grade ACN solvent for lucigenin studies.

Preparation of EYPC–LUVs⊃Lucigenin: Vesicles were prepared according to the reported protocol.[35]

4.4.5.3.1. Chloride influx study of compound 1

In a dry and clean fluorescence cuvette, 1975 µL of $NaNO_3$ buffer and 25 µL of vesicles were taken and placed in the fluorescence instrument (t = 0 s) equipped with a magnetic stirrer. An ionic gradient between extra- and intravesicular medium was created by adding 33.3 µL of 2 M NaCl salt in the cuvette at t = 20 s. Further, at t = 100 s channel forming molecule **1** was added with different concentrations and the fluorescence emission intensity of lucigenin was monitored at λ_{em} = 535 nm (λ_{ex} = 455 nm) over the course of time. Finally, at t = 300 s 25 µL of 10%, Triton-X 100 was added into the cuvette for the complete destruction of the chloride gradient.

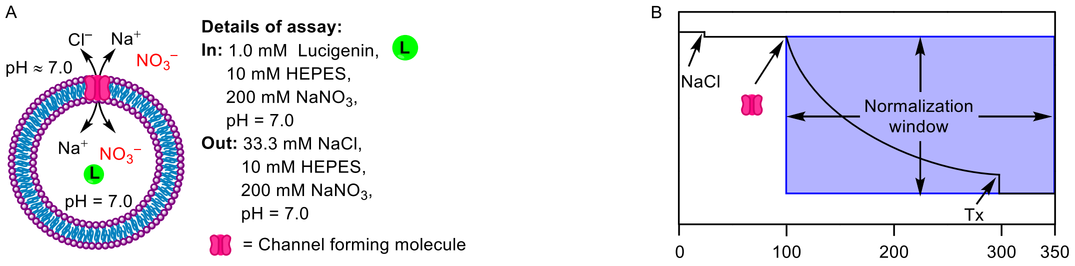

Figure 4.12 Schematic representation of ion transport activity across EYPC–LUVs⊃lucigenin vesicle (A), and normalization window for same fluorescence kinetics experiment of ion transport (B).

The time-dependent data were normalized to percent change in fluorescence intensity using Equation 4:

$$I_F = [(I_t - I_0) / (I_\infty - I_0)] \times (-100) \qquad \text{Equation 4}$$

where, I_0 is the initial intensity, I_t is the intensity at time t, and I_∞ is the final intensity after the addition of Triton X-100.

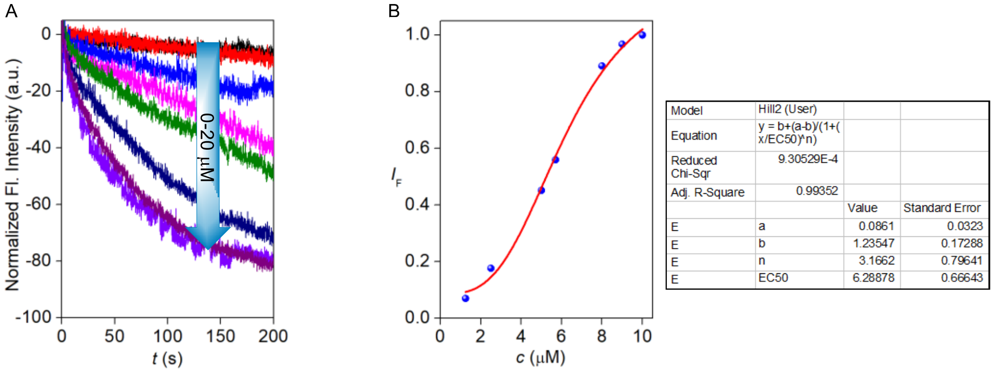

Model	Hill2 (User)		
Equation	y = b+(a-b)/(1+(x/EC50)^n)		
Reduced Chi-Sqr	9.30529E-4		
Adj. R-Square	0.99352		
		Value	Standard Error
E	a	0.0861	0.0323
E	b	1.23547	0.17288
E	n	3.1662	0.79641
E	EC50	6.28878	0.66643

Figure 4.13 Concentration-dependent study of compound **1** across EYPC–LUVs⊃Lucigenin (B), and Hill plot analysis of compound **1** at t = 190 s (C).

4.4.5.3.2. Cation selectivity assay across EYPC–LUVs⊃Lucigenin

In a dry and clean fluorescence cuvette, 1975 μL of $NaNO_3$ buffer and 25 μL of vesicles were taken and placed in the fluorescence instrument (t = 0 s) equipped with a magnetic stirrer. An ionic gradient between the extra- and intravesicular medium was created by adding 33.3 μL of 2 M MCl salt ($M^+ = Li^+$, Na^+, K^+, Rb^+, and Cs^+) in the cuvette at t = 20 s. Further, at t = 100 s the channel forming molecule **1** (7 μM) was added and fluorescence emission intensity of lucigenin was monitored at λ_{em} = 535 nm (λ_{ex} = 455 nm) over a course of time. Finally, at t = 300 s 25 μL of 10%, Triton-X 100 was added into the cuvette for the complete destruction of the chloride gradient.

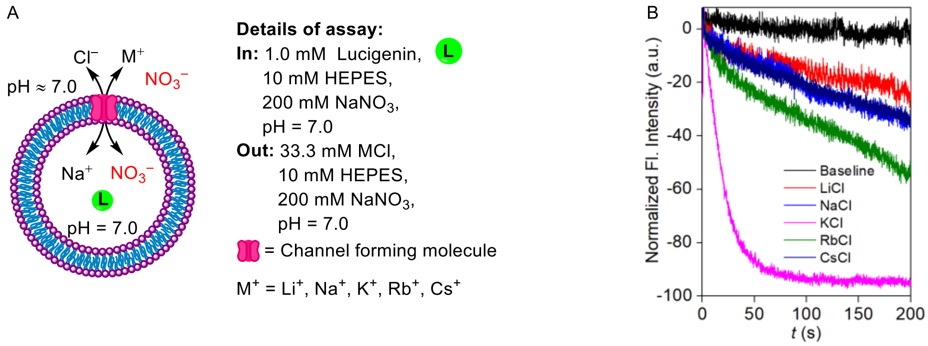

Figure 4.14 Schematic illustration of cation selectivity assay using EYPC–LUVs⊃Lucigenin (A), Cation selectivity study of compound **1** (7 µM) across EYPC–LUVs⊃Lucigenin (B).

4.4.5.4. Mechanistic studies of ion transport

4.4.5.4.1. Ion transport activity across EYPC–LUVs⊃Lucigenin in the presence of valinomycin

Direct insight into the symport mechanism (i.e. transport of two different ions in the same directions across the membrane) of compound **1** was investigated by lucigenin assay in the presence of valinomycin (a K^+ ion carrier). Ion transport activity of compound **1** was monitored in a vesicle entrapped with lucigenin (1 mM) and $NaNO_3$ buffer (10 mM HEPES, 200 mM $NaNO_3$, pH = 7.0) suspended in 2 M KCl solution with and without valinomycin. No significant enhancement in chloride influx activity of **1** in the presence of valinomycin gave direct experimental insight into the symport mechanism of ion transport.

Preparation of EYPC–LUVs⊃Lucigenin: The vesicles were prepared following a reported protocol.[35]

Symport mechanism: In clean and dry fluorescence cuvette 1975 µL $NaNO_3$ buffer solution (10 mM HEPES, 200 mM $NaNO_3$, pH = 7.0) and 25 µL EYPC–LUVs⊃Lucigenin vesicles were taken and slowly stirred in fluorescence instrument equipped with a magnetic stirrer (at t = 0 s). The time-dependent fluorescence intensity of lucigenin was monitored at λ_{em} = 535 nm (λ_{ex} = 455 nm). A solution of 2 M KCl (33.3 µL) was added at t = 20 s to create a chloride gradient between intra- and extravesicular system, followed by the addition of valinomycin (0.5 µM) at t = 50 s and channel-forming molecule **1** (4 µM) at t = 100 s. Finally, the destruction of the chloride gradient was done by the addition of 25 µL of 10 % Triton X-100 at t = 300 s. The time-dependent data were normalized to percent change in fluorescence intensity using Equation 4

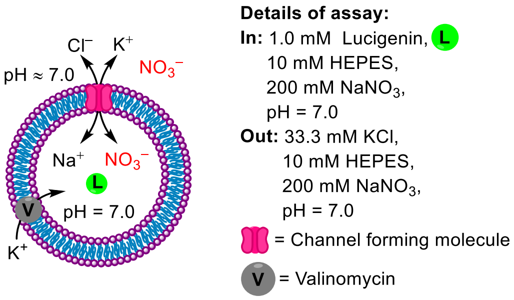

Figure 4.15 Schematic illustration of Valinomycin assay using EYPC–LUVs⊃Lucigenin.

4.4.5.4.2. NO_3^-/SO_4^{2-} assay[28]

The ion transport mechanism of compound **1** was reconfirmed by NO_3^-/SO_4^{2-} assay with lucigenin dye. Ion transport activity of compound **1** was monitored in vesicles entrapped with lucigenin (1 mM) and NaCl buffer (10 mM HEPES, 200 mM NaCl, pH = 7.0) suspended in iso-osmolar $NaNO_3/Na_2SO_4$ buffer solution (10 mM HEPES, 200 mM $NaNO_3$/ 66.6 mM Na_2SO_4, pH = 7.0). No significant enhancement in chloride efflux activity of **1** by varying the external anionic salt ($NaNO_3$ and Na_2SO_4), gave direct experimental proof of the symport mechanism.

Preparation of EYPC–LUVs⊃Lucigenin with intravesicular Cl^-: A solution (1 mL) of EYPC lipid (25 mg/mL) dissolved in $CHCl_3$ was taken in a clean and dry 10 mL small round bottom flask. The solvents were evaporated slowly by a stream of nitrogen, followed by drying under a vacuum for at least 5 h. After that, 1 mL of 1 mM *N,N′*-dimethyl-9,9′-biacridinium dinitrate (lucigenin) in 200 mM NaCl (dissolved in 10 mM HEPES buffer with pH = 7.0) was added, and the suspension was hydrated for 1 h with occasional vortexing of 4-5 times and then subjected to freeze-thaw cycle (22 times, liquid nitrogen and 55 °C water bath). The vesicle solution was extruded through a polycarbonate membrane with 200 nm pores 21 times (must be an odd number) to give vesicles with a mean diameter of ~ 200 nm. The unentrapped extravesicular lucigenin was then removed by size exclusion column chromatography (Sephadex G-50) using 200 mM NaCl buffer solution as an eluent. The vesicles were diluted to 4 mL with 200 mM NaCl. Final conditions: ~ 5 mM EYPC; inside: 1 mM lucigenin, 10 mM HEPES, 200 mM NaCl, pH 7.0; outside: 10 mM HEPES, 200 mM NaCl, pH 7.0.

Effect of extravesicular NO_3^- and SO_4^{2-} on the chloride efflux from EYPC–LUVs⊃Lucigenin: In a clean and dry fluorescence cuvette, 50 μL of the above lipid solution and 1950 μL of an iso-osmolar solution of different NaX ($X^- = NO_3^-$ and SO_4^{2-}) salts were taken and kept in slowly stirring condition by a magnetic stirrer equipped with the fluorescence instrument ($t = 0$ s). Time-dependent lucigenin fluorescence emission intensity was monitored at $\lambda_{em} = 535$ nm ($\lambda_{ex} = 450$ nm) after the addition of the compound **1** (4 μM) at $t =$

100 s. Finally, at t = 300 s, 25 μL of 10% Triton X-100 was added to lyse all vesicles for 100% chloride efflux. Fluorescence intensities (F_t) were normalized to fractional emission intensity I_F using Equation 2.

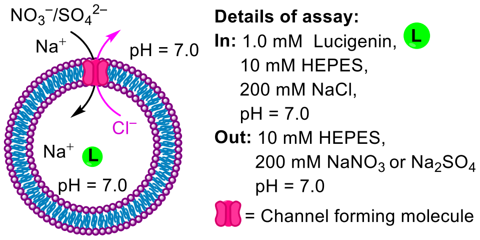

Figure 4.16 Schematic illustration of NO_3^-/SO_4^{2-} assay using EYPC–LUVs⊃Lucigenin.

4.4.5.5. ^{39}K NMR experiment as a proof of K$^+$ ion transport[29–31]

Preparation of vesicles and buffers: All buffers and vesicles were prepared by following the reported literature protocol.[31]

Experimental procedure: 180 μL EYPC–LUVs suspension, 120 mL conductivity water, 100 μL D_2O, 100 μL shift reagent, and the required amount of compound **1** (dissolved in HPLC DMSO) were mixed in an NMR tube and kept at 25 °C for 30 min. ^{39}K NMR spectrum was recorded for each concentration of samples after 30 min. The rate constant values for K$^+$ transport were calculated by using Equation 5.

$$K_{obs} = {}^{1}/_{\tau} = (v - v_0) \qquad \text{Equation 5}$$

where, v = half line widths in the presence of compound **1**, v_0 = half line widths in the absence of compound **1**.

All half line widths were calculated by using the TopSpin 4.1.4 software programme.

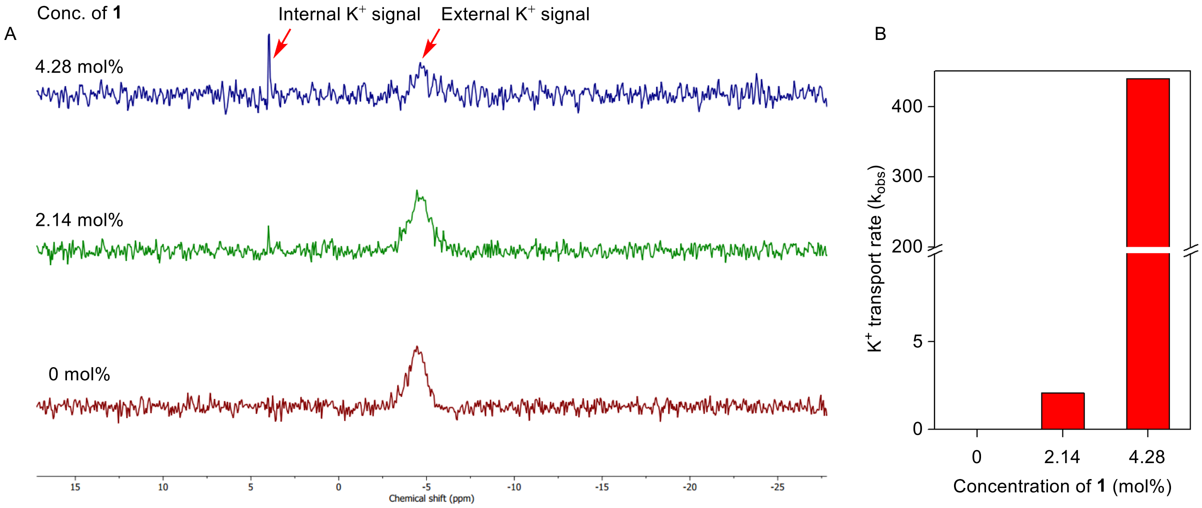

Figure 4.17 Change in intravesicular and extravesicular ^{39}K signal with increase in the concentration of compound **1** (A), calculated K$^+$ ion transport rate at different concentrations of compound **1** (B).

4.4.5.6. pH-dependent ion transport selectivity

Buffer and stock solution preparation: $NaNO_3$ buffer (200 mM $NaNO_3$, 5 mM citrate buffer for pH = 4.0; 5 mM phosphate buffer for pH = 5.0, 7.0, 7.4, and 8) was prepared by dissolving in autoclaved water. pH was maintained by the addition of NaOH solution. All stock solutions of compound **1** were prepared in HPLC grade ACN solvent for the studies.

Preparation of EYPC–LUVs⊃Lucigenin: Vesicles were prepared according to the reported protocol.[35]

Assay details: In a dry and clean fluorescence cuvette, 25 µL of vesicles and 1975 µL of $NaNO_3$ buffer (200 mM $NaNO_3$, 5 mM citrate buffer for pH = 4.0; 5 mM phosphate buffer for pH = 5.0, 7.0, 7.4, and 8) with different pH values were taken and placed in the fluorescence instrument (t = 0 s) equipped with a magnetic stirrer. An ionic gradient between extra- and intravesicular medium was created by adding 33.3 µL of 2 M MCl salt ($M^+ = Na^+$ or K^+) in the cuvette at t = 20 s. Further, at t = 100 s the channel forming molecule **1** (10 µM) was added, and the fluorescence emission intensity of lucigenin was monitored at λ_{em} = 535 nm (λ_{ex} = 455 nm) over the course of time. Finally, at t = 300 s 25 µL of 10%, Triton-X 100 was added into the cuvette for the complete destruction of the chloride gradient.

4.4.5.7. UV-titration experiments of compound 1

Initially, the UV-vis absorption spectra of the compound **1** (60 µM) was checked in the CH_3CN:HEPES (3:2, v/v, pH = 7.4) solution. $CuCl_2$ was added sequentially to the solution, and after each addition, UV-vis absorption spectra were collected. A prominent change in the UV-vis spectra validated the effective binding of the Cu^{2+} ion with compound **1**. Change in the absorbance at λ = 288 nm was noted down to evaluate the stoichiometry of compound **1** and Cu^{2+} ion from the Job's plot. Job's plot indicated the formation of 2:1 host:guest complex between the compound **1** and Cu^{2+} ion.

Further, to understand the reversibility in the complexation and decomplexation process, change in the UV-vis spectra was monitored upon sequential addition of the 1 equiv $CuCl_2$ and 1.1 equiv of K_2EDTA. Interestingly, efficient reversible complexation and decomplexation were observed upon sequential addition of the $CuCl_2$ and K_2EDTA even up to five cycles. This data indicated that compound **1** can be used as a potential reversible ligand-gated transport system.

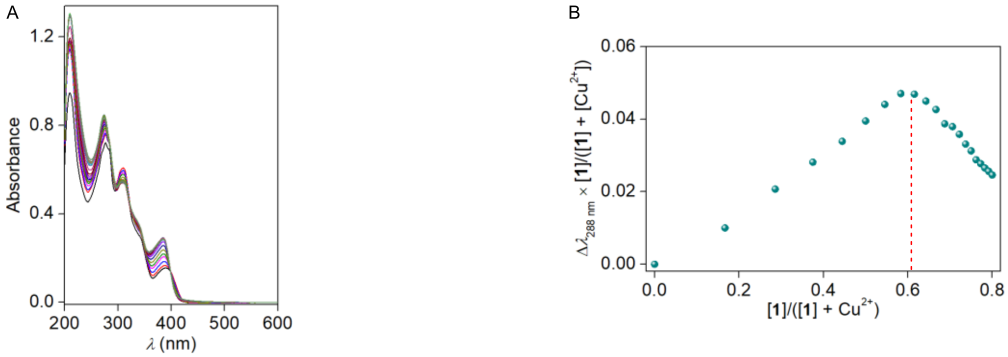

Figure 4.18 Change in UV-vis spectra of compound **1** with the increase in the concentration of $CuCl_2$ in CH_3CN:HEPES (3:2, v/v, pH = 7.0) solution at 25 °C (A), and calculated Job's plot from the UV-titration experiment (B).

4.4.5.8. Ligand-gated reversible OFF–ON ion transport activity

Buffer and stock solution preparation: HEPES buffer (10 mM HEPES, 100 mM KCl, pH = 7.0) was prepared by dissolving an accurate amount of solid HEPES in autoclaved water. Then, the required amount of solid NaCl salt was dissolved into it, and finally, the pH was maintained at 7.0 with the addition of NaOH solution. All stock solutions of compound **1** were prepared in HPLC grade DMSO solvent for ligand-gated reversible OFF-ON ion transport studies.

Preparation of EYPC–LUVs⊃HPTS: Vesicles were prepared according to the reported protocol.[35]

Ion transport activity: In a clean and dry fluorescence cuvette, 25 μL of vesicles, 1975 μL of KCl buffer (10 mM HEPES, 100 mM KCl, pH = 7.0) and compound **1** (working concentration 1 μM) was taken with and placed on the fluorescence instrument (t = 0 s) equipped with a magnetic stirrer. At t = 20 s, 20 μL of 0.5 M NaOH solution was added to initiate the ion transport process by creating a pH gradient between the intravesicular and extravesicular medium. The fluorescence emission intensity of HPTS dye (F_t) was monitored at λ_{em} = 510 nm (λ_{ex} = 450 nm). 1 equiv of $CuCl_2$ and 1.1 equiv of EDTA were sequentially added at 2 min intervals to turn OFF and turn ON the transport activity, respectively. Finally, at t = 620 s, 25 μL of 10% Triton X-100 was added to the cuvette to lyze the vesicles in order to achieve 100 % fluorescence activity of HPTS dye.

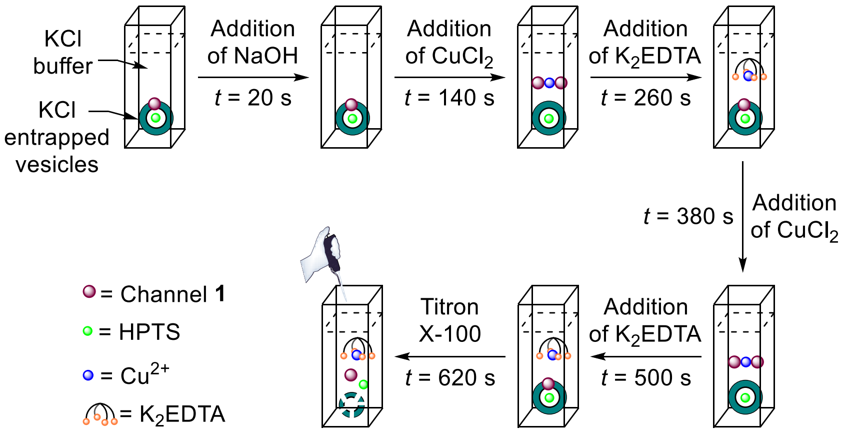

Figure 4.19 Schematic illustration of assay details of reversible OFF–ON ion transport activity of channel forming compound **1** across EYPC–LUVs⊃HPTS.

The time axis was normalized according to Equation 6

$$t = t - 20 \qquad \text{Equation 6}$$

The time-dependent data were normalized to percent change in fluorescence intensity using Equation 2.

4.4.6. Planar bilayer conductance measurements[20]

Bilayer lipid membrane (BLM) was formed with diphytanoylphosphatidylcholine (dphpc) lipid (Avanti Polar Lipids), dissolved in n-decane (20 mg/mL) across an aperture of 150 µM diameter in a polystyrene cup (Warner Instrument, USA). Both chambers (cis and trans) were filled with a symmetrical 1 M KCl buffer solution (10 mM HEPES, 1 M KCl, pH = 7.0). The Cis chamber was connected with BC 535 head-stage (Warner Instrument, USA), and the trans chamber was held at the virtual ground with Ag-AgCl electrodes. Compound **1** (5 µM) was added to the cis chamber, and the solution was stirred with a magnetic stirrer for around 10 min. A distinct square top channel opening and closing events were observed after applying both +ve and –ve voltages. Currents were low pass filtered at 1 kHz using pClamp9 software (Molecular Probes, USA) and an analog-to-digital converter (Digidata 1440, Molecular Probes). All data were analyzed using the software pClamp 10.7.0.3. The average current was calculated from this trace, and then conductance and other calculations were made accordingly.

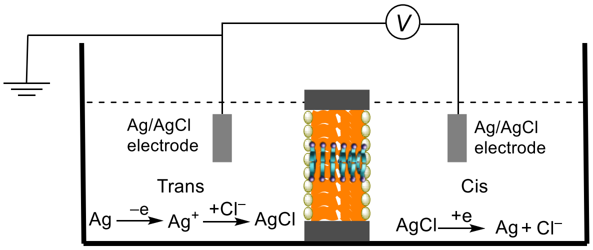

Figure 4.20 Systematic representation of bilayer lipid membrane experiment.

4.4.6.1. Single-channel conductance calculation

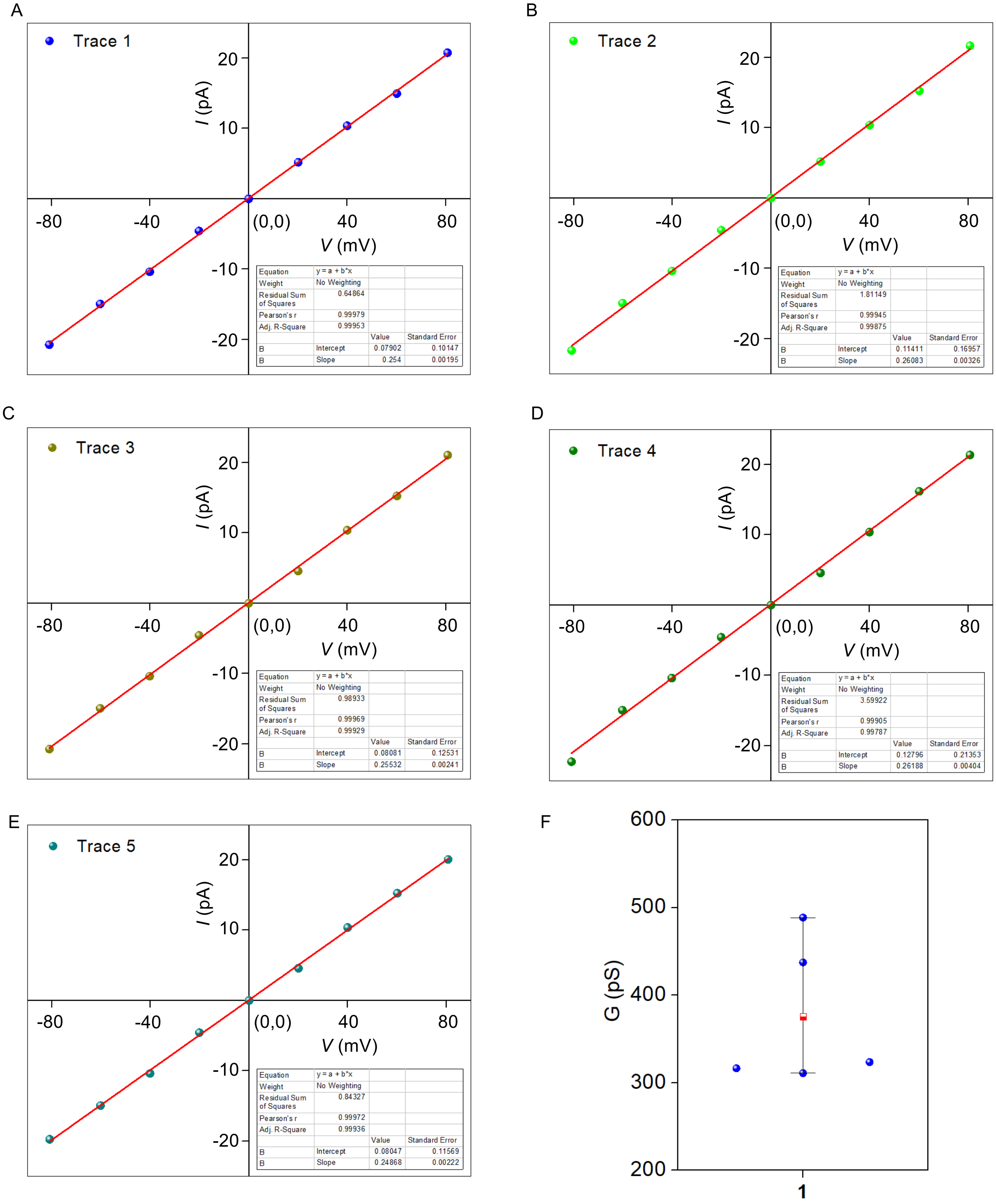

A

Equation	y = a + b*x		
Weight	No Weighting		
Residual Sum of Squares	0.64864		
Pearson's r	0.99979		
Adj. R-Square	0.99953		
		Value	Standard Error
B	Intercept	0.07902	0.10147
B	Slope	0.254	0.00195

B

Equation	y = a + b*x		
Weight	No Weighting		
Residual Sum of Squares	1.81149		
Pearson's r	0.99945		
Adj. R-Square	0.99875		
		Value	Standard Error
B	Intercept	0.11411	0.16957
B	Slope	0.26083	0.00326

C

Equation	y = a + b*x		
Weight	No Weighting		
Residual Sum of Squares	0.98933		
Pearson's r	0.99969		
Adj. R-Square	0.99929		
		Value	Standard Error
B	Intercept	0.08081	0.12531
B	Slope	0.25532	0.00241

D

Equation	y = a + b*x		
Weight	No Weighting		
Residual Sum of Squares	3.59922		
Pearson's r	0.99905		
Adj. R-Square	0.99787		
		Value	Standard Error
B	Intercept	0.12796	0.21353
B	Slope	0.26188	0.00404

E

Equation	y = a + b*x		
Weight	No Weighting		
Residual Sum of Squares	0.84327		
Pearson's r	0.99972		
Adj. R-Square	0.99936		
		Value	Standard Error
B	Intercept	0.08047	0.11569
B	Slope	0.24868	0.00222

Figure 4.21 All five traces of *I*-*V* plots of compound **1** in symmetrical cis/trans = 1 M KCl /1 M KCl (A, B, C, D, E); box plot of the averaged V_{rev} from five experiments (represented as blue circles) (F).

Table 4.1 Table for experimentally calculated single-channel conductance of compound **1**.

Entry	Slope	G (pS)
1	0.31110	311.10
2	0.43749	437.49
3	0.31650	316.50
4	0.48862	488.62
5	0.32359	323.59
		Average = 375.5

4.4.6.2. Channel diameter calculation

Channel diameter was calculated by using Hille's equation,

$$1/g = (l + \pi d/4) \times (4\rho/\pi d^2) \qquad \text{Equation 7}$$

where, g = corrected conductance (obtained by multiplying measured conductance with the Sansom's correction factor), l = thickness of the membrane = 34 Å, and ρ = resistivity of 1 M KCl solution = 9.44 Ω·cm) and d = diameter of the ion channel.

The experimentally evaluated average channel diameter = 6.7 ± 1 Å.

4.4.6.3. Anion/cation selectivity in BLM

The cis and trans chambers were filled with unsymmetrical KCl solutions. The cis chamber was filled with 1.0 M KCl solution, and the trans chamber was filled with 0.5 M KCl. Compound **1** (5 µM) was added to the cis chamber and stirred for 10 min. The average reversal potential was calculated to be –11.47 mV, and the calculated permeability ratio was $P_{Cl^-}/P_{K^+} = 0.35 \pm 0.9$ (Equation 8).

The permeability ratio ($P_{\mathrm{Cl}^-}/P_{\mathrm{K}^+}$) was calculated by using the Goldman-Hodgkin-Katz equation,

$$\frac{P_{Cl^-}}{P_{K^+}} = \frac{a_{K^+_{cis}} - a_{K^+_{trans}} \times \exp(-\frac{V_{rev}F}{RT})}{a_{Cl^-_{cis}} \times \exp(-\frac{V_{rev}F}{RT}) - a_{Cl^-_{trans}}} \qquad \text{Equation. 8}$$

where, $\frac{P_{Cl^-}}{P_{K^+}}$ = anion/cation permeability ratio; $a_{K^+_{cis}}$ = K^+ activity in the cis chamber; $a_{K^+_{tras}}$ = K^+ activity in the trans chamber; $a_{Cl^-_{cis}}$ = Cl^- activity in the cis chamber; $a_{Cl^-_{trans}}$ = Cl^- activity in the trans chamber; V_{rev} = reversal potential; F = Faraday constant; R = gas constant; T = temperature (K).

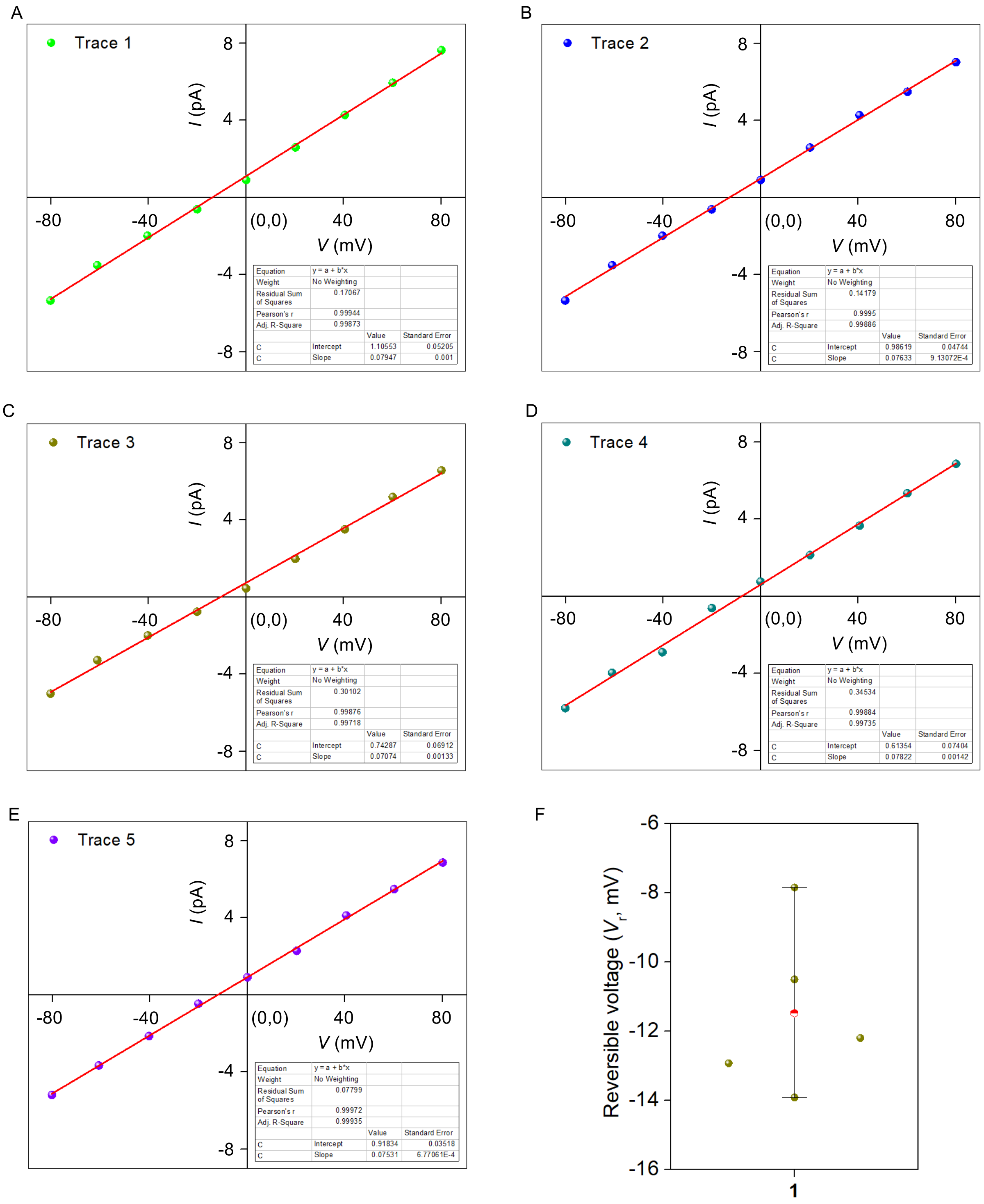

A

Equation	y = a + b*x		
Weight	No Weighting		
Residual Sum of Squares	0.17067		
Pearson's r	0.99944		
Adj. R-Square	0.99873		
		Value	Standard Error
C	Intercept	1.10553	0.05205
C	Slope	0.07947	0.001

B

Equation	y = a + b*x		
Weight	No Weighting		
Residual Sum of Squares	0.14179		
Pearson's r	0.9995		
Adj. R-Square	0.99886		
		Value	Standard Error
C	Intercept	0.98619	0.04744
C	Slope	0.07633	9.13072E-4

C

Equation	y = a + b*x		
Weight	No Weighting		
Residual Sum of Squares	0.30102		
Pearson's r	0.99876		
Adj. R-Square	0.99718		
		Value	Standard Error
C	Intercept	0.74287	0.06912
C	Slope	0.07074	0.00133

D

Equation	y = a + b*x		
Weight	No Weighting		
Residual Sum of Squares	0.34534		
Pearson's r	0.99884		
Adj. R-Square	0.99735		
		Value	Standard Error
C	Intercept	0.61354	0.07404
C	Slope	0.07822	0.00142

E

Equation	y = a + b*x		
Weight	No Weighting		
Residual Sum of Squares	0.07799		
Pearson's r	0.99972		
Adj. R-Square	0.99935		
		Value	Standard Error
C	Intercept	0.91834	0.03518
C	Slope	0.07531	6.77061E-4

Figure 4.22 All five traces of *I*-*V* plots of compound **1** in symmetrical cis/trans = 1 M KCl /0.5 M KCl (A, B, C, D, E); box plot of the averaged V_{rev} from five experiments (represented as dark yellow circles) (F).

Table 4.2 Table for experimentally calculated permeability ratio for anion/cation selectivity of compound **1**.

Cis/Trans = 1.0 M KCl/0.5 M KCl			
Entry	Reversal voltage V_r (mV)	$\frac{P_{Cl^-}}{P_{K^+}}$	$\frac{P_{K^+}}{P_{Cl^-}}$
1	– 13.911	0.18	5.67
2	– 12.920	0.24	4.24
3	– 10.501	0.40	2.48
4	– 7.844	0.63	1.59
5	– 12.194	0.28	3.53
	Average = – 11.47	Average = 0.35	Average = 3.5

4.4.6.4. Cation/cation selectivity in BLM[36]

Table 4.3 Table for experimentally calculated permeability ratio for cation/cation selectivity of compound **1**.

Cis/Trans = 1.0 M NaCl/1.0 M KCl		
Entry	Reversal voltage V_r (mV)	$\frac{P_{K^+}}{P_{Na^+}}$
1	– 35.800	4.03
2	– 31.362	3.39
3	– 25.099	2.66
4	– 31.542	3.41
5	– 36.047	4.07
	Average = – 31.97	Average = 3.51

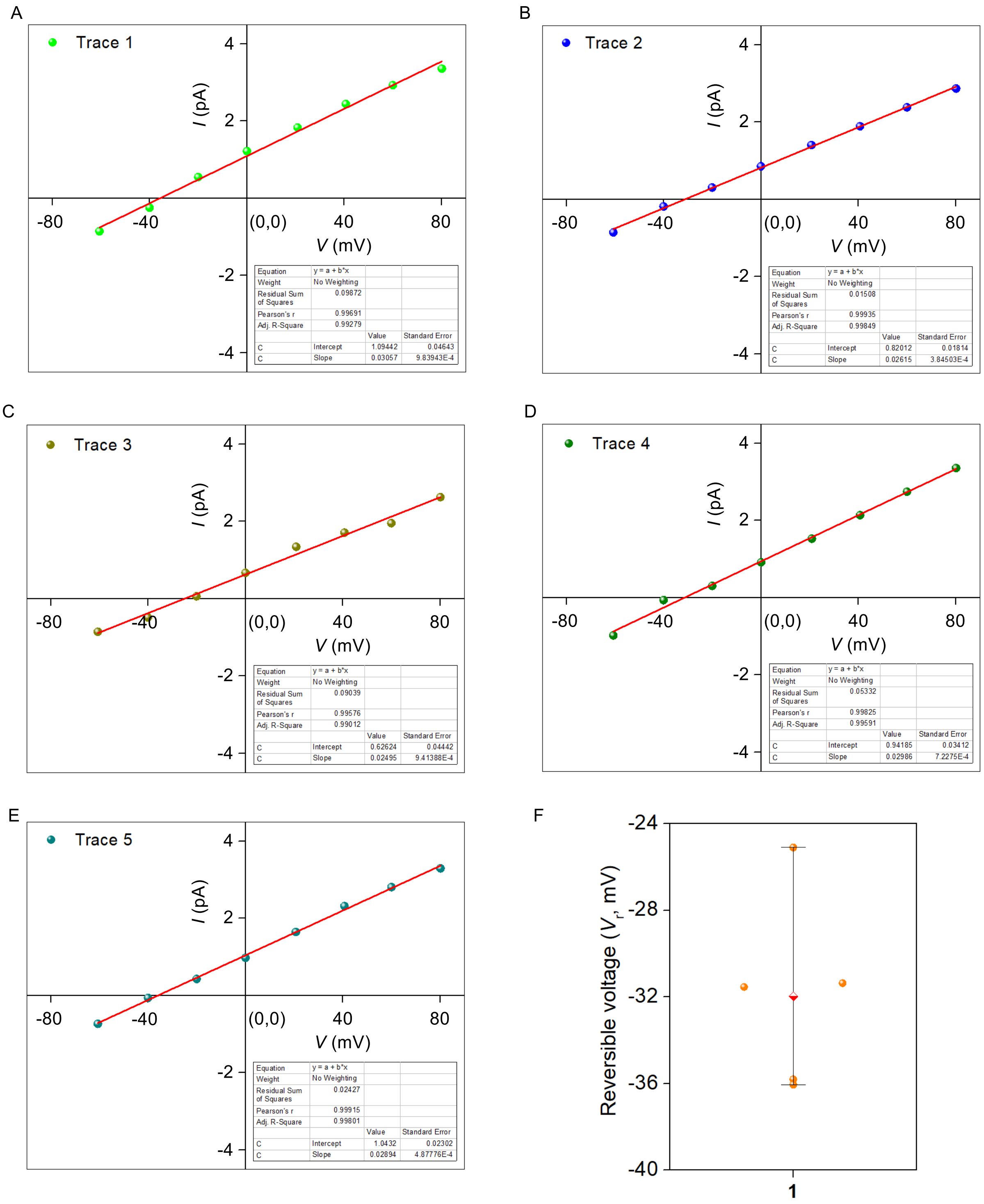

A

Equation	y = a + b*x		
Weight	No Weighting		
Residual Sum of Squares	0.09872		
Pearson's r	0.99691		
Adj. R-Square	0.99279		
		Value	Standard Error
C	Intercept	1.09442	0.04643
C	Slope	0.03057	9.83943E-4

B

Equation	y = a + b*x		
Weight	No Weighting		
Residual Sum of Squares	0.01508		
Pearson's r	0.99935		
Adj. R-Square	0.99849		
		Value	Standard Error
C	Intercept	0.82012	0.01814
C	Slope	0.02615	3.84503E-4

C

Equation	y = a + b*x		
Weight	No Weighting		
Residual Sum of Squares	0.09039		
Pearson's r	0.99576		
Adj. R-Square	0.99012		
		Value	Standard Error
C	Intercept	0.62624	0.04442
C	Slope	0.02495	9.41388E-4

D

Equation	y = a + b*x		
Weight	No Weighting		
Residual Sum of Squares	0.05332		
Pearson's r	0.99825		
Adj. R-Square	0.99591		
		Value	Standard Error
C	Intercept	0.94185	0.03412
C	Slope	0.02986	7.2275E-4

E

Equation	y = a + b*x		
Weight	No Weighting		
Residual Sum of Squares	0.02427		
Pearson's r	0.99915		
Adj. R-Square	0.99801		
		Value	Standard Error
C	Intercept	1.0432	0.02302
C	Slope	0.02894	4.87776E-4

Figure 4.23 All five traces of *I*-*V* plots of compound **1** in symmetrical cis/trans = 1 M NaCl /1 M KCl (A, B, C, D, E); box plot of the averaged V_{rev} from five experiments (represented as dark orange circles) (F).

4.4.6.5. Anion/anion selectivity in BLM[36]

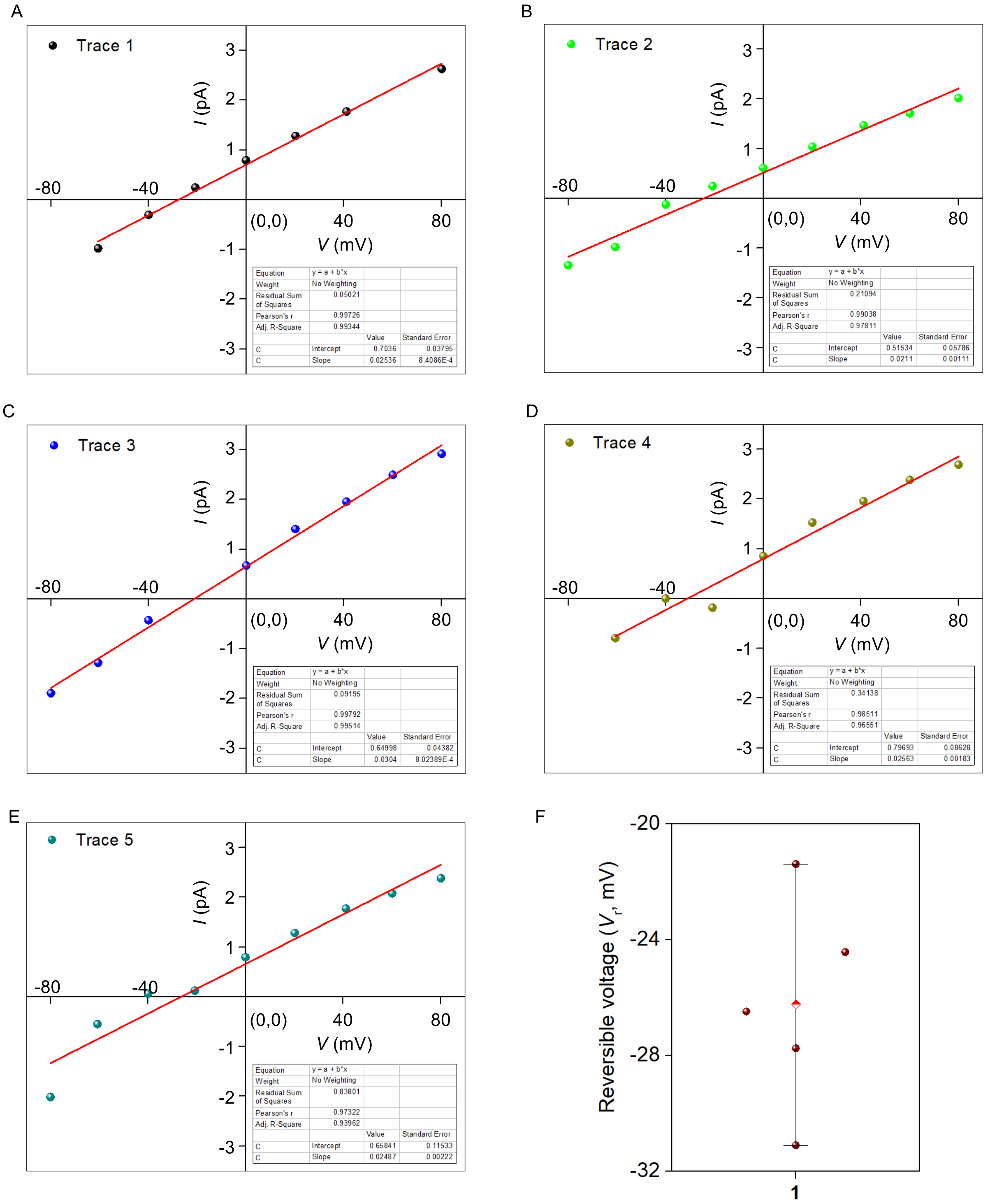

Equation	y = a + b*x		
Weight	No Weighting		
Residual Sum of Squares	0.05021		
Pearson's r	0.99726		
Adj. R-Square	0.99344		
		Value	Standard Error
C	Intercept	0.7036	0.03795
C	Slope	0.02536	8.4086E-4

Equation	y = a + b*x		
Weight	No Weighting		
Residual Sum of Squares	0.21094		
Pearson's r	0.99038		
Adj. R-Square	0.97811		
		Value	Standard Error
C	Intercept	0.51534	0.05786
C	Slope	0.0211	0.00111

Equation	y = a + b*x		
Weight	No Weighting		
Residual Sum of Squares	0.09195		
Pearson's r	0.99792		
Adj. R-Square	0.99514		
		Value	Standard Error
C	Intercept	0.64998	0.04382
C	Slope	0.0304	8.02389E-4

Equation	y = a + b*x		
Weight	No Weighting		
Residual Sum of Squares	0.34138		
Pearson's r	0.98511		
Adj. R-Square	0.96551		
		Value	Standard Error
C	Intercept	0.79693	0.08628
C	Slope	0.02563	0.00183

Equation	y = a + b*x		
Weight	No Weighting		
Residual Sum of Squares	0.83801		
Pearson's r	0.97322		
Adj. R-Square	0.93962		
		Value	Standard Error
C	Intercept	0.65841	0.11533
C	Slope	0.02487	0.00222

Figure 4.24 All five traces of *I*-*V* plots of compound **1** in symmetrical cis/trans = 1 M NaCl /1 M NaBr (A, B, C, D, E); box plot of the averaged V_{rev} from five experiments (represented as wine circles) (F).

Table 4.4 Table for experimentally calculated permeability ratio for anion/anion selectivity of compound **1**.

Cis/Trans = 1.0 M NaCl/1.0 M NaBr		
Entry	Reversal voltage V_r (mV)	$\frac{P_{Cl^-}}{P_{Br^-}}$
1	– 27.744	2.95
2	– 24.424	2.59
3	– 21.381	2.29
4	– 30.094	3.23
5	– 26.474	2.80
	Average = – 9.76	Average = 2.57

4.4.6.6. Ligand-gated reversible OFF-ON ion channel activity

To address the ligand-gated OFF-ON transport activity of the ion channel, electrophysiological experiments were carried out with compound **1**. Compound **1** (5 µM) was added in the cis chamber during the electrophysiological experiment, and both the opening-closing event and *I-V* plot were noticed over a period of time. To turn OFF the ion channel activity of compound **1**, 1 equiv. $CuCl_2$ (5 µM) was added to the cis chamber as a water solution. Interestingly, an instant turn OFF the opening-closing event was noticed, verifying that the ion channel activity of compound **1** was diminished in the presence of $CuCl_2$. Additionally, a decrease in the *I-V* plot was noticed after adding $CuCl_2$ in the cis chamber, clarifying that there was minimal current flow in the presence of $CuCl_2$. Further, to turn ON the ion channel activity of the compound **1**, 1.1 equiv. of the K_2EDTA was added in the cis chamber. It is expected that K_2EDTA will bind the Cu^{2+} ion and make the compound **1** free. Hence, it can regenerate the self-assembled parallel rosette ion channel structure in the membrane, initiate the opening-closing events and initiate the current flow across the membrane. Interestingly, we noticed significant channel opening-closing events after adding the K_2EDTA in the cis chamber, verifying the regeneration of the self-assembled ion channel structure in the membrane. It was also noteworthy that the current flow also increased, which was evident from the *I-V* plot, validating that compound **1** regenerated its efficiency in its ion flow across the membrane.

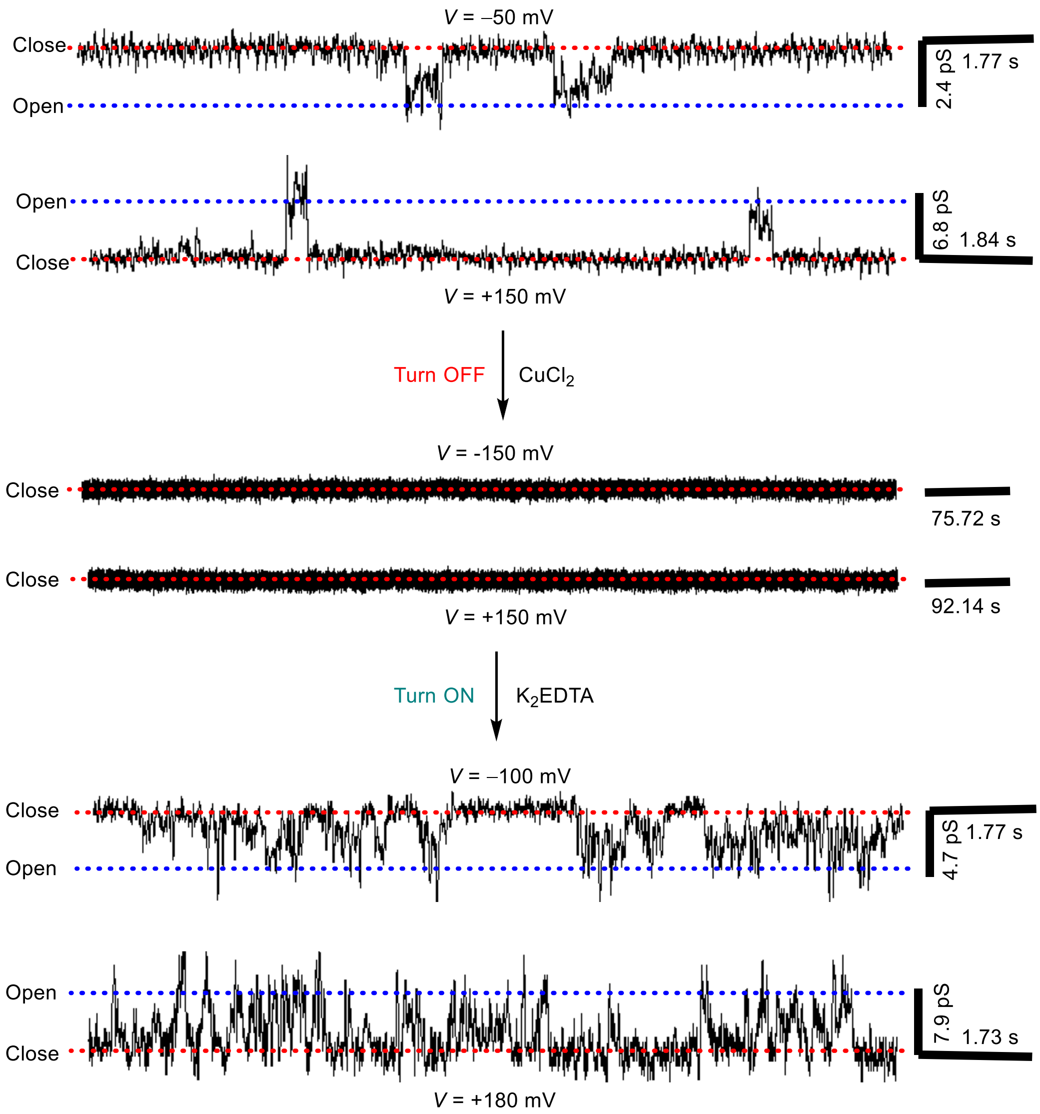

Figure 4.25 Ligand-gated reversible OFF-ON opening-closing events of channel forming compound **1** in the presence of the $CuCl_2$ and K_2EDTA under symmetric 1 M KCl buffer (10 mM HEPES, 1 M KCl, pH = 7.0).

4.4.7. Theoretical studies

4.4.7.1. System setup and simulation model

Initially, the synthetic channel structure, comprising 18 monomers organized in six consecutive layers, was subjected to minimization using the MAESTRO software.[37] Subsequently, the semi-minimized channel structure was utilized to construct the channel/membrane assembly using the membrane builder protocol of CHARMM-GUI,[38,39] following the reported guidelines.[40] This process involved object reading, appropriate orientation, and packing within the lipid bilayer assembly after determining the system size. The resulting channel/membrane complex featured the self-assembled channel structure positioned centrally within the lipid bilayer membrane, comprising six repetitive layers built with 18 monomers in total. The membrane bilayer consisted of 1,2-diphytanoyl-sn-glycero-3-phosphocholine (DPhPC) lipids, totalling 144 units evenly distributed across each leaflet (with each leaflet containing 72 lipid units). Subsequently, the channel/membrane complex was enclosed within a rectangular box measuring 7.7 × 7.7 × 9.0 nm³. The system was then solvated with sufficient water to maintain a 1 M KCl salt concentration in each aqueous compartment, separated by the lipid bilayer. Detailed simulation system specifications are provided in Table 4.5. The channel structure was modeled using the general AMBER forcefield (GAFF),[41–43] while the lipid membrane employed CHARMM36m forcefield parameters.[44–46] Water molecules were represented using CHARMM-TIP3P parameters.[47]

Table 4.5 Details of the simulation system with compound **1**.

Box dimension	**No. of water molecules**	**No. of K^+ ions**	**No. of Cl^- ions**
$7.7 \times 7.7 \times 9.0$ nm^3	9771	175	175

4.4.7.2. Simulation method

All simulations were conducted under periodic boundary conditions (PBC) in all three dimensions (along X, Y, and Z axis). For handling long-range electrostatic interactions, the particle mesh Ewald (PME) method[47] with cubic interpolation was employed. Short-range electrostatic interactions were truncated at 1.2 nm. Neighbour lists were updated every 20 steps. The LINCS algorithm[48] was utilized to constrain hydrogen bonds within membrane and channel monomers, while the SETTLE algorithm[49] was applied to maintain water molecule rigidity during simulation. Lennard Jones interactions were truncated at a distance of 1.2 nm using the Verlet cut-off scheme[50] with dispersion corrections. Initially, the system underwent energy minimization with specific restraints via the steepest-descent algorithm, followed by six successive equilibration steps of 10 ns each. During equilibration, the restraints on the system were gradually lowered in each consecutive step. An average temperature of 298 K and pressure of 1.0 bar were maintained during the equilibration process using the Berendsen thermostat[51] and Berendsen barostat.

After equilibration, each system underwent a final NPT production run for 1.0 μs under slight restraint conditions applied to each channel structure. During production simulation, the average temperature of 298 K was maintained using the Nose-Hoover thermostat[52] with a relaxation constant of 1.0 ps, individually coupling the channel structure, membrane bilayer, and solvent. The pressure was maintained at 1.0 bar using the Parrinello-Rahman barostat[53] with a coupling constant of 5 ps and a compressibility factor of 4.5×10^{-5} bar under semi-isotropic coupling conditions (coupled separately along the XY and Z directions) to ensure a tensionless bilayer during the simulation. A time step of 2 fs (during the production run) was chosen utilizing the leapfrog integrator. All simulations were performed using GROMACS software version 20x.

4.4.7.3. Results and discussion

MD simulation revealed the efficient transport of both the ions (K^+ and Cl^-) through the trimeric rosette channel constructed from compound **1** (Figure 4.4A). The simulation snapshot showed the presence of both K^+ and Cl^- ions within the channel lumen, pointing towards the capability of the supramolecular channel to transport each of the types of ions through it.

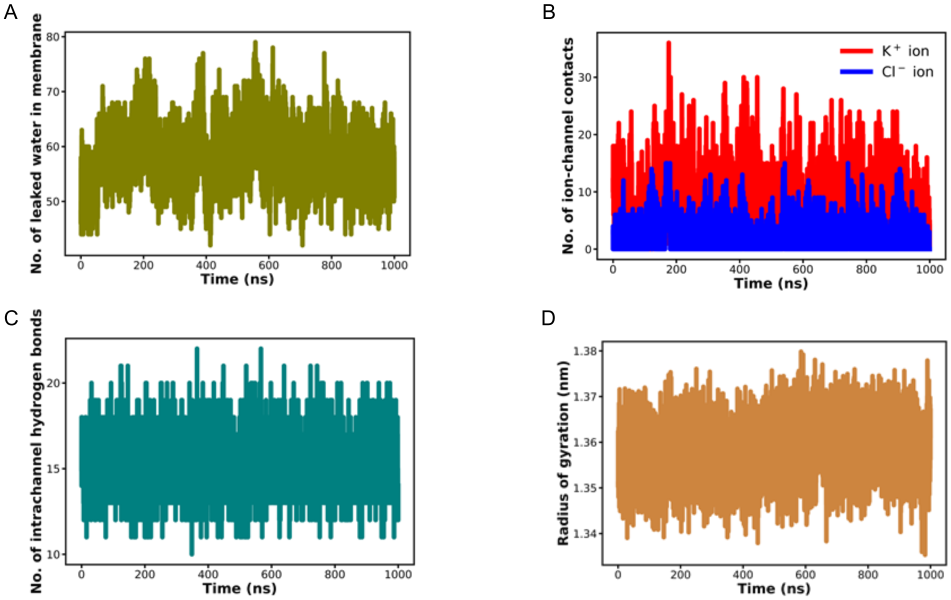

Figure 4.26 The count of leaked water molecules in the membrane through the channel structure (A). The count interaction of each of the K^+ (red) and Cl^- (blue) ions with the channel during the course of simulation (B). The time profile of the number of intra-channel hydrogen bonding (C). The time profile of radius of gyration of the channel during simulation (D).

Further, to attain a quantitative estimation of ion transport through the channel, the number of both the cations and anions that get leaked through the channel was calculated (Figure 4.4C). Multiple instances of leakage of each of the ions have been observed through the channel, suggesting the efficiency of the channel in transporting both ions together.

Further, the count of each of the ions that get permeated through the channel has been calculated. It was noticed that both types of ions are favourably transported through the channel, suggesting the capability of the channel to allow the movement of both ions from one compartment to the other through it (Figure 4.4B). Careful observation in (Figure 4.4B, C) suggested the transport of more cations compared to that of the anions through the channel, most likely attributed to the smaller size of the K^+ ions relative to the larger anions. Taken together, our study illustrates the facile transport of both ions through the synthetic channel, highlighting a greater extent of cation passage than anion, in agreement with the experimental results.

Investigation of the count of water molecules traversing through the channel suggested the sufficient presence of water within the channel core (Figure 4.26A), which provides favourable solvation for the passing ions within the channel lumen and thus makes the ion transport process easy and facile. Therefore, it can be inferred that the presence of an adequate amount of water within the channel core assists in ion transport by maintaining a favourable solvent-rich environment.

Moreover, to acquire mechanistic insights into ion transport and elucidate the sensitivity of the transport process, we scrutinized the crucial interactions facilitating ion movement within the channel structure. An investigation of the count of interactions between the ions and the channel residues as they get transported through the channel indicated that the ion traversal through the channel occurs via establishing direct contact with the channel (Figure 4.26B). Moreover, it was noticed that intra-channel hydrogen bonding is not considerably affected (Figure 4.26C) during the course of ion movement through the channel, which in turn helped facilitate ion transport and maintain the overall stability of the channel in the membrane (Figure 4.26D).

[Note: All MD simulation studies in this chapter were carried out by Dr. Jagannath Mondal and associates from TIFR Hyderabad.]

4.5. NMR Data

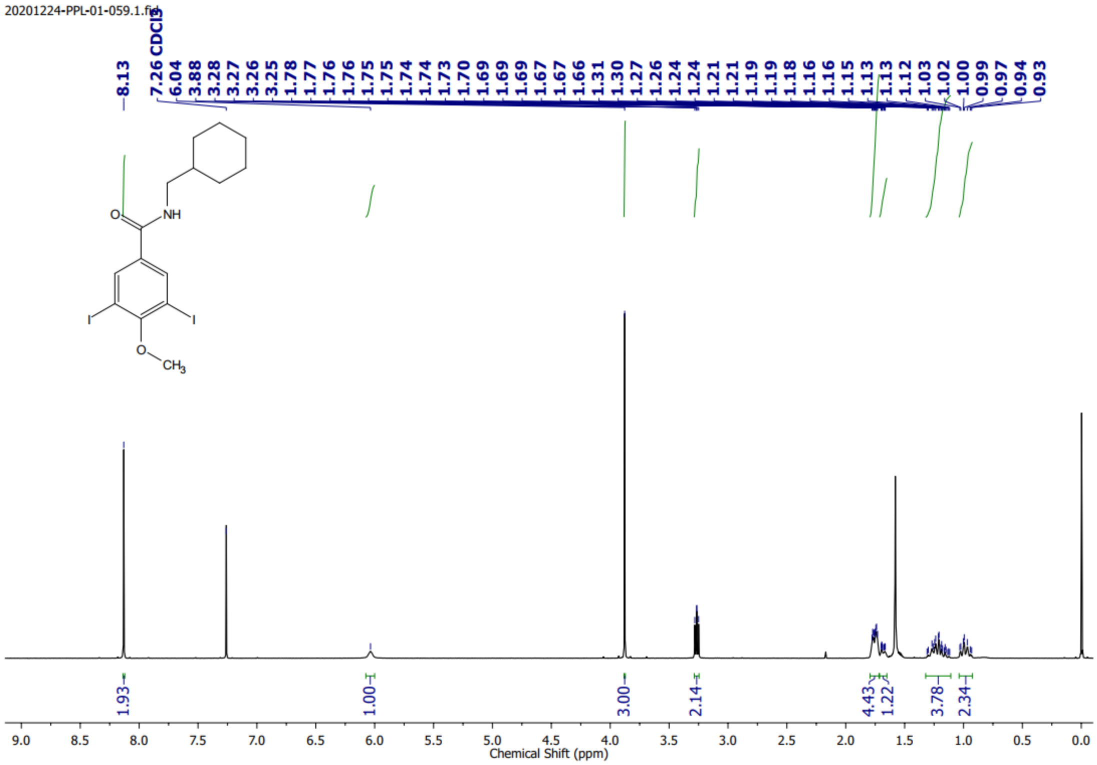

Figure 4.27 ^{1}H NMR (400 MHz) spectrum of compound **3** in $CDCl_3$ solvent.

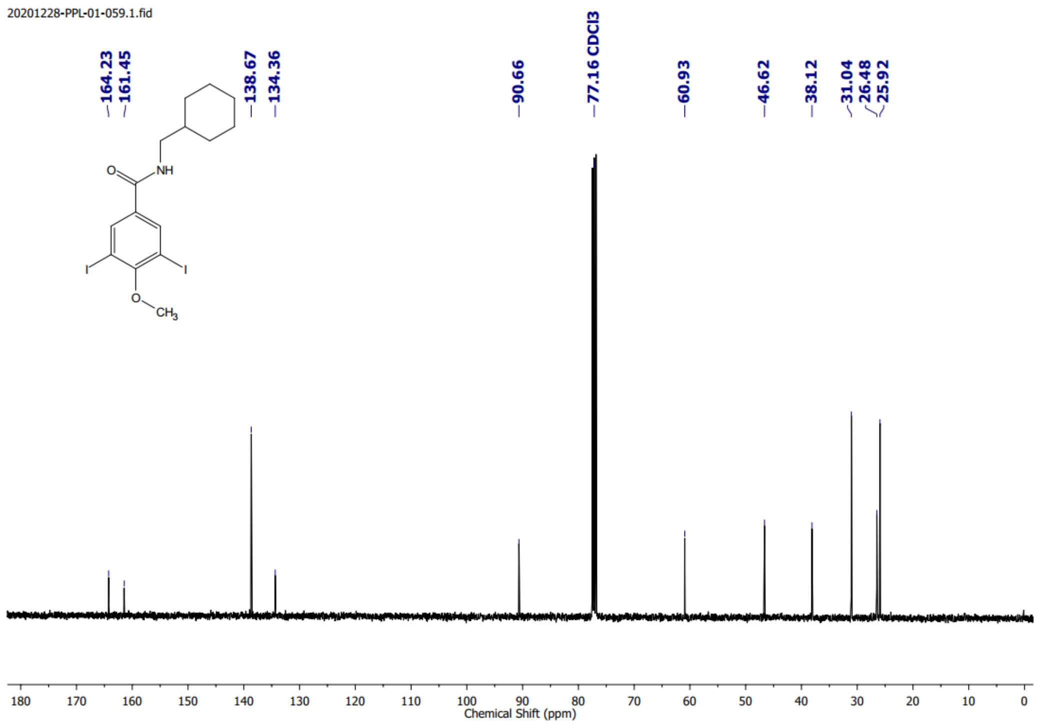

Figure 4.28 ^{13}C NMR (101 MHz) spectrum of compound **3** in $CDCl_3$ solvent.

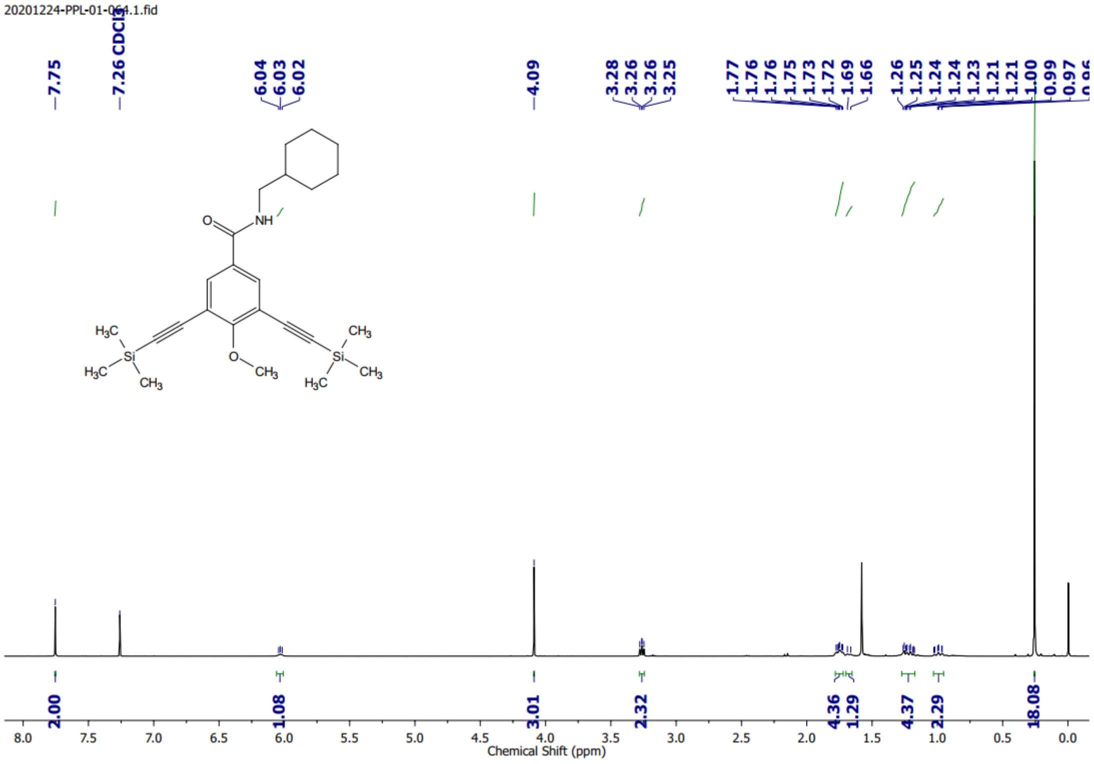

Figure 4.29 ^{1}H NMR (400 MHz) spectrum of compound **4** in $CDCl_3$ solvent.

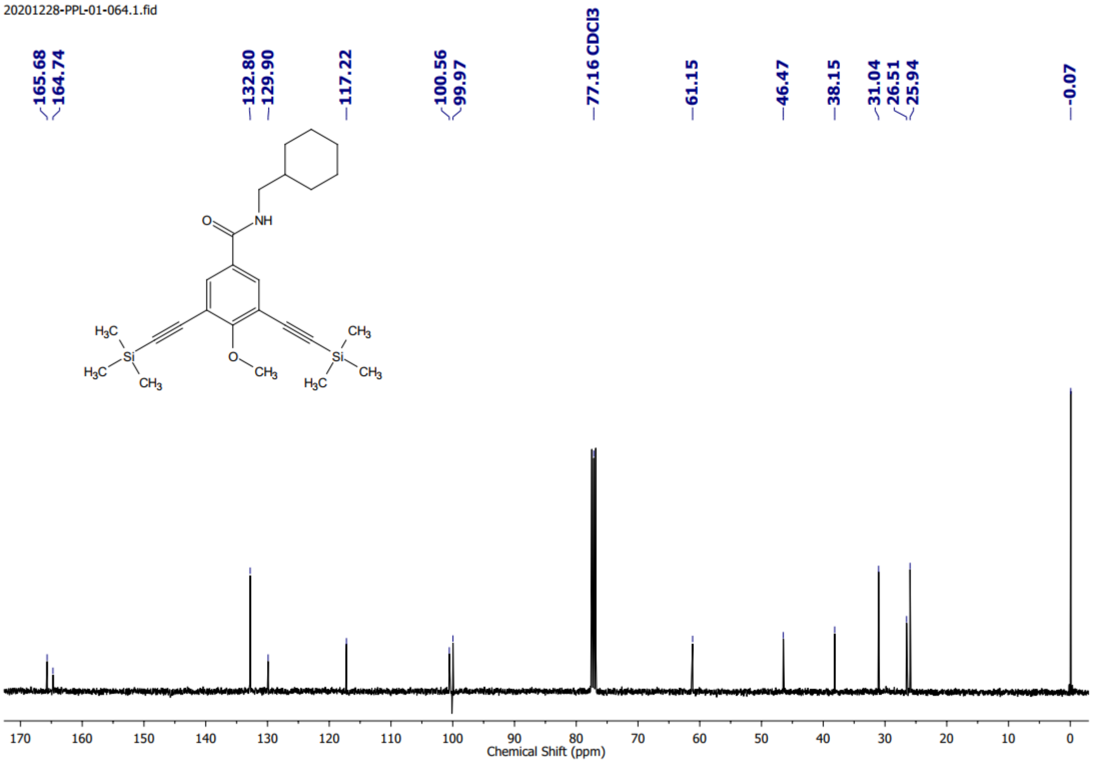

Figure 4.30 ^{13}C NMR (101 MHz) spectrum of compound **4** in $CDCl_3$ solvent.

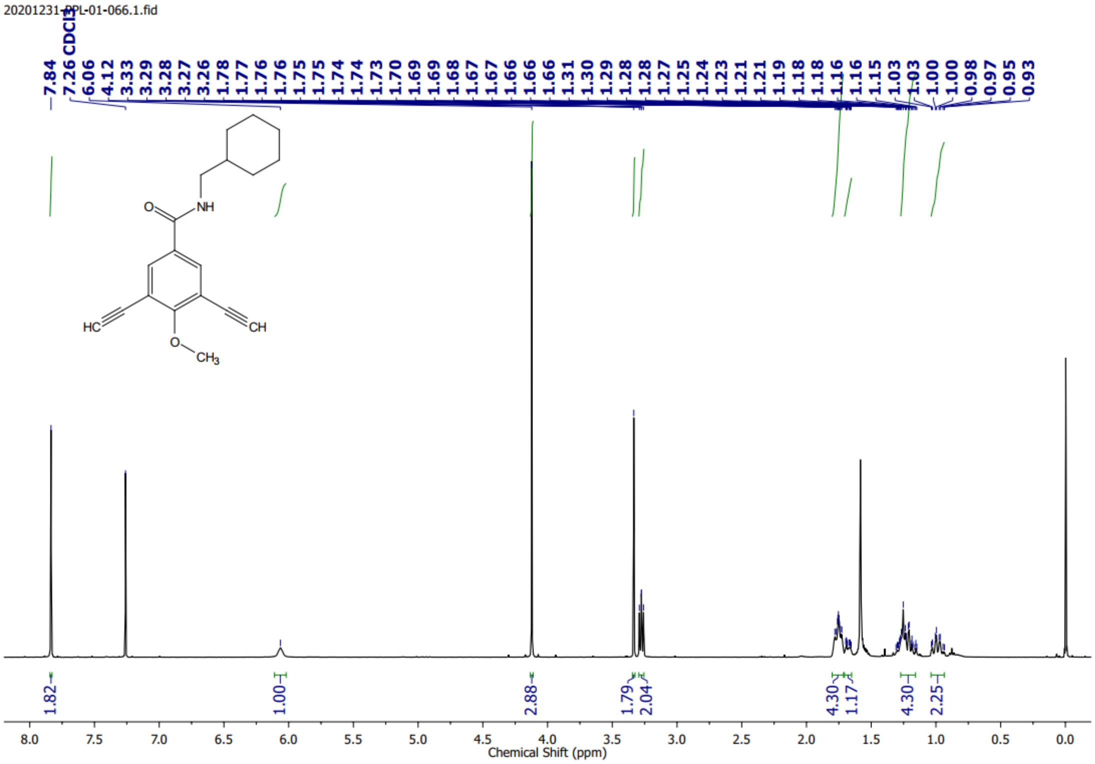

Figure 4.31 ^{1}H NMR (400 MHz) spectrum of compound **5** in $CDCl_3$ solvent.

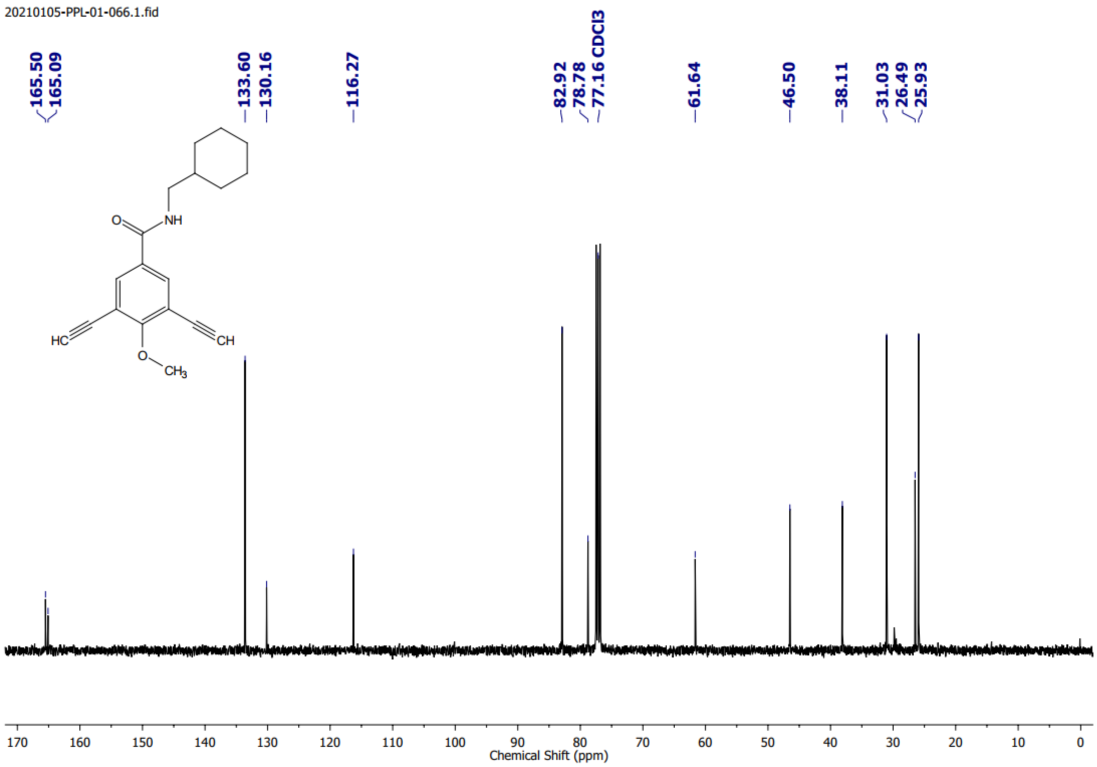

Figure 4.32 ^{13}C NMR (101 MHz) spectrum of compound **5** in $CDCl_3$ solvent.

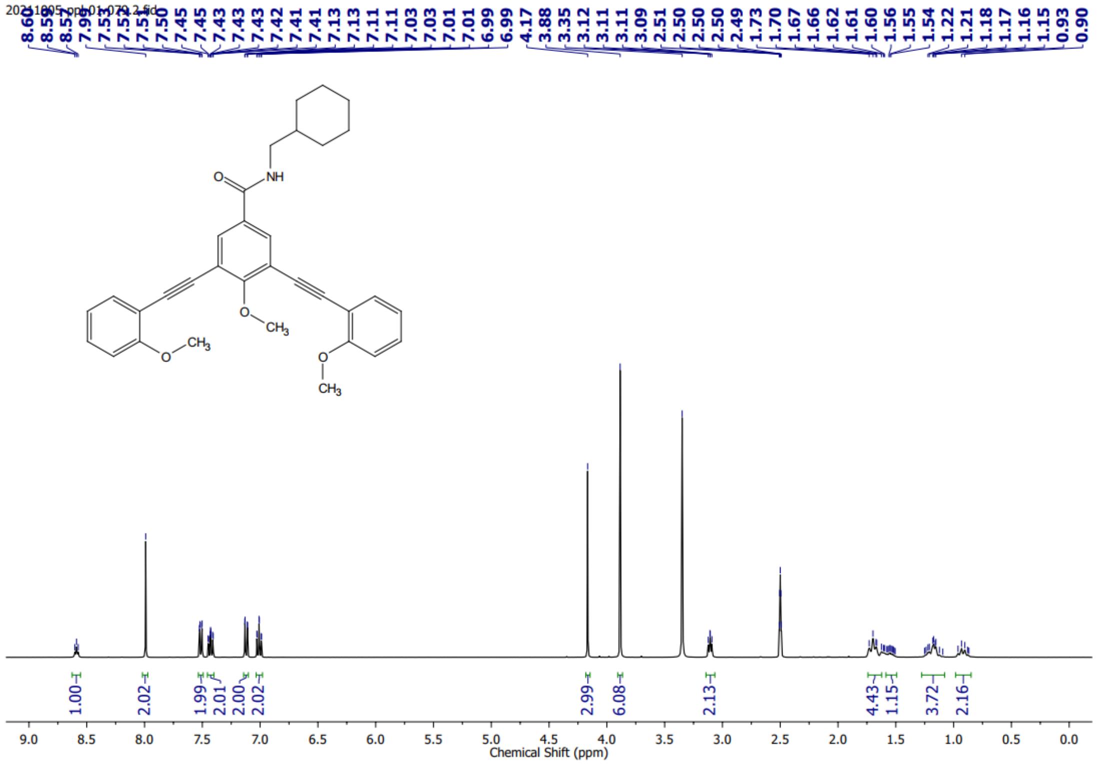

Figure 4.33 ^{1}H NMR (400 MHz) spectrum of compound **6** in DMSO-d_6 solvent.

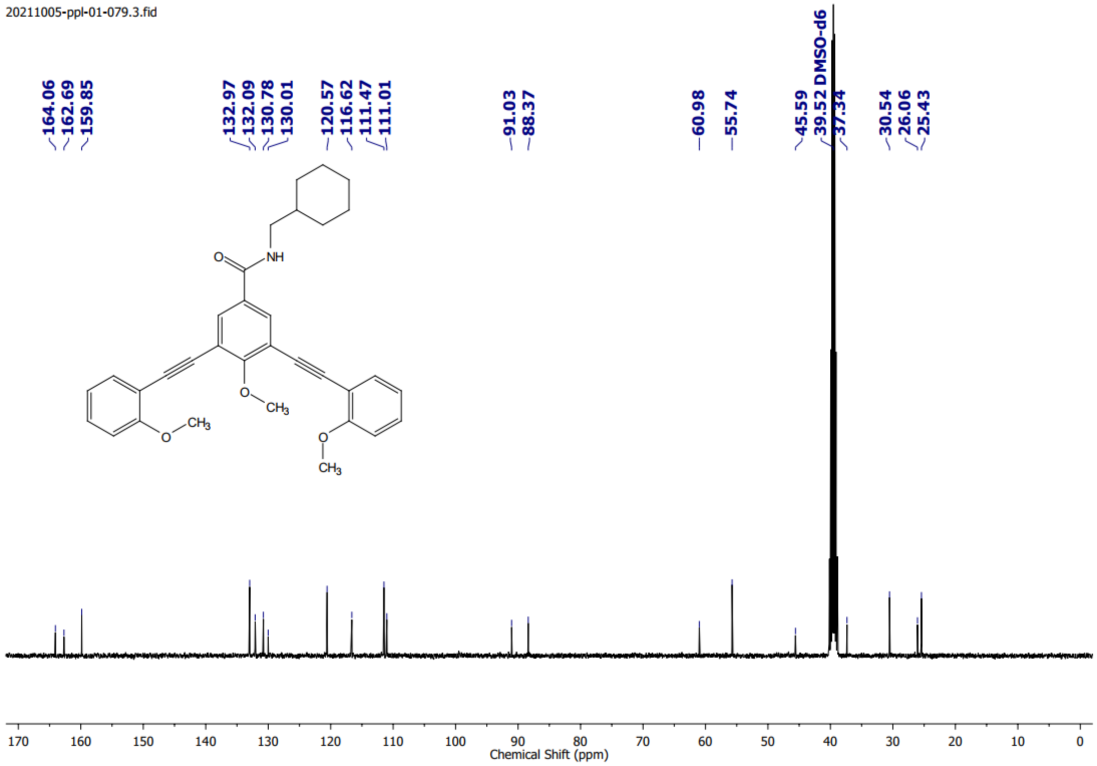

Figure 4.34 ^{13}C NMR (101 MHz) spectrum of compound **6** in DMSO-*d*$_6$ solvent.

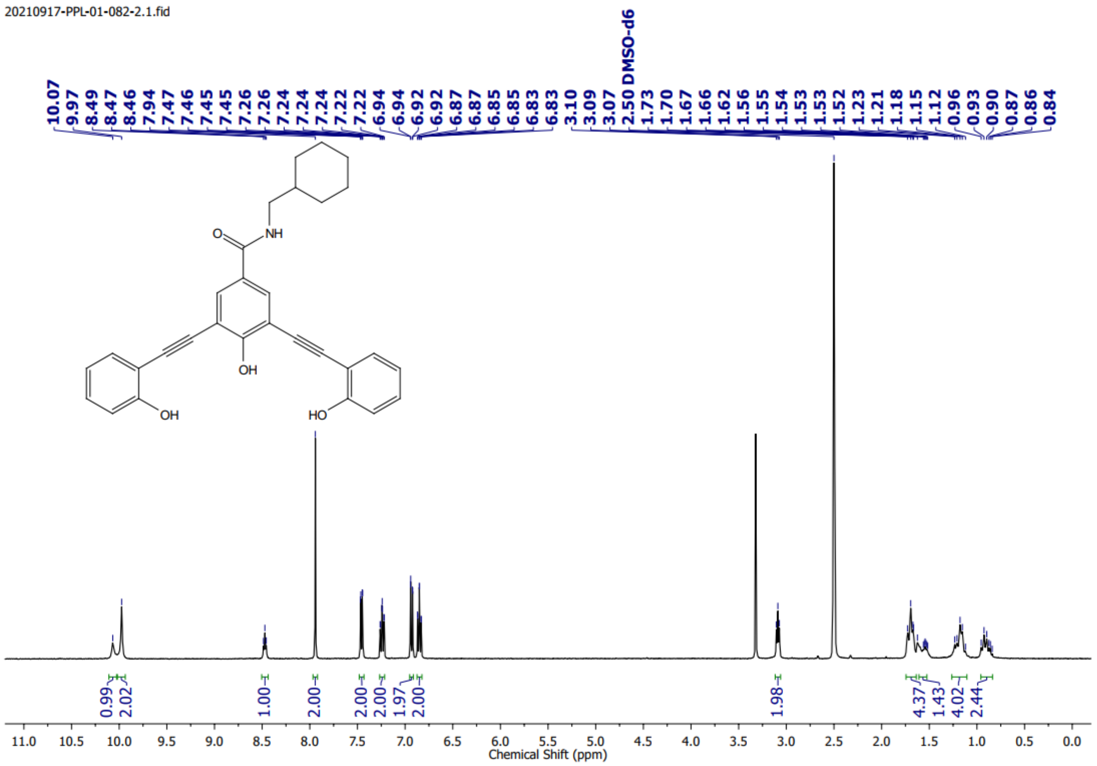

Figure 4.35 ^{1}H NMR (400 MHz) spectrum of compound **1** in DMSO-*d*$_6$ solvent.

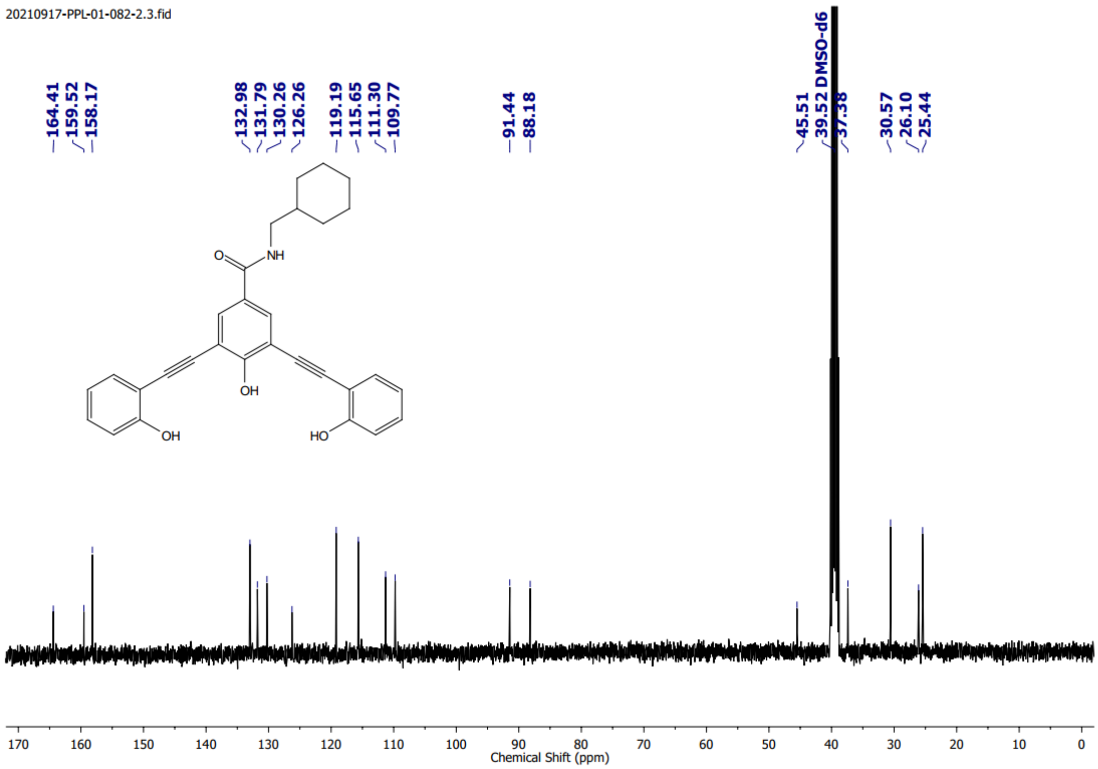

Figure 4.36 ^{13}C NMR (101 MHz) spectrum of compound **1** in DMSO-d_6 solvent.

4.6. References

(1) Portulano, C.; Paroder-Belenitsky, M.; Carrasco, N. *Endocr. Rev.* **2014**, *35*, 106–149.

(2) Kanner, B. I.; Zomot, E. *Chem. Rev.* **2008**, *108*, 1654–1668.

(3) Russell, J. M. *Physiol. Rev.* **2000**, *80*, 211–276.

(4) Payne, J. A.; Rivera, C.; Voipio, J.; Kaila, K. *Trends Neurosci.* **2003**, *26*, 199–206.

(5) Blaesse, P.; Airaksinen, M. S.; Rivera, C.; Kaila, K. *Neuron* **2009**, *61*, 820–838.

(6) Strømgaard, K. *Chem. Rec.* **2005**, *5*, 229–239.

(7) Hucho, F.; Weise, C. *Angew. Chem., Int. Ed.* **2001**, *40*, 3100–3116.

(8) Martinac, B. *J. Cell Sci.* **2004**, *117*, 2449–2460.

(9) Jin, P.; Jan, L. Y.; Jan, Y.-N. *Annu. Rev. Neurosci.* **2020**, *43*, 207–229.

(10) Brohawn, S. G. *Ann. N. Y. Acad. Sci.* **2015**, *1352*, 20–32.

(11) Labarca, P.; Bacigalupo, J. *J. Bioenerg. Biomembr.* **1988**, *20*, 551–569.

(12) Filosa, J. A.; Putnam, R. W. *Am. J. Physiol. Cell Physiol.* **2003**, *284*, 145–155.

(13) Bernard, G.; Shevell, M. I. *Pediatr. Neurol.* **2008**, *38*, 73–85.

(14) Tedesco, M. M.; Ghebremariam, B.; Sakai, N.; Matile, S. *Angew. Chem., Int. Ed.* **1999**, *38*, 540–543.

(15) Talukdar, P.; Bollot, G.; Mareda, J.; Sakai, N.; Matile, S. *Chem. Eur. J.* **2005**, *11*, 6525–6532.

(16) Futaki, S.; Fukuda, M.; Omote, M.; Yamauchi, K.; Yagami, T.; Niwa, M.; Sugiura, Y. *J. Am. Chem. Soc.* **2001**, *123*, 12127–12134.

(17) Wilson, C. P.; Webb, S. J. *Chem. Commun.* **2008**, 4007–4009.

(18) Peters, A. D.; Borsley, S.; Della Sala, F.; Cairns-Gibson, D. F.; Leonidou, M.; Clayden, J.; Whitehead, G. F. S.; Vitórica-Yrezábal, I. J.; Takano, E.; Burthem, J.; Cockroft, S. L.; Webb, S. J. *Chem. Sci.* **2020**, *11*, 7023–7030.

(19) Muraoka, T.; Endo, T.; Tabata, K. V.; Noji, H.; Nagatoishi, S.; Tsumoto, K.; Li, R.; Kinbara, K. *J. Am. Chem. Soc.* **2014**, *136*, 15584–15595.

(20) Malla, J. A.; Umesh, R. M.; Vijay, A.; Mukherjee, A.; Lahiri, M.; Talukdar, P. *Chem. Sci.* **2020**, *11*, 2420–2428.

(21) Malla, J. A.; Sharma, V. K.; Lahiri, M.; Talukdar, P. *Chem. Eur. J.* **2020**, *26*, 11946–11949.

(22) Chattopadhayay, S.; Wanjari, P.; Talukdar, P. *Chem. Sci.* **2024**, *15*, 17017–17025.

(23) Mondal, D.; Sathyan, A.; Shinde, S. V.; Mishra, K. K.; Talukdar, P. *Org. Biomol. Chem.* **2018**, *16*, 8690–8694.

(24) Roy, A.; Gautam, A.; Malla, J. A.; Sarkar, S.; Mukherjee, A.; Talukdar, P. *Chem. Commun.* **2018**, *54*, 2024–2027.

(25) Mondal, D.; Ahmad, M.; Dey, B.; Mondal, A.; Talukdar, P. *Nat. Commun.* **2022**, *13*, 6507.

(26) Ahmad, M.; Metya, S.; Das, A.; Talukdar, P. *Chem. Eur. J.* **2020**, *26*, 8703–8708.

(27) Malla, J. A.; Upadhyay, A.; Ghosh, P.; Mondal, D.; Mondal, A.; Sharma, S.; Talukdar, P. *Org. Lett.* **2022**, *24*, 4124–4128.

(28) Busschaert, N.; Wenzel, M.; Light, M. E.; Iglesias-Hernández, P.; Pérez-Tomás, R.; Gale, P. A. *J. Am. Chem. Soc.* **2011**, *133*, 14136–14148.

(29) Madhavan, N.; Gin, M. S. *ChemBioChem* **2007**, *8*, 1834–1840.

(30) Madhavan, N.; Robert, E. C.; Gin, M. S. *Angew. Chem., Int. Ed.* **2005**, *44*, 7584–7587.

(31) Benke, B. P.; Behera, H.; Madhavan, N. *Eur. J. Org. Chem.* **2020**, *2020* (44), 6898–6902.

(32) Maslowska-Jarzyna, K.; Korczak, M. L.; Chmielewski, M. J. *Front. Chem.* **2021**, *9*, 1–10.

(33) Shinde, S. V.; Talukdar, P. *Angew. Chem., Int. Ed.* **2017**, *56*, 4238–4242.

(34) Malla, J. A.; Roy, A.; Talukdar, P. *Org. Lett.* **2018**, *20*, 5991–5994.

(35) Chattopadhayay, S.; Banzal, K. V; Talukdar, P. *Angew. Chem., Int. Ed.* **2024**, e202414354.

(36) Huang, W.-L.; Wang, X.-D.; Ao, Y.-F.; Wang, Q.-Q.; Wang, D.-X. *J. Am. Chem. Soc.* **2020**, *142*, 13273–13277.

(37) S. Schrödinger Release 2022–1: Maestro, LLC, NewYork, **2021** https://www.schrodinger.com.

(38) Klauda, J. B. *J. Chem. Phys.* **2018**, *149*, 220901.

(39) Jo, S.; Kim, T.; Iyer, Vidyashankara, G.; Im, W. J. *J. Comput. Chem.* ***2008**, 29, 1859–1865*.

(40) Jo, S.; Lim, J. B.; Klauda, J. B.; Im, W. *Biophys. J.* **2009**, *97*, 50–58.

(41) Wang, J.; Wolf, R. M.; Caldwell, J. W.; Kollman, P. A.; Case, D. A. *J. Comput. Chem.* **2004**, *25*, 1157–1174.

(42) Sprenger, K. G.; Jaeger, V. W.; Pfaendtner, J. *J. Phys. Chem. B* **2015**, *119*, 5882–5895.

(43) Wang, J.; Wolf, R. M.; Caldwell, J. W.; Kollman, P. A.; Case, D. A. *J. Comput. Chem.* **2004**, *25*, 1157–1174.

(44) Klauda, J. B.; Venable, R. M.; Freites, J. A.; O'Connor, J. W.; Tobias, D. J.; Mondragon-Ramirez, C.; Vorobyov, I.; MacKerell, Alexander D., J.; Pastor, R. W. *J. Phys. Chem. B* **2010**, *114*, 7830–7843.

(45) Huang, J.; Rauscher, S.; Nawrocki, G.; Ran, T.; Feig, M.; De Groot, B. L.; Grubmüller, H.; MacKerell, Alexander D., J. *Nat. Methods* **2016**, *14*, 71–73.

(46) Brooks, B.R., Brooks III, C.L., Mackerell Jr., A.D., Nilsson, L., Petrella, R.J., Roux, B., Won, Y., Archontis, G., Bartels, C., Boresch, S., Caflisch, A., Caves, L., Cui, Q., Dinner, A.R., Feig, M., Fischer, S., Gao, J., Hodoscek, M., Im, W. and Kuczer, K. *J. Comput. Chem.* **2009**, *30*, 1545–1614.

(47) Jorgensen, W. L.; Chandrasekhar, Jayaraman Madura, J. D.; Impey, R. W.; Klein, M. L. *Mol. Phys.* **1977**, *34*, 525–537.

(48) Hess, B.; Bekker, H.; Berendsen, H. J. C.; Fraaije, J. G. E. M. *J. Comput. Chem.* **1997**, *18*, 1463–1472.

(49) Miyamoto, S.; Kollman, P. A. *J. Comput. Chem.* **1992**, *13*, 952–962.

(50) Páll, S.; Hess, B. *Comput. Phys. Commun.* **2013**, *184*, 2641–2650.

(51) Berendsen, H. J. C.; Postma, J. P. M.; Van Gunsteren, W. F.; Dinola, A.; Haak, J. R. *J. Chem. Phys.* **1984**, *81*, 3684–3690.

(52) Evans;, D. J.; Holian, B. L. *J. Chem. Phys.* **2008**, *4074*, 4069–4074.

(53) Parrinello, M.; Rahman, A. *J. Appl. Phys.* **1981**, *52*, 7182–7190.

Chapter 5

Meta-Dipropynylbenzene-Based Reversibly Ligand-Gated Dimeric Barrel-Rosette Channel with OFF–ON Proton Transport Activity

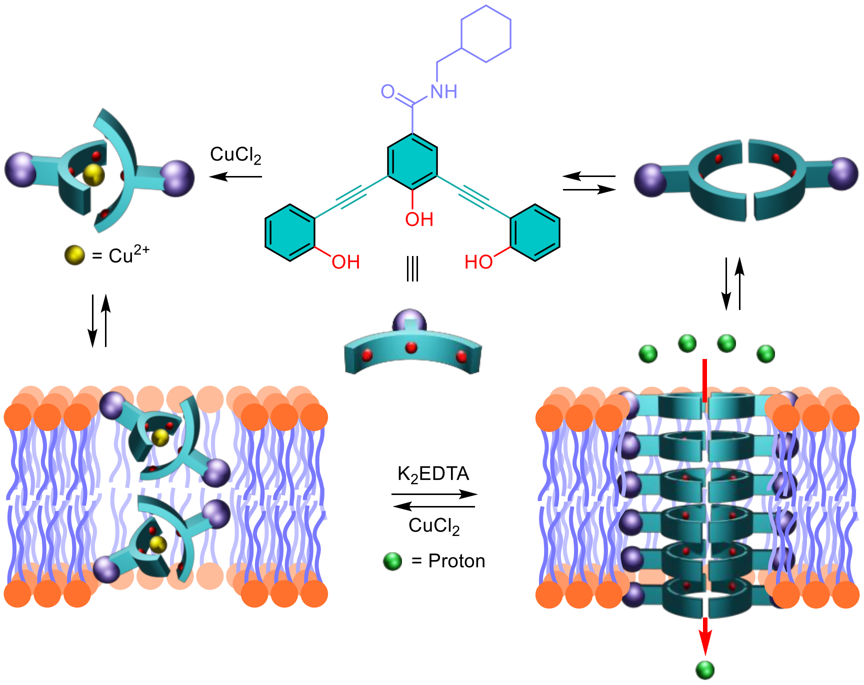

5.1. Introduction

Proton transfer stands out as perhaps the most vital and widespread chemical reaction that forms the backbone of biochemical activities, influencing the behaviour of ion channels, enzyme actions, charge distribution across membranes, pH modulation, etc.[1,2] The pH within various cellular compartments is meticulously controlled, as this regulation is crucial for the effective functioning of multiple organelles. The movement of protons across cellular membranes, aided by mechanisms like symporters, antiporters, and proton-pumping ATPases, is a fundamental aspect of the cellular system that sustains specific pH levels in cellular compartments,[3] which range from the lysosome (pH ≈ 4.7) to the cytosol (pH ≈ 7.2) and mitochondria (pH ≈ 8).[4,5] Therefore, incorporating proton pathways into synthetic frameworks is essential for enhancing proton transport; hence, deriving design principles from enzymes with well-characterized proton pathways would lay a solid foundation for the creation of synthetic conduits. Despite being relatively small and having a higher charge density than other ions, the movement of protons remains a considerable hurdle. However, this transport process demands a thoughtful arrangement of proton transfer residues and/or water molecules to facilitate effective transit. While certain proton pathways, like those present in bacteriorhodopsin[6–8] and cytochrome c oxidase,[9,10] have been thoroughly explored, the specific design principles for proton channels—including the necessary number of residues, their spatial arrangement, the number of pathways within a given molecule, and the pertinent pKa values of the involved residues—are still insufficiently understood.

A voltage-gated Hv1 protein channel facilitates the efflux of H^+ ions from the intracellular environment, thereby inducing alterations in the pH gradients across the membrane bilayer.[11] Moreover, one of the smallest M2 protein channels obtained from the *Influenza A virus* has a single transmembrane helix, which forms four tightly packed transmembrane helices to generate the conducting pore. Presence of the His37 residue near the centre of the transmembrane helix, acting as the pH-sensor of the channels. During proton translocation, it first binds to the histidine residues (His37), which act like a selectivity filter, and the water wires form across the conducting pathway.[12] Matile and coworkers introduced pioneer examples of rigid rod-shaped polyols for the transmembrane transport of protons.[13,14] Later, different scaffolds, including pillar[n]arene,[15] foldamers,[16,17] metal-organic frameworks (MOFs),[18] and nanotube[19] based channels were used to decorate the synthetic mimic of proton channels. The decoration of these synthetic proton channels will help us understand proton translocation in complex membrane environments and also help us become enlightened about alternative biomedical applications. According to our best knowledge, none of the synthetic proton channels controlled its proton transport by response to an external stimulus. Therefore, there is a high demand for the construction of the stimulus-controlled proton channel system in which OFF-ON proton transport can be achieved by utilizing the external stimulus.

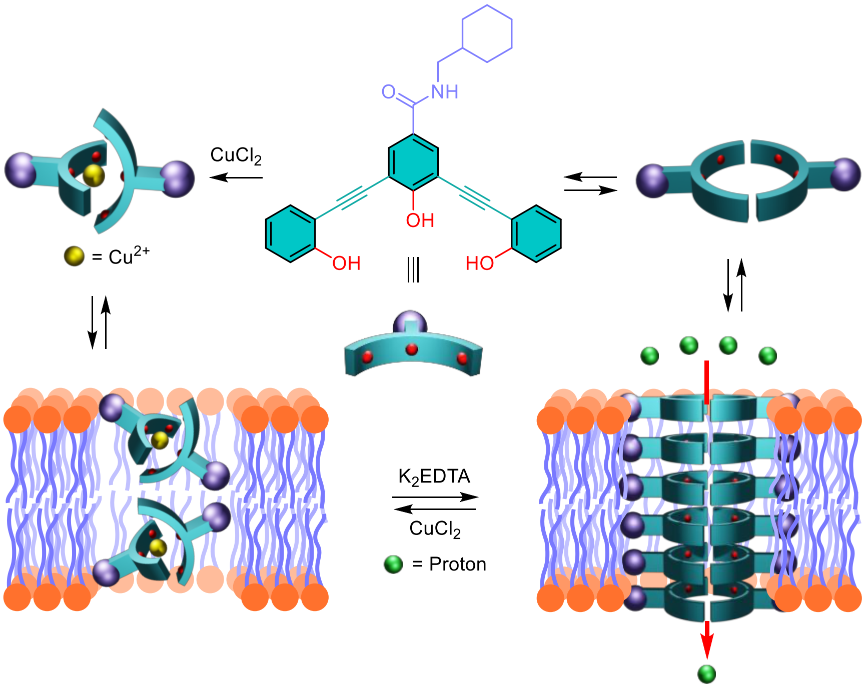

Figure 5.1 Structure of proton channel-forming compound **1** and its ligand-gated reversible OFF-ON proton transport activity in the presence of $CuCl_2$ and K_2EDTA across the bilayer membrane.

Herein, for the inaugural example, we present a reversible ligand-gated *meta*-dipropynylbenzene-based dimeric rosette proton channel having ligand-responsive reversible OFF-ON proton transport properties across the lipid bilayer membrane (Figure 5.1). Incorporating an amide linker in the design facilitates efficient aggregation, thereby enhancing the self-assembly of the molecule through the establishment of intermolecular hydrogen bonding interactions. The tri-phenolic core, which is linked to a rigid acetylene moiety, possesses the capability to retain water molecules via the formation of hydrogen bonding interactions. These water molecules can establish a continuous water wire within the cavity of the dimeric rosette of compound **1**, which is instrumental in promoting the effective translocation of protons across the membrane in accordance with the Grotthuss mechanism. It is expected that the introduction of $CuCl_2$ in conjunction with compound **1** will yield a dimeric $Cu^{2+}\cdot(\mathbf{1})_2$ complex, consequently disrupting the water wire present within the dimeric rosette of compound **1**. Therefore, the formation of an assembled dimeric rosette channel within the bilayer membrane will be inhibited. Furthermore, the subsequent addition of dipotassium ethylenediaminetetraacetic acid (K_2EDTA) is expected to remove Cu^{2+} from the $Cu^{2+}\cdot(\mathbf{1})_2$ complex. This regenerates the unbound compound **1**, which can be reassembled within the bilayer for the formation of a self-assembled dimeric barrel-rosette and re-establish the proton translocation pathway through the regeneration of the water wire. Hence, it is anticipated that the sequential addition of $CuCl_2$ and K_2EDTA will enable the reversible OFF-ON proton transport activity of compound **1** within the bilayer membrane.

5.2. Results and discussions

5.2.1. Synthesis

Compound **1** was synthesized using the same protocol described in ***Chapter 4***.

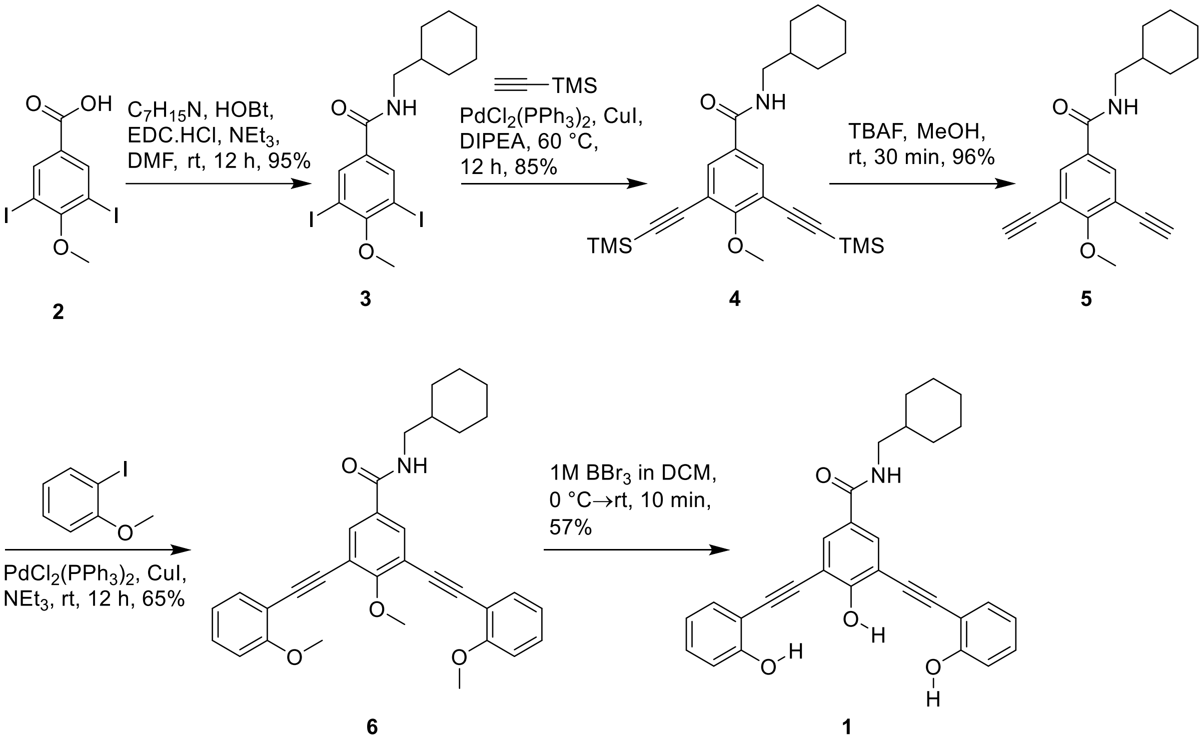

Scheme 5.1 Synthetic scheme for the compound **1**.

5.2.2. Membrane colocalization of compound 1

To understand the colocalization of compound **1**, giant unilamellar vesicles (GUVs) were prepared, and imaging was carried out by using fluorescence microscopy. To understand the vesicle formation, Texas Red dye was used to mark the membrane of the GUVs. GUVs were prepared separately in the presence and absence of compound **1**, and all of the GUVs were imaged in fluorescence microscopy. During imaging of the GUVs, a nice red fluorescence was observed, indicating the formation of the GUVs and confirming the membrane tagging by the Texas Red. On the contrary, in the presence of compound **1** (25 nM), we noticed the presence of blue fluorescence in the 365 nm channel, indicating the presence of compound **1** in the membrane (Figure 5.2). The overlay image demonstrated that both the Texas Red and compound **1** colocalize at the same place, which validated the efficient colocalization of compound **1** in the vesicular membrane.

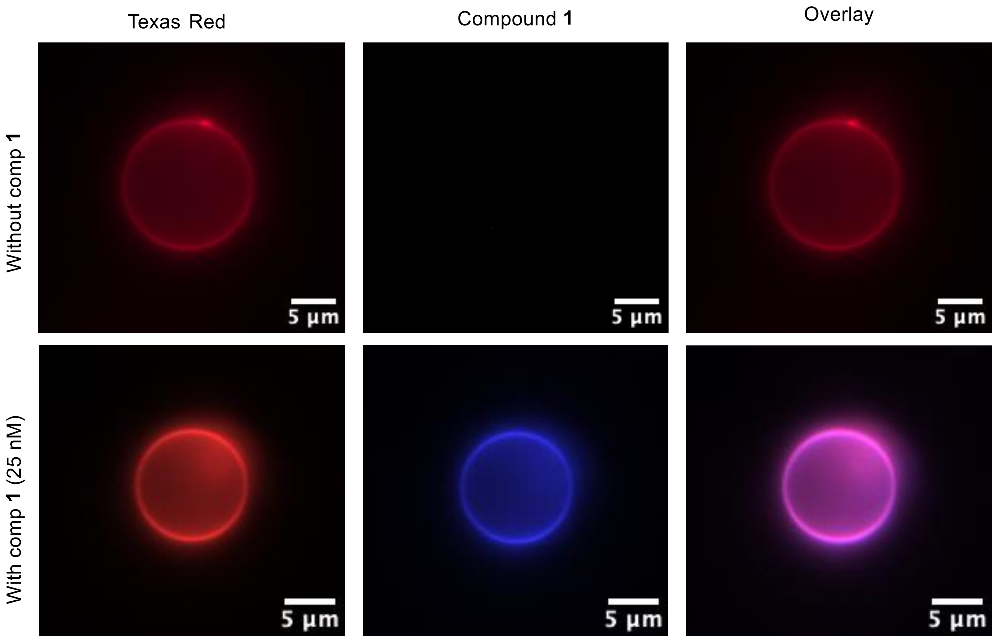

Figure 5.2 Colocalization of compound **1** (20 nM) on vesicular membrane monitored through fluorescence microscopy.

5.2.3. Morphological change of compound 1 in the presence of HCl

Field emission scanning electron microscopy (FESEM) was employed to elucidate the morphological characteristics of compound **1** by varying concentrations, both in the presence and absence of hydrochloric acid (HCl). In the absence of HCl, compound **1** exhibited a helical fibril morphology. The introduction of HCl resulted in the emergence of a pronounced rod-like morphology (Figure 5.7), suggesting that the presence of HCl did not disrupt the self-assembly of compound **1**; rather, it facilitated the robust aggregation of compound **1**.

5.2.4. Crystal structure of compound 1

To uncover the assembly of compound **1**, it was crystallized through the gradual evaporation of the methanol solvent. The crystallographic analysis of compound **1** revealed that the water molecule is coordinated by the hydroxyl (-OH) moiety of compound **1**. Within each layer, water molecules are interconnected by hydrogen bonding, thereby establishing a water wire within the cavity of the dimeric rosette of compound **1**. Additionally, the interlayer assembly of compound **1** was stabilized by the intermolecular H-bonding and π-π stacking interactions (Figure 5.3). The observation of the water chain within the cavity of the dimeric rosette suggested the potential for proton transport via the Grotthuss mechanism.

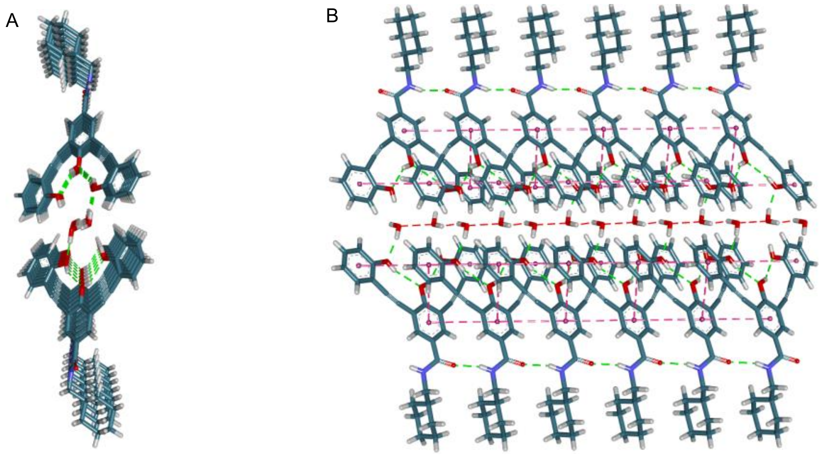

Figure 5.3 Top (A) and side (B) view the self-assembled structure of compound **1** in the licorice model.

5.2.5. Ion transport studies

HPTS-based assays were initially conducted to understand the proton transport behaviour of compound **1** across egg yolk phosphatidylcholine large unilamellar vesicles (EYPC–LUVs) by creating a pH gradient (pH_{in} = 7.0 and pH_{out} = 6.4).[17] Concentration-dependent studies of compound **1** indicated the efficient influxing of the proton across the vesicular membranes (Figure 5.9A). Hill analysis (Figure 5.9B) validated compound **1** has a half-maximal effective concentration (EC_{50}) value (0.709 ± 0.06 µM, 1.05 mol% with respect to the lipid) and Hill coefficient (n) $\approx$ 2, validating the involvement of the two monomeric units to form an active rosette structure in the membrane which efficiently translocate the proton. Further, a pH-dependent proton influxing activity was investigated across the EYPC–LUVs⊃HPTS by varying the extravesicular pH, maintaining the intravesicular pH = 7.0. If proton transport occurred via the water wire in accordance with the Grotthuss mechanism, facilitated by the dimeric rosette of compound **1**, it is anticipated that a reduction in the extravesicular pH will lead to the disassembly of the water wire structure due to the protonation of the hydroxyl (-OH) moiety of compound **1**. Consequently, a significant diminution in proton influx is predicted. Interestingly, with the reduction of the extravesicular pH, a notable decrease in proton influx was recorded for compound **1** (Figure 5.10), corroborating that proton transport predominantly occurs through the water wires in alignment with the Grotthuss mechanism.

To elucidate the ion selectivity characteristics of compound **1** at the specific concentration at which it facilitates proton transport, both cation and anion selectivity[20] assessments were conducted utilizing EYPC–LUVs⊃HPTS. Remarkably, we observed an imperceptible cation and anion transport activity of compound **1** at a concentration of 625 nM (Figure 5.4A, B), thereby substantiating that within the defined proton transport concentration parameters, compound **1** is incapable of mediating cation or anion transport. To further substantiate the Cl^- ion transport by compound **1** within the designated proton transport concentration parameters, Cl^- ion influx was evaluated employing a halide-sensitive lucigenin dye across EYPC–LUVs⊃Lucigenin.[21] An indistinguishable Cl^- transport activity of compound **1** was observed even at a concentration of 1.25 µM (Figure 5.13C), indicating that within this concentration range, compound **1** is unable to facilitate the transport of the Cl^- ion across the membrane, which also aligned with the data obtained from the HPTS assay. Furthermore, a highly potential sensitive safranin O dye was employed to examine the efficacy of the proton transport mechanism mediated by compound **1** across EYPC–LUVs.[17] If proton transport occurs via compound **1**, an elevation in the membrane potential is anticipated, which will increase the fluorescence intensity of the safranin O dye. Importantly, the presence of compound **1** resulted in an enhancement of the fluorescence intensity of the safranin O dye (Figure 5.4C), analogous to the behaviour exhibited by the established protonophore carbonyl cyanide-p-trifluoromethoxyphenylhydrazone (FCCP). Conversely, compound **SCS-01-136** (previously identified in ***Chapter 2*** as compound **1b**), which is recognized for its ability to transport both cations and anions through an electroneutral symport mechanism, did not demonstrate any enhancement in the fluorescence activity of the safranin O dye. This data further reconfirmed the validation of proton transport mediated by compound **1** across the membrane.

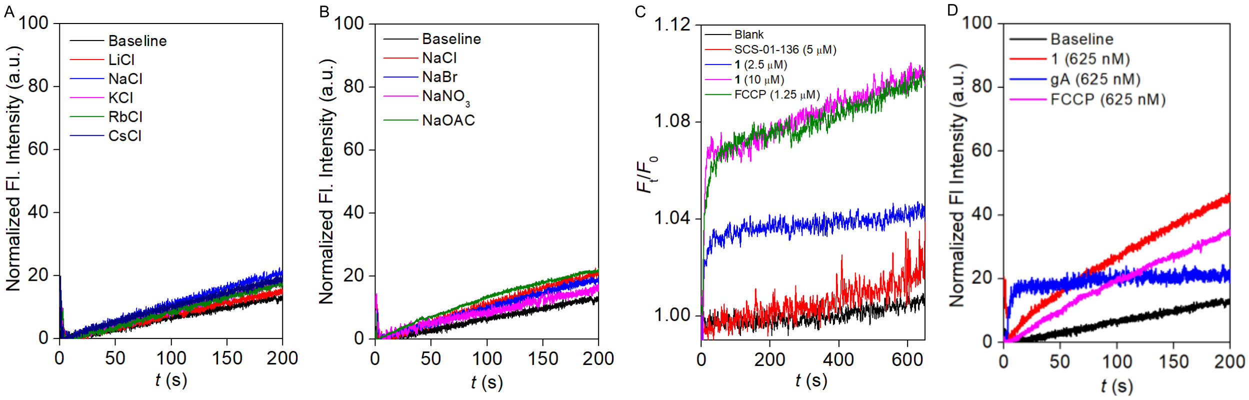

Figure 5.4 Cation (A) and anion (B) selectivity of the compound **1** across EYPC–LUVs⊃HPTS. Change in the Safranin O fluorescence intensity in the presence of compound **1**, FCCP and **SCS-01-136** across EYPC–LUVs (C). Proton transport activity of compound **1** using EYPC–LUVs⊃HPTS (D).

To investigate the efficacy of proton transport mediated by compound **1**, a comparative analysis was conducted with the well-established protonophore FCCP and the natural channel gramicidin (gA), utilizing a recognized proton transport assay across EYPC–LUVs⊃HPTS while maintaining the intravesicular NaCl buffer (10 mM HEPES, 100 mM NaCl, pH = 7.0) and an extravesicular Na_2SO_4 buffer (10 mM HEPES, 66.6 mM NaCl, pH = 7.0).[22] The assay revealed a notable increase in HPTS fluorescence activity subsequent to the addition of compound **1** (625 nM). Given that at this concentration, neither cation nor anion transport is facilitated by compound **1**, the observed enhancement in fluorescence activity must be attributed to the translocation of H^+ or OH^- ion across the membrane. Notably, comparative analyses of the proton transport activity indicated that compound **1** exhibited approximately 1.3 and 2 times higher proton transport activity compared to FCCP and gA, respectively (Figure 5.4D). To ascertain the specific ion transport mechanism of compound **1**, alterations in the extravesicular pH were monitored in the presence of the coupling agent valinomycin (K^+ ion transporter) with a ΔpH of 3 across the membrane. It was observed that the pH variation was markedly more pronounced in the presence of valinomycin when proton transport occurred in the direction from pH = 4.0 to 7.0, as compared to the direction from pH = 7.0 to 10.0. This significant pH alteration in the direction from pH = 4.0 to 7.0 (Figure 5.17) validated that compound **1** preferentially facilitates the transport of H^+ ions over OH^- ions. To elucidate whether the H^+ transport mechanism occurs in the form of H_3O^+ or as H^+ through the dimeric rosette of compound **1**, a 5(6)-carboxyfluorescein (CF) based assay was performed.[23] The investigation into the fluorescence quenching of the CF dye across EYPC–LUVs⊃CF was carried out in the presence of a hypertonic sucrose solution in the extravesicular medium. No discernible change in the fluorescence quenching of the CF dye was detected in the presence of compound **1** (Figure 5.20), whereas gramicidin exhibited a significant fluorescent quenching due to the efflux of H_2O. Consequently, this experiment validated that while gramicidin transports H^+ in the form of H_3O^+, compound **1** facilitated the transport of H^+ in the form of H^+ by utilizing the water wire of the dimeric rosette of compound **1**.

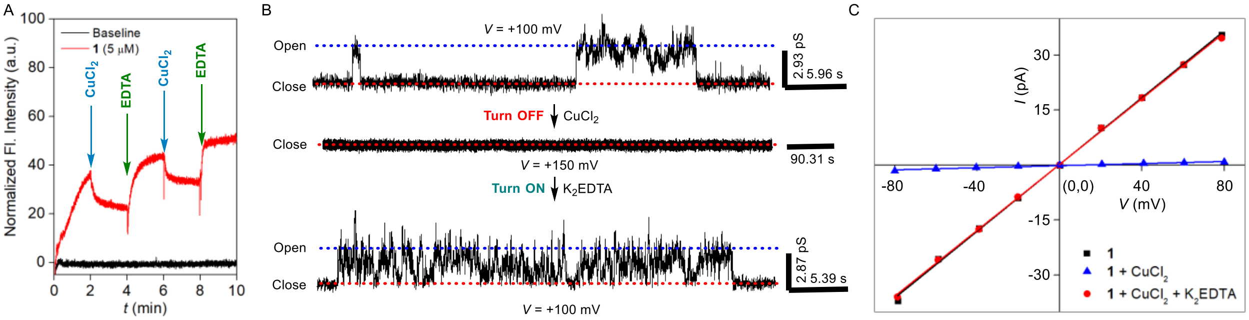

Figure 5.5 Ligand-gated reversible OFF-ON proton transport activity through the dimeric rosette of compound **1** across EYPC–LUVs⊃HPTS (A). Ligand-gated reversible OFF-ON opening-closing events of channel forming compound **1** in the presence of the $CuCl_2$ and K_2EDTA under symmetric 1 M HCl solution (B). Change in the *I-V* plot of channel forming compound **1** in the presence of the $CuCl_2$ and K_2EDTA under symmetric 1 M HCl solution (C).

The effect of compound **1** on the membrane integrity was tested by using both the 5(6)-carboxyfluorescein (CF) (Figure 5.18) and calcein (Figure 5.19) dye across EYPC–LUVs.[24] Both the CF and calcein are self-quenching dyes whose fluorescence activity remains in a quenching state at high concentrations, which can be regained in diluted conditions. Irrespective of the entrapped dye, no enhancement in the fluorescence activity was observed in the presence of compound **1** at different concentrations. This data validated that compound **1** neither formed any large pores nor disintegrated the membrane. Further, to address the mode of the proton transport, an electrophysiological experiment was carried out.[16] A prominent opening-closing event of compound **1** was noticed at different holding potentials in the presence of the symmetrical 1 M HCl salt, validating the formation of a channel in the membrane for the translocation of the protons. The experimentally evaluated average single-channel conductance of compound **1** was found to be 457.4 pS with cis/trans = 1 M HCl/ 1 M HCl setup.

Finally, the ligand-gated response of compound **1** (5 μM) in the context of proton transport was examined across the EYPC–LUVs⊃HPTS by establishing a ΔpH of 0.8 between the intra- and extravesicular medium (Figure 5.5A). Notably, adding the $CuCl_2$ (0.5 equiv) effectively interrupted the proton transport mechanism, thereby indicating the OFF state of proton translocation. This OFF state can be explained by the formation of $Cu^{2+}\cdot(\mathbf{1})_2$, which disrupts the integrity of the water wire. Consequently, protons are unable to translocate under these specific conditions. The subsequent addition of K_2EDTA (0.6 equiv) rapidly instigated an increase in HPTS fluorescence activity, attributable to the reconstitution of the water wire through the formation of the self-assembled dimeric rosette structure of compound **1**, thereby confirming the ON state of the transport process. Eventually, this OFF-ON transport activity was observed in the repeating cycles, indicating the reversible OFF-ON ligand-gated proton transport by compound **1**. The reversible OFF-ON proton channel formation by compound **1** was also investigated by using the bilayer lipid membrane (BLM) by sequential addition of the $CuCl_2$ and K_2EDTA (Figure 5.5B). Interestingly, the addition of the $CuCl_2$ rapidly turns off the opening-closing events at different holding potentials, validating the OFF state of channel **1**. A sequential addition of the K_2EDTA regenerates the free channel **1** from $Cu^{2+}\cdot(\mathbf{1})_2$ complex and turns on the opening-closing event, confirming the ON state of the channel **1**. Furthermore, a change in current with voltage was analyzed from the *I-V* plot. It is noteworthy that the addition of $CuCl_2$ drastically decreases the single-channel conductance due to the inability to transport any protons. The addition of the K_2EDTA regenerated the single channel conductance, which is comparable to the initial value, divulging the regeneration of the efficient proton fluxing across the membrane (Figure 5.5C). This data corroborated its reversible ligand-gated OFF-ON response towards the proton transport process.

5.2.6. Theoretical calculations

Finally, molecular dynamics (MD) simulation of the dimeric rosette of a hexameric assembly of compound **1** was investigated with the K^+Cl^- salts to understand the channel formation and the capability of K^+ and Cl^- ion transport through the dimeric rosette of compound **1**. The detailed MD simulation studies revealed the dimeric rosette of compound **1** is incapable of facilitating the transport of either of K^+ or Cl^- through the translocation pathway (Figure 5.6B). Further investigation revealed the presence of a stable array of single water molecules throughout the MD simulation (Figure 5.6A), indicating the stable water wire may provide the path for proton translocation by following the Grotthuss mechanism.

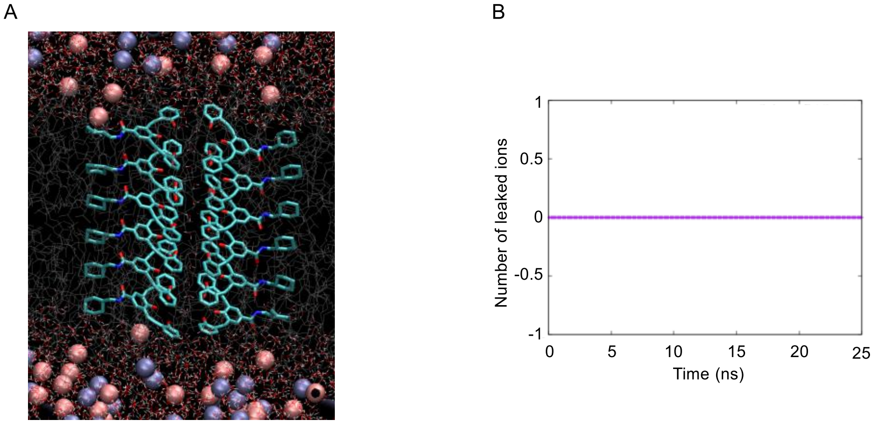

Figure 5.6 A representative snapshot depicting the no transport of K^+ and Cl^- ions (shown in red and blue spheres, respectively) and water through the dimeric rosette of compound **1** within the membrane separating the two aqueous compartments containing 1 M KCl salt (A). Number of leaked ions through the dimeric rosette of compound **1** in the membrane from one compartment to the other during the course of the simulation (B).

5.3. Conclusion

In conclusion, we have presented a synthetic proton channel system based on a *meta*-dipropynylbenzene-derived barrel rosette architecture for transmembrane transport of protons. A concentration-dependent investigation of compound **1** substantiates the determination of the half-maximal effective concentration (EC_{50}) value (0.709 ± 0.06 μM, 1.05 mol% relative to the lipid) and a Hill coefficient (n) ≈ 2, thereby confirming the participation of two monomeric units in the formation of an active rosette structure within the membrane, which facilitated the efficient translocation of protons. An examination of the ion selectivity of compound **1** within the defined proton transport concentration range demonstrated the absence of cation and anion transport across the membrane. Additionally, a potential sensitive safranin O dye provided further corroboration of the proton transport characteristics exhibited by compound **1**. Comparative analysis of proton transport activity indicated that compound **1** possesses 1.3 and 2 times higher proton transport activity than the FCCP and gramicidin, respectively. A detailed assessment confirmed compound **1** preferentially transports H^+ ions over OH^- ions. A CF-based H_2O transport assay established that compound **1** did not facilitate the transport of H^+ ions in the form of H_3O^+ but instead mediated the transport of H^+ ions as H^+ by utilizing a water wire. Leveraging the fluorescence properties of compound **1**, fluorescence imaging of Giant unilamellar vesicles (GUVs) containing compound **1** validated the colocalization of the compound within the bilayer membrane. The membrane leakage assay, utilizing both CF and calcein, confirmed that compound **1** did not induce the formation of large pores or disrupt membrane integrity. The mode of proton transport mechanisms was conducted through electrophysiological experiments, which verified establishing an ion channel within the bilayer membrane with an average single channel conductance of 457.4 pS. Finally, detailed experimental investigations with EYPC–LUVs⊃HPTS and electrophysiological experiment validated its ligand-gated reversible OFF-ON proton transport behaviour.

5.4. Experimental section

5.4.1. General methods

Egg yolk phosphatidylcholine (EYPC) was obtained from Avanti Polar Lipids as a solution in $CHCl_3$ (25 mg/mL). HEPES buffer, HPTS, Lucigenin, Safranin O, Calcein, 5(6)-carboxyfluorescein, Texas Red, Triton X–100, NaOH, and inorganic salts were purchased of molecular biology grade from Sigma and Invitrogen. Large unilamellar vesicles (LUVs) were prepared using a mini extruder equipped with a polycarbonate membrane of 100 nm or 200 nm pore size, purchased from Avanti Polar Lipids.

5.4.2. Physical measurements

The pH of buffer solutions was adjusted using the Hanna HI98108 $PHep^+$ pH meter. ChemBio Draw 21.0.0 software was used to draw structures and process figures. All buffer solutions were prepared from the autoclaved water. Fluorescence experiments were recorded on Fluoromax-4 and Fluoromax+ from Jobin Yvon Edison, equipped with an injector port and magnetic stirrer in a microfluorescence cuvette. The extravesicular dye was removed by performing gel chromatography using Sephadex G-50. The fluorescence studies have proceeded using Origin 8.5 software. Conductance measurement through ion channel was carried out in a planar bilayer lipid membrane (BLM) workstation obtained from Warner Instrument, consisting of head-stage and its corresponding amplifier BC-535, 8-pole bessel filter LPF-8, Axon CNS Digidata 1440A, and pClamp 10 software. The conductance data were analyzed using Clampfit 10.6 software.

5.4.3. Synthetic procedures

Synthetic procedure and characterization of all synthesized compounds are reported in ***Chapter 4***.

5.4.4. Membrane colocalization of compound 1

To understand the colocalization of compound **1**, giant unilamellar vesicles (GUVs) were prepared, and imaging was carried out by using fluorescence microscopy.

Giant unilamellar vesicles were prepared by using polyvinyl alcohol. Initially, place a clean glass coverslip on a hot plate set to 50 °C, then add a drop of 5% degassed Polyvinyl alcohol (PVA) onto the coverslip and leave it to dry and form a thin film (usually takes 10 min). Add 3 µL of 1 mM EYPC lipid stock in chloroform with and without compound **1** to the dry PVA separately while on the hot plate. Leave both of them for a few seconds in a vacuum till all the chloroform evaporates. Peel off the PVA film, immerse it in

200 μL of PBS in an Eppendorf, and kept it undisturbed for 30 min. Finally, pipette the buffer in and out a few times to release GUVs from the PVA film.

To understand the vesicle formation Texas Red dye was used to mark the membrane of the GUVs.

5.4.5. Morphological study with field emission scanning electron microscopy (FESEM)

Compound **1** with 10 μM concentration in $CHCl_3$ solvent and a mixture of compound **1** and HCl (1:1) were drop-casted carefully on a silicon wafer and dried. The change in the surface morphology of compound **1** in the presence of HCl was investigated in the solid state and was examined by FESEM studies.

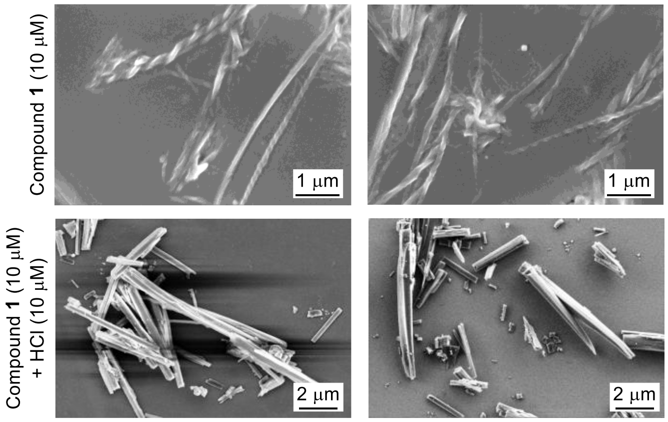

Figure 5.7 FESEM images of morphology changes of compound **1** in the presence of HCl in $CHCl_3$ solvent at 298 K.

5.4.6. Transport studies

5.4.6.1. Proton transporting activity studies across EYPC–LUVs⊃HPTS

Buffer and stock solution preparation: Phosphate buffers (10 mM phosphate buffer, pH = 7.0 and 10 mM phosphate buffer, pH = 6.4) were prepared by dissolving an accurate amount of solid sodium phosphate dibasic heptahydrate and sodium phosphate monobasic monohydrate in autoclaved water. The pH was maintained at 6.4 and 7.0 by adding NaOH solution. All stock solutions of compound **1** were prepared in HPLC grade DMSO solvent for HPTS-based transport studies.

Preparation of EYPC–LUVs⊃HPTS: Vesicles were prepared according to the reported protocol.[24]

Final conditions: ~ 5.0 mM EYPC, Inside: 1 mM HPTS, 10 mM phosphate buffer, pH = 7.0, Outside: 10 mM phosphate buffer, pH = 7.0.

Proton influx across EYPC–LUVs⊃HPTS: In a clean and dry fluorescence cuvette, 1975 μL of buffer (10 mM phosphate buffer, pH = 6.4) was taken with 25 μL of vesicles and placed on the fluorescence instrument (t = 0 s) equipped with a magnetic stirrer. The fluorescence emission intensity of HPTS dye (F_t) was monitored at λ_{em} = 510 nm (λ_{ex} = 450 nm) after adding compound **1** at t = 100 s. Finally, at t = 150 s, 25 μL of 10% Triton X-100 was added to the cuvette to lyze the vesicles in order to achieve 100 % fluorescence activity of HPTS dye.

The time axis was normalized according to Equation 1

$$t = t - 100 \qquad \text{Equation 1}$$

The time-dependent data were normalized to percent change in fluorescence intensity using Equation 2.

$$I_F = [(I_t - I_0) / (I_\infty - I_0)] \times (-100) \qquad \text{Equation 2}$$

where, I_0 is the initial intensity, I_t is the intensity at time t, and I_∞ is the final intensity after the addition of Triton X-100.

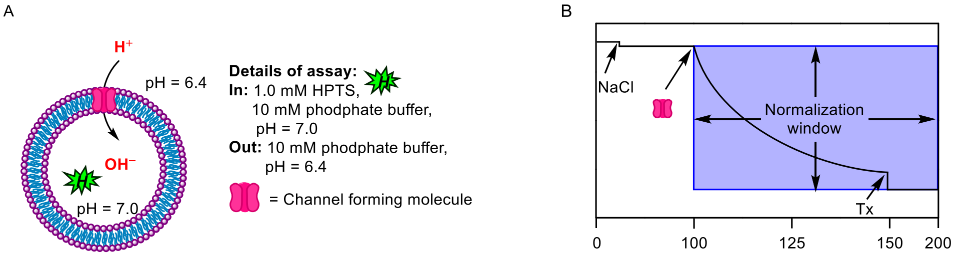

Figure 5.8 Schematic illustration of proton transport activity using EYPC–LUVs⊃HPTS (A), representative fluorescence kinetics experiment of proton transport (B).

Concentration-dependent proton influx study:

The fluorescence kinetics was investigated with different concentrations of transporter molecules over the course of time. The Hill plot was analyzed at $t = 30$ s to get effective concentration (EC_{50}, i.e. the concentration of transporter required to achieve 50% transport activity) and Hill coefficient (n) by using the Hill equation.

$$Y = Y_\infty + (Y_0 - Y_\infty) / [1 + (c/EC_{50})^n] \qquad \text{Equation 3}$$

where, Y_0 = fluorescence intensity just before the channel addition ($t = 0$ s), Y_∞ = fluorescence intensity with excess channel concentration, c = concentration of channel compound, and n = Hill coefficient.

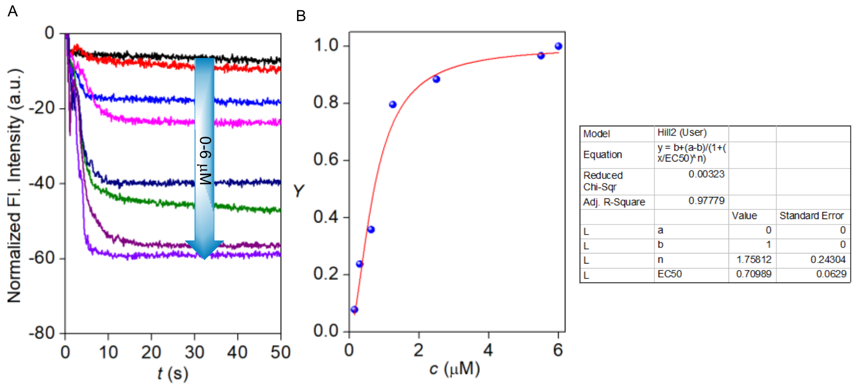

Model	Hill2 (User)		
Equation	y = b+(a-b)/(1+(x/EC50)^n)		
Reduced Chi-Sqr	0.00323		
Adj. R-Square	0.97779		
		Value	Standard Error
L	a	0	0
L	b	1	0
L	n	1.75812	0.24304
L	EC50	0.70989	0.0629

Figure 5.9 Concentration-dependent proton transport study of compound **1** across EYPC–LUVs⊃HPTS (A), and Hill plot analysis of compound **1** at $t = 30$ s (B).

5.4.6.2. pH dependent proton influxing activity studies across EYPC–LUVs⊃HPTS

Buffer and stock solution preparation: 10 mM buffers (10 mM citrate buffer for pH = 3.0, 4.0; 10 mM phosphate buffer for pH = 5.0, 6.4) were prepared by dissolving an accurate amount of salts in autoclaved water. The pH was maintained by adding NaOH solution. All stock solutions of compound **1** were prepared in HPLC grade DMSO solvent for HPTS-based transport studies.

Preparation of EYPC–LUVs⊃HPTS: Vesicles were prepared according to the reported protocol.[24] Final conditions: ~ 5.0 mM EYPC, Inside: 1 mM HPTS, 10 mM phosphate buffer, pH = 7.0, Outside: 10 mM phosphate buffer, pH = 7.0.

Assay details: In a clean and dry fluorescence cuvette, 1975 µL of buffer (10 mM citrate buffer or phosphate buffer, pH = 3.0 or 4.0 or 5.0 or 6.4) was taken with 25 µL of vesicles and placed on the fluorescence instrument (t = 0 s) equipped with a magnetic stirrer. The fluorescence emission intensity of HPTS dye (F_t) was monitored at λ_{em} = 510 nm (λ_{ex} = 450 nm) after the addition of compound **1** at t = 100 s. Finally, at t = 150 s, 25 µL of 10% Triton X-100 was added to the cuvette to lyze the vesicles in order to achieve 100 % fluorescence activity of HPTS dye.

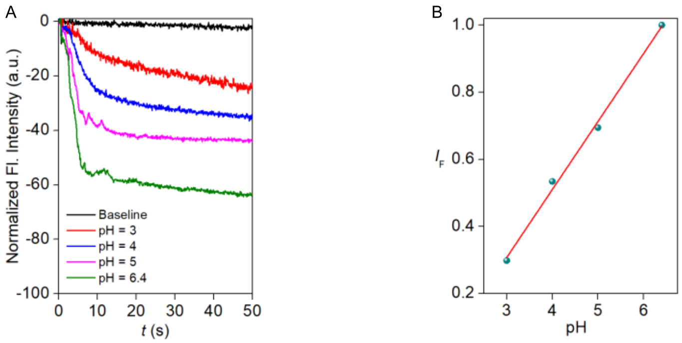

Figure 5.10 pH-dependent proton influx of compound **1** (625 nM) across EYPC–LUVs⊃HPTS (A), and correlation of the transport activity with extravesicular pH changes (B).

5.4.6.3. Ion selectivity study across EYPC–LUVs⊃HPTS

5.4.6.3.1. Anion selectivity

Buffer and stock solution preparation: Different NaX (where, X^- = Cl^-, Br^-, NO_3^-, and OAc^-) buffer (10 mM HEPES, 100 mM NaX, pH = 7.0) was prepared by dissolving an accurate amount of solid HEPES in autoclaved water. Then, the required amount of solid NaX salt was dissolved into it, and finally, the pH was maintained at 7.0 by the addition of NaOH solution. All stock solutions of compound **1** were prepared in HPLC grade DMSO solvent for ion selectivity studies.

Anion selectivity assay: In a clean and dry fluorescence cuvette, 1975 µL of NaX buffer and 25 µL of vesicles were taken and placed on the fluorescence instrument (t = 0 s) equipped with a magnetic stirrer. At

t = 20 s, 20 μL of 0.5 M NaOH solution was added to it to create a pH gradient across the lipid bilayer membrane (pH_{in} = 7.0 and pH_{out} = 7.8). Channel-forming compound **1** (625 nM) was added at t =100 s, and the fluorescence emission intensity of HPTS was monitored at λ_{em} = 510 nm (λ_{ex} = 450 nm) over the course of time. Finally, at t = 300 s 25 μL of 10%, Triton X-100 was added to lyze the vesicle for the complete distraction of pH gradient across the lipid bilayer.

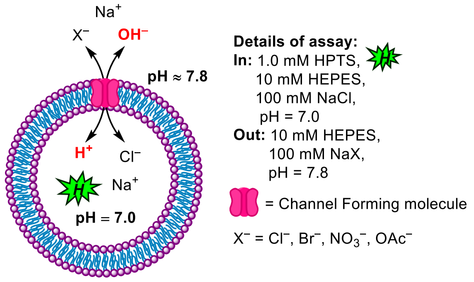

Figure 5.11 Schematic illustration of anion selectivity assay of compound **1** using EYPC–LUVs⊃HPTS.

The time-dependent data were normalized to percent change in fluorescence intensity using Equation 4:

$$I_F = [(I_t - I_0) / (I_\infty - I_0)] \times (100) \qquad \text{Equation 4}$$

where, I_0 is the initial intensity, I_t is the intensity at time t, and I_∞ is the final intensity after the addition of Triton X-100.

5.4.6.3.2. Cation selectivity

Buffer and stock solution preparation: Different MCl (M^+ = Li^+, Na^+, K^+, Rb^+, and Cs^+) buffer (10 mM HEPES, 100 mM MCl, pH = 7.0) was prepared by dissolving an accurate amount of solid HEPES in autoclaved water. Then, the required amount of solid MCl salt was dissolved into it, and finally, the pH was maintained at 7.0 by the addition of NaOH solution. All stock solutions of compound **1** were prepared in HPLC grade DMSO solvent for ion selectivity studies.

Cation selectivity assay: In a clean and dry fluorescence cuvette, 1975 μL of MCl buffer and 25 μL of vesicles were taken and placed on the fluorescence instrument (t = 0 s) equipped with a magnetic stirrer. At t = 20 s, 20 μL of 0.5 M NaOH solution was added to it to create a pH gradient across the lipid bilayer membrane (pH_{in} = 7.0 and pH_{out} = 7.8). Channel-forming compound **1** (625 nM) was added at t =100 s, and the fluorescence emission intensity of HPTS was monitored at λ_{em} = 510 nm (λ_{ex} = 450 nm) over the course of time. Finally, at t = 300 s 25 μL of 10%, Triton X-100 was added to lyze the vesicle for the complete distraction of pH gradient across the lipid bilayer.

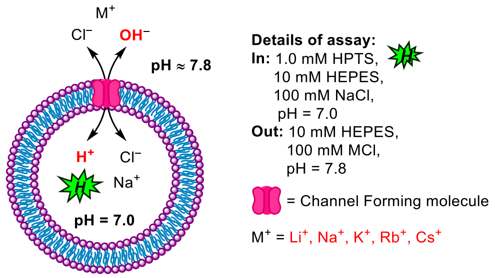

Figure 5.12 Schematic illustration of cation selectivity assay of compound **1** using EYPC–LUVs⊃HPTS.

5.4.6.4. Transport assays across EYPC–LUVs⊃Lucigenin

Buffer and stock solution preparation: $NaNO_3$ buffer (10 mM HEPES, 200 mM $NaNO_3$, pH = 7.0) was prepared by dissolving an accurate amount of solid HEPES in autoclaved water. Then, the required amount of solid $NaNO_3$ salt was dissolved into it, and finally, the pH was maintained at 7.0 by the addition of NaOH solution. All stock solutions of compound **1** were prepared in HPLC grade ACN solvent for lucigenin studies.

Preparation of EYPC–LUVs⊃Lucigenin: Vesicles were prepared according to the reported protocol.[24]

Cl^- influx study of compound 1 across EYPC–LUVs⊃Lucigenin

In a dry and clean fluorescence cuvette, 1975 μL of $NaNO_3$ buffer and 25 μL of vesicles were taken and placed in the fluorescence instrument (t = 0 s) equipped with a magnetic stirrer. An ionic gradient between extra- and intravesicular medium was created by adding 33.3 μL of 2 M NaCl salt in the cuvette at t = 20 s. Further, at t = 100 s channel forming molecule **1** was added with different concentrations and the fluorescence emission intensity of lucigenin was monitored at λ_{em} = 535 nm (λ_{ex} = 455 nm) over the course of time. Finally, at t = 300 s 25 μL of 10%, Triton-X 100 was added into the cuvette for the complete destruction of the chloride gradient.

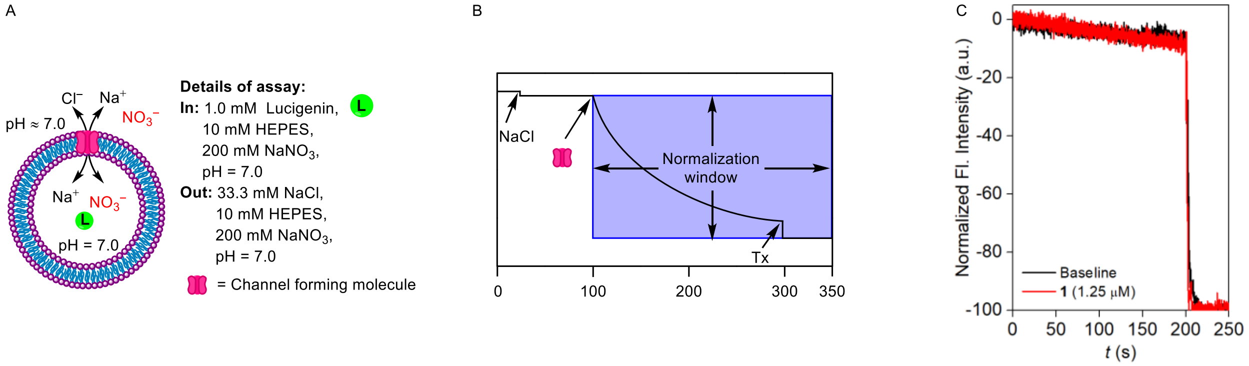

Figure 5.13 Schematic representation of ion transport activity across EYPC–LUVs⊃lucigenin vesicle (A), and normalization window for same fluorescence kinetics experiment of ion transport (B). Chloride influx by compound **1** across EYPC–LUVs⊃Lucigenin (C).

5.4.6.5. Safranin O assay[17]

Buffer and stock solution preparation: Different HEPES buffers (10 mM HEPES, pH = 6.4 and 10 mM HEPES, pH = 7.0) were prepared by dissolving an accurate amount of solid HEPES in autoclaved water. Then, the pH was maintained by adding NaOH solution. All stock solutions of compound **1** were prepared in HPLC grade DMSO solvent for ion selectivity studies.

Preparation of vesicles: In a dry and clean 10 mL round bottom flux, 1 mL of egg yolk phosphatidylcholine (EYPC, 25 mg/mL in $CHCl_3$) was dried by purging nitrogen gas with continuous rotation to make a thin transparent film of EYPC. Then, to remove a trace amount of $CHCl_3$, it was kept under a high vacuum for 4 h. Further, the dried thin film was hydrated with 1 mL HEPES buffer (10 mM HEPES, pH = 7.0), and the suspension was vortexed for 1 h at 10 min intervals. This hydrated suspension was subjected to 23 cycles of freeze-thaw (liquid N_2 and 55 °C hot water bath) followed by extrusion through 200 nm pore size containing polycarbonate membrane 23 times (must be an odd number) in order to achieve uniform distribution of LUVs of an average 200 nm diameter. Collected vesicles were diluted to 6 mL. Final conditions: ~ 5.0 mM EYPC, Inside: 10 mM HEPES, pH = 7.0, Outside: 10 mM HEPES, pH = 7.0.

Assay details: In clean and dry fluorescence cuvette, 1950 µL $NaNO_3$ buffer solution (10 mM HEPES, pH = 6.4), 50 µL vesicles, and Safranin O (400 nM) were taken and slowly stirred in a fluorescence instrument equipped with a magnetic stirrer (at t = 0 s). Channel-forming molecule **1** at different concentrations was added at t = 50 s, and the time-dependent fluorescence intensity of Safranin O was monitored at λ_{em} = 581 nm (λ_{ex} = 522 nm) up to t = 700 s.

The X-axis was normalized by following Equation 5

$$t = t - 50 \qquad \text{Equation 5}$$

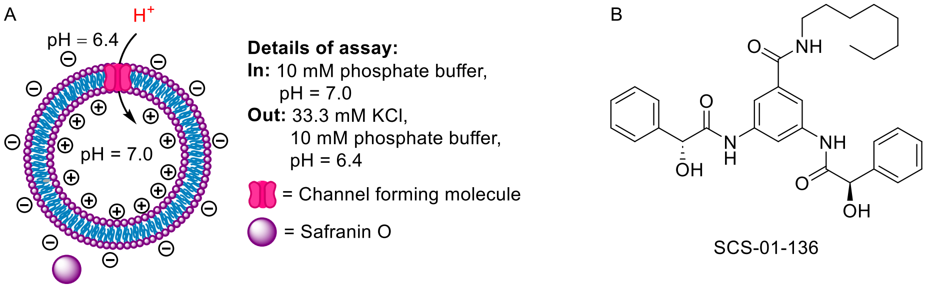

Figure 5.14 Schematic illustration of Safranin O assay using EYPC–LUVs (A) and the structure of control compound SCS-01-136 used in Safranin O assay (B).

5.4.6.6. Proton transport assay[22]

Buffer and stock solution preparation: NaCl buffer (10 mM HEPES, 100 mM NaCl, pH = 7.0) and Na_2SO_4 buffer (10 mM HEPES, 66.6 mM Na_2SO_4, pH = 7.0) were prepared by dissolving an accurate amount of solid HEPES in autoclaved water. Then, the required amount of solid NaCl or Na_2SO_4 salt was dissolved into it, and finally, the pH was maintained at 7.0 by the addition of NaOH solution. All stock solutions of compound **1** were prepared in HPLC grade DMSO solvent for ion selectivity studies.

Preparation of vesicles: Vesicles were prepared by using the reported literature protocol.[22]

Final conditions: ~ 5.0 mM EYPC, Inside: 10 mM HEPES, 100 mM NaCl, pH = 7.0, Outside: 10 mM HEPES, 66.6 mM NaCl, pH = 7.0.

Assay details: In a clean and dry fluorescence cuvette, 1975 µL of Na_2SO_4 buffer (10 mM HEPES, 66.6 mM Na_2SO_4, pH = 7.0) was taken with 25 µL of vesicles and placed on the fluorescence instrument (t = 0 s) equipped with a magnetic stirrer. At t = 20 s, 20 µL of 0.5 M NaOH solution was added to create a pH gradient between the intravesicular and extravesicular medium ($\Delta pH \approx 0.8$). The fluorescence emission intensity of HPTS dye (F_t) was monitored at λ_{em} = 510 nm (λ_{ex} = 450 nm) after the addition of the channel-forming molecule **1** (625 nM) at t = 100 s. Finally, at t = 300 s, 25 µL of 10% Triton X-100 was added to the cuvette to lyze the vesicles in order to achieve 100 % fluorescence activity of HPTS dye.

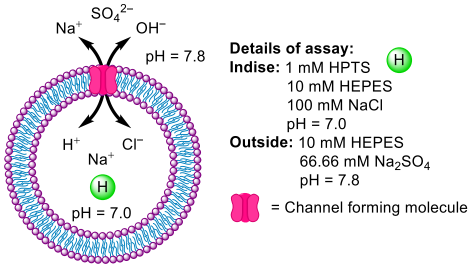

Figure 5.15 Schematic illustration of proton transport assay using EYPC–LUVs.

5.4.6.7. Proton transport assay by pH electrode

Buffer and stock solution preparation: Buffer solutions (300 mM KGluconate, 10 mM phosphate buffer or tris buffer, pH = 4.0 or 7.0 or 10.0) were prepared by dissolving the required amount of solid KGluconate salt along with the salts required to make the respective buffers. Finally, the pH was maintained by adding NaOH or HCl solution. All stock solutions of compound **1** were prepared in HPLC grade DMSO solvent for the study.

Preparation of vesicles: In a 10 mL round bottom flask, 1 mL EYPC chloroform solution (25 mg/mL) was taken. A lipid−thin layer was created by the slow purging of the nitrogen gas. It was further dried under a high vacuum pump for 4 h to remove traces of chloroform. Then, the lipid was rehydrated by intravesicular KGluconate buffer solution (300 mM KGluconate, 10 mM phosphate buffer, pH = 4.0 or 300 mM KGluconate, 10 mM tris buffer, pH = 7.0) and subjected to a vortex to mix lipid suspension properly. 23 freeze−thaw cycles were performed on the lipid suspension by alternatingly freezing lipid suspension in −78 °C liquid nitrogen, thawing to a 55 °C water bath, and keeping it for aging for 10 min. The suspension was extruded 23 times through a 200 nm polycarbonate membrane (Whatman NucleporeTM). Subsequently, the vesicles were dialyzed (Spectra/Pore® membrane MWCO 1 kD) twice against the required extravesicular solution (300 mM KGluconate, 10 mM phosphate buffer, pH = 7.0 or 300 mM KGluconate, 10 mM tris buffer, pH = 10.0) to replace the extravesicular solutions with the required buffers.

Final conditions: ≈ 32.4 mM EYPC, Inside: 10 mM phosphate buffer, 300 mM KGluconate, pH = 4.0 or 10 mM tris buffer, 300 mM KGluconate, pH = 7.0, Outside: 10 mM phosphate buffer, 300 mM KGluconate, pH = 7.0 or 10 mM tris buffer, 300 mM KGluconate, pH = 10.0.

Assay details: In a clean and dry three naked glass cuvettes, 1900 µL of required extravesicular buffer (10 mM phosphate buffer, 300 mM KGluconate, pH = 7.0 or 10 mM tris buffer, 300 mM KGluconate, pH = 10.0) and 100 µL of vesicles were added (*t* = 0 s) equipped with a magnetic stirrer. pH change was monitored with a pH electrode. At *t* = 50 s, valinomycin (1 µM) and *t* = 100 s, the channel-forming molecule **1** (5.5 µM) was added into it. Finally, at *t* = 300 s, 25 µL of 10% Triton X-100 was added to the cuvette to lyze the vesicles in order to achieve maximum pH change.

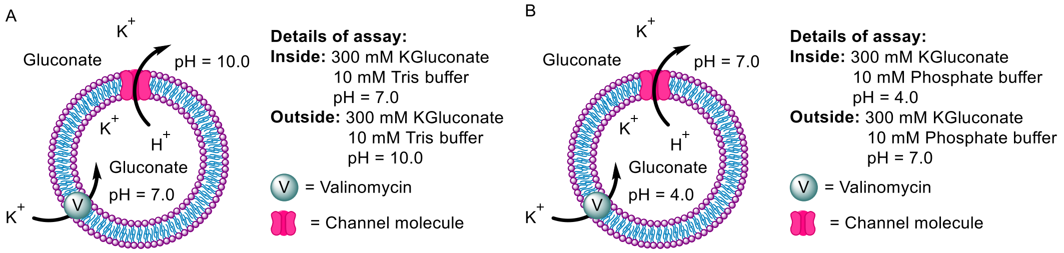

Figure 5.16 Schematic representation of the proton transport assay by pH electrode in the presence of valinomycin under two different experimental conditions (A, B).

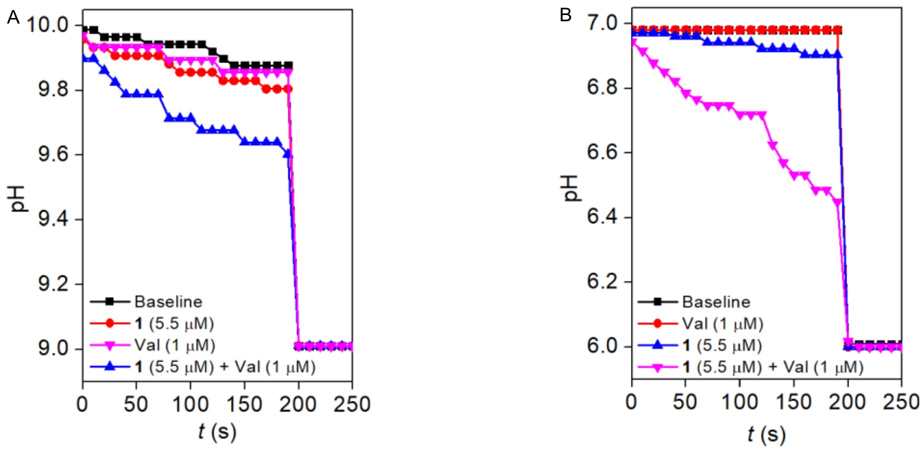

Figure 5.17 Change in the pH during proton transport by compound **1** in the presence of valinomycin with $pH_{int} = 7.0$, $pH_{out} = 10.0$ (A) and $pH_{int} = 4.0$, $pH_{out} = 7.0$ (B).

5.4.6.8. Evaluation of membrane stability and channel nature

5.4.6.8.1 CF leakage assay[24]

Preparation of EYPC-LUVs⊃CF vesicles: In a clean and dry small (10 mL) round bottom flask, 0.5 mL egg yolk phosphatidylcholine (EYPC, 25 mg/mL stock in $CHCl_3$) was added. A thin lipid film was prepared by evaporating a solution of EYPC lipid by purging the N_2 flow and keeping it for the high vacuum for 4 h to remove a trace amount of $CHCl_3$. After that lipid film was hydrated with 0.5 mL buffer (10 mM HEPES, 10 mM NaCl, 50 mM CF, pH 7.0) for 1 h with occasional vortexing of 4-5 times and then subjected to freeze-thaw cycle (≥ 20 times). The vesicle solution was extruded through a polycarbonate membrane with 200 nm pores 23 times (has to be an odd number. The extracellular dye was removed by size exclusion chromatography (Sephadex G-50) with HEPES buffer (10 mM HEPES, 100 mM NaCl, pH 7.0). Final concentration: ~ 2.5 mM EYPC lipid; intravesicular solution: 10 mM HEPES, 10 mM NaCl, 50 mM CF, pH 7.0; extravesicular solution: 10 mM HEPES, 100 mM NaCl, pH 7.0.

CF assay details: In clean and dry fluorescence cuvette, 1950 μL of HEPES buffer solution (10 mM HEPES, 100 mM NaCl, pH 7.0) and 50 μL EYPC–LUVs⊃CF were taken. The suspension was kept in a slow stirring condition in the fluorescence instrument equipped with a magnetic stirrer at t = 0 s. The fluorescence intensity was monitored as a course of time at λ_{em} = 517 nm (λ_{ex} = 492 nm). At t = 100 s channel, channel-forming molecule compound **1** was added to it at different concentrations. Finally, vesicles were lysed by the addition of 10% Triton X–100 (25 μL) at t = 300 s for 100% efflux of CF dyes. The time-dependent data were normalized to fractional (in percentage) fluorescence intensity using Eq. S2 and time axis (X–axis) were normalized using Equation 1.

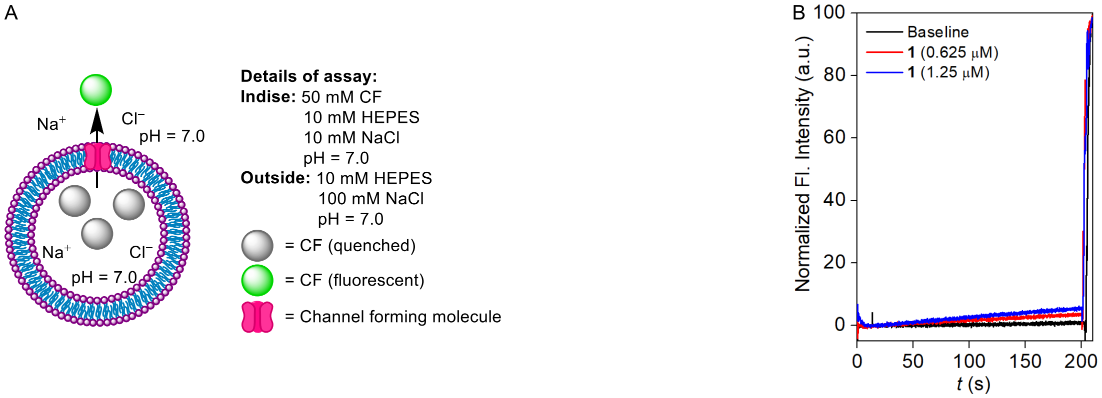

Figure 5.18 Schematic representation of CF assay across EYPC–LUVs⊃CF (A) and fluorescence kinetics experiment of channel-forming compound **1** at different concentrations (B).

5.4.6.8.2 Calcein leakage assay[24]

EYPC–LUVs were loaded with self-quenching dye calcein (50 mM). At high concentrations, calcein shows self-fluorescence quenching, but the efflux of calcein through pores formed by compound **1** was followed by an increase in calcein fluorescence emission intensity. Two different buffer solutions were prepared for the assay. Buffer A: 10 mM HEPES, pH = 7.0; Buffer B: 10 mM HEPES, 150 mM NaCl, pH = 7.0.

Preparation of EYPC–LUVs⊃calcein vesicles: A thin film of EYPC lipid was prepared by evaporating 0.5 ml of EYPC lipid solution (25 mg/mL) in $CHCl_3$ by the flow of nitrogen, and then it was kept in vacuo (4 h) to remove trace amount of $CHCl_3$. After 4 h it was hydrated with 50 mM calcein dissolved in 0.5 mL buffer A, followed by vortex treatment at 10 min intervals for 1 h. This hydrated suspension was subjected to 21 cycles of freeze-thaw (liquid N_2, 55 °C) followed by extrusion through 200 nm pore size containing polycarbonate membrane 21 times (must be an odd number), in order to achieve the vesicles of an average 200 nm diameter. Extravehicular calcein dyes were removed by gel filtration (using Sephadex G-50) with buffer A solution (10 mM HEPES, pH = 7.0), and diluted with the same buffer to 3 mL to get EYPC–LUVs⊃Calcein.

Calcein assay: In clean and dry fluorescence cuvette, 1950 µL of buffer B solution (10 mM HEPES, 150 mM NaCl, pH = 7.0.) and 50 µL EYPC–LUVs⊃Calcein were taken. The suspension was kept in a slow stirring condition in the fluorescence instrument equipped with a magnetic stirrer at $t = 0$ s. The fluorescence intensity was monitored as a course of time at $\lambda_{em} = 520$ nm ($\lambda_{ex} = 490$ nm). At $t = 100$ s, channel forming molecule **1** was added into it at different concentrations. Finally, vesicles were lysed by the addition of 10% Triton X–100 (25 µL) at $t = 300$ s for 100% efflux of calcein dyes. The time-dependent data were normalized to fractional (in percentage) fluorescence intensity using Equation 4, and the time axis (X–axis) was normalized using Equation 1.

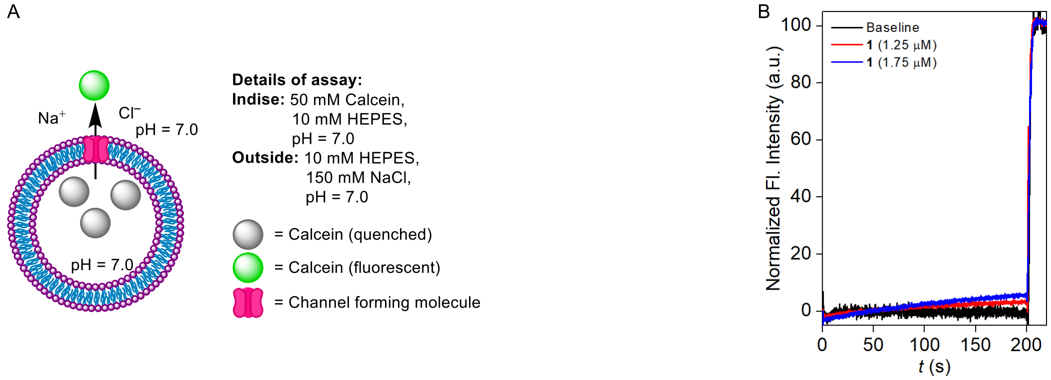

Figure 5.19 Schematic representation of calcein assay across EYPC–LUVs⊃calcein (A) and fluorescence kinetics experiment of channel forming compound **1** at different concentrations (B).

5.4.6.9. Assessment of water transportation ability[23]

Buffer and stock solution preparation: HEPES buffers (10 mM HEPES, 100 mM KCl, pH = 7.0 and 800 mM sucrose, 10 mM HEPES, 100 mM NaCl, pH 7.0) was prepared by dissolving an accurate amount of solid HEPES in autoclaved water. Then, the required amount of solid NaCl and sucrose were dissolved into it, and finally, the pH was maintained at 7.0 by adding NaOH solution.

Vesicle preparation for water transport assay: Initially, 0.5 mL of a DOPC lipid solution (25 mg/mL in chloroform) was added into a 10 mL round-bottom flask, after which a requisite quantity of the channel-forming molecule (expressed as mol% relative to the lipid) in chloroform was incorporated. Subsequently, the trace amount of chloroform present in the compound-lipid mixture was removed by a gentle stream of nitrogen gas to form a thin lipid film. Thereafter, any residual chloroform in the compound-lipid preparation was removed by subjecting the mixture for 4 h to high vacuum conditions. The resulting thin lipid film was then rehydrated with a buffer solution (0.5 mM CF, 10 mM HEPES, 100 mM NaCl, at a pH of 7.0) followed by a sequence vortexing conducted 6 times (each for a duration of 10 min). Subsequently, the hydrated vesicle suspension underwent 23 freeze-thaw cycles utilizing liquid nitrogen and a water bath maintained at 55 °C, after which extrusions were performed 23 times (must be an odd number) through a 200 nm polycarbonate membrane. The extruded vesicles were then diluted to a final volume of 3 mL with the aforementioned buffer solution (10 mM HEPES, 100 mM NaCl, pH 7.0) to achieve the targeted mol% of the compound relative to lipid, under the assumption of no lipid loss throughout the entirety of the procedure. Final conditions: inside: 0.5 mM CF, 10 mM HEPES, 100 mM NaCl, pH 7.0, outside: 10 mM HEPES, 100 mM NaCl, pH 7.0.

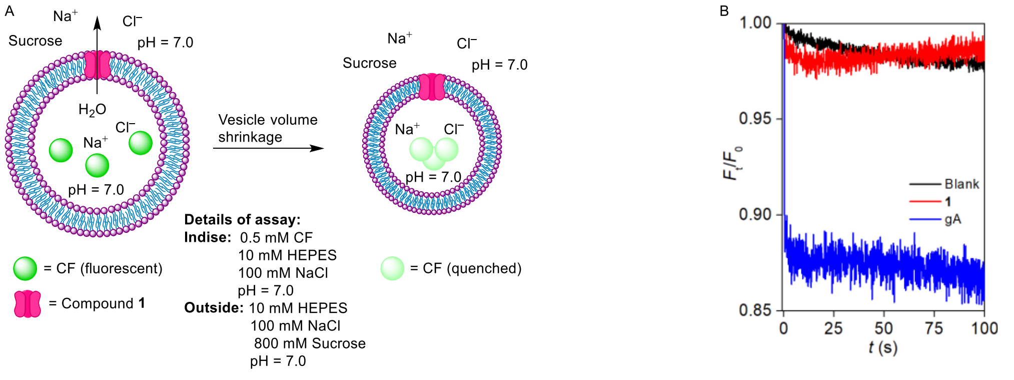

Figure 5.20 Schematic representation of water transport assay across EYPC–LUVs⊃CF (A) and fluorescence kinetics experiment for water transport by channel forming compound **1** (0.924 mol%) and gramicidin (0.000000000148 mol%) (B).

Assay detail for water transport studies: The above-mentioned vesicle solution was mixed to an equal volume of 800 mM sucrose solution (800 mM sucrose, 10 mM HEPES, 100 mM NaCl, pH

7.0) by using the spex® stopped-flow accessory. The shrinkage in the size of the vesicles was monitored through a change in CF fluorescence intensity with time at λ_{em} = 517 nm (λ_{ex} = 492 nm), which was monitored on a Horiba FluoroMax+ instrument.

5.4.6.10. Ligand-gated reversible OFF–ON ion transport activity

Buffer and stock solution preparation: HEPES buffer (10 mM HEPES, pH = 7.0) was prepared by dissolving an accurate amount of solid HEPES in autoclaved water. Then, the pH was maintained at 7.0 by adding NaOH solution. All stock solutions of compound **1** were prepared in HPLC grade DMSO solvent for ligand-gated reversible OFF-ON ion transport studies.

Preparation of EYPC–LUVs⊃HPTS: Vesicles were prepared according to the reported protocol.[24] Final conditions: ~ 5.0 mM EYPC, Inside: 1 mM HPTS, 10 mM HEPES, pH = 7.0, Outside: 10 mM HEPES, pH = 7.0.

Ion transport activity: In a clean and dry fluorescence cuvette, 25 μL of vesicles, 1975 μL of HEPES buffer (10 mM HEPES, pH = 7.0) and compound **1** (5 μM) were taken with and placed on the fluorescence instrument (*t* = 0 s) equipped with a magnetic stirrer. At *t* = 20 s, 20 μL of 0.5 M NaOH solution was added to initiate the ion transport process by creating a pH gradient between the intravesicular and extravesicular medium. The fluorescence emission intensity of HPTS dye (F_t) was monitored at λ_{em} = 510 nm (λ_{ex} = 450 nm). 0.5 equiv of $CuCl_2$ and 0.6 equiv of EDTA were sequentially added at 2 min intervals to turn OFF and turn ON the transport activity, respectively. Finally, at *t* = 620 s, 25 μL of 10% Triton X-100 was added to the cuvette to lyze the vesicles in order to achieve 100 % fluorescence activity of HPTS dye.

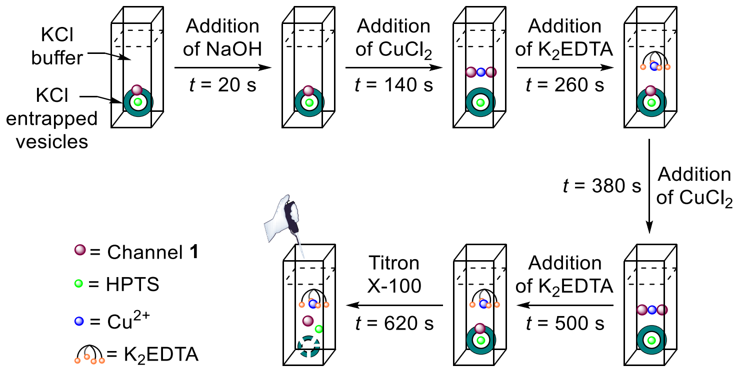

Figure 5.21 Schematic illustration of assay details of reversible OFF–ON proton transport activity of channel forming compound **1** across EYPC–LUVs⊃HPTS.

The time axis was normalized according to Equation 6

$$t = t - 20 \qquad \text{Equation 6}$$

The time-dependent data were normalized to the percent change in fluorescence intensity using Equation 4.

5.4.7. Planar bilayer conductance measurements[16]

Bilayer lipid membrane (BLM) was formed with diphytanoylphosphatidylcholine (dphpc) lipid (Avanti Polar Lipids), dissolved in n-decane (20 mg/mL) across an aperture of 150 μM diameter in a polystyrene cup (Warner Instrument, USA). Both chambers (cis and trans) were filled with a symmetrical 1 M HCl solution. The Cis chamber was connected with BC 535 head-stage (Warner Instrument, USA), and the trans chamber was held at the virtual ground with Ag-AgCl electrodes. Compound **1** (1 μM) was added to the cis chamber, and the solution was stirred with a magnetic stirrer for around 10 min. A distinct square top channel opening and closing events were observed after applying both +ve and –ve voltages. Currents were low pass filtered at 1 kHz using pClamp9 software (Molecular Probes, USA) and an analog-to-digital converter (Digidata 1440, Molecular Probes). All data were analyzed using the software pClamp 10.7.0.3. The average current was calculated from this trace, and then conductance and other calculations were made accordingly.

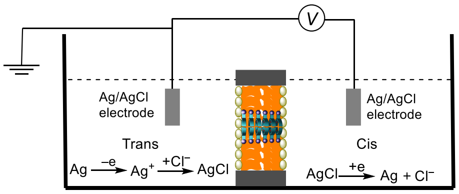

Figure 5.22 Systematic representation of bilayer lipid membrane experiment.

5.4.7.1. Single-channel conductance calculation

To understand the change in the current with a change in the voltage of channel forming compound **1**, a symmetric cis/trans = 1 M HCl/ 1 M HCl setup was used. Interestingly, we found a significant change in the current with changing in the voltage, validating that compound **1** can efficiently flux the proton across the membrane.

The experimentally evaluated average single-channel conductance of channel **1** was found to be 457.4 pS (Figure 5.5C).

5.4.7.2. Ligand-gated reversible OFF-ON proton channel activity

To address the ligand-gated OFF-ON transport activity of the proton channel, electrophysiological experiments were carried out with compound **1**. Compound **1** (1 μM) was added in the cis chamber during the electrophysiological experiment, and both the opening-closing event and *I-V* plot were noticed over a period of time. To turn OFF the proton channel activity of compound **1**, 0.5 equiv. of $CuCl_2$ (0.5 μM) as a water solution was added into the cis chamber. Interestingly, an instant turn OFF the opening-closing event was noticed, verifying that the proton channel activity of compound **1** was diminished in the presence of $CuCl_2$. Additionally, a decrease in the *I-V* plot was noticed after adding $CuCl_2$ in the cis chamber, clarifying that there was minimal current flow in the presence of $CuCl_2$. Further, to turn ON the ion channel activity of compound **1**, 0.6 equiv. of the K_2EDTA was added in the cis chamber. It is expected that K_2EDTA will bind the Cu^{2+} ion and make the compound **1** free. Hence, it can regenerate the self-assembled parallel rosette proton channel structure in the membrane, initiate the opening-closing events and initiate the current flow across the membrane. Interestingly, we noticed significant channel opening-closing events after adding the K_2EDTA in the cis chamber, verifying the regeneration of the self-assembled proton channel structure in the membrane. It was also noteworthy that the current flow also increased, which was evident from the *I-V* plot, validating that compound **1** regenerated its efficiency in its proton flow across the membrane.

5.4.8. Single crystal X-ray diffraction study

The single crystals of compound **1** were grown from acetonitrile allowing slow evaporation of the MeOH solvent with time. X-ray diffraction data on single crystals of **1** was collected on a Bruker D8 Venture Duo X-ray diffractometer equipped with a Microfocus X-ray source (operated at 50 W; 50 kV/1 mA) and graded multilayer optics for monochromatic Mo Kα radiation (λ = 0.71073 Å) with a focused X-ray beam and a Photon 100 CMOS chip based detector system at 150 K. The crystal was mounted on nylon Cryo Loops (Hampton Research) with Paraton-N (Hampton Research). The data integration and reduction were processed with SAINT software.1 A multi-scan absorption correction was applied to the collected reflections. The structure was solved by a direct method using SHELXTL3,4 and was refined on F2 with a full-matrix least squares technique using the SHELXL 5 program package. All of the hydrogen atoms were refined anisotropically. All of the hydrogen atoms were located in successive difference fourier maps, and they were treated as riding atoms using SHELXL default parameters. The structures were examined using the Adsym subroutine in PLATON to ensure that no additional symmetries could be applied to the models.

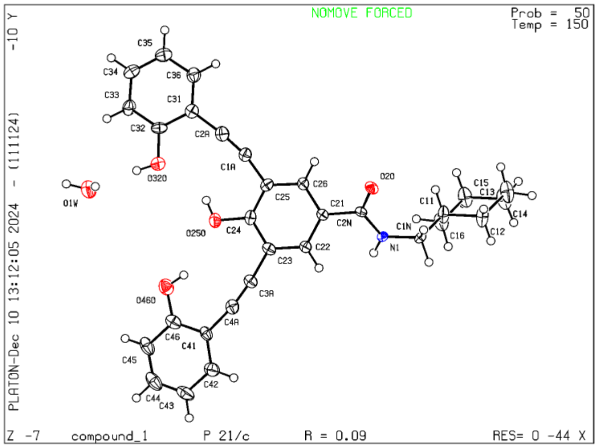

Figure 5.23 Ellipsoid plot of the crystal structure of compound **1**.

Table 5.1 Crystal data and structure refinement for compound_1

Identification code	Compound_1
Empirical formula	C30 H29 N O5
Formula weight	483.54
Temperature	150(2) K
Wavelength	0.71073 Å
Crystal system	Monoclinic
Space group	P 21/c
Unit cell dimensions	a = 24.237(13) Å α= 90°. b = 5.020(3) Å β= 108.007(15)°. c = 21.289(11) Å γ = 90°.
Volume	2463(2) Å^3
Z	4
Density (calculated)	1.304 Mg/m^3
Absorption coefficient	0.089 mm^{-1}
F(000)	1024
Crystal size	0.34 x 0.21 x 0.15 mm^3
Theta range for data collection	1.931 to 25.106°.
Index ranges	-28<=h<=28, -5<=k<=5, -25<=l<=23
Reflections collected	51439
Independent reflections	4320 [R(int) = 0.2316]
Completeness to theta = 25.106°	99.2 %
Absorption correction	Semi-empirical from equivalents
Max. and min. transmission	0.7452 and 0.5029
Refinement method	Full-matrix least-squares on F^2
Data / restraints / parameters	4320 / 0 / 332
Goodness-of-fit on F^2	1.054
Final R indices [I>2sigma(I)]	R1 = 0.0861, wR2 = 0.1736
R indices (all data)	R1 = 0.1507, wR2 = 0.2008
Extinction coefficient	0.0016(8)
Largest diff. peak and hole	0.913 and -0.335 e.Å^{-3}

5.4.9. Theoretical studies

5.4.9.1. System setup and simulation model

Initially, the synthetic channel structure, comprising 12 monomers organized in six consecutive layers, was subjected to minimization using the MAESTRO software.[25] Subsequently, the semi-minimized channel structure was utilized to construct the channel/membrane assembly using the membrane builder protocol of CHARMM-GUI,[26,27] following the reported guidelines.[28] This process involved object reading, appropriate orientation, and packing within the lipid bilayer assembly after determining the system size. The resulting channel/membrane complex featured the self-assembled channel structure positioned centrally within the lipid bilayer membrane, comprising six repetitive layers built with 12 monomers in total. The membrane bilayer consisted of 1,2-diphytanoyl-sn-glycero-3-phosphocholine (DPhPC) lipids, totaling 144 units evenly distributed across each leaflet (with each leaflet containing 72 lipid units). Subsequently, the channel/membrane complex was enclosed within a rectangular box measuring 7.7 × 7.7 × 9.0 nm^3. The system was then solvated with sufficient water to maintain a 1 M KCl salt concentration in each aqueous compartment, separated by the lipid bilayer. Detailed simulation system specifications are provided in Table 5.2. The channel structure was modeled using the general AMBER forcefield (GAFF),[29–31] while the lipid membrane employed CHARMM36m forcefield parameters.[32–34] Water molecules were represented using CHARMM-TIP3P parameters.[35]

Table 5.2 Details of the simulation system with compound **1**.

Box dimension	No. of water molecules	No. of K^+ ions	No. of Cl^- ions
7.7×7.7×9.0 nm^3	9771	175	175

5.4.9.2. Simulation method

All simulations were conducted under periodic boundary conditions (PBC) in all three dimensions (along X, Y, and Z axis). For handling long-range electrostatic interactions, the particle mesh Ewald (PME) method[35] with cubic interpolation was employed. Short-range electrostatic interactions were truncated at 1.2 nm. Neighbour lists were updated every 20 steps. The LINCS algorithm[36] was utilized to constrain hydrogen bonds within membrane and channel monomers, while the SETTLE algorithm[37] was applied to maintain water molecule rigidity during simulation. Lennard Jones interactions were truncated at a distance of 1.2 nm using the Verlet cut-off scheme[38] with dispersion corrections. Initially, the system underwent energy minimization with specific restraints via the steepest-descent algorithm, followed by six successive equilibration steps of 10 ns each. During equilibration, the restraints on the system were gradually lowered in each consecutive step. An average temperature of 298 K and pressure of 1.0 bar were maintained during the equilibration process using the Berendsen thermostat[39] and Berendsen barostat.

After equilibration, each system underwent a final NPT production run for 1.0 µs under slight restraint conditions applied to each channel structure. During production simulation, the average temperature of 298 K was maintained using the Nose-Hoover thermostat[40] with a relaxation constant of 1.0 ps, individually coupling the channel structure, membrane bilayer, and solvent. The pressure was maintained at 1.0 bar using the Parrinello-Rahman barostat[41] with a coupling constant of 5 ps and a compressibility factor of 4.5

× 10^{-5} bar under semi-isotropic coupling conditions (coupled separately along the XY and Z directions) to ensure a tensionless bilayer during the simulation. A time step of 2 fs (during the production run) was chosen utilizing the leapfrog integrator. All simulations were performed using GROMACS software version 20x.

[Note: All MD simulation studies in this chapter were carried out by Dr. Jagannath Mondal and associates from TIFR Hyderabad.]

5.5. References

(1) Aoi, W.; Marunaka, Y. *Biomed Res. Int.* **2014**, *2014*, 598986.

(2) Silverstein, T. P. *Front. Mol. Biosci.* **2021**, *8*, 764099.

(3) Freeman, S. A.; Grinstein, S.; Orlowski, J. *Physiol. Rev.* **2023**, *103*, 515–606.

(4) Harlan E. Ives and Floyd C. Rector, J. *J. Clin. Invest.* **1984**, *73*, 285–290.

(5) Casey, J. R.; Grinstein, S.; Orlowski, J. *Nat. Rev. Mol. Cell Biol.* **2010**, *11*, 50–61.

(6) Lanyi, J. K. *J. Biol. Chem.* **1997**, *272*, 31209–31212.

(7) Bondar, A. N.; Elstner, M.; Suhai, S.; Smith, J. C.; Fischer, S. *Structure* **2004**, *12*, 1281–1288.

(8) Luecke, H.; Richter, H. T.; Lanyi, J. K. *Science* **1998**, *280*, 1934–1937.

(9) Faxén, K.; Gilderson, G.; Ädelroth, P.; Brzezinski, P. *Nature* **2005**, *437*, 286–289.

(10) Brändén, G.; Gennis, R. B.; Brzezinski, P. *Biochim. Biophys. Acta* **2006**, *1757*, 1052–1063.

(11) Li, S. J.; Zhao, Q.; Zhou, Q.; Unno, H.; Zhai, Y.; Sun, F. *J. Biol. Chem.* **2010**, *285*, 12047–12054.

(12) Huang, R. B.; Du, Q. S.; Wang, C. H.; Chou, K. C. *Biochem. Biophys. Res. Commun.* **2008**, *377*, 1243–1247.

(13) Ni, C.; Matile, S. *Chem. Commun.* **1998**, 755–756.

(14) Weiss, L. A.; Sakai, N.; Ghebremariam, B.; Ni, C.; Matile, S. *J. Am. Chem. Soc.* **1997**, *119*, 12142–12149.

(15) Si, W.; Chen, L.; Hu, X. B.; Tang, G.; Chen, Z.; Hou, J. L.; Li, Z. T. *Angew. Chem., Int. Ed.* **2011**, *50*, 12564–12568.

(16) Shen, J.; Ye, R.; Liu, Z.; Zeng, H. *Angew. Chem., Int. Ed.* **2022**, *61*, e202200259.

(17) Yan, T.; Liu, S.; Xu, J.; Sun, H.; Yu, S.; Liu, J. *Nano Lett.* **2021**, *21*, 10462–10468.

(18) Li, X.; Zhang, H.; Hou, J.; Ou, R.; Zhu, Y.; Zhao, C.; Qian, T.; Easton, C. D.; Selomulya, C.; Hill, M. R.; Wang, H. *J. Am. Chem. Soc.* **2020**, *142*, 9827–9833.

(19) Wu, C.-Y.; Su, S.; Zhang, X.; Liu, R.; Gong, B.; Lu, Z.-L. *Angew. Chem., Int. Ed.* **2023**, *62*, e202303242.

(20) Malla, J. A.; Upadhyay, A.; Ghosh, P.; Mondal, D.; Mondal, A.; Sharma, S.; Talukdar, P. *Org. Lett.* **2022**, *24*, 4124–4128.

(21) Chattopadhayay, S.; Ghosh, A.; Mukhopadhyay, T. K.; Sharma, R.; Datta, A.; Talukdar, P. *Angew. Chem., Int. Ed.* **2023**, *62*, e202313712.

(22) Mondal, D.; Dandekar, B. R.; Ahmad, M.; Mondal, A.; Mondal, J.; Talukdar, P. *Chem. Sci.* **2022**, *13*, 9614–9623.

(23) Itoh, Y.; Chen, S.; Hirahara, R.; Konda, T.; Aoki, T.; Ueda, T.; Shimada, I.; Cannon, J. J.; Shao, C.; Shiomi, J.; Tabata, K. V.; Noji, H.; Sato, K.; Aida, T. *Science* **2022**, *376*, 738–743.

(24) Chattopadhayay, S.; Banzal, K. V.; Talukdar, P. *Angew. Chem., Int. Ed.* **2024**, e202414354.

(25) S. Schrödinger Release 2022–1: Maestro, LLC, NewYork, **2021** https://www.schrodinger.com.

(26) Klauda, J. B. *J. Chem. Phys.* **2018**, *149*, 220901.

(27) Jo, S.; Kim, T.; Iyer, Vidyashankara, G.; Im, W. J. *J. Comput. Chem.* **2008**, *29*, 1859–1865.

(28) Jo, S.; Lim, J. B.; Klauda, J. B.; Im, W. *Biophys. J.* **2009**, *97*, 50–58.

(29) Wang, J.; Wolf, R. M.; Caldwell, J. W.; Kollman, P. A.; Case, D. A. *J. Comput. Chem.* **2004**, *25*, 1157–1174.

(30) Sprenger, K. G.; Jaeger, V. W.; Pfaendtner, J. *J. Phys. Chem. B* **2015**, *119*, 5882–5895.

(31) Wang, J.; Wolf, R. M.; Caldwell, J. W.; Kollman, P. A.; Case, D. A. *J. Comput. Chem.* **2004**, *25*, 1157–1174.

(32) Klauda, J. B.; Venable, R. M.; Freites, J. A.; O'Connor, J. W.; Tobias, D. J.; Mondragon-Ramirez, C.; Vorobyov, I.; MacKerell, Alexander D., J.; Pastor, R. W. *J. Phys. Chem. B* **2010**, *114*, 7830–7843.

(33) Huang, J.; Rauscher, S.; Nawrocki, G.; Ran, T.; Feig, M.; De Groot, B. L.; Grubmüller, H.; MacKerell, Alexander D., J. *Nat. Methods* **2016**, *14*, 71–73.

(34) Brooks, B.R., Brooks III, C.L., Mackerell Jr., A.D., Nilsson, L., Petrella, R.J., Roux, B., Won, Y., Archontis, G., Bartels, C., Boresch, S., Caflisch, A., Caves, L., Cui, Q., Dinner, A.R., Feig, M., Fischer, S., Gao, J., Hodoscek, M., Im, W. and Kuczer, K. *J. Comput. Chem.* **2009**, *30*, 1545–1614.

(35) Jorgensen, W. L.; Chandrasekhar, Jayaraman Madura, J. D.; Impey, R. W.; Klein, M. L. *Mol. Phys.* **1977**, *34*, 525–537.

(36) Hess, B.; Bekker, H.; Berendsen, H. J. C.; Fraaije, J. G. E. M. *J. Comput. Chem.* **1997**, *18*, 1463–1472.

(37) Miyamoto, S.; Kollman, P. A. *J. Comput. Chem.* **1992**, *13*, 952–962.

(38) Páll, S.; Hess, B. *Comput. Phys. Commun.* **2013**, *184*, 2641–2650.

(39) Berendsen, H. J. C.; Postma, J. P. M.; Van Gunsteren, W. F.; Dinola, A.; Haak, J. R. *J. Chem. Phys.* **1984**, *81*, 3684–3690.

(40) Evans;, D. J.; Holian, B. L. *J. Chem. Phys.* **2008**, *4074*, 4069–4074.

(41) Parrinello, M.; Rahman, A. *J. Appl. Phys.* **1981**, *52*, 7182–7190.

Overall Conclusion

In summary, we have developed small molecule-based synthetic transporter systems that transport ions via a channel mechanism. In **Chapter 2**, we discussed the introduction of the new core motif for efficient cotransport of both cation and anion having profound selectivity towards $K^+ClO_4^-$ ions. In **Chapter 3**, we have demonstrated the new architectural design of "Pinakindole catenane" as a synthetic wobbler ion channel system. NMR studies validated the molecular flipping of the "Pinakindole catenane" in the presence of the Na^+ and Cl^- salts to bind the respective ions in the corresponding ion binding pockets. Detailed ion transport studies indicated that compounds can efficiently transport cation and anion via a symport mechanism by forming an ion channel in the bilayer membrane. In **Chapter 4**, a meta-dipropynylbenzene-based trimeric barrel-rosette ion channel was presented. NMR and transport studies demonstrated its capacity for the synergistic transport of cations and anions via the symport process. The reversible OFF-ON cotransport was facilitated by the sequential addition of $CuCl_2$ and K_2EDTA, representing a pioneering instance of a cation-anion symporter with ligand-gated reversible transport activity. In **Chapter 5**, we introduced the first example of reversible ligand-gated meta-dipropynylbenzene-based dimeric barrel-rosette channel for proton transport. Transport studies confirmed that the dimeric rosette efficiently transports protons through a water wire, exhibiting 1.3 and 2 times increased activity compared to FCCP and gramicidin. The reversible OFF-ON proton transport was mediated by the sequential addition of $CuCl_2$ and K_2EDTA, underscoring its ligand-gated mechanism in proton transport.